POLITECNICO DI MILANO
Dottorato di Ricerca in Bioingegneria
Ph.D. Programme in Bioengineering

Luca Possenti

Modeling of microvasculature in uremic patients

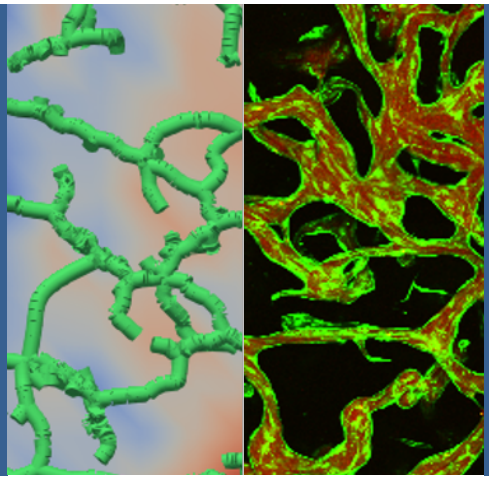

POLITECNICO DI MILANO
DEPARTMENT OF CHEMISTRY, MATERIALS AND CHEMICAL ENGINEERING "GIULIO NATTA"
DOCTORAL PROGRAMME IN BIOENGINEERING

MODELING OF MICROVASCULATURE IN UREMIC PATIENTS

Doctoral Dissertation of:
Luca Possenti

Supervisor:
Prof. Maria Laura Costantino
Prof. Paolo Zunino

Tutor:
Prof. Giancarlo Pennati

The Chair of the Doctoral Program:
Prof. Andrea Aliverti

Year 2018 Cycle XXXI

To my family

'Essentially, all models are wrong,
but some are useful'

George Box

'As the island of knowledge grows,
so do the shore of our ignorance
the boundary between
the known and the unknown'

Marcelo Gleiser

Acknowledgments

At the end of this work, I really want to express my gratitude to all the people that make this possible.

First, I thank my supervisor Prof. Maria Laura Costantino for supporting me along this research path, and for trusting me and my work. A special gratitude to Giustina Casagrande Ph.D., who follows my work helping in the definition of each step and always encouraging me to do more.

I am truly grateful to Prof. Paolo Zunino. The third and the fourth chapter would not have been in this dissertation without his help, his passion for this work, and his mathematical and numerical competences.

A particular thanks to Prof. Roger Kamm for his support on the project and for hosting me in the Mechanobiology lab. I want to thanks also the 'Fondazione fratelli Agostino Enrico Rocca' for the possibility to spend some months in Boston doing research in such a prestigious campus.

I am also sincerely grateful to Matteo Moretti Ph.D. and Chiara Arrigoni Ph.D. for their precious contributes in the experimental activities and in the 'Rocca Fellow' application.

A great thanks also to the people who share their time, their knowledge and their experience:

Francesco and Camilla for the Artificial Organs Lab, and all the colleagues of the Laboratory of Biological Structure mechanics (LaBS);

researchers of the Cell and Tissue Engineering Laboratory at the Galeazzi Orthopaedic Hospital, and in particular Martina Crippa, who taught me how to keep cells alive working in the hood;

researchers of the the Mechanobiology lab at the Massachusetts Institute of Technology, especially Giovanni Offeddu Ph.D., for sharing experimental knowledge, protocols and space in the lab.

I want to thank all the students who contribute to these results with their works. In particular, I want to thank Simone Di Gregorio, who contributes first as a student and then as a colleague.

Finally, I am grateful to Ilaria Forasacco for the detailed revision of the thesis.

Luca

Abstract

MICROVASCULAR alterations have recently been reported in patients affected by chronic kidney disease treated by hemodialysis therapy. How these microvascular alterations are related to the pathology is still an open and complex question. Such alterations are likely to be related to the non-physiological flow rates of fluids and solutes removed from blood in the artificial filter. The artificial treatment increases the instantaneous mass- and fluid-flow rates which have to be washed out from the interstitium into the blood compartment, thus over-stressing the microvascular wall membrane. This membrane alteration affects the fluid balance, the distribution of solutes, and the delivery of nutrients to the tissues and may contribute to an abnormal vascular development and morphology. In addition, the presence of uremic toxins (currently more than one hundred have been identified) induces further alteration on the microvascular membrane wall. However, very few studies have addressed how these toxins affect the microvasculature.

To address this complex scenario, a wide modeling approach was designed. It is composed of three different models, which can share information and results to better describe the complex phenomena involved:

- lumped parameter model of the arterial circulation;
- multiscale 3D-1D model of the microvasculature;
- *in vitro* model of the microvasculature.

The lumped parameter model was based on previous works describing the arterial circulation including peripheral vascular districts and vascular regulations (chapter 2). A single peripheral district was analyzed to detail its description with particular reference to the fluid balance. Tests have been conducted by considering some uremic parameters alterations, and highlighting the need for a comprehensive modeling approach.

The second computational approach consists in a multiscale model of the microvasculature, accounting for its geometry and solved by finite element method. It exploits a framework of partial differential equations on domains with different dimensions (3D for the interstitium and 1D for the vasculature). Based on previous works on advanced mathematical methods and their development, the proposed model accounts for a non-linear contribution of the lymphatic system, the rheological effect of red blood cells and their heterogeneous distribution along the vascular network (chapter 3). The model was tested on a number of different cases before being applied to address uremic microvasculature, leveraging on available data from literature (chapter 4). Tests have assessed the contributions of the different relevant factors and how test-driven results actually match with *in vivo* literature-driven data. Moreover, a sensitivity analysis was conducted to appreciate the parameter alterations induced by the pathology.

The in vitro model was proposed to analyze alterations of the capillary membrane induced by the presence of uremic toxins (chapter 5). Namely, the effects of urea have been assessed by using different techniques. The experimental setup was computationally analyzed to investigate the actual rise of the trans-mural pressure between the vasculature and the gel surrounding it.

Finally the models' improvements and their interactions have been discussed, along with their limitations (chapter 6). This work has paved the way for a modeling support to the current research activities on microvascular alterations in uremic patients.

Contents

Glossary of Acronyms

AKI	Acute kidney injury
BSA	Body surface area
CD31	Cluster of differentiation 31 (Platelet/endothelial cell adhesion molecule-1)
CKD	Chronic kidney disease
COP	Colloid osmotic pressure
DAPI	4',6-diamidino-2-phenylindole
EC	Endothelial cell
ECM	Extra-cellular matrix
eGFR	estimated glomerular filtration rate
ESRD	End-stage renal disease
FB	Fibroblast
FEM	Finite element method
FRAP	Fluorescence recovery after photo-bleaching
FVM	Finite volume method
GAGs	Glycosaminoglycans
HA	Hyaluronic acid
HLF	Human lung fibroblast
Hoechst	Bisbenzimide
HUVEC	Human umbilical vein endothelial cell
ISF	Interstitial fluid
MSC	Mesenchymal stem cell
NFR	Net filtration rate
PDE	Partial differential equation

PDMS	Poly(dimethylsiloxane)
RBC	Red blood cell
ROI	Region of interest
RRT	Renal replacement therapy
TNFα	Tumor necrosis factor α
(VE)-cadherin	Vascular endothelial cadherin
VEGF	Vascular endothelial growth factor
ZO-1	Zonula occludens-1

Dimensionless numbers

Pe	Peclet number
Re	Reynolds number
Wo	Womersley number

CHAPTER 1

Introduction

The present chapter provides a description of renal diseases and microvasculature based on the state of the art, the anatomy, and the physiology. In addition, the aim of the work is presented highlighting the connection between microvascular alterations and renal diseases.

1.1 Renal diseases

The treatment of renal diseases by means of artificial devices started during the second world war, when Willem J. Kolff, a pioneer in bioengineering, designed the first dialysis tratment [1] and the first successful hemodialysis was performed in a human being [2, 3]. Since then, both better comprehension of the pathologies and technological development have constantly improved the treatment of renal diseases [2]. On the other hand, the mortality rate associated with the loss of kidney functions is still too large and comparable to some malignancies [4]. Certainly, the kidneys play a key role in many homeostatic functions and their failure heavily affects them. First, they remove waste products, such as the end products of metabolism. Additionally, they participate in different regulatory processes, contributing to the balancing of (i) body fluids, (ii) electrolytes, (iii) acid-base equilibrium, (iv) arterial pressure, and participating in (v) red blood cells (RBC) production, (vi) gluconeogenesis, and (vii) hormones secretion and excretion [5, 6]. Therefore, renal failure induces imbalances within the body, in terms of fluids, solutes, and hormonal functions.

Despite many causes may lead to renal diseases outbreak, renal failure is commonly classified into two different categories: acute kidney injury (AKI) and chronic kidney disease (CKD) [6]. The first is characterized by a quick loss of renal functions, which can be partial or total. This injury can often be treated to achieve the recovery of renal functions. AKI has been defined on the basis of the serum creatinine concentration and urine output [7–9]. CKD is instead a long-term progressive loss of renal functions [5, 6]. The relation between AKI and CKD has been also studied, suggesting a causal relation [10]. CKD is classified in different stages on the basis of the residual renal function by the estimated glomerular filtration rate (eGFR) [11]. A total of five stages have been defined depicting this progressive loss from the normal value of the eGFR which is over $90\,ml/min/1.73\,m^2\ BSA$. In the first stage, a kidney damage is present without affecting the eGFR. Starting from the second stage, eGFR decrease to: $60 - 89\,ml/min/1.73\,m^2\ BSA$ (stage 2); $30 - 59\,ml/min/1.73\,m^2\ BSA$ (stage 3); $15 - 29\,ml/min/1.73\,m^2\ BSA$ (stage 4); lower than $15\,ml/min/1.73\,m^2\ BSA$ or undergoing dialysis (stage 5). In the last stage, also called end-stage renal disease (ESRD), renal functions need to be replaced by a renal replacement therapy (RRT) (section 1.1.1). Typical symptoms of renal failure are: (i) peripheral edema, (ii) absent urination, (iii) sleep disorders, (iv) fatigue or weakness, (v) restless legs, (vi) anemia, (vii) nausea, (viii) coma [6, 12]. Even if uremia and CKD are often used as synonyms, they are technically different. Uremia is defined as the accumulation of some solutes, therefore referred as uremic toxins [12, 13]. This retention of toxins (section 1.1.2) is consequent to CKD and

in particular to ESRD, due to the inability of the kidneys to clear them. Renal diseases may have different causes: diabete mellitus (23 %), glomerulonephritis (15 %), hypertension (13 %), polycystic kidneys (6 %), pyelonephritis (6 %), renal vascular disease (2 %) [13, 14]. In addition, they are associated with other pathologies such as cardiovascular diseases, mineral and bone disorders, and neurological disorders [12, 15–20]. In particular cardiovascular diseases are known as common comorbidities and they are responsible for a big portion of the mortality in ESRD patients [12,21,22]. Even though all the processes involved in cardiovascular abnormalities in those patients are not fully understood [16], they are reported as (i) platelet-related abnormalities, (ii) dialysis-related injury, (iii) ventricular hypertrophy and dilation, (iv) vascular calcification, (v) heart failure [15, 16, 22].

The incident population, namely the number of new ESRD patients, has been estimated at $117\ pmp$ (per million population) by ERA-EDTA in the 2016 annual report with reference to Europe [14], and $357\ pmp$ by USRDS for 2015 with reference to US [21]. The same documents report a total number of patients undergoing RRT equal to $831\ pmp$ and $2024\ pmp$ respectively. Considering also stages prior to ESRD, the USRDS data report gives an estimate of $14.8\,\%$ of the adult US population affected in the period 2011-2014. The survival rate of patients on dialysis is about 50 % in 5 years [14]. Moreover, renal diseases have a strong social and economic impact. First, the need for RRT affects patient's quality of life, frequently causing psychological issues that turn into strong implications for their family too [12]. In terms of economic impact, only in the US in 2015, the cost related to ESRD has been reported to be 34 billions of dollars, rising up to almost 100 billions if all CKD stages are considered [21].

1.1.1 Renal replacement therapy [6]

Even when the treatment of choice for CKD is kidney transplantation, due to the discrepancies between the number of patients and the available donors [14, 21] most patients with ESRD are treated with dialysis. In addition, dialysis can also be used as "bridge-to-transplantation", in order to keep the patients alive while waiting for a donor. The aims of dialysis are: (i) to remove the excess of uremic toxins and water and (ii) to restore the physiological electrolyte balance in the blood. This therapy does not substitute the hormonal function of the kidney which has to be fulfilled by pharmacological treatment. The term dialysis was first introduced by Thomas Graham in the late 1800s to describe his experiments with hydrous metal oxide colloids [23]. The first application to animal models was developed by Abel in 1913 [24]. At this point, some key points were already clear, such as the need of anticoagulant to avoid blood clotting outside the body and the relation between the efficiency of the treatment and the area of the membrane, used to separate blood and dialysate (i.e. the fluid used to clean blood). This method was applied

to humans for the first time in 1915 by Haas [25], who first added a pump to flow blood in the extracorporeal circuit. A revolutionary step was made in the 1940's by Kollf, who understood that these methods could be used to treat patients with renal failure [1]. His work led to the first successful treatment on a human, making a patient survive an acute renal failure [6]. The dialysis machine used was composed of 40 meters of sausage skin around a cylindrical drum and ultra-filtration, namely the removal of fluids, was obtained by osmotic pressure difference. A few years later Alwall used pumps to achieve ultra-filtration by hydraulic pressure differences [26]. Another important improvement was the introduction of hollow fiber membrane to separate blood and dialysate [27] which allows a great filtering surface area while keeping the priming volume small. Then another step to manage chronic renal failure was taken by providing a feasible routine access to the vascular system. Nowadays, the treatment is classified on the basis of the predominant used phenomenon: hemodialysis (HD), when solutes are removed mainly by diffusion, and hemofiltration, when convection is prevailing. In the first case, the efficiency of toxins removal is related to their dimensions, whereas in the second one small and middle toxins are removed at a similar rate [13]. When both the phenomena happen significantly, the treatment is named hemodiafiltration (HDF). Some observational studies and clinical trials have confirmed the efficacy of HDF in reducing patient's mortality (e.g. [28]). All these progress regard hemodialysis, but also peritoneal dialysis (PD) is possible. In this treatment, the blood is purified inside the body, employing the peritoneum as the interface between blood and dialysate solution. This method is less commonly used compared to hemodialysis which accounts for $85\,\%$ of the treatment in Europe in 2016 [14].

1.1.2 Fluid and solutes homeostasis [5]

Fluid volume is regulated in the body by eliminating the proper amount of water and ensuring appropriate fluid exchanges across different body compartments. Usually, the intake of fluids is about $2300\ ml/day$, because of ingestion but also due to the metabolic production; i.e. water is a waste product of carbohydrates oxidation. This amount of fluid is then eliminated by the so-called insensible loss (evaporation by respiration and from the skin), by sweat, excrement and urine production by kidneys. To fulfill their regulatory function, these organs can vary urine production over a wide range: from 0.5 to $20l/day$.

All these fluids are distributed through the body in different 'compartments'. With reference to an average $70\ kg$ man, the intracellular fluid is about $28\ l$ on the overall $42\ l$. The remaining $14\ l$ are divided between the interstitial fluid (about $11\ l$) and plasma ($3\ l$). Therefore three different compartments are defined: (i) intracellular space, (ii) interstitial space, and (iii) intra-vascular space (figure 1.1). These spaces are separated by cell membrane and capillary membrane respectively. Since these membranes are perme-

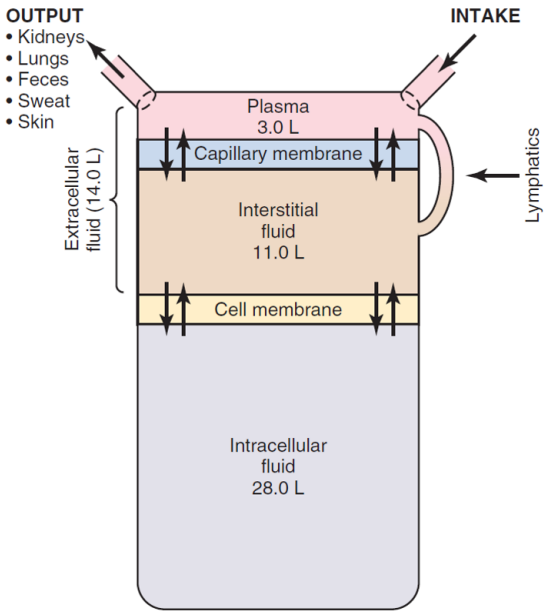

Figure 1.1: *Schematic of body compartments with reference to a* 70 kg *man. Used with permission from [5].*

able, fluids exchanges can happen between these compartments. In addition, the interstitial space is connected to the intra-vascular space by the lymphatic system, which drains fluids from tissues. When considering the fluid transport throughout the semi-permeable membrane, both hydraulic and osmotic pressure should be considered [29]. For example, both the aforementioned pressures are different in the intravascular and in the interstitial compartment, namely between the two side of the capillary membrane. This phenomenon is typically described by means of the so-called Starling's equation:

$$j_v = L_p \left((p_v - p_t) - \sum_k \sigma_k \left(\pi_{k,v} - \pi_{k,i} \right) \right) \tag{1.1}$$

where j_v is the flow rate per unit area, L_p is the hydraulic conductivity of the capillary membrane, p and π indicate the hydraulic and the osmotic pressure respectively, and σ_k is the reflection coefficient for the solute k. When referred to plasma proteins, the osmotic pressure is often called colloid osmotic pressure (COP) or oncotic pressure. A change in one of these physical quantities will results in a change of j_v eventually leading to a different condition or volume distribution. Under typical pathological conditions of CKD, accumulation of fluid in the interstitial space may occur [30]. This fluid accumulation is combined with an increase of interstitial pressure, which also depends on the inter-

stitial swelling [5, 30]. When performing hemodialysis, fluids are withdrawn from the dialyzer, which is connected to the patient's vascular system. Therefore, the plasma volume decreases, leading to an increase of hematocrit and solutes (i.e. proteins concentration). Intra-dialytic hypotensions may happen if this volume is not properly restored by a movement of fluids from the interstitial space to the vascular system, namely the plasma refilling [31–33]. This phenomenon is very important, and it happens within the microvasculature and through the capillary wall membrane. As a consequence, microvasculature and capillary wall properties, i.e. hydraulic conductivity, play a key role. It will be deeper analyzed in the section 1.3.

Analyzing the composition of fluids in these compartments, a similarity between intravascular and interstitial fluids has been observed. The main difference between them is the presence of plasma proteins. Since they can difficulty pass through the capillary membrane, only a small amount of them is found in the interstitial space [34]. On the contrary, the capillary lymphatic membrane is very permeable to proteins so that they can be cleared from the interstitial space, keeping their concentration low [35, 36]. Due to this difference in plasma protein and due to their net charge, also the Donnan-Gibbs effect should be considered when describing solute kinetics [37]. Indeed the concentration of cations in plasma is slightly higher than in interstitial fluid. The typical ionic composition of both the extra-cellular fluid and the intracellular fluid are summarized in figure 1.2. Alterations

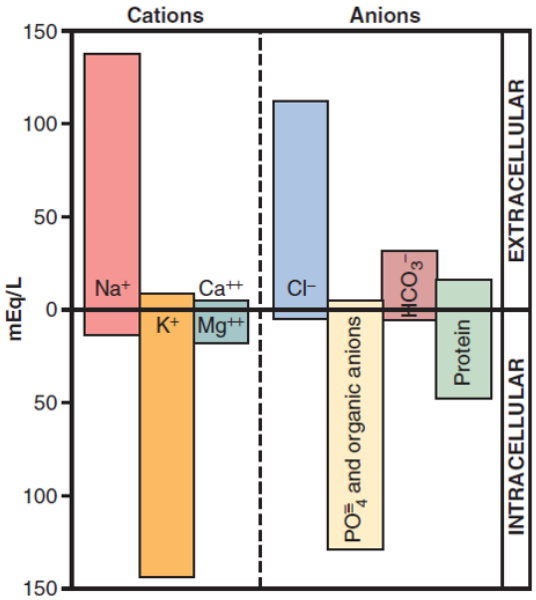

Figure 1.2: *Body fluids composition. Used with permission from [5].*

in plasma electrolytes balance have been reported as a consequence of uremic pathology. Such variations are reported to be different between patients [38]. In addition, these unbalances have different consequences [39]: (i) effects on blood volume, and therefore hyper- or hypo-tension [40]; (ii) cardiovascular disease and heart rhythm alterations [41,42]; (iii) atherosclerosis or renal bone diseases [43]. Also, accumulation of other solutes characterizes the uremic pathology. With an important work, Vanholder et al. [44] have analyzed a great number of works in the literature by identifying a list of 90 uremic toxins (table 1.1).

Both normal and uremic concentrations have been addressed in the study and also the ratio between them has been computed. They have also classified the uremic toxins in three different classes: small water-soluble molecules (smaller than $500\,Da$), protein-bound molecules and middle molecules (bigger than $500\,Da$). Such a classification is useful because their dimension can affect the removal efficiency [18]. Another classification, based on chemical structure, has also been proposed [45]. An update of those data has been published by the same group in 2012 [46], adjusting the proposed reference values and adding newly identified uremic toxins considering also studies published between 2003 and 2012. The specific effects of these uremic toxins are still not fully understood [6], but that study has at least paved the way for a systematic analysis aimed at a better understanding of solutes toxicity. For example, the persistent inflammation reported by those patients [47,48] is in agreement with the presence of $TNF\alpha$ [49,50].

1.1.3 Modeling approaches

With reference to renal diseases, fluid homeostasis has been modeled mainly by compartmental models. In this modeling approach, the body is divided in different compartments, and variations of volumes and solute concentrations are described by ordinary differential equations. Different configurations are available in literature from single-pool models, two-pool models, and more complex models. Single pool models have been historically used to estimate the right dose of dialysis in terms or urea removal (i.e. $K\,t\,/V$, where K is the dialyzer clearance rate for the specific solute, t is the time of treatment, and V is the solute distribution volume). They work quite well for small solutes not involved in solutes compartmentalization [6,33]. In addition, single or pseudo-one compartment models have been used to address variations of single solutes during dialysis treatment (e.g. [51,52]). To better describe the kinetics of larger solutes (e.g. β2-microglobulin) or solutes involved in compartmentalization, two or more compartments are usually used [53]. Among them, Casagrande et al [54] have considered a multi-compartment model composed of four different compartments, along with the three membranes between them: dialyzer membrane, capillary membrane and cellular membrane (figure 1.3).

Table 1.1: *Uremic toxins reported by [18, 44].*

Small, water-soluble molecules	1-Methyladenosine, 1-Methylguanosine, 1-Methylinosine, Asymmetrical dimethylarginine, α-Keto-δ-guanidinovaleric acid, α-N-acetylarginine, Arab(in)itol, Arginic acid, Benzylalcohol, β-Guanidinopropionic acid, β-Lipotropin Creatine, Creatinine, Cytidine, Dimethylglycine, Erythritol, γ-Guanidinobutyric acid, Guanidine, Guanidinoacetic acid, Guanidinosuccinic acid, Hypoxanthine, Malondialdehyde, Mannitol, Methylguanidine, Myoinositol, N2, N2-dimethylguanosine, N4-acetylcytidine, N6-methyladenosine, N6-threonylcarbamoyladenosine, Orotic acid, Orotidine, Oxalate, Phenylacetylglutamine, Pseudouridine, Symmetrical dimethylarginine, Sorbitol, Taurocyamine, Threitol, Thymine, Uracil, Urea, Uric acid, Uridine, Xanthine, Xanthosine, 2-Methoxyresorcinol
Protein-bound molecules	2-Methoxyresorcinol, 3-Deoxyglucosone, CMPF,Fructoselysine, Glyoxal, Hippuric acid, Homocysteine, Hydroquinone, Indole-3-acetic acid, Indoxyl sufate, Kinurenine, Kynurenic acid, Leptin, Melatonin, Methylglyoxal, N-carboxymethyllysine, p-Cresol, Pentosidine, Phenol, P-OH-hippuric acid, Putrescine, Quinolinic acid, Retinol-binding protein, Spermidine, Spermine
Middle molecules	Adrenomedullin, Atrial natriuretic peptide, β2-Microglobulin, β-Endorphin, Cholecystokinin, Clara cell protein, Complement factor D, Cystatin C, Degranulation-inhibiting protein I, Delta-sleep-inducing peptide, Endothelin, Hyaluronic acid, Interleukin-1β, Interleukin-6, k-Ig light chain, λ-Ig light chain, Leptin, Methionine-enkephalin, Neuropeptide Y, Parathyroid hormone, Retinol-binding protein, Tumor necrosis factor-α

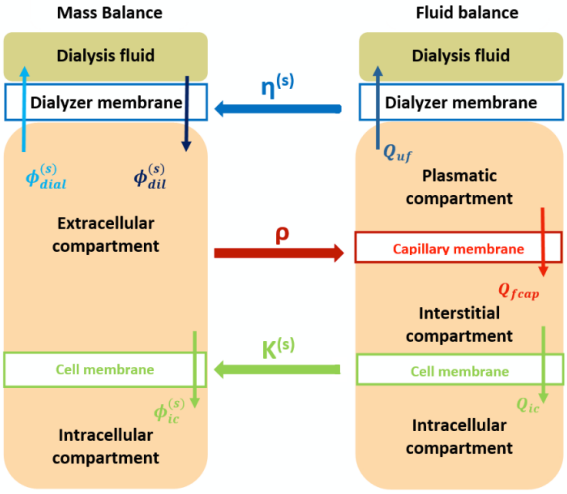

Figure 1.3: *Schematic of the compartmental model used in [53] and [54], to study fluid balance and to identify patient specific parameters. Used with permission from [53].*

Moreover, in a subsequent work, the authors have applied a Bayesian approach to estimate patient-specific parameters with the final aim of treatment tailoring [53]. In a few works, fluid balance and plasma refilling have been directly addressed considering also proteins, and thus accounting for oncotic pressures [33, 55–57]. Such models are typically two-compartment models (intra-vascular and interstitial compartment) used to describe the fluid exchange across the capillary membrane. Some of them have included a modeling of the lymphatic system [55, 56], also addressing patient-specific parameters identification [55].

1.2 Microvasculature [5]

The main function of the vascular system is to transport nutrients to tissues within the body and to carry out waste products from them. To this aim, in an adult and healthy subject about $5\,l$ of blood flow into the body every minute. The importance of this transport is evident considering oxygen transport. The characteristic diffusion time t can be computed as $t = x^2/2D$, where x is the distance to be covered and D is the diffusion coefficient [58]. Considering a typical value for D_{O_2}, such as $10^{-5}\,cm^2/s$, the characteristic time is $1.25\,s$ for $50\,\mu m$ but it reaches $500\,s$ for $1\,mm$. Such time is not compatible with life, therefore the convective transport is necessary.

The vascular system is usually divided into systemic and pulmonary circulation. The former supplies blood to the body whereas the latter carries the blood to the lungs where the oxygen and carbon dioxide are exchanged with the air. A schematic of both is shown in figure 1.4. Starting from the heart, arteries are split into smaller vessels up to the cap-

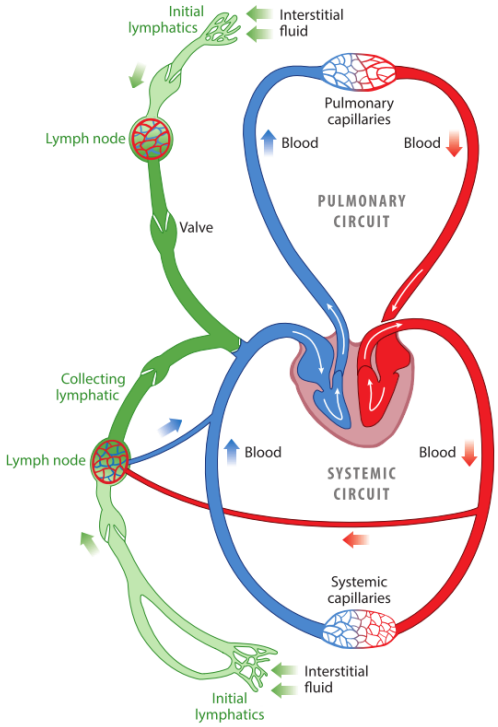

Figure 1.4: *Structure of the cardiovascular and the lympahtic system. Used with permission from [36].*

illaries, and then they start to merge again in the venous side of the vascular system to collect blood and bring it back to the heart. Along this path, the diameter of the vessels gets smaller as they approach the peripheral circulation and start to rise again within the venous side. However, the total cross section of vessels (i.e. the cross section that all the vessels of the same typology would have if merged side by side) is larger in the peripheral circulation, with about three orders of magnitude between aortic and capillaries cross sections [59,60]. For this reason, the mean velocity is higher in big vessels (e.g. tens of cm/s

Table 1.2: *Vessel typical dimension and velocity. Adapted from [60].*

Vessel	Diameter (cm)	Total cross-section (cm^2)	Avg. velocity (cm/s)
Aorta	2.5	4.5	48
Large arteries	0.4	20	45
Arterioles	5×10^{-3}	5.7×10^{7}	5
Capillaries	8×10^{-4}	1.6×10^{10}	0.1
Venules	2×10^{-3}	1.3×10^{9}	0.2
Veins	0.5	200	10

in the aorta) than in the microvasculature (e.g. order of magnitude mm/s). The hydraulic pressure falls along the vasculature and is different between systemic and pulmonary circulation (figure 1.5). Both fluid velocity and pressure are characterized by oscillations due to heart pumping. These variations are damped along the vasculature leading to almost steady flow within the capillaries.

The flow within capillaries can be analyzed by a fluid dynamic approach computing dimensionless number in order to figure out the nature of the flow. First, the Reynolds number Re is used to address the presence of laminar of flow:

$$Re = \frac{v\, D\, \rho}{\mu}$$

where v is the average velocity, D is the characteristic dimension of the channel, ρ is the fluid density, and μ is the fluid viscosity. Considering typical values of microvasculature, the order of magnitude for Re is $10^{-3} - 10^{-2}$ [61]. Thus the flow can be considered laminar. Another meaningful dimensionless number is the Womersley number Wo:

$$Wo = \frac{D}{2}\sqrt{\frac{\rho\, 2\pi f}{\mu}}$$

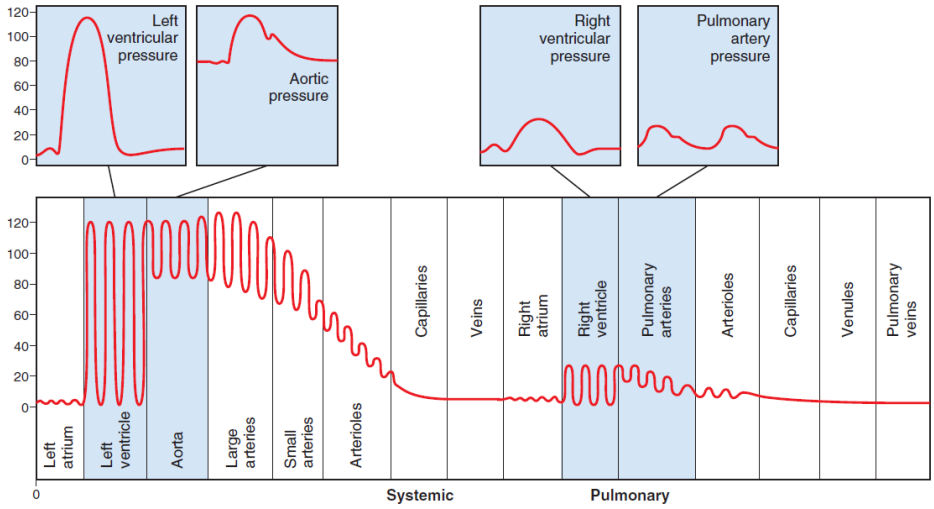

Figure 1.5: *Hydraulic pressure within vessels with reference to a person in horizontal position. Both systemic and pulmonary circulation are shown. Used with permission from [5].*

It describes the time variation of the flow, justifying the steady state assumption if $Wo < 1$ as in the microvasculature [60]. Therefore the flow within the microvasculature is considered to be laminar and steady, given that both the Reynolds and the Womersley number are small.

1.2.1 Microvascular environment

Even if morphology and functionality of microvascular environment are highly tissue-dependent, it is typically described listing three main component: microvessels, interstitial space and lymphatic system (figure 1.6).

Microvascular vessels are typically classified as arterioles, capillaries, and venules. Arterioles and venules are characterized by a branching structure, and they are connected to the bigger vasculature [63]. They have a diameter in the range of tens of μm [60, 61], and their role is mainly convective transport of blood within tissues. Arterioles are also directly involved in flow regulation, being subject to vascular tone alterations due to metabolic signals, myogenic response and shear stress [64, 65]. The capillaries instead tend to form a more *'network-like'* structure. Their diameter approaches the dimension of red blood cells (RBC) - that is $8\,\mu m$. In addition, the leakiness of their wall (both in terms of fluids and solutes) allows the delivery of nutrients and the withdrawal of waste products from tissues [63]. The thin capillary wall ($\simeq 0.5\,\mu m$) and the small distance between capillary

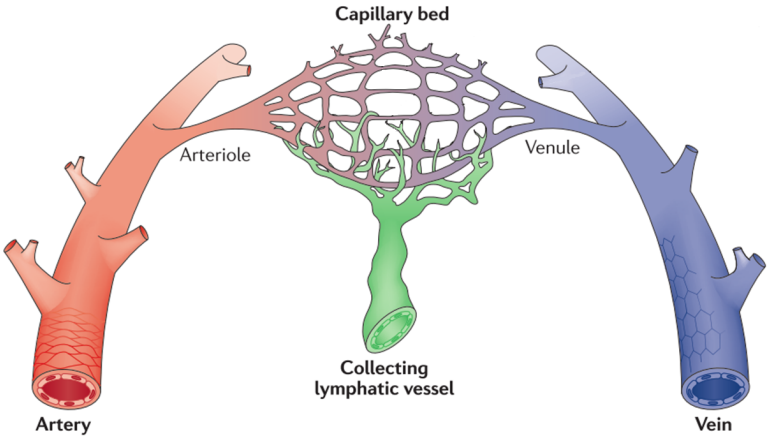

Figure 1.6: *Components of the microvascular environment. Adapted with permission from [62].*

and cells ($\simeq 50 - 100\,\mu m$) allow an efficient exchange. Capillaries are classified by the characteristics of their wall [66]. *Continuous capillaries* are the most common within the body. They are made of a single sheet of endothelial cells (EC), linked by *tight-junctions* (e.g. VE-cadherin and other cell membrane adhesion proteins). In such junctions, ECs are not directly in contact with each other, and the small gaps ($\simeq 10 - 15\,nm$), which are formed between them, are named *inter-cellular clefts*. These clefts are present in most tissues. However, more tight capillaries junctions are reported in the brain [67]. On the contrary, much larger *inter-cellular cleft* are present in the liver and in the spleen, because ECs are not so tightly connected. Indeed these capillaries are referred to as *discontinuous capillaries*. The last type of capillaries characterizes kidneys, and in particular, the glomerulus. In these specific regions *fenestrated capillaries* allow a great filtration of solutes and fluids by an extra-cellular pathway, through windows named fenestrae [68].
Debated components of microvasculature are *capillary sphincters*. In most physiology textbooks, they are described as a smooth muscle fiber surrounding the capillary where they originate from the *metarteriole*. The contraction of this fibers leads to non-continuous flow in a phenomenon named *vasomotion* [5, 66]. This structure was first described with reference to mesenteric circulation in the first decades of the 1900s (e.g. [69]). In a comprehensive and 'historical' review, Sakai and Hosoyamada [70] have analyzed multiple studies describing microvasculature anatomy in different tissues. They have concluded that *metarteriole* and *capillary sphincters* cannot be considered as a universal component of microvasculature, but more unique features of mesenteric circulation.
Another important component of capillary wall is the glycocalyx (often referred to as en-

dothelial surface layer). It is a complex network of glycosaminoglycans (GAGs) and sialoglycans proteins, that coats the inner surface of capillaries with a layer of $60 - 570\,nm$ [34]. This structure has been looked into over the last decades, and some studies have described how it is involved in blood rheology within capillaries and filtration of fluid and solutes [34, 61].

The second main component of microvascular environment, the interstitium, has been described in physiology textbooks as the space between cells, accounting for one-sixth of the total body volume [5]. It is composed of both fluid, therefore named interstitial fluid (ISF), and solid structure, the extra-cellular matrix (ECM) [71]. The composition of such a structure is greatly tissue-dependent, and it affects mechanical properties, cell-cell signaling, and movement of fluid flow through the interstitium. However, as a general description, collagen (which composes more than two-thirds of ECM proteins in many soft tissues) and proteoglycans are the most common component of ECM (figure 1.7). The

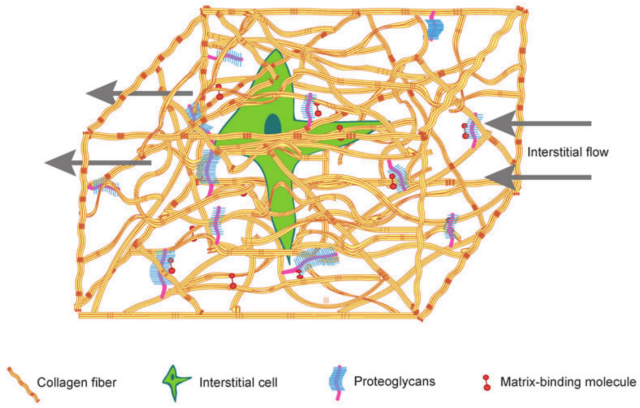

Figure 1.7: *ECM structure, adapted with permission from [71].*

latter are highly hydrated big molecules (several hundreds on Da) composed by carbohydrates (e.g. heparan sulfate, chondroitin sulfate, dermatan sulfate) denominated GAGs and a protein core, often hyaluronic acid (HA).

In a very recent paper, Benias and colleagues [72] have described fluid-filled spaces in different tissues, namely extra-hepatic bile duct, peri-bronchial and peri-arterial tissues, submucosae of the entire gastrointestinal tract and urinary bladder, and dermis. These space may be important in our understanding of pathologies such as edema, fibrosis and cancer metastasis. Their finding expands the classical view of interstitium characterized by a very low portion of free fluid [5].

Characteristic values of interstitial fluid velocity are still not well determined and affected

by pathological states such as inflammation or edema [71]. However, on the basis of some measurements the order of magnitude expected is $0.1 - 2\,\mu m/s$ [73–75]. Interstitial pressure is reported to be tissue-dependent, with values close to the atmospheric pressures along with also slightly sub-atmospheric [36, 76–78]. In addition, interstitial fluid pressure has been related to the ISF volume. Accumulation of fluid leads to higher pressure. This rising has been quantified by the interstitial compliance, which is computed by the volume variation over the pressure variation starting for a given pressure/volume. Interestingly, the compliance of interstitium is dependent on the tissue swelling, producing a strong non-linearity in the pressure-volume relation (figure 1.8) [79].

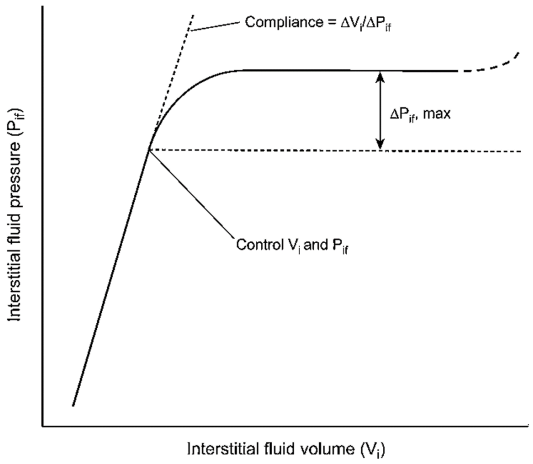

Figure 1.8: *Relation between interstitial pressure and interstitial volume showing a non-linear relation between them. From [79].*

Lastly, the lymphatic capillaries complete the microvascular environment [36]. They are the first vessels of the lymphatic system, which is responsible for returning fluids from the interstitium to blood, significantly contributing to fluid balance. In addition, it is involved in immune system response. Our comprehension of the lymphatic system is still not complete, but it has significantly improved in the last decades. For example, lymphatic vessels have recently been found also in brain tissues [80]. With regards to anatomy, primary and secondary valves have been identified and described along with fibrillin filaments [36, 81–84]. Primary valves are located in the lymphatic capillaries. The wall of these microvessels is composed of a monolayer of lymphatic endothelial cells without a continuous basement membrane. These cells are organized in a *'oak leaf configuration'* forming button-like junctions. For these reasons, lymphatic capillaries are very permeable to proteins, clearing them from ISF. This, in conjunction with the high reflection to plasma

proteins of the capillary membrane, leads to low plasma protein concentration within the interstitium. Moreover, lymphatic capillaries are linked to the ECM through fibrillin filaments [36, 78, 85, 86]. Thanks to these structures, collapsing of lymphatic capillaries is prevented, and the swelling of the tissue is directly linked to lymphatic membrane hydraulic conductivity. Indeed, an interstitial volume increase stretches the ECM eventually dilating capillary and increasing wall conductivity [81]. Secondary valves, instead, characterize vessels downstream lymphatics capillaries. They are arranged in lymphangions, namely the functional units defined by an upstream and a downstream valve. These two types of valves contribute to the unidirectional net flow within the lymphatic system under physiological conditions [36, 81, 82, 87–90]. The lymphatic flow rate has been described in literature with reference to interstitial fluid pressure (figure 1.9) [5, 56]. This relation is described as non-linear, with a first increase of lymphatic flow rate up to a plateau, which defines a relative maximum increase.

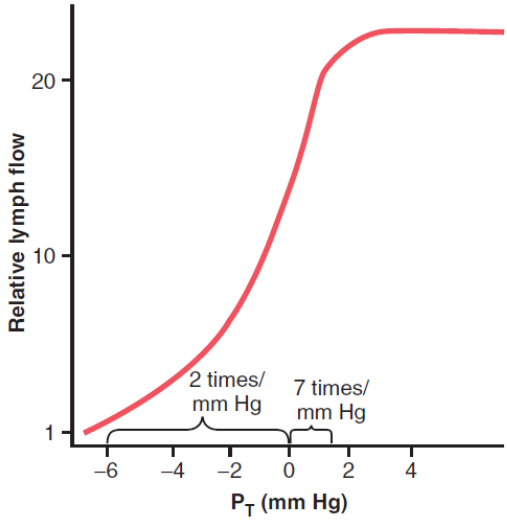

Figure 1.9: *Relation between interstitial pressure and lymphatic flow rate. Used with permission from [5].*

1.2.2 Peculiarity of microvasculature

When describing blood flow in microvasculature, namely when the dimension of RBC ($8\,\mu m$) is not negligible with respect to the vessel diameter, three different phenomena must be considered, since they characterize the microvasculature and lead to significant differences with respect to macrovasculature:

- Fåhraeus effect [91];
- Fåhraeus - Lindqvist effect [92];
- Zweifach - Fung effect [93, 94].

The Fåhraeus effect was named after Robin Fåhraeus who first observed the phenomenon [91]. It describes the tendency of RBC to migrate towards the center of the microvessel leaving a plasma layer near the wall (figure 1.10). Due to this fact, RBCs are in the region

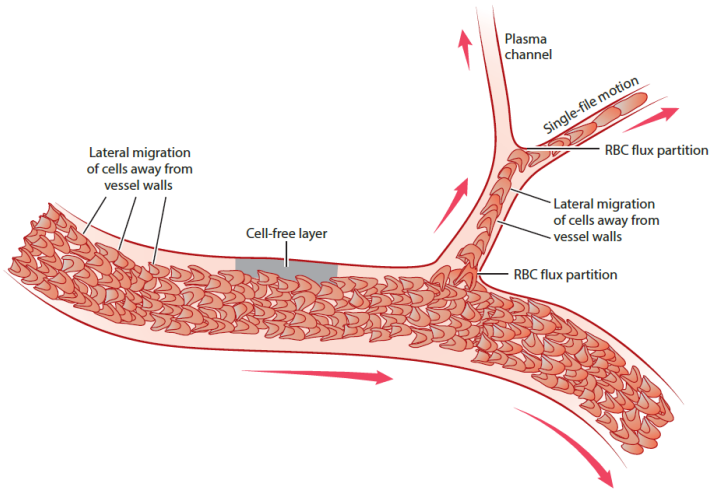

Figure 1.10: *Drawing showing the Fåhraeus effect, with the formation of a cell-free layer and the Zweifach - Fung effect producing hematocrit heterogeneity. Used with permission from [61].*

of the vessel with greater velocity. Therefore the averaged velocity of RBC is greater than the averaged bulk flow velocity. A further consequence of the RBC concentration within the center of the vessel regards the hematocrit. Considering the traditional bench composed of two reservoirs linked by a small tube, differences have been reported between the hematocrit in the feeding reservoir, the tube, and the discharge reservoir. Given this experimental evidence, two different definitions of hematocrit are commonly used when describing microvasculature: tube hematocrit and discharge hematocrit. The first is defined as volume over volume ratio, as done referring to big vessels, the latter instead as a flow rates ratio: $RBC\ flow\ rate\ /blood\ flow\ rate$ [61]. In addition, the velocity ratio has been correlated to the hematocrit ratio: $H_t/H_d = V_{bulk}/V_{RBC}$ [95].

The formation of a plasma-free layer close to the wall is also the basis of the Fåhraeus -

Lindqvist effect [92]. Fåhraeus and Lindqvist observed a marked decrease in fluid apparent viscosity as the diameter of the glass pipe falls below $300\,\mu m$ (figure 1.11).

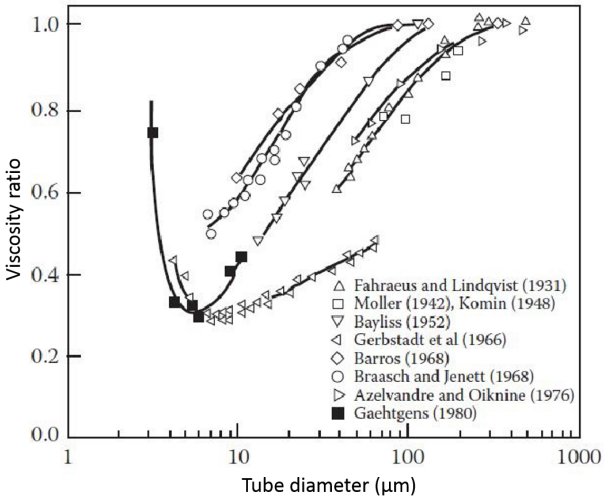

Figure 1.11: *Data showing the Fåhraeus - Lindqvist effect in glass tubes in terms of viscosity ratio (apparent viscosity over viscosity within a big vessel) function of the tube diameter. Used with permission from [96].*

The apparent viscosity is defined as the viscosity of the fluid assuming it as a Newtonian fluid. Then, relative viscosity is given by the ratio $\mu_{apparent}/\mu_{plasma}$. Due to the interaction between RBC and the wall of the pipe, the apparent viscosity increases as the diameter approaches RBC characteristic dimension. Analyzing multiple studies, Pries and colleagues [97] have developed an empirical relation to figure out the relative viscosity depending on the vessel diameter and the discharge hematocrit:

$$\mu_{vitro} = 1 + (\mu_{0.45} - 1) \cdot \frac{(1 - H_D)^C - 1}{(1 - 0.45)^C - 1} \tag{1.2}$$

where

$$C = (0.8 + e^{-0.075D}) \cdot \left(-1 + \frac{1}{1 + 10^{-11} D^{12}} \right) + \frac{1}{1 + 10^{-11} D^{12}}$$

$$\mu_{0.45} = 220e^{-1.3D} + 3.2 - 2.44e^{-0.06D^{0.645}}.$$

When the measurement of the apparent viscosity was conducted in microvessels, even if the experiments were technically very difficult, a higher apparent viscosity was found. Therefore, Pries and colleagues [98] reformulated their empirical equations providing an

in vivo formulation:

$$\mu_{vivo} = \left[1 + (\mu^*_{0.45} - 1) \cdot \frac{(1 - H_D)^C - 1}{(1 - 0.45)^C - 1} \cdot \left(\frac{D}{D - 1.1}\right)^2\right] \cdot \left(\frac{D}{D - 1.1}\right)^2 \quad (1.3)$$

where

$$\mu^*_{0.45} = 6 \cdot e^{-0.085D} + 3.2 - 2.44 \cdot e^{-0.06D^{0.645}}.$$

A comparison between the two formulation is shown in figure (figure 1.12). Four different cases, corresponding to four values of H_D, are shown using both the formulations. The dotted lines describe the *in vitro* formulation whereas the solid ones the *in vivo* formulation. These formulations are similar for big vessel diameters (e.g. mm scale vessels) but they substantially differ for capillary-scale vessels. In particular given a vessel diameter, the *in vivo* formulation produces a greater apparent viscosity compared to the *in vitro* one. The main reason for this difference has been later identified in the presence of the

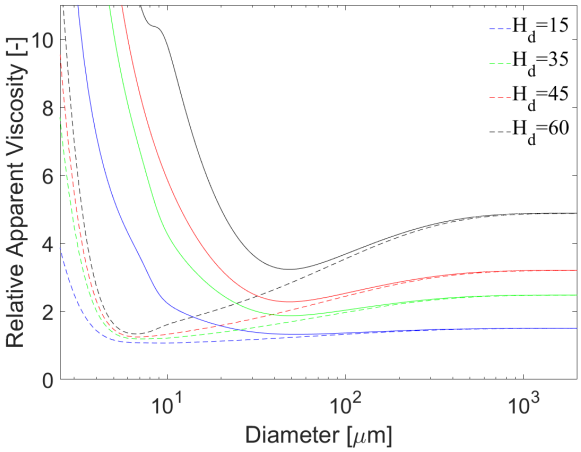

Figure 1.12: *Comparison of the Fåhraeus - Lindqvist effect in glass tubes and in capillary vessels [99] computed on the basis of [97] and [98]. Solid line: in vivo prediction (capillary vessels); dotted line: in vitro prediction (glass tubes).*

glycocalyx, which reduces the available lumen for plasma and RBC flow [100].

The Zweifach - Fung effect [93,94] concerns the heterogeneous distribution of RBC in presence of bifurcations. Indeed, fewer RBCs enter a vessel with lower flow rate, because it receives more flow from the plasma layer (figure 1.10) [61]. It is still unclear whether this phenomenon is mostly due to differences in fluid velocity of flow rate [94, 101–104]. First experiments by Schimid-Schönbein and colleagues had shown alterations of RBCs distribution in an animal model due to flow rate variations [105]. Some years later, Pries and

colleagues [104, 106] developed an empirical relation based on an animal model, accounting for the flow rate distribution and diameter of the vessels composing the bifurcation. This relation is widely used in computational models (e.g. [107–111]). Another approach to describe this phenomenon has been proposed by Gould and Linninger [112]. Their model does not include the possibility of zero hematocrit branches, although it has been observed *in vivo*. In their work, the model was compared to the aforementioned failing to show a better agreement with experimental data. However, their model can be easily extended to include also trifurcations. Considering that (i) the flow rate within the network is influenced by apparent viscosity and therefore by hematocrit and that (ii) the hematocrit distribution is influenced by flow rate at the bifurcations, the computational modeling approach must be iterative to solve this inter-dependency. In recent studies, other possible aspects of the phenomena have been analyzed such as the influence of bifurcation angle [113] or the possible inversion of this effects [114, 115].

1.2.3 Fluid exchange [34]

Fluid exchange across the microvascular wall has traditionally been described following the fundamental principle formulated by Starling [29]. Performing animal experiments with an isotonic saline solution, he described the capillary wall as a semipermeable membrane. In addition, he also observed that some plasma proteins leak into the interstitium, highlighting imperfect semi-permeability. For a general solute, the degree of leakiness can be quantified by the Staverman's reflection coefficient σ, where $\sigma = 0$ means that the solute can freely travel across the membrane, whereas $\sigma = 1$ stands for perfect impermeability [116]. At a later time, following thermo-dynamics principles, Kedem and Katchalsky [117] formalized what is currently known as the Straling's classical principle (1.1). Given than the interstitial fluid and plasma differ mainly by the presence of macromolecules and that $\sigma_{macromolecules} \simeq 1$ whereas $\sigma_{small\ solutes} < 0.1$ the equation 1.1 can be simplified as:

$$j_v = L_p \Big((p_v - p_t) - \sigma \, (\pi_v - \pi_i) \Big) \tag{1.4}$$

where $sigma$, π_v, and π_i are referred to the macromolecules. Several studies have supported this theory (e.g. [118–120]). This model is the most used to describe filtration from the vasculature in computational models. Several years later, Michel and Phillips [121] proposed a model based on the continuously renewing of the ISF that led to the following equation:

$$j_v = L_p \left((p_v - p_t) - \sigma^2 \, \pi_v \, \frac{1 - e^{-Pe}}{1 - \sigma \, e^{-Pe}} \right) \tag{1.5}$$

where $Pe = j_v \, (1 - \sigma) \, / \, p_d$ with p_d is the permeability of the capillary wall to plasma proteins. In the resulting equation of the model, j_v is depending on itself and therefore it

cannot be computed directly. More recently, Michel [122] and Weinbaum [123] independently suggested that glycocalyx have effects on the filtration. According to their models, the concentration of proteins in *subglycocalyx region* should be considered instead of the interstitial. In this region, the protein concentration should be low because of the high reflection coefficient and the outward flow preventing backward diffusion. For this reason, they have proposed the following model:

$$j_v = L_p \Big((p_v - p_t) - \sigma \left(\pi_v - \pi_g \right) \Big) \tag{1.6}$$

where π_g is referred to the *subglycocalix region*. These last two models are still not widely used in computational modeling, probably because of intrinsic difficulties in the computation (i.e. self-dependence of j_v or the need of subglycocalyx region modeling).

1.2.4 Modeling approaches

Microvasculature has been studied by means of different approaches, including *in vivo*, *in vitro*, and *in silico* studies. Without aiming for a full literature review of the *in vivo* techniques, two of them are here reported: intravital microscopy [124] and CytoCam-incident dark field (and its precursor side-stream dark field) [125]. Such procedures are used to study the microvasculature under both healthy and pathological conditions (i.e. cancer) involving human subjects (e.g. [126]) or animals (e.g. [127]).

Focusing more on modeling approaches, two very different options are available: *in vitro* and *in silico* studies.

For the former, microfluidics has provided feasible tools allowing researchers to better control their experiments. With reference to the aim of this work, interesting microfluidic models can be classified in two main categories: models involving cellular capillary vessels (i.e. made by endothelial cells) and models not involving them (figure 1.13). This last category comprehends devices made by poly(dimethylsiloxane)(PDMS) with microchannels. They have been used to test and analyze blood rheological properties, the Zweifach - Fung effect, RBC properties, and to provide organ-specific models [114, 131–135]. Geometrical fine control and geometrical repeatability are the main advantages of this approach. But the geometry is also one of its disadvantages. Indeed, the channel cross-section is rectangular due to building procedure limitation.

On the other hand, a microfluidic device can also be used to culture cells. An extensive review of recent advances in the use of such devices to study microvasculature and vascularization has been published by [129]. These devices can be divided into two different subcategories: patterned vascular channels and self-assembled networks. The patterned vascular channels are devices in which the vascular architecture is achieved by scaffolding, creating channels via a temporary scaffold or directly within the PDMS/gel and seed-

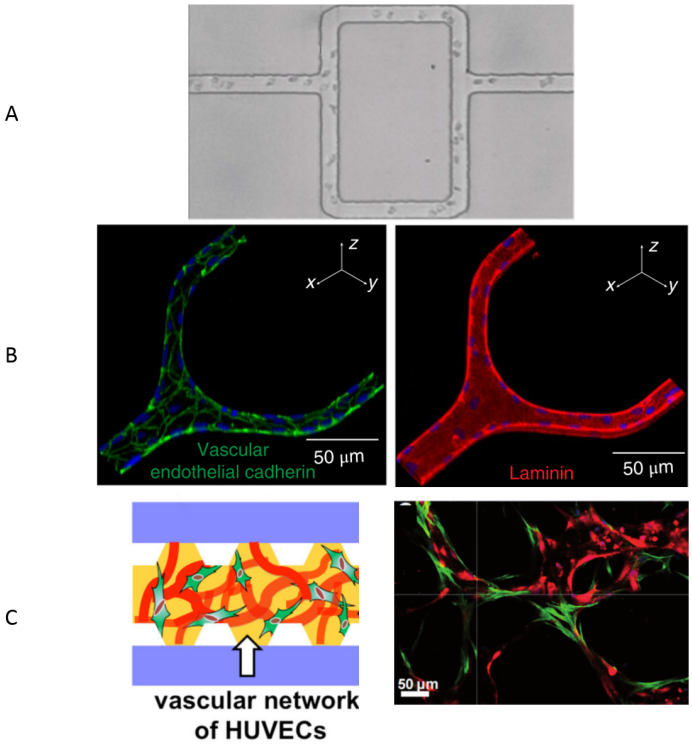

Figure 1.13: *Summary of in vitro approaches for microvasculature modeling. (a) PDMS chip with RBC, used to study the Zweifach - Fung effect, from [114]. (b) Channel in a PDMS chip covered by endothelial cells to obtain a perfusable network with high controlled geometry, used with permission from [128]. (c) Self assembled network in a porous gel (green: endothelial cells; red: mesenchimal stem cells) [129] - used with permission from [130] - Reproduced by permission of The Royal Society of Chemistry.*

ing cells on it. A recent example can be found in the work of Qiu and colleagues [128], in which they build a perfusable and endothelialized patterned microvasculature to study endothelial barrier dysfunction. In this example, vessels have still been created based on a rectangular cross-section pattern. The self-assembled network, instead, is typically based on PDMS devices in which hydrogels are incorporated. These gels, usually fibrin or collagen-based [129, 136], are enriched with endothelial cells (EC). Different types of ECs have been used, including human dermal microvascular ECs, bovine pulmonary artery ECs, human umbilical vein ECs (HUVEC), human blood outgrowth ECs, endothelial progenitor cell [136]. Among them HUVECs are the most used cells, accounting for half of the published works when Morin and Tranquillo wrote their review in 2013 [136]. These

ECs typically form a self-assembled perfusable network within 4-7 days, and thereafter signals produced by support cells, such as mesenchymal stem cells (e.g. [130]) or fibroblast (e.g [137]), are required to avoid network regression [129]. These self-assembled networks are typically used to study permeability of the wall membrane to solutes (e.g. [130, 138]) or cancer cell intra- and extra-vasation (e.g. [139–141]).

The *in silico* approach for describing microvascular networks is characterized by different methods and different scales [142]. Since relevant phenomena happen at different spatial scales, modeling all of them remains a major challenge suggesting that a multiscale approach is required. Numerical methods are now more widely used because of their ability to handle also complex networks. The applied methods are very different: full 3D approach with dissipative particle dynamics [143] or immersed boundary methods [144,145]; the lattice Boltzmann method [146]; the Green function [147,148]; the approximation with porous medium [149–151] or multiple-network poroelastic theory [152, 153]; application of Poiseuille's law in a discrete network geometry [101, 109, 111, 150, 154, 155] also considering filtration [156]; 3D approach focused on elementary repetitive unit [157]; 1D approximation of vessels [158, 159]; and coupling of 1D capillary flow with 3D interstitial flow [160–163]. Some common features can be found in these works. First, the Pouiseuille's law is widely used to describe flow within capillaries, often adopting the apparent viscosity concept to account for RBC and vessel diameter effects on blood rheology. In addition, the hematocrit heterogeneity in the microvasculature is directly addressed [107, 108, 111, 112, 164, 165]. Secondly, the interstitium is described as a porous medium by means of Darcy's law. When considered, the coupling between these two domains because of filtration is described by the classical Starling's principle (equation 1.4). The contribute of the lymphatic system to fluid balance, when considered, is usually described by a relation similar to Starling's principle (equation 1.4) neglecting any osmotic pressure difference due to the high permeability of the lymphatic capillaries. An interesting approach is related to the coupling of reduced a 1D model for the capillary network with a 3D porous model describing the interstitium. In subsequent works [161, 162, 166, 167], the mathematical grounds for a multiscale 3D-1D model have been built. This approach is very promising to model microvasculature, also aspiring to model large microvascular bed, thanks to the fact that 1D and 3D discretization can be handled separately.

1.3 Microcirculation and renal disease

As described in the section 1.1.2, the microvasculature plays a key role in the processes related to fluid and solutes homeostasis. Indeed, such equilibrium is maintained thanks to a flux of solutes and water through the capillary wall membrane. When patients are treated with intermittent hemodialysis, the most common treatment for CKD, the key role of microvasculature is even more stressed. During the time between two subsequent dialysis sessions, those patients accumulate fluids (and uremic toxins) which are then removed by the treatment. If the rate of removal of fluid from the vascular compartment by the dialyzer is not compensated by the plasma refilling, namely fluid recovery from the interstitium, the blood volume decreases. Therefore hypotension episodes may happen, and frequent episodes can produce consequences on multiple organs [31–33]. In addition, some solutes suffer from compartmentalization, namely its distribution within the whole the body, involving vascular, interstitial and intracellular compartments [6]. This phenomenon affects the removal efficiency of toxins, since the removal rate reached within the dialyzer is limited by the rate of exchange between these compartments. For example, a uremic toxin that is accumulated within both the vascular and the interstitial space is initially removed from blood by the dialyzer. Then, a withdrawn from the interstitium happens because of the difference in concentration and possible convective phenomena due to fluid absorption from interstitium. Such a phenomenon is affected by the properties of the microvascular wall, resulting in a better removal of small solutes, namely toxins that can pass through the membrane easily. Therefore, the understanding of microvascular wall properties is necessary to accurately model fluid and uremic toxin removal, eventually aiming to a better design of the therapy. Moreover, uremic toxins affect multiple organs within the body (e.g. kidneys, heart, liver, intestinal mucosa, brain, and lungs) but also cells and tissues (e.g. leukocytes, endothelium and ECs, epithelial cells, pancreatic cells) [45, 168, 169]. In particular, the resulting endothelial dysfunction has been described as increased expression of atherosclerosis (also related to leukocyte activation), loss of vessel wall compliance, vascular calcification, abnormalities of vascular repair [45]. Recently, also the toxicity of urea has been reconsidered along with the effect of uric acid [170]. In particular, Vanholder and colleagues have reviewed different works in literature, addressing urea toxicity in *in vitro* or *animal* experiments [168].

Multiple works have been conducted in the past 3 decades to address microvascular changes in CKD patients both in terms of structural alterations (e.g. capillary density) and functional ones (e.g. peripheral blood flow). One of the main reasons leading to this type of research is the relation between cardiovascular disease and CKD. Therefore, one of the research questions was whether alterations in microcirculation are related to CKD and, if

yes, whether those alterations may explain the relation between the two diseases. Since skin microcirculation can be investigated with fewer problems and with a low invasive techniques with respect to other districts, it has been studied more frequently. In addition, based on the hypothesis that alterations in skin microcirculation are representative of those in other microvascular beds such as the heart or the kidneys, impaired microcirculation may contribute to CKD cardiovascular consequences [171–173]. However, the endothelial dysfunction is still not fully understood [174]. Pipili and colleagues have reported a correlation between the adequacy of dialysis, addressed by means of a single-pool $Kt\,/\,V$, and changes in microcirculation. They measure microvascular alterations by near-infrared spectroscopy addressing muscle oxygen saturation [175]. Intracranial hemorrhages are associated with CKD along with cerebral microbleeds, which have been successfully used to predict the first [176]. They are consistent with the inflammatory state reported in CKD patients. Micro-inflammation in uremic patients has been correlated also with extracellular overhydration [177]. In two subsequent works, Mistrik and colleagues have analyzed cutaneous blood flow and its relation with dialysis therapy [178, 179]. A heterogeneous decrease in blood flow has been reported in the different analyzed areas. In addition, they succeed in correlating serum albumin level with the decrease of cutaneous blood flow and with skin defect development. These findings are in agreement with those of Seliger and colleagues, who found out that microvascular endothelial dysfunction correlates to albumin level [180]. If such a phenomenon affects the heart, the microvascular impairment may lead to the cardiac dysfunction described in CKD patients [181]. This functional microvascular impairment has been also reported by El-Nahid et al. [182]. Their work focuses on skin microcirculation comparing healthy subjects with patients undergoing hemodialysis treatment, also considering hypertension. Both capillary density and peripheral flow have been analyzed, reporting differences only as for the latter. Capillary density alterations have been described in different other studies on both animal and human subjects. It is usually analyzed computing the total vessel density, namely the number of vessel per area/volume in a region of interest, and the perfused vessel density, counting only the vessels reached by RBC. First evidences were reported more than 25 years ago, when Amann and colleagues reported a reduction in capillary density analyzing the myocardium of uremic rats [183]. These results have contributed to the idea that microvasculature is involved in CKD - cardiovascular disease correlation [184]. Capillary density has also been analyzed in patients with hypertension, finding a lower density only in the retina but not in the skin [172]. Recently, macro- and micro-circulation discrepancy has been reported in CKD patients along with microvascular impairment in sub-lingual microcirculation using sidestream dark field [185]. These findings suggest that microvascular impairment may not be detected by analyzing only macrovascular variable (e.g. heart

rate and pressure). In addition, it suggests that the interaction between macro- and microvasculature is complex, and one can be altered without significantly affecting the other. This may also be linked to vascular regulation processes. The sub-lingual impairment has been reported also when comparing healthy subjects to patients undergoing dialysis, but not when testing kidney transplant recipients (figure 1.14) [126]. Few months ago, Prom-

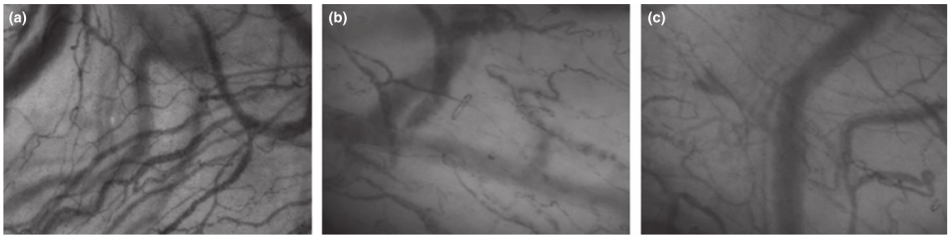

Figure 1.14: *Sublingual microcircualtion in (a) healthy volunteer, (b) dialysis patient, and (c) kidney transplant recipient. Used with permission from [126].*

mer and colleagues succeeded in finding a correlation between capillary density and urea concentration (as a market for uremia progression) in mice [186]. A reduction of capillary density has also been reported in omental tissues from children undergoing peritoneal dialysis [187].

The only work addressing directly the hydraulic conductivity of the capillary wall was performed using an animal model [127]. They perfused vessels of a frog mesentery using healthy and uremic plasma. Interestingly, they reported alterations in the semipermeable capability of the capillary membrane, reporting an increase of the hydraulic conductivity and a decrease of the reflection coefficient. From these results, authors have concluded that one or more uremic toxins affect the capillary wall membrane. This is also in agreement with the presence of pro-inflammatory substances, such as $TNF\alpha$, among uremic toxins. Finally, differences in microvascular impairment have been reported analyzing dialysis (before, during, and after the therapy) of diabetic and non-diabetic patients [188]. This phenomenon may originate from alterations in vascular regulation.

1.4 Aim of the work

Microvascular impairment in CKD is still not completely understood, even though it has been studied with reference to different tissues and employing different experimental and *in vivo* models. Neither its correlation with cardiovascular disease is sufficiently described. However, an increasing evidence of microvascular impairment is being developed. The description of these phenomena would be useful to properly understand occurrences in dialysis at different scales, elucidating the role of microvasculature, and eventually leading to better dialysis prescription. In this scenario, the modeling of microvasculature for uremic patients can play a pivotal role, allowing the description of involved phenomena or partially reproducing microvascular environment to analyze the microvascular response to uremic toxins. Thus, aims of the work are directly related to the modeling of involved phenomena and they are described by the following:

- propose and test both computational and experimental modeling approaches for microvasculature with particular reference to uremic pathology;
- build and organize a structure of computational and experimental tools which can benefit from the possible interactions between them.

CHAPTER 2

From vascular to microvascular models

In this chapter, the need for a comprehensive modeling approach is discussed. Such an approach is composed of three different models and their interactions. One of them is analyzed and used in this chapter to highlight the motivations of the modeling approach. The performed activities are listed and their role in the process toward the final development of the model is highlighted. Finally, the arrangement of the following chapters is presented, providing a first overview of the work.

In the first chapter, renal diseases and microvasculature have been described along with their current modeling approaches. Despite the big amount of information we have, such as the constantly improving identification of uremic toxins, lots of phenomena are still not fully understood (e.g. the effects of uremic toxins on the glycocalix, or on the capillary wall membrane). In this framework, microvasculature modeling in uremic patients has a central role, enabling a deeper investigation. The better understanding of what is going on in the microvasculature of these patients may eventually lead to a better capability of treatment planning and design. But first, some critical points should be considered. The microvasculature is connected to the macrovasculature and is immersed in the patient's tissue interstitium. The interaction of macro- and micro-vasculature is very complex and mediated by peripheral regulation, which, as all regulatory processes in our body, aims to maintain body homeostasis (i.e. perfusion of tissues, vascular pressure). Therefore, thanks to these regulation processes, alterations of macro- or micro-vasculature may not show in the other one. For example, discrepancies have been found in macro- and micro-vascular impairment referring to CKD patients [185]. In addition, microvascular impairment has been reported in literature in terms of reduced blood flow [175, 178, 179, 182] and reduced capillary density [126, 183–185]. Whether this microvascular impairment is related to other comorbidities and complications is still unclear. Surely, a lower capillary density raises the distance between cells and capillaries, therefore rising the distance nutrients have to travel. A lower peripheral blood flow instead reduces the supply of nutrients within tissues. Such phenomena may cause tissue damage. As an example, considering the cutaneous tissue, a correlation has been found between microvascular impairment and skin defect formation [179]. In addition, alterations in the microvasculature may induce impairments in fluid and solutes exchange, affecting the solutes compartmentalization and their removal from the interstitium. Finally, uremic toxins have effects on cells within the body. A great work has been conducted in order to identify them, and to figure out the typical concentration in both healthy subject and uremic patients [44, 45, 169]. It is still unclear which one of these toxins have more effect on microvasculature, but, thanks to the work of Harper [127], we know that they do have an effect on capillary membrane properties. Given the complexity of the phenomena, a comprehensive modeling approach is required to describe and study them. The modeling approach proposed in this work is a combination of three different models describing both macro- and micro-vasculature and their interaction:

- a lumped parameters model of the arterial circulation;
- a multiscale 3D-1D model of microvasculature;
- an *in vitro* model of the microvasculature.

2.1 The lumped parameter model

The first model is a lumped parameter model of the arterial circulation. This model has been proposed by Lanzarone and colleagues [189] (figure 2.1). It has been based on dif-

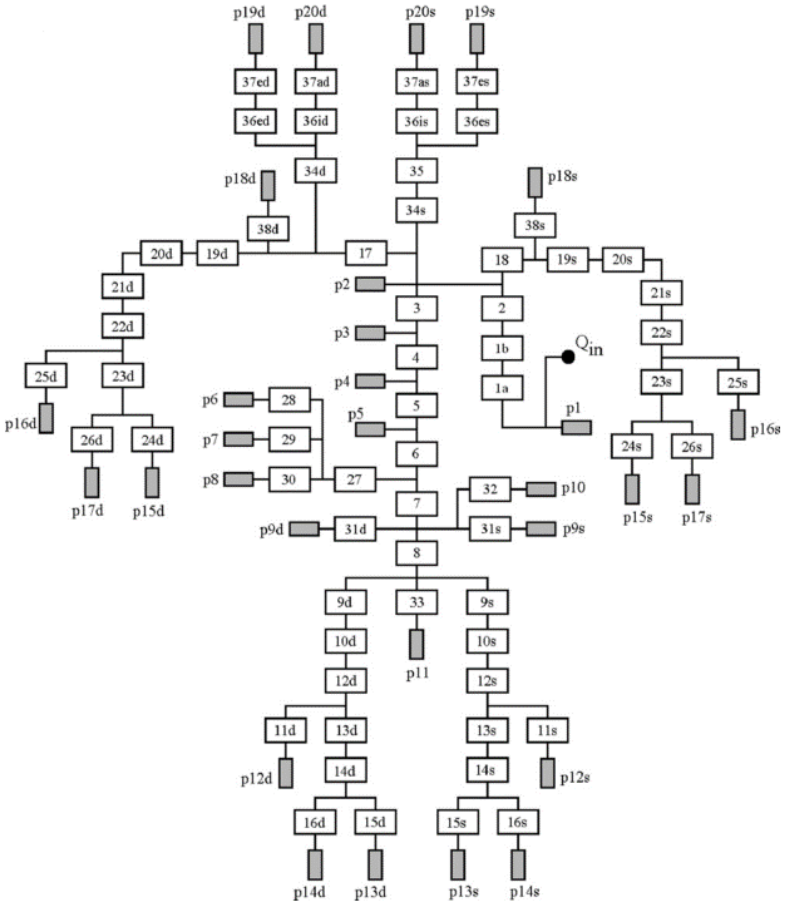

Figure 2.1: *Schematic of the lumped parameter model developed by Lanzarone [189]. White blocks represent big vessels, grey blocks stand for peripheral districts. Reprinted with permission from [189].*

ferent studies regarding arterial circulation which derived their description by the initial work of Westerhof and colleagues [190]. The novelty of Lanzarone's work was the introduction of the peripheral districts, namely the microvasculature up to the venule, also including peripheral vascular regulations. As a consequence, they were able to study and compare vascular resistances in physiological and extra-corporeal circulation due to car-

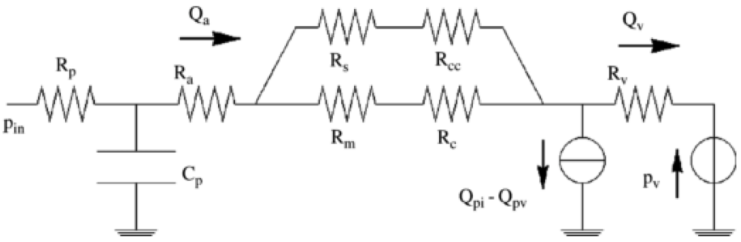

Figure 2.2: *Schematic of the peripheral district. From [189].*

diopulmonary bypass. The model is composed of 64 blocks describing big vessels and 30 blocks describing peripheral districts. Each block is described by means of block-specific parameters to describe the heterogeneity of the circulation. These parameters have been computed according to available literature data, considering cylindrical vessels and blood properties (i.e. viscosity and density, expressed as a function of the hematocrit). In particular, when modeling the peripheral districts (figure 2.2), the inertia of blood flow has been neglected. These districts are composed mainly of resistive components, accounting only for the compliance of terminal arteries. In addition, they have been described considering the number of vessels. For example, capillaries have been modeled by the resistance R_c and R_{cc}, which have been computed by considering N parallel vessel. This generator is important in the presented analysis because it describes the filtration from the capillary vessels. The second generator has been used to set one of the boundary conditions of the system, by specifying the venular pressure, constant for all the districts and equal to $4\,mmHg$. The other boundary condition has been specified at the inlet of the system, by setting the inlet flow rate according to the Swanson and Clark expression [191].

2.1.1 Assessment of the fluid dynamics within the vasculature

As first step of this work, the model has been used to analyze the steady and laminar approximations, which are useful in the description of flow within the microvasculature. To this aim, the uncontrolled version of the model has been used, namely the model in which all the vascular regulations are turned off. When simulating physiological conditions, their action induces small variations of the resistance (i.e. the vessel radii). As a consequence, under these conditions, their effect on blood velocity within the vessels is negligible. The flow rate within capillaries has been derived from the model, and then the velocity characterizing each peripheral district has been computed by considering the number of modeled parallel vessels. The average velocity is lower than $1\,mm/s$ in the capillary vessels of

all the peripheral districts, namely a bit low but not far from the average values reported in the microvasculature. Then, the Reynolds number has been computed, resulting in $Re \simeq 10^{-2}$. To compute the Womersley number Wo, the signal of the velocity over time has been analyzed by Matlab® using the discrete Fourier transform. By plotting the intensity-frequency graph, a higher limit for the signal has been identified in $10\,Hz$, i.e. in all the districts, the signal is well included in the range $0 - 10\,Hz$. Consequently, $10\,Hz$ has been used to compute the Womersley number, as a worst case for the majority of the districts. It results in $Wo \simeq 0.5$ and $Wo^2 \simeq 0.025$. Therefore, by these results, viscous forces dominate the inertial forces in agreement with [192].

2.1.2 Improving peripheral description

The peripheral description of the lumped parameter model has been improved to better describe the fluid balance. To this end, a single peripheral district has been studied without coupling it with the overall system. In particular, the splanchnic periphery (p6 in figure 2.1) has been studied. At this point, the structure of the peripheral districts is equal for all districts. Therefore, one district is representative of the others. The specific district has been chosen between the core body compartments, avoiding districts depicting kidneys. The new peripheral description has been obtained by changing the resistances arrangement, the description of the interstitial pressure and the lymphatic flow rate, and the rheology description. The new schematic proposed for the periphery is shown in figure 2.3. It is based on the previous schematic proposed by Lanzarone and colleagues, and in particular, it differs for the shunt vessels, which by-pass the capillary bed solely. The peripheral district is composed by terminal arterioles (which are the last vessels including a compliance effect), arterioles, small arterioles, capillary vessels, shunt vessels and venules (figure 2.3).

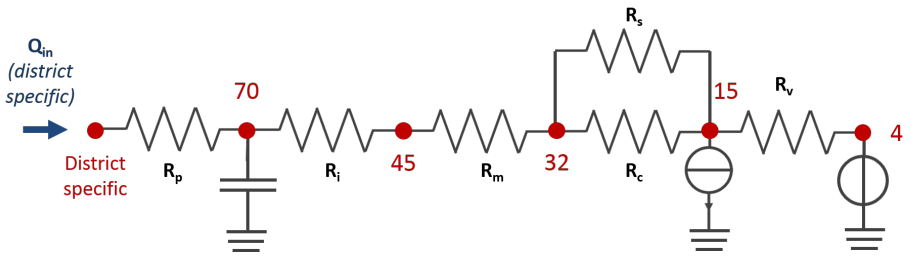

Figure 2.3: *The new schematic proposed to describe the peripheral districts. Reference pressure are shown in red.*

Shunt vessel characterizes only some types of tissue (e.g. some parts of the skin [193]), but

since peripheral networks describe vasculature of several different tissues, they have been included in all the districts. As done by Lanzarone and colleagues, mean values of pressure have been specified along points of the peripheral district to compute the resistances (figure 2.3). However, capillary inlet pressure (the pressure upstream of the capillary resistances R_c) has been modified according to literature data [194]. On the contrary, the reference flow rate and the inlet pressure are tissue-specific and they have been computed on the basis of data reported in [195]. Due to mass conservation, at the equilibrium (i.e. no net flow rate entering the capacity) the flow rate flowing into the vessel p, i, and m is the same. The flow rate Q_v has been computed as $Q_{in} - filtration$. The latter has been defined to emulate the overall filtration rate $2\,ml/min$. As a consequence each peripheral network should filter $\frac{2\,ml/min}{5\,l/min}\,Q_{in}$. As previously done by Lanzarone et al., the number of vessels can be determined starting from the resistance of a single vessel, computed by means of geometrical relations. At this point, two differences have been introduced. The first one, as anticipated, regards the rheological description of blood. As the flow velocity falls below $1\,mm/s$, some changes in the apparent viscosity may happen in small vessels, due to the interaction with the glycocalyx (e.g. [196, 197]). To model this dependency, the Casson model has been adopted defining (i) the viscosity at high shear rates as done by Lanzarone and colleagues (i.e. following the formulation of Pries and colleagues [98]), and (ii) the yielding shear stress τ_y as defined by [198]. A further variation of Lanzarone's model regards the dimension of the capillary vessels. They have been computed to satisfy the following criteria referring to the total number of vessels within the body: (i) the relation Δp-Q, as done by Lanzarone et al.; (ii) an overall S/V equal to $70\,cm^{-1}$ [199], to achieve a good estimate of the total lateral surface area. In figure 2.4, a surface is presented in the 3D plot of S/V depending on the considered radius and length of the capillaries. Such surface satisfies the first criteria, namely the overall relation Δp - Q is guaranteed. From that result, the radius and the length of the capillary vessel have been selected as $4\,\mu m$ and $1.7\,mm$ respectively. Those results are close to the range of the data reported *in vivo*. Therefore, the radius and length for each vessel typology are reported in the table 2.1. Regarding the lymphatic drainage, it has been defined following the works of [30, 56] (figure 2.5). For clarity, it means that the lymphatic drainage referred to the physiological working point $p_t = -1\,mmHg$ has been defined as $2\,ml/min$. Such a formulation and its derivation will be further described in the chapter 3. This formulation is applicable to the whole body. In order to describe each peripheral district, the expression has been scaled by $N_{c,i}/N_{c,tot}$:

$$Lf(l/min) = \frac{N_{c,i}}{N_{c,tot}} * \left(\Phi_{max} - \frac{\Phi_{max} - \Phi_{min}}{1 + exp(\frac{p_T - 2}{slope\ factor})}\right) \qquad if\ V_i \geqq V_{i,basal}\ ,$$

$$Lf(l/min) = 0 \qquad if\ V_i < V_{i,basal}\ ,$$

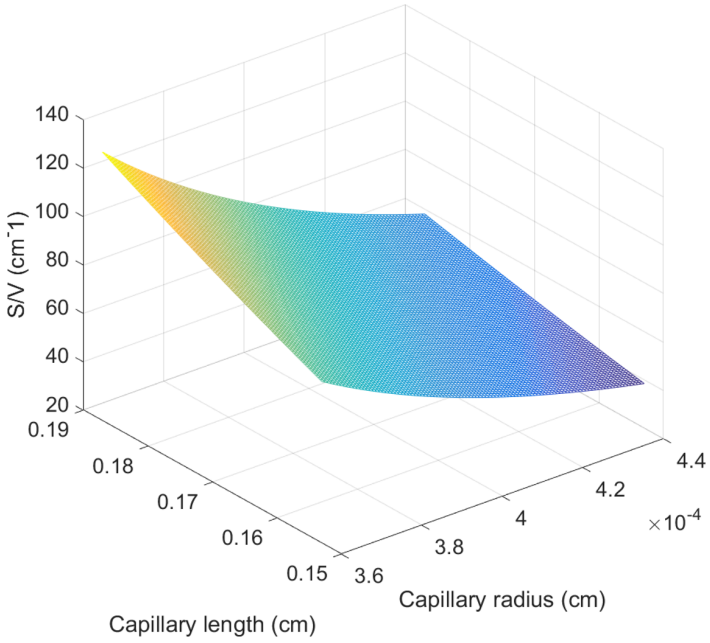

Figure 2.4: *3D profile of the S/V ratio depending on radius and length modeled for the capillaries. The plotted surface satisfies the imposed Δp-Q relation.*

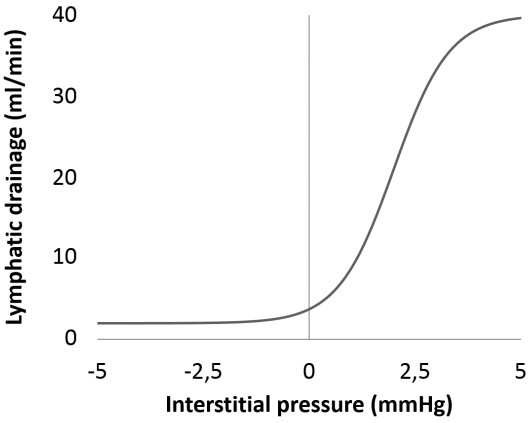

Figure 2.5: *Graph of the interstitial pressure - lymphatic drainage implemented. Values of the lymphatic drainage are referred to the overall model. They have been split in the peripheral districts.*

Table 2.1: *Values of length and radius for each vessel modeled.*

Vessel	Terminal artery (p)	Arteriole (i)	Terminal arteriole (m)	Capillary (c)	Shunt (s)	Venule (v)
Radius (μm)	250	25	15	4	15	30
Length (cm)	15	1.5	0.5	0.17	0.65	2

where the values of Φ_* have been derived from [30, 56]. This is based on the assumption that the more vascular capillaries are present in a tissue, the more lymphatic vessels are present, and consequently, the more drainage is produced. This assumption will be further discussed in section 2.1.4. The interstitial pressure-volume relation has been described by means of a third-grade polynomial. Data for the interpolation have been derived by [5] and scaled to match the pressure reported by [30]. To refer this relation to each peripheral district, it has been derived in terms of $V_i/V_{basal,i}$ as shown in figure 2.6. To test the im-

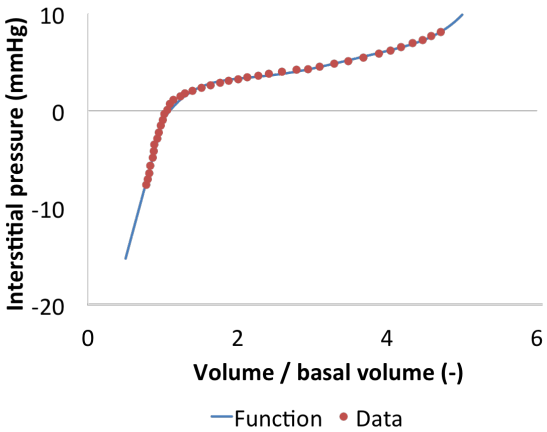

Figure 2.6: *Graph of the interstitial pressure - volume relation implemented.*

proved schematic, different simulations have been run. The aim of the first computational test is to verify the fluid balance of the model under physiological conditions.
Moreover, the test has been conducted both with and without factoring the lymphatic flow

rate, in order to show its fundamental contribution. Then, the effect of the oncotic pressures π, the reflection coefficient σ and filtration coefficient L_p have been analyzed. In addition, the effect of the inlet pressure has been tested by comparing three simulations varying the inlet pressure of $+10mmHg$ and $-10mmHg$. All the simulations have been run simulating $1000\,s$, data referred to the last $200\,s$ have been exported, and the average quantities are referred to the last $20\,s$.

2.1.3 Simulation of fluid balance

Results of the simulations are shown in this paragraph from the simpler to the more complex considered setup. First, the model has been studied referring to physiological conditions. To this end, the inlet pressure for the considered peripheral district has been set equal to $92.3\,mmHg$, as reported by Lanzarone et al. [189]. Analyzing the results, the agreement of the pressure values with the expected values has been confirmed as shown in figure 2.7. Moreover, even if a net filtration rate is reported, the interstitial volume is still

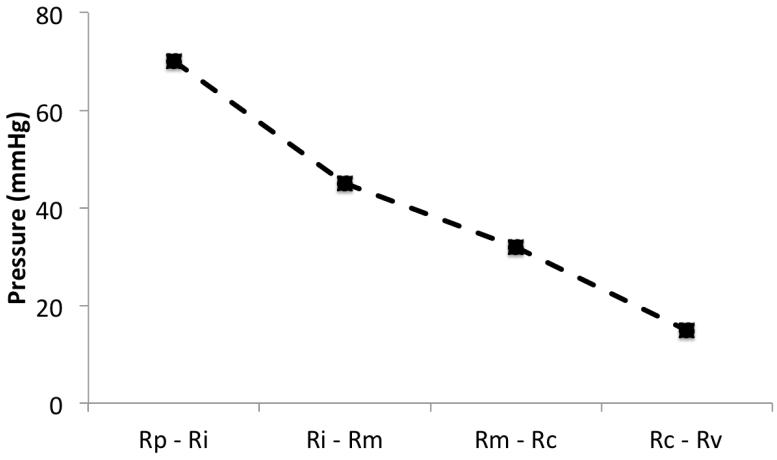

Figure 2.7: *Pressure along the peripheral network when simulating physiological reference conditions without considering vascular regulations.*

equal to the basal volume value (figure 2.8). This is due to the action of the lymphatic system, which drains fluid from the interstitium. More precisely, when the lymphatic drainage balances the net filtration rate, no variation of the interstitial volume is reported over time. The net filtration rate is also consistent with the expected value. Indeed, taking this peripheral district as representative and scaling up this value to match the entire model, the overall net filtration rate is $\simeq 2\,ml/min$ [5]. Conversely, if the lymphatic drainage is not

considered, the net filtration rate is not balanced by the lymphatic system and the interstitial volume starts to increase. Such a condition evolves up to a null net filtration rate to achieve the condition in which $\frac{dV}{dt} = 0$. In particular, due to the rising in the interstitial volume, the interstitial pressure will increase, producing a decrease in the net filtration rate. The small magnitude of the filtrated fluid volume with respect to the interstitial volume (i.e. with reference to the whole body $2\,ml/min$ vs $11\,l$) implies a long time constant. At the end of this time, the increase in volume is about 1%. Consequently, the net filtration rate decrease due to the rise in interstitial pressure.

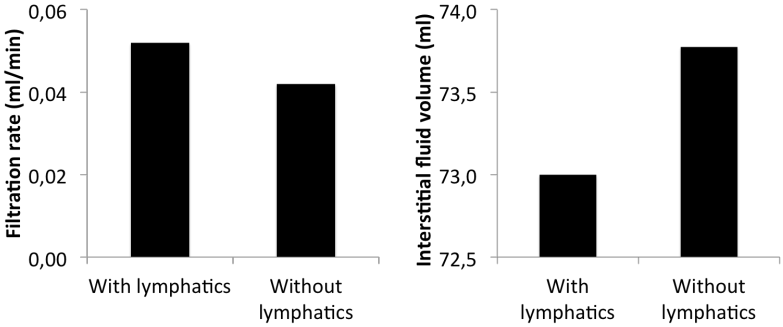

Figure 2.8: *Comparison of net filtration rate and interstitial volume in two simulations with reference physiological values, which differ for the presence of the lymphatic drainage.*

A subsequent test concerns the effects of $\Delta\pi$, σ and L_p variations (figure 2.9). These parameters have been varied with reference to uremic conditions. Therefore, the following parameter have been set: $\Delta\pi = 19\,mmHg$ [54, 200, 201], $\sigma = 0.75$, and $L_{p,uremic} = 8.8\,L_{p,physiologic}$ [127], where physiological hydraulic conductivity $L_{p,physiologic}$ has been set from [162]. Such variations will be further discussed in the chapter 4. They resulted in negligible variations of the inlet flow rate and the capillary pressure. Indeed, because of different filtration rate, the flow rate at venule level is slightly different, lightly influencing the pressures upstream and consequently the flow rates themselves. Conversely, the alterations of the filtration rate and the interstitial volume are definitely more marked. The increased filtration rate induces a variation of the interstitial volume. Therefore, the net filtration rate is greater than the lymphatic drainage inducing fluid accumulation in the interstitium, namely edema. The system reaches the equilibrium condition only when the increase of the interstitial volume, and therefore in the interstitial pressure, induces a greater lymphatic drainage that counterbalances the greater filtration rate.

A variation of the net filtration rate has been induced by variation of the inlet pressure

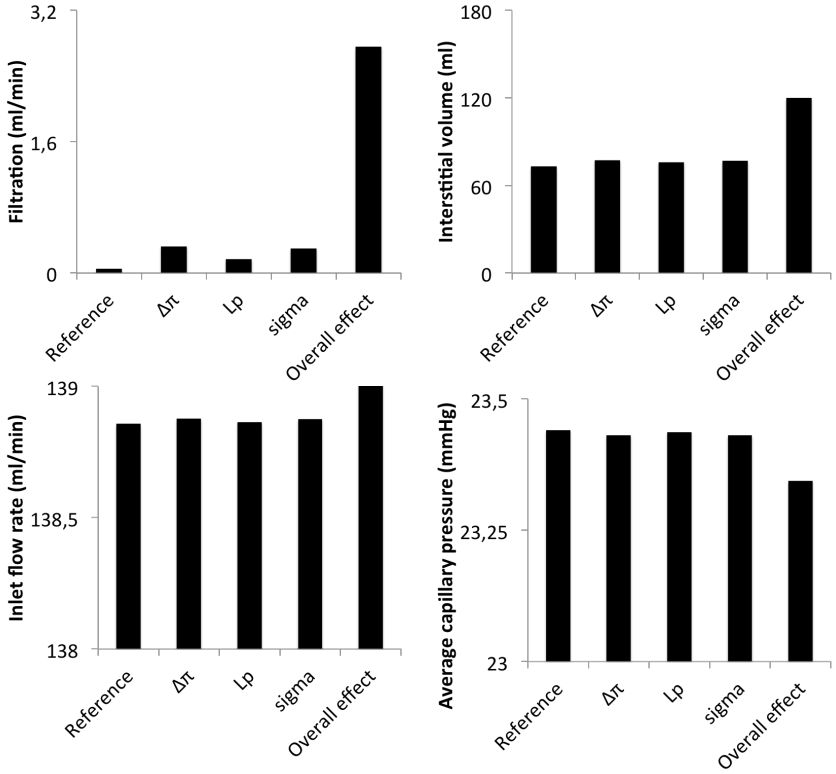

Figure 2.9: *Alterations of filtration rate (left top), interstitial fluid volume (right top), inlet flow rate (left bottom), capillary pressure (right bottom) due to variations of $\Delta\pi$, σ, and L_p from their physiological reference to their uremic values.*

(figure 2.10). The capillary pressure is linearly influenced by these variations. This is consistent with the pure resistive nature of the district when considering steady flow. Indeed, this condition can be described as voltage (or pressure) divider. As a consequence, the variation of pressure in the vessels R_c is only a portion of the variation applied at the inlet. Even if the variations of the average capillary pressure are small, they are sufficient to move the peripheral conditions from the equilibrium point, causing variations of the interstitial volume. In particular, an average capillary pressure lower than the physiological reference results in a lower interstitial volume, due to net movement of fluid from the interstitial space to the vasculature. Conversely, a higher average capillary pressure results in fluid accumulation, with considerations similar to what was already said for the variations of $\Delta\pi$, σ, and L_p.

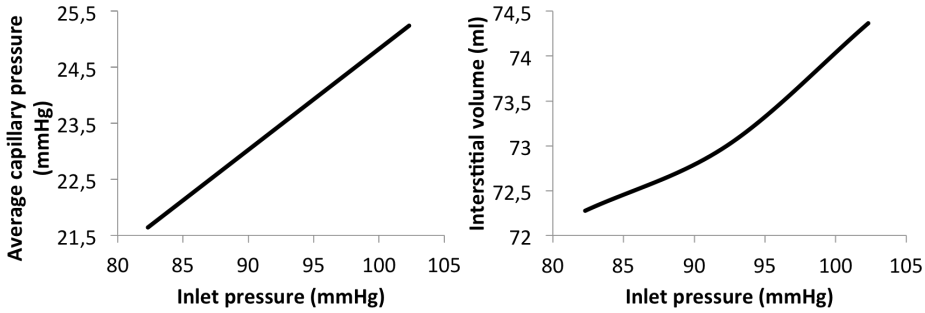

Figure 2.10: *Variation of the average capillary pressure and the interstitial volume due to alteration of the inlet pressure.*

2.1.4 Discussion

Results have confirmed the improvement of the fluid balance description in the proposed lumped parameter model. Indeed, if scaled to the overall model, the resulting net filtration rate agrees with the physiologic value expected under physiological conditions [5]. Moreover, under the same conditions, the lymphatic drainage has been correctly accounted for, avoiding fluid accumulation, i.e. edema (figure 2.8). However, the assumption used to split the lymphatic drainage into the peripheral blocks should be further discussed. By such means, a greater number of capillaries produces a larger filtration, that is balanced by a greater lymphatic drainage. This is consistent with the fact that the lymphatic vascular system is intimately related to capillary beds. Conversely, some differences in the lymphatic vascular anatomy have been reported between tissues [202, 203]. Once this variability is understood and the difference between peripheries is quantified, it can be included in the model. This would produce a more accurate model accounting also for existing differences in the peripheral lymphatic vasculature. Moreover, the effect of lymph absorption at the lymph nodes can be accounted for, by building the model on a greater reference value for lymphatic drainage. Such a modification will be discussed afterwards in the work.

A further modeling approach to be discussed is the formulation of the apparent viscosity. Even if the dependence on the shear rate has been included, and it agrees with the more detailed model presented in [196], this description is not related with the interaction with the glycocalyx but it is purely phenomenological. Indeed, this description is worth a deeper experimental analysis. This shear rate dependence will be further discussed along the work.

In addition, alterations of $\Delta\pi$, L_p, σ, and inlet pressure have been studied. Even con-

sidering only one peripheral district, these two computational tests allow the identification of two different microvascular conditions, in particular in terms of net filtration rate, which either have or not have been linked to a consistent change in vascular pressure upstream the peripheral district. Consequently, a deeper description of microvasculature alone is not sufficient to model the complex phenomena involved in uremic alterations. These results support the work towards a comprehensive multiscale model of both the macro- and the micro-circulation, gaining the spatial description by means of the 3D-1D model, without losing information related to the macrocirculation influence.

2.2 The multiscale 3D-1D model

The second and main approach considered is a multiscale 3D-1D model of microcirculation (figure 2.11). The mathematical bases for this model have been developed by re-

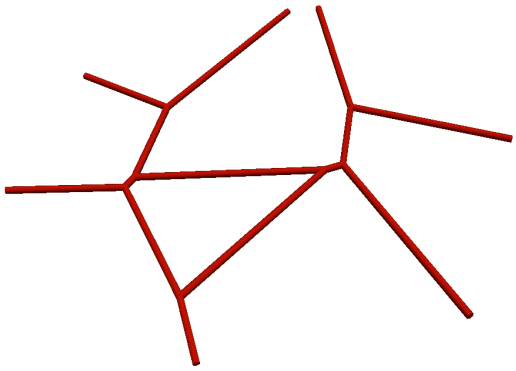

Figure 2.11: *Example of a vascular geometry of the multiscale 3D-1D model.*

searchers at the MOX lab, in Politecnico di Milano [161, 162, 166, 167]. It allows the description of a complex geometrical network, by reducing it to one dimension, therefore, describing vessels with their centerline. An important feature consists in the ability of the model to account for the coupling between the vasculature and the surrounding environment. The use of such models enables a deeper description of the microvascular environment by including variables spatial dependence. Similar models have been used in literature to describe microvascular environment with particular reference to the oncological application. In this work, this model has been used to describe the fluid balance with focus on the microvasculature. To this aim, the model has been derived to include the coupling of the microvasculature with the interstitium, also considering not straight vessels. Complex geometries can be included in the model concerning both three-dimensional arrangement of the vessels and their radius heterogeneity. Fåhraeus - Lindqvist and Zweifach - Fung effects have been included in the model since they characterize the blood flow in the microvasculature. In addition, oncotic pressure differences and lymphatic drainage have been included to guarantee a proper modeling of the fluid balance.

2.3 The *in vitro* model

Conversely, the third approach consists in an experimental model of the *in vitro* vasculature in a microfluidics chip (figure 2.12). A self-assembled vascular network is generated

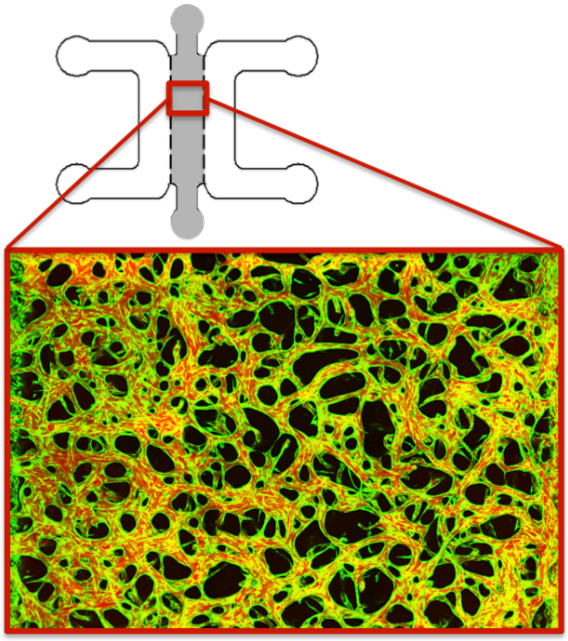

Figure 2.12: *Scheme of the in vitro model used. Microvascular network of EC (green) perfused with red fluorescent dextran.*

within a hydrogel using endothelial cells and then tested using fluorescent labeled dextran. These models are usually applied to study the microvasculature (i.e. permeability of the capillary membrane). Moreover, they are also considered to build *in vitro* models of different pathologies. In this work, such a modeling approach has been adopted to study the microvascular wall membrane alterations induced by uremic toxins. To this aim, a trans-mural pressure between the microvasculature and the surrounding environment has been considered, enabling the analysis of the membrane properties. Such a technology enables the analysis of microvascular alterations due to the presence of pathological conditions, such as the presence of uremic toxins, by providing an experimental tool to test them. The experimental setup has also been analyzed by computational analyses to investigate the trans-mural pressure formation.

2.4 Models interactions and outline of the work

The three models together constitute a comprehensive modeling approach, whose purpose is to describe phenomena at different scales allowing a better understanding of them. A schematic of the overall modeling approach is presented in figure 2.13. Starting from previous models of the arterial circulations, a more detailed analysis has been considered in this work. As shown in the first section of this chapter, the possible interactions between the lumped parameter model and these detailed models may enable the analysis of complex phenomena involved in uremic pathology. Namely, the 3D-1D model and the *in vitro* models provide a more detailed description of the microvasculature, whereas the lumped parameter model accounts for the interaction with the macrovasculature. In addi-

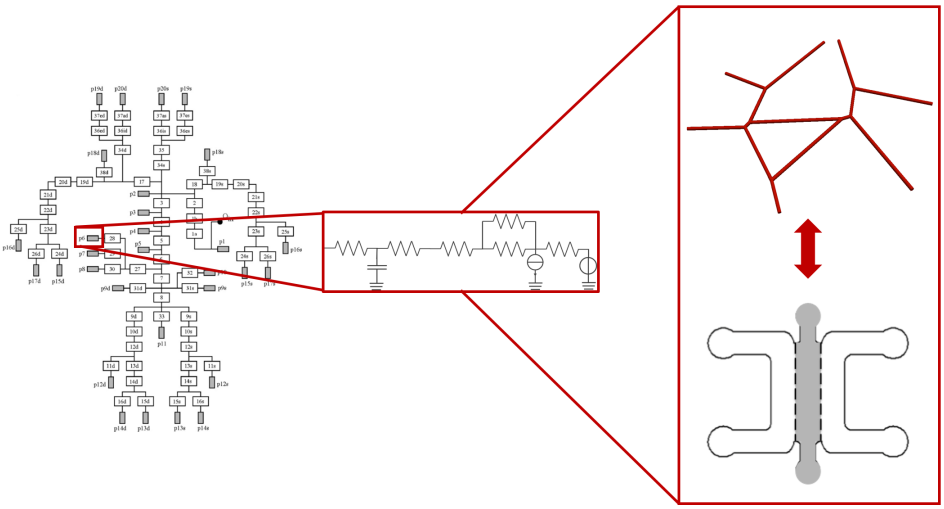

Figure 2.13: *Schematic of overall modeling approach.*

tion, one of the advantages of this modeling approach consists in the possibility of models interactions. In particular, the two computational models share a description of the microvasculature. The first one enables the study of peripheral pressure variations due to pathological conditions. In addition, fluid dynamics within the peripheral district has been analyzed, supporting the viscous forces dominance assumption. Deriving the description of pathological variations of microvascular pressures from the lumped parameter model, the 3D model can be used to address spatial effects and study them. This study may also result in an improvement of the peripheral description in the lumped parameter, composing a modeling loop, which will eventually lead to a more accurate model. The *in vitro* model allows the analysis of capillary membrane alterations, studying specific effect of uremic

toxins. Therefore, information about the alterations of the hydraulic conductivity and the reflection coefficient can be used to improve both computational models. Moreover, it enables the study of solutes permeability through capillary wall, helping the investigation of solutes removal. In addition, the 3D computational model can be used to describe the fluid dynamics within the chip, to confirm experimental assumptions and helping in experimental design.

The development of such a comprehensive model requires extensive research efforts, also considering the collection of clinical/experimental data for model validation. This work represents a methodological step in the definition of the models, paving the way for subsequent studies aimed at the systematic investigation of uremic vascular alterations.
In particular, research activities have been conducted to:

- include in the 3D-1D model a non-linear description of the lymphatic drainage (Chapter 3)
- describe the hematocrit heterogeneity within the capillary bed, considering Zweifach - Fung and Fåhraeus - Lindqvist effect, namely considering the blood rheology dependent on hematocrit and vessel diameter (Chapter 3);
- simulate uremic microvasculature with the known literature data, and comparing them to *in vivo* evaluation (Chapter 4);
- perform a sensitivity analysis of the 3D-1D model developed, with reference to filtration and interstitial pressure (Chapter 4);
- develop *ad hoc* experimental setup to analyze capillary wall properties, and using it to describe urea effect (Chapter 5).

The work is then completed by a general discussion addressing the limitation and the potentiality of the presented work (Chapter 6).

CHAPTER 3

A multiscale 3D-1D model of microcirculation

The multiscale 3D-1D model of microcirculation is described in this chapter, starting from the strong formulation up to the discrete form. In addition, an artificial generator of microvascular geometries and some test cases have been described. The content of this chapter is based on two different manuscripts:

- *'A computational model for microcirculation including Fåhraeus - Lindqvist effect, plasma skimming and fluid exchange with the tissue interstitium' by Possenti et al., International Journal for Numerical Methods in Biomedical Engineering (in press);*
- *'Numerical simulations of the microvascular fluid balance with a non-linear model of the lymphatic system' by Possenti et al., Microvascular Research (in press).*

In the first chapter, the state of the art of *in silico* modeling of microvasculature has been described. The computational problem has been addressed with several different approaches. The model presented in this work will describe both the microvasculature and the interstitium, along with the interaction between them, because of the semi-permeability of the capillary membrane. To this end, a multiscale approach is adopted, considering a one-dimensional (1D) vascular network in a three-dimensional (3D) porous media. Therefore, from a mathematical point of view, the model consists of coupled partial differential equations (PDEs) on manifolds with heterogeneous dimensionality. This approach was first proposed by D'Angelo [161, 166] and it has been mathematically and numerically developed in several works [162, 167, 204]. In such works, the model has been described as Poiseuille flow for straight vessels (with constant viscosity), Darcy flow within the interstitium, and the coupling between them (first three point of the following list). The here presented model has been rigorously derived from the governing equation of flow accounting for:

- coupled vascular and interstitial flow, namely describing leaky channels;
- complex geometries;
- radii heterogeneity along the vascular network;
- curvature of the vessels;
- oncotic pressure differences between vasculature and interstitium;
- lymphatic drainage from the interstitium;
- blood rheology dependence on hematocrit (Fåhraeus - Lindqvist effect);
- heterogeneity of RBC distribution along the network (Zweifach - Fung effect).

The derivation of the model is presented in the following paragraphs starting from the fluid dynamics model (including coupled flow, radii heterogeneity, curvature of the vessels, and oncotic pressures) followed by the RBCs model (accounting for RBC heterogeneity along the network and its effect on blood rheology). Then, the lymphatic drainage modeling is described. Moreover, a generator of artificial networks is presented. Finally, some test cases are discussed.

3.1 A 3D-3D analytical model

The model of fluid transport is built with reference to two different domains: Ω_t, the interstitium, and Ω_v the vasculature (figure 3.1). The surface Γ is defined as $\Gamma = \partial\Omega_v \cap \partial\Omega_t$, namely the interface between the two domains, therefore depicting the capillary membrane. The interstitium Ω_t has been described as a porous medium, characterized by a

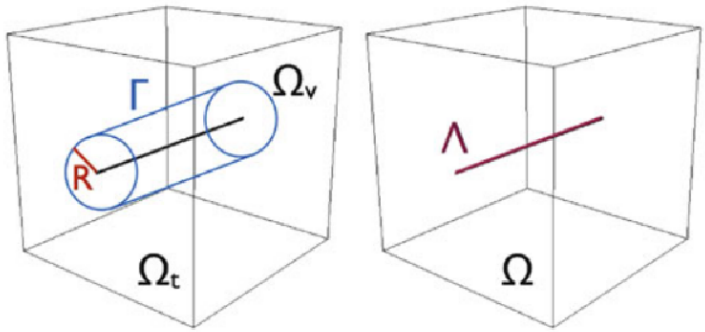

Figure 3.1: *Scheme of the two domains for a simple straight vessel with one straight vessel. Ω_t is the interstitium, Ω_v the vessel characterized by its radius R, and Γ is the outer surface of the domain Ω_v. From [205]*

hydraulic conductivity K. Two assumptions are presented here, in order to write the starting equations of the model.

- Steady flow. As described in the first chapter, this assumption is reasonable ($Wo < 1$) and widely used in computational model of the microvasculature. Thus, any possible transient phenomena is neglected.
- Body forces. Any body force (i.e. gravity, inertia) is neglected.

Being $\boldsymbol{x} \in \Omega$ the spatial coordinate, the problem (equation 3.1) has been written in terms of the fluid velocity $\boldsymbol{u} = \boldsymbol{u}(\boldsymbol{x})$ and the fluid hydraulic pressure $p = p(\boldsymbol{x})$, using the subscripts t and v when referring to Ω_t and Ω_v respectively:

$$\begin{cases} \boldsymbol{u}_t + \dfrac{\mathrm{K}}{\mu_t}\nabla p_t = 0 & \text{in } \Omega_t \\ \nabla \cdot \boldsymbol{u}_t + \phi_{lymphatics} = 0 & \text{in } \Omega_t \\ \rho_v(\boldsymbol{u}_v \cdot \nabla)\boldsymbol{u}_v = -\nabla p_v + \mu_v \Delta \boldsymbol{u}_v & \text{in } \Omega_v \\ \nabla \cdot \boldsymbol{u}_v = 0 & \text{in } \Omega_v \end{cases} \tag{3.1}$$

where $\phi_{lymphatics}$ is the volumetric term accounting for the lymphatic drainage (further discussed in the section 3.2.3), and ρ_v and μ_v are the density and the viscosity of the fluid inside the vasculature. To couple the two domains, fluid transport across the capillary membrane should be considered by setting the proper boundary condition on Γ:

$$\boldsymbol{u}_t \cdot \boldsymbol{\tau}_k = 0, \quad \text{on } \Gamma \quad \boldsymbol{u}_v \cdot \boldsymbol{n} = \boldsymbol{u}_t \cdot \boldsymbol{n} = f \tag{3.2}$$

where $\boldsymbol{\tau}_k$ are the tangential binormal vectors with $k = 1, 2$, and $\boldsymbol{n}$ is the normal outward vector. The first condition is describing a wall boundary condition, namely the *no-slip* condition. The second one is describing the fluid flux across the capillary membrane by means of the function f. In this work, the classical Starling principle is applied (section 1.2.3), leading to the following expression:

$$f = L_p\Big((p_v - p_t) - \sigma(\pi_v - \pi_t)\Big) \tag{3.3}$$

where π stands for oncotic pressure. This $(\pi_v - \pi_t)$ is assumed independent from the spatial coordinate $\boldsymbol{x}$.

3.2 The 3D-1D multiscale model

The model presented in the previous paragraph has been reduced to achieve a 3D-1D multiscale model, following the procedures described in [161, 162, 167, 205, 206]. In these previous works, Poiseuille flow has been coupled with Darcy flow to describe the microvascular environment considering straight vessels. To achieve the 3D-1D description, the domain Ω_v is reduced to its centerline Λ (figure 3.1). Based on this reduction, the local cylindrical coordinate is defined as $\boldsymbol{x} = (r, \theta, s)$ at each point of the centerline of the vessels. Consequently, the radial, circumferential and axial vectors are denoted by $\boldsymbol{e}_r, \boldsymbol{e}_\theta, \boldsymbol{e}_s$. Considering these definitions, the one-dimensional model that describes the bulk flow within the vasculature is obtained based on the following assumptions.

- Circular vessel cross section. Namely, the intersection between the vessel and the plane orthogonal to its axial vector $\boldsymbol{e}_s$ is always a circle.
- Dominance of the axial velocity. The other two components (i.e. the radial and circumferential velocity) are negligible compared to the axial component, allowing us to describe the velocity as $\boldsymbol{u}_v = u_v(r, \theta, s)\, \boldsymbol{e}_s$.
- Dominance of viscous forces. This assumption is justified by the low Reynolds number characterizing the microcirculation (as described in the first chapter).

Therefore, the equations relative to the vascular domain Ω_v have been written as:

$$\begin{cases} -\mu_v \Delta u_v + \partial_s p = 0 \\ \partial_s u_v = 0 \\ u_r = u_\theta = 0 \qquad\qquad \forall (r, \theta, s) \in \Omega_v \\ \partial_r p_v = 0 \\ \partial_\theta p_v = 0 \end{cases} \tag{3.4}$$

where ∂_* indicates the partial derivative in the direction $*$ and Δ denotes the Laplace operator with respect to cylindrical coordinates $\Delta u = 1/r \partial_r (r \partial_r u) + 1/r^2 \partial_\theta^2 u + \partial_s^2 u$.

To proceed with the one-dimensional reduction, a parametric description of a generic curvilinear vessel has been introduced. Then, a decomposition of the velocity profile has been used to obtain the final form of the equation.

At this point, for each curvilinear vessel the parametric *arc length* has been defined as $\boldsymbol{\Psi} : \mathbb{R} \to \mathbb{R}^3$ such that $\boldsymbol{\Psi} \in C^3(\mathbb{R})$ and $\|d_z \boldsymbol{\Psi}(z)\| = 1$ for any $z \in [0, L]$ being

L the length of a generic branch of the capillary network. From this parameterization, $s = \int_0^z \|d_\zeta \mathbf{\Psi}(\zeta)\| d\zeta = z$. In addition, the curvature of the arc can be computed for a given z as $\kappa = \|d_{zz}\mathbf{\Psi}(z)\|$. The center of the osculating circle in that point is $1/\kappa$ times far in the direction specified by the unitary centripetal vector $\boldsymbol{N}(z) = d_z\mathbf{\Psi}(z)/\kappa$ (figure 3.2).

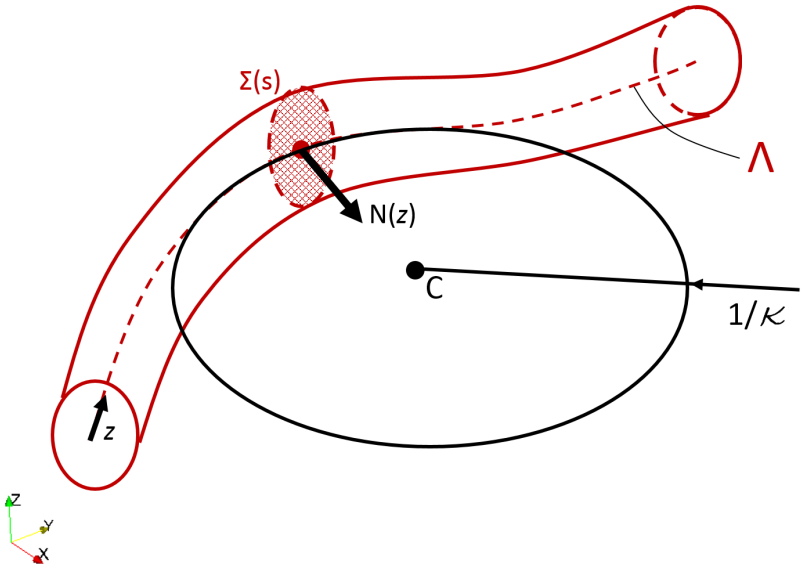

Figure 3.2: *Example of the parameterization of a single capillary vessel. The centerline is indicated by Λ. It is described in the 3D space (x,y,z) by the function $\mathbf{\Psi}(z)$. The osculating circle, which has a radius equal to $1/\kappa$, is drawn with reference to the red point. Originating from this point, the unitary centripetal vector $\boldsymbol{N}(z)$ points towards the center of the circle.*

Then, the axial velocity has been decomposed highlighting a shape factor $\Phi(r,\theta)$ and the mean or bulk velocity of the blood stream $\overline{u}_v$ (referred to the cross section identified by the arc length s, therefore denoted by $\Sigma(s)$ - figure 3.2):

$$u_v(r,\theta,s) = \overline{u}_v(s)\Phi(r,\theta). \tag{3.5}$$

Accordingly:

$$\overline{u}_v(s) = \frac{1}{\pi R^2}\int_{\Sigma(s)} u_v \, d\sigma\,, \quad \overline{p}_v(s) = \frac{1}{\pi R^2}\int_{\Sigma(s)} p_v \, d\sigma\,. \tag{3.6}$$

The shape factor $\Phi(r,\theta)$ is composed of two different elements, defined in a way that

allows us to separate r and θ contribution:

$$\Phi(r,\theta) = \phi(r/R)(1 + ar\cos\theta + br\sin\theta + cr^2\cos\theta\sin\theta + dr^2\cos^2\theta + er^2\sin^2\theta)\,, \quad (3.7)$$

where a, b, c, d, e are parameters to be determined. The first part $\phi(r/R)$, namely the radially symmetric part of $\Phi(r,\theta)$ is typically modeled as:

$$\phi(r/R) = \frac{\gamma+2}{\gamma}\left(1-(r/R)^{\gamma}\right).$$

The Poiseuille's flow, characterized by a parabolic profile, is obtained for $\gamma = 2$ which results in: $\phi(r/R) = 2\left(1-(r/R)^2\right)$. To define the second part of the shape factor $\Phi(r,\theta)$, the parameters a, b, c, d, e should be determined on the basis of $\mathbf{\Psi}$, i.e. to obtain $\Phi(r,\theta,\psi)$. To this end, some additional assumptions are required.

- Symmetry of the profile. First, a reference for θ should be defined. For each cross section, the reference is defined such as the axis $\theta = 0$ is collinear with the vector $\boldsymbol{N}$. In this way, we can reasonable require that in each cross section $\Phi(r,\theta,\psi) = \Phi(r,-\theta,\psi) \quad \forall r,\theta,\psi$. As a consequence, the parameters b and c must be equal to 0.

- Linear dependence. The correction factor (i.e. the second part of $\Phi(r,\theta,\psi)$) of the velocity profile at any point s is assumed to be linearly dependent on the distance from the center of the osculating circle to this point.

Consequently, the velocity profile must be null in the center of the osculating circle C. Therefore, $\Phi(r = 1/\kappa, \theta = 0, \psi) = 0$ gives $d = -a\kappa - \kappa^2$. A further consequence is that all the points $1/\kappa$ far from the center C must have the same correction factor. If we express those points with reference to r and θ, a set of points is obtained as:

$$\varphi = \{(r,\theta): \quad r = \frac{2\cos\theta}{\kappa}, \quad \theta \in [-\frac{\pi}{2};+\frac{\pi}{2}]\}.$$

As stated above, all these points have the same correction factor $\Phi(r,\theta,\psi)$. Among them, the point with $r = 0$ has $\Phi(r=0,\theta,\psi) = \phi(0)$, namely showing that for those points the correction factor is 1. Therefore, $\forall(r,\theta) \in \varphi$:

$$0 = ar\cos\theta + dr^2\cos^2\theta + er^2\sin^2\theta = 2\frac{a}{\kappa}\cos^2\theta + 4\frac{d}{\kappa^2}\cos^4\theta + 4\frac{e}{\kappa^2}\cos^2\theta\sin^2\theta.$$

This relation is naturally satisfied for $\theta = \pm\pi/2$. For all the other points, i.e. the interval $(-\pi/2;\pi/2)$, the following equation can be obtained dividing the previous one by $2\cos^2\theta/\kappa^2$:

$$0 = a\kappa + 2d\cos^2\theta + 2e\sin^2\theta.$$

To define the remaining two parameters a and e, such relation has been tested in two particular cases ($\theta = \pi/4$ and $\theta = \pi/3$), leading to:

$$\begin{cases} 0 = a\kappa + 2d(\frac{1}{2}) + 2e(\frac{1}{2}) = a\kappa + d + e = a\kappa - \kappa^2 - a\kappa + e = e - \kappa^2. \\ \\ 0 = a\kappa + 2d(\frac{1}{4}) + 2e(\frac{3}{4}) = a\kappa + \dfrac{d}{2} + \dfrac{3e}{2} \end{cases} \tag{3.8}$$

Therefore $e = \kappa^2$, $a = -2\kappa$ and $d = \kappa^2$. Consequently, the velocity profile has been expressed as:

$$u_v(r, \theta, s) = \overline{u}_v(s)\, \phi(rR^{-1})\, (1 + r^2\kappa^2(\psi) - 2\kappa(\psi) r \cos\theta). \tag{3.9}$$

Using this profile, the reduced model for flow can be derived starting from equations 3.4, integrating them on a portion of vessel P. This portion is delimited by two cross sections $\Sigma(s_1), \Sigma(s_2)$, where $s_2 > s_1$. Starting from the continuity equation, and noting that $\boldsymbol{n} = \boldsymbol{e}_s$ on $\Sigma(s_1)$ and $\Sigma(s_2)$, the model can be obtained as follows:

$$0 = \int_P \nabla \cdot \boldsymbol{u}_v d\Omega = \int_{\partial P} \boldsymbol{u}_v \cdot \mathbf{n}\, d\sigma = \int_{\Sigma(s_1)} \boldsymbol{u}_v \cdot \boldsymbol{n} d\sigma + \int_{\Sigma(s_2)} \boldsymbol{u}_v \cdot \boldsymbol{n}\, d\sigma + \int_\Gamma \boldsymbol{u}_v \cdot \boldsymbol{n}\, d\sigma\,. \tag{3.10}$$

Now, recalling from equations 3.2 and 3.3 that

$$\boldsymbol{u}_v \cdot \boldsymbol{n} = L_p\Big((p_v - p_t) - \sigma(\pi_v - \pi_t)\Big) \quad \text{ on } \Gamma$$

and defining

$$\overline{\overline{p}}_t(s) = \frac{1}{2\pi R} \int_{\partial\Sigma(s)} p_t\, d\sigma \tag{3.11}$$

the following expression has been obtained:

$$\begin{aligned} 0 &= -\int_{\Sigma(s_1)} u_v\, d\sigma + \int_{\Sigma(s_2)} u_v\, d\sigma + \int_\Gamma L_p\Big((p_v - p_t) - \sigma(\pi_v - \pi_t)\Big)\, d\sigma \\ &\simeq -\overline{u}_v(s_1)\pi R^2(s_1) + \overline{u}_v(s_2)\pi R^2(s_2) + \int_{s_1}^{s_2} 2\pi R\, L_p\Big((p_v - \overline{p}_t) - \sigma(\pi_v - \pi_t)\Big) dz \\ &= \int_{s_1}^{s_2} [2\pi R\, L_p\Big((\overline{p}_v - \overline{\overline{p}}_t) - \sigma(\pi_v - \pi_t)\Big) + \partial_s(\pi R^2 \overline{u}_v)] dz\,. \end{aligned} \tag{3.12}$$

In this process, the vessel radius is assumed to be small in comparison to the domain Ω. Thus, considering the linearity of the function $L_p\Big((p_v - p_t) - \sigma(\pi_v - \pi_t)\Big)$, the subsequent statement holds true:

$$\begin{aligned} \int_\Gamma f(p_t, p_v)\, d\sigma &= \int_{s_1}^{s_2} \int_0^{2\pi} f(p_t, p_v) R(s) d\theta\, ds \\ = \int_{s_1}^{s_2} \int_0^{2\pi} f(p_t, \overline{p}_v) R(s) d\theta\, ds &= \int_{s_1}^{s_2} 2\pi R(s) f(\overline{\overline{p}}_t, \overline{p}_v)\, ds\,. \end{aligned}$$

Moreover, according to equations 3.4 and 3.6, the pressure is constant in a cross-section, namely $\overline{p}_v(s) = p_v(r, s, \theta)$.

Applying the same technique to the momentum equation:

$$\begin{aligned}
&\int_P \Delta u_v \, d\Omega = \int_{\partial P} \nabla u_v \cdot \boldsymbol{n} \, d\sigma \\
&= -\int_{\Sigma(s_1)} \partial_s u_v \, d\sigma + \int_{\Sigma(s_2)} \partial_s u_v \, d\sigma + \int_\Gamma \nabla u_v \cdot \boldsymbol{n} \, d\sigma = \int_\Gamma \nabla u_v \cdot \boldsymbol{e}_r \, d\sigma \\
&= \int_\Gamma \partial_r u_v d\sigma = \int_\Gamma \overline{u}_v(s) \partial_r \Phi(r, \theta) d\sigma \\
&= \int_\Gamma \overline{u}_v(s) R^{-1} \phi'(rR^{-1})(1 - 2\kappa r \cos\theta + \kappa^2 r^2) + \phi(rR^{-1})(2\kappa^2 r - 2\kappa\cos\theta) \, d\sigma \\
&= \int_{s_1}^{s_2} \int_0^{2\pi} \overline{u}_v(s) \Big(R^{-1} \phi'(1)(1 - \kappa\cos\theta + \kappa^2 R^2) + \phi(1)(2\kappa^2 R - 2\kappa\cos\theta) \Big) R d\theta ds.
\end{aligned}$$

Noting that $\phi(1)$, namely ϕ computed for $r = R$, is 0 due to boundary condition (equation 3.2), and to the periodicity of $cos\theta$, the expression can be simplified as:

$$\int_P \Delta u_v \, d\Omega = \int_{s_1}^{s_2} 2\pi \phi'(1)(1 + \kappa^2 R^2) \overline{u}_v(s) \, ds,$$

leading to the 1D form of the momentum equation:

$$-2\pi \mu_v(s) \phi'(1) \Big(1 + \kappa^2(s) R^2 \Big) \overline{u}_v(s) + \pi R^2 \partial_s \overline{p}_v(s) = 0.$$

This 1D model must be coupled with the domain Ω_t, described by means of the porous media equation. Following the approach proposed in [162], the interaction of the manifold Λ with the bulk domain Ω_t is modeled by means of the distribution of concentrated sources on Λ. Consequently, the domain Ω_t is identified with Ω, and a new term has been inserted in the left-hand side of the Ω continuity equation. To guarantee mass conservation, this new term must be opposite to $2\pi R \, L_p \Big((\overline{p}_v - \overline{\overline{p}}_t) - \sigma(\pi_v - \pi_t) \Big)$ and be multiplied by δ_Λ, namely a distribution of Dirac masses along the manifold Λ.
Therefore, the 3D-1D problem is summarized as follow:

$$\begin{cases}
\boldsymbol{u}_t + \dfrac{\mathrm{K}}{\mu_t} \nabla p_t = 0 & \text{in } \Omega \\
\nabla \cdot \boldsymbol{u}_t + \phi_{lymphatics} - 2\pi R \, L_p \Big((\overline{p}_v - \overline{\overline{p}}_t) - \sigma(\pi_v - \pi_t) \Big) \delta_\Lambda = 0 & \text{in } \Omega \\
-2\pi \mu_v(s) \phi'(1) \Big(1 + \kappa^2(s) R^2 \Big) \overline{u}_v(s) + \pi R^2 \partial_s \overline{p}_v(s) = 0 & \text{in } \Lambda \\
\partial_s(\pi R^2 \overline{u}_v) + 2\pi R \, L_p \Big((\overline{p}_v - \overline{\overline{p}}_t) - \sigma(\pi_v - \pi_t) \Big) = 0 & \text{in } \Lambda
\end{cases} \tag{3.13}$$

3.2.1 Extension to a capillary network

To model flow in a more complex topology, such as a capillary network, the model should be generalized. To this end, the network has been decomposed in a number N_b of uncoupled branches. Each of them is described by the previously discussed parameterization, namely by the arc length s_i. A unitary tangent vector $\lambda_i(s_i)$ has also been defined, accounting for an arbitrary vessel orientation. Therefore, the differentiation is defined by the projection of ∇ along $\boldsymbol{\lambda}_i$, i.e. $\partial_{s_i} := \boldsymbol{\lambda}_i \cdot \nabla$ on Λ_i. As stated, the vessels are uncoupled using this description. Aiming to describe the flow within the network, they must be coupled, enforcing the proper constraints at the junctions $\boldsymbol{y}_j$, i.e. at the connection between two or more vessels. These have been mathematically defined as:

$$\boldsymbol{y}_j = \boldsymbol{\Psi}_i(s_i^*) = \boldsymbol{\Psi}_{\hat{\imath}}(s_{\hat{\imath}}^*),\ s_i^* \in \{0, L_i\}\ \forall i, \hat{\imath} = 1, \dots, N.$$

A network is consequently characterized by a finite number of branches N and a finite number of junctions M. All the other vessel endpoints, i.e. points not classified as junctions, can be either dead ends if they end within the domain Ω, or boundary ends, if they end crossing the boundary $\partial\Omega$. The former are indicated by $\boldsymbol{z}$ and the corresponding vessels i are grouped in the set $\mathcal{E}$, whereas the latter by $\boldsymbol{x}$ and in the set $\mathcal{B}$. For each junction $\boldsymbol{y}_j$, the set of branches $\mathcal{K}_j$ which composes the junction is defined such that $\boldsymbol{\Psi}_i(s_i^*) = \boldsymbol{y}_j$, namely including all the indices i of the branches. An example of this classification is shown in figure 3.3. Now, two different classifications of the sets $\mathcal{K}_j$ are presented because they will be useful in the derivation of the model. The first one is based on the vessel orientation, namely the geometric orientations of the domain Λ_i and therefore of their meshes, whereas the second one is based on the flow direction. Clearly, the last is defined when the simulation is running, and it depends on the applied boundary conditions, whereas the first does not. Considering $\boldsymbol{e}_s$ as the *outgoing* tangential unit vector at the each of the two endpoints of the branch, the following set of branches are defined:

- $\mathcal{K}_j^+$, the outgoing branches of a junction, as the branches which belong to $\mathcal{K}_j$ satisfying $\boldsymbol{\lambda}_i \cdot \boldsymbol{e}_s(s_i) > 0$, where depending on which end is involved in the junction $s_i = 0$ or $s_i = L$;

- $\mathcal{K}_j^-$, the ingoing branches of a junction, as done in the previous point with the condition $\boldsymbol{\lambda}_i \cdot \boldsymbol{e}_s(s_i) < 0$;

- $\mathcal{K}_j^{out}$, the outflow branches of a junction, based on the direction of flow, as the branches which belong to $\mathcal{K}_j$ satisfying $\overline{u}_v(s_i)\boldsymbol{\lambda}_i \cdot \boldsymbol{e}_s(s_i) > 0$, where depending on which end is involved in the junction $s_i = 0$ or $s_i = L$;

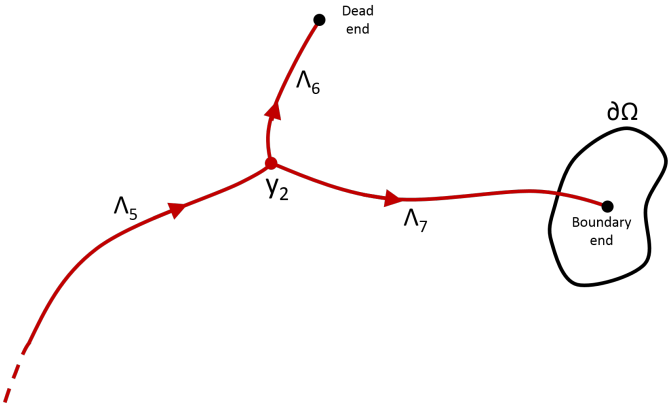

Figure 3.3: *Example of a junction $\boldsymbol{y}_j$, with $j = 2$. This junction is composed by the vessels Λ_i with $i = \{5, 6, 7\}$. Therefore, the set of indices $\mathcal{K}_2 = \{5, 6, 7\}$. In particular, given the orientation of mesh indicated by the arrows, the set of outgoing points $\mathcal{K}_2^+ = \{6, 7\}$ whereas the set of ingoing points $\mathcal{K}_2^- = \{5\}$. In addition, an example of dead and boundary end is shown using the other end-point of the vessel Λ_6 and Λ_7 respectively.*

- $\mathcal{K}_j^{in}$, the inflow branches of a junction, as done in the previous point with the condition $\overline{u}_v(s_i)\boldsymbol{\lambda}_i \cdot \boldsymbol{e}_s(s_i) < 0$.

The same classification can be applied also to the boundary ends, namely the ends grouped in the set $\mathcal{B}$, separating $\boldsymbol{x}^{in}$ and $\boldsymbol{x}^{out}$. Such a classification will be useful to prescribe boundary conditions of the problem.

Once junctions have been defined, the proper constraints to connect all the branches of the network can be defined. At each junction, the continuity of pressure and mass conservation have been enforced:

$$\sum_{i \in \mathcal{K}_j} \pi R_k^2 \overline{u}_{v,i} = 0,\ j = 1, 2, \ldots, M\,, \quad \overline{p}_{v,i} = \overline{p}_{v,\hat{\imath}},\ i, \hat{\imath} \in \mathcal{K}_j,\ j = 1, 2, \ldots, M\,. \tag{3.14}$$

To complete the extension of the 1D model of blood flow, the appropriate conditions must be applied to dead and boundary ends. To ensure mass conservation, i.e. with a condition similar to 3.14, a no-flow condition must be enforced at dead ends, namely:

$$piR^2 \overline{u}_v|_{\boldsymbol{z}_i} = 0,\ i \in \mathcal{E}\,,$$

where $|_{\boldsymbol{z}_i}$ is a shorthand notation for the evaluation of the whole term in the point $\boldsymbol{z}_i$. At the boundary ends, instead, boundary conditions are applied. In this work, Dirichlet conditions have been considered, leading to

$$\overline{p}_v|_{\boldsymbol{x}_i} = g_v \quad i \in \mathcal{B}\,,$$

where g_v is the function which prescribes pressure values along the boundary of the domain. Summarizing, the model can be written as:

$$\begin{cases} \nabla \cdot \boldsymbol{u}_t - 2\pi R(s) L_p \Big((\overline{p}_v - \overline{\overline{p}}_t) - \sigma(\pi_v - \pi_t) \Big) \delta_\Lambda + \phi_{lymphatics} = 0 & \text{in } \Omega \\ \boldsymbol{u}_t + \frac{\mathrm{K}}{\mu_t} \nabla p_t = 0 & \text{in } \Omega \\ \partial_s \Big(\pi R_i^2(s) \overline{u}_{v,i}(s) \Big) + 2\pi R_i(s) L_p \Big((\overline{p}_v - \overline{\overline{p}}_t) - \sigma(\pi_v - \pi_t) \Big) & \text{on } \Lambda_i,\ i = 1, \dots, N\,, \\ -2\mu_{v,i}(s)\phi'(1) \Big(1 + \kappa_i^2(s) R_i^2(s) \Big) \overline{u}_{v,i}(s) + R_i^2(s) \partial_s \overline{p}_{v,i}(s) = 0 & \text{on } \Lambda_i,\ i = 1, \dots, N\,, \\ \sum_{i \in \mathcal{K}_j} \pi R_k^2 \overline{u}_{v,i}|_{\boldsymbol{y}_j} = 0, & j = 1, 2, \dots, M\,, \\ \overline{p}_{v,i}|_{\boldsymbol{y}_j} = \overline{p}_{v,\hat{\imath}}|_{\boldsymbol{y}_j} & i, \hat{\imath} \in \mathcal{K}_j,\ j = 1, 2, \dots, M\,, \\ \pi R^2 \overline{u}_v|_{\boldsymbol{z}_i} = 0 & i \in \mathcal{E}\,, \\ \overline{p}_v|_{\boldsymbol{x}_i} = g_v & i \in \mathcal{B}\,. \end{cases} \tag{3.15}$$

3.2.2 Modeling Fåhraeus - Lindqvist and Zweifach - Fung effects

As described in the section 1.2.2, the Fåhraeus, Fåhraeus - Lindqvist, and Zweifach - Fung effects characterize the microvasculature. To account for them in the model, the transport of RBCs should be modeled. In this way, the viscosity of the fluid can be expressed as $\mu_v = \mu_v(H_d, D)$, and the heterogeneity of hematocrit in the network can be considered. To this aim, a 1D model of RBCs transport is coupled with the fluid dynamic model (equation 3.15). Such a model has been built on the following assumptions.

- Steady flow. As done for the flow model, also the RBC distribution has been modeled under steady conditions.

- Advection dominated regime. This assumption allows neglecting the diffusion or RBCs in the blood. The validity of this assumption has been addressed by computing the Péclét number $Pe = (LU)/D_{RBC}$, adopting $L \simeq 10\,\mu m$ as characteristic scale, $U \simeq 1\,mm/s$ as the average velocity within capillaries and $D_{RBC} \simeq 10^{-12} m^2/s$ as the diffusivity of RBC in water [207, 208]. The resulting $Pe \simeq 10^4$ justifies the assumption of advection dominated RBCs transport.

- Absence of reaction. Reaction terms in the equation have been neglected, namely no production or consumption of RBCs has been considered.

- No RBCs leak off. The RBCs are considered unable to cross the capillary membrane.

- Absence of trifurcations. The networks considered for the RBCs transport are characterized by junctions with a maximum number of vessel M equal to 3. Thus, they can be classified as *trivial junctions* (i.e. $M = 2$), *bifurcations* (i.e. $M = 3$, $card(\mathcal{K}_j^{in}) = 1$) and *anastomosis* (i.e. $M = 3$, $card(\mathcal{K}_j^{in}) = 2$). A scheme of these three types of junctions is provided in figure 3.4.

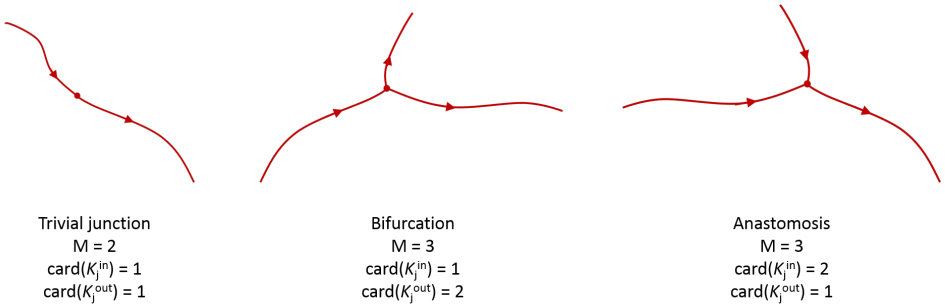

Figure 3.4: *Example of a trivial junction, a bifurcation, and an anastomosis. The arrows indicate the direction of flow.*

Under these assumptions, the flow rate of RBCs Q_H is conserved along a vessel, namely $\partial_s Q_H = 0$ on Λ_i. Recalling the definition of discharge hematocrit, Q_H can be substituted by $\pi R^2 \overline{u}_v H_d$, obtaining:

$$\partial_s \Big(\pi R_i^2 \overline{u}_{v,i} H_{d,i} \Big) = 0 \text{ on } \Lambda_i, \ i = 1, 2, \dots, N \,. \tag{3.16}$$

For clarity, from now on H_d is indicated with H. The previous equation can be rearranged to obtain:

$$\pi R_i^2 \overline{u}_{v,i} \partial_s H_i + \partial_s \Big(\pi R_i^2 \overline{u}_{v,i} \Big) H_i(s) = 0 \text{ on } \quad \Lambda_i, \ i = 1, 2, \dots, N \,.$$

Combining this last equation with equation 3.15:

$$\pi R_i^2 \overline{u}_{v,i} \partial_s H_i - 2\pi R_i L_p \Big((\overline{p}_v - \overline{\overline{p}}_t) - \sigma(\pi_v - \pi_t) \Big) H_i(s) = 0 \quad \text{on } \Lambda_i, \ i = 1, 2, \dots, N \,. \tag{3.17}$$

At this point, it is evident that a variation of H may occur along the vessel. In particular, considering a vessel (i.e. $R_i \neq 0$) with flowing blood (i.e. $\overline{u}_{v,i} \neq 0$ and $H_{d,i} \neq 0$) characterized by filtration/absorption of fluid (i.e. $2\pi R_i L_p \Big((\overline{p}_v - \overline{\overline{p}}_t) - \sigma(\pi_v - \pi_t) \Big) \neq 0$), the variation of H results as:

$$\partial_s H_{d,i} = \frac{2\pi R_i L_p \Big((\overline{p}_v - \overline{\overline{p}}_t) - \sigma(\pi_v - \pi_t) \Big) H_{d,i}(s)}{\pi R_i^2 \overline{u}_{v,i}} \quad \text{on } \Lambda_i, \ i = 1, 2, \dots, N \,.$$

The required boundary conditions for this pure advection equation should be specified in the inflow point of the vessels solely. These can be either boundary inflow points or junction points. For the former, Dirichlet boundary condition has been applied, specifying the value of H. Certainly, as done for the 3.15, junctions should be considered to describe the network. The mass conservation at a junction j reads as:

$$\sum_{i \in \mathcal{K}_j^{out}} \pi R_i^2 \overline{u}_{v,i} H_{d,i} = \sum_{i \in \mathcal{K}_j^{in}} \pi R_i^2 \overline{u}_{v,i} H_{d,i} \,. \tag{3.18}$$

Such equation is sufficient to close the problem in presence of *trivial junctions* and *anastomosis* in which $card(\mathcal{K}_j^{out}) = 1$ (figure 3.4). To handle the case $card(\mathcal{K}_j^{out}) = 2$, namely to describe the Zweifach - Fung effect at bifurcations, the model proposed by [104,106] has been adopted. Considering a bifurcation composed by a parent vessel f and two daughter vessels α and β, their model allows us to write:

$$H_\alpha = F_{QE\alpha} H_f Q_f / Q_\alpha \,, \quad H_\beta = (1 - F_{QE\alpha}) H_f Q_f / Q_\beta \,. \tag{3.19}$$

where the coefficient $F_{QE\alpha}$ is determined on the basis of the blood flow rate and geometrical parameters of the bifurcation, and Q_* stands for blood flow rate, i.e. $Q_* = \pi R_*^2 \overline{u}_{v,*}$. Being $F_{QB\alpha} = Q_\alpha / Q_f$ and $F_{QE\alpha} = (Q_\alpha H_\alpha)/(Q_f H_f)$, the coefficient $F_{QE\alpha}$ is computed as:

$$\begin{cases} F_{QE\alpha} = 0 & if\ F_{QB\alpha} \leq X_0 \\ \text{logit}(F_{QE\alpha}) = A + B\text{logit}(\frac{F_{QB\alpha} - X_0}{1 - 2X_0}) & if\ X_0 < F_{QB\alpha} < 1 - X_0 \\ F_{QE\alpha} = 1 & if\ F_{QB\alpha} \geq 1 - X_0 \end{cases}$$

where A, B are fixed parameters determined in [98], $\text{logit}(x) = \ln[x/(1-x)]$ and X_0 is the fractional blood flow rate under which any RBCs will flow into the daughter branch α.

This RBCs transport model is then coupled with 3.15 because of the Fåhraeus - Lindqvist effect, namely because $\mu_v = \mu_v(H, D)$. Among the several models that have been developed in literature to describe this effect, the formulation of Pries and colleagues has been implemented in the model [98]. Therefore, the viscosity of blood is described as $\mu_v = \mu_{plasma}(T) * \mu_{apparent}(H, D)$. Then $\mu_{plasma}(T)$ has been computed as follow:

$$\mu_{plasma} = 1.8 \mu_{H_2O} = 1.8 \frac{\mu_0}{1 + 0.0337T + 0.00022T^2}. \tag{3.20}$$

The apparent viscosity $\mu_{apparent}(H, D)$ has been described following the relations reported in their study (further described in the section 1.2.2). Only the main relationship is here reported:

$$\mu_{apparent} = \left[1 + (\mu_{0.45}^* - 1) \cdot \frac{(1-H)^C - 1}{(1-0.45)^C - 1} \cdot \left(\frac{D}{D - 1.1}\right)^2\right] \cdot \left(\frac{D}{D - 1.1}\right)^2 . \tag{3.21}$$

Summarizing, the 3D-1D model is:

$$
\begin{cases}
\nabla \cdot \boldsymbol{u}_t - 2\pi R(s) L_p \Big((\overline{p}_v - \overline{\overline{p}}_t) - \sigma(\pi_v - \pi_t) \Big) \delta_\Lambda + \phi_{lymphatics} = 0 & \text{in } \Omega \\
\boldsymbol{u}_t + \frac{\mathrm{K}}{\mu_t} \nabla p_t = 0 & \text{in } \Omega \\
\partial_s \Big(\pi R_i^2(s) \overline{u}_{v,i}(s) \Big) + 2\pi R_i(s) L_p \Big((\overline{p}_v - \overline{\overline{p}}_t) - \sigma(\pi_v - \pi_t) \Big) & \text{on } \Lambda_i,\ i = 1, \dots, N\,, \\
-2\mu_{v,i}(s) \phi'(1) \Big(1 + \kappa_i^2(s) R_i^2(s) \Big) \overline{u}_{v,i}(s) + R_i^2(s) \partial_s \overline{p}_{v,i}(s) = 0 & \text{on } \Lambda_i,\ i = 1, \dots, N\,, \\
\sum_{i \in \mathcal{K}_j} \pi R_k^2 \overline{u}_{v,i}|_{\boldsymbol{y}_j} = 0, & j = 1, 2, \dots, M\,, \\
\overline{p}_{v,i}|_{\boldsymbol{y}_j} = \overline{p}_{v,\hat{\imath}}|_{\boldsymbol{y}_j} & i, \hat{\imath} \in \mathcal{K}_j,\ j = 1, 2, \dots, M\,, \\
\pi R^2 \overline{u}_v|_{\boldsymbol{z}_i} = 0 & i \in \mathcal{E}\,, \\
\overline{p}_v|_{\boldsymbol{x}_i} = g_v & i \in \mathcal{B}\,, \\
\pi R_i^2 \overline{u}_{v,i} \partial_s H_{d,i} - 2\pi R_i L_p \Big((\overline{p}_v - \overline{\overline{p}}_t) - \sigma(\pi_v - \pi_t) \Big) H_{d,i}(s) = 0 & \text{on } \Lambda_i,\ i = 1, \dots, N\,, \\
\sum_{i \in \mathcal{K}_j^{out}} \pi R_i^2 \overline{u}_{v,i} H_{d,i} = \sum_{i \in \mathcal{K}_j^{in}} \pi R_i^2 \overline{u}_{v,i} H_{d,i}, & j = 1, 2, \dots, M\,, \\
H = H_{in} & i \in \partial\Lambda_{in}\,.
\end{cases}
\tag{3.22}
$$

3.2.3 Lymphatic drainage description

As described in the introduction, the lymphatic system withdraws fluids from the interstitial space. When its contribution is included in this kind of models, the geometry of lymphatic capillaries is usually not considered, but the drainage is modeled as a distributed sink in the domain Ω. Therefore, a coefficient $S/V|_{LF}$ is required to specify the exchange surface area per unit volume of Ω. In the majority of literature works, the lymphatic drainage is described by a linear function of the interstitial pressure p_t and the lymphatic pressure p_l solely [78,157,162,209]. The oncotic pressure difference across the lymphatic capillary membrane is neglected because of its higher permeability to proteins. Consequently, the lymphatic drainage ($\varphi_{lymphatics}$) is usually described as:

$$
\varphi_{lymphatics} \;=\; L_{pLF} \left(\frac{S}{V} \right)_{LF} (p_t - p_l)\ . \tag{3.23}
$$

In this work, a new description of the lymphatic drainage based on a non-linear relation to the interstitial hydraulic pressure has been proposed. Thus, following the physiologic description, the net lymphatic flow rate is modeled as a distributed sink defined by a sigmoid function (3.24), considering a saturation flow rate, leading to the following expression of

the lymphatic drainage:

$$\varphi_{lymphatics} = \varphi_{max} - \frac{\varphi_{max} - \varphi_{min}}{1 + \exp(\frac{p_t - p_{50}}{slope\ factor})} \tag{3.24}$$

where φ_{max} and φ_{min} are the maximum and the minimum lymphatic drainage respectively, $p50$ is referred to the interstitial pressure corresponding to $\varphi_{lymphatics} = mean(\varphi_{min}, \varphi_{max})$, and $slope\ factor$ determines the slope of the function. To identify parameter values, information reported by Chamney and colleagues [56] and Ebah and colleagues [30] have been considered. Thus, parameters have been computed by the following procedure:

- the intestitial pressure at the physiological working point is defined as slightly negative ($-1\,mmHg$);
- the lymphatic drainage at the physiological working point, namely $\varphi_{lymphatics}(-1\,mmHg) = 6.85 \times 10^{-7}\,s^{-1}$, is defined performing a scaling by the total interstitial volume [5] to obtain a volumetric term, that is the lymphatic drainage per unit volume;
- the interval (p_{min}, p_{max}) (figure 3.5) is equal to $6\,mmHg$ and it is defined as the range of interstitial pressure in which the lymphatic drainage increases, i.e. the difference between the physiological working point and the point with the maximum lymphatic drainage;
- the maximum lymphatic drainage, namely $\varphi_{lymphatics,max} = 1.717 \times 10^{-5}\,s^{-1}$ is defined following the scaling procedure used for the physiological drainage;
- the maximum slope of the curve is obtained at the center of the interval (p_{min}, p_{max}), so that $p_{50} = 2\,mmHg$.

The resulting $slope\ factor$ is $0.66\,mmHg$. Because of this derivation, the model proposed is not considering differences among different tissues [84, 90]. However, the model is general as for lymphatic drainage description, namely if a tissue-specific relation between lymphatic drainage and the interstitial pressure were available, it could be easily implemented in the model. The proposed model is shown in figure 3.5.

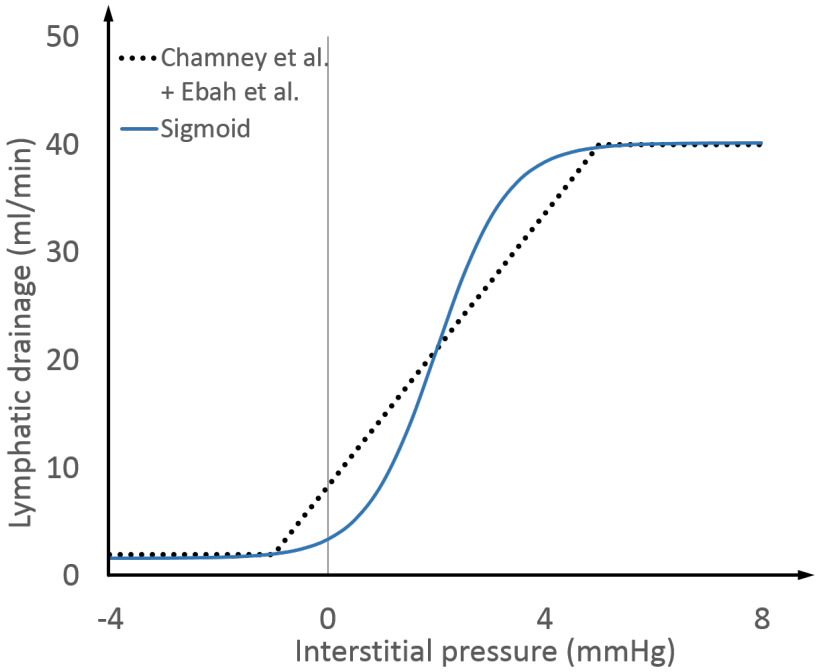

Figure 3.5: *Sigmoid function describing the lymphatic drainage along with data from [30, 56] used to compute parameters. For drawing the graph, lymphatic drainage has been scaled up to the overall extra-vascular volume.*

3.3 Weak 3D-1D problem

The mathematical ground of the weak problem has been addressed in several works, which proved the existence of a solution in the weak (or variational) sense [161, 166, 204, 210]. Following the process described in [204], Darcy's equation has been multiplied by a test function $\boldsymbol{v}_t \in \boldsymbol{V}_t = \boldsymbol{H}_{div}(\Omega)$:

$$\frac{\mu_t}{K}\Big(\,\mathbf{u}_t\,,\,\boldsymbol{v}_t\,\Big)_\Omega + \Big(\,\nabla p_t\,,\,\boldsymbol{v}_t\,\Big)_\Omega = 0 \quad \forall \boldsymbol{v}_t \in \boldsymbol{V}_t\,, \tag{3.25}$$

where, with a standard notation, $\Big(\,\cdot\,,\,\cdot\,\Big)_*$ indicates the inner product over the domain $*$. Using the Green's formula:

$$\Big(\,\nabla p_t\,,\,\boldsymbol{v}_t\,\Big)_\Omega = -\Big(\,p_t\,,\,\nabla\cdot\boldsymbol{v}_t\,\Big)_\Omega + \Big(\,p_t\,,\,\boldsymbol{v}_t\cdot\boldsymbol{n}_t\,\Big)_{\partial\Omega} = -\Big(\,p_t\,,\,\nabla\cdot\boldsymbol{v}_t\,\Big)_\Omega + \Big(\,g_t\,,\,\boldsymbol{v}_t\cdot\boldsymbol{n}_t\,\Big)_{\partial\Omega}$$

where g_t is a prescribed value of the interstitial pressure at the artificial boundaries of the tissue slab, namely $\partial\Omega$.
The test function for the continuity equation on Ω is $q_t \in Q_t = L^2(\Omega)$:

$$\Big(\,\nabla\cdot\mathbf{u}_t\,,\,q_t\,\Big)_\Omega - \Big(\,2\pi R f(\overline{\overline{p}}_t, \overline{p}_v)\delta_\Lambda\,,\,q_t\,\Big)_\Omega + \Big(\,\phi_{lymphatics}\,,\,q_t\,\Big)_\Omega = 0 \quad \forall q_t \in Q_t, \tag{3.26}$$

where $f(\overline{\overline{p}}_t, \overline{p}_v)$ has been used for notation convenience to indicate $L_p\Big((\overline{p}_v - \overline{\overline{p}}_t) - \sigma(\pi_v - \pi_t)\Big)$.
The equation describing the blood flow in the 1D network has been multiplied by πR_i^2 and by a test function $v_{v,i} \in V_{v,i} \in H^1(\Lambda_i)$. In addition a sum of each vessel contribution has been performed, obtaining:

$$\sum_i \Big(\,-2\frac{\mu_{v,i}}{R_i^2}\phi'(1)\Big(1+\kappa_i^2 R_i^2\Big)\pi R_i^2\overline{u}_{v,i}\,,\,v_{v,i}\,\Big)_{\Lambda_i} + \sum_i \Big(\,\partial_s\overline{p}_{v,i}\,,\,\pi R_i^2 v_{v,i}\,\Big)_{\Lambda_i} = 0 \quad \forall v_v \in V_v. \tag{3.27}$$

Using again the Green's formula:

$$\begin{aligned}\sum_i &\Big(\,\partial_s\overline{p}_{v,i}\,,\,\pi R_i^2 v_{v,i}\,\Big)_{\Lambda_i} \\ &= -\sum_i \Big(\,\overline{p}_{v,i}\,,\,\partial_s(\pi R_i^2 v_{v,i})\,\Big)_{\Lambda_i} + \sum_i \Big[\overline{p}_{v,i}\pi R_i^2 v_{v,i}|_{s=L} - \overline{p}_{v,i}\pi R_i^2 v_{v,i}|_{s=0}\Big].\end{aligned}$$

Since the pressure is continuous at junction points, the last two terms can be rearranged considering the junctions:

$$\sum_i \left[\overline{p}_{v,i}\pi R_i^2 v_{v,i}|_{s=L} - \overline{p}_{v,i}\pi R_i^2 v_{v,i}|_{s=0}\right] = \sum_j \overline{p}_v|_{\boldsymbol{y}_j}\left[\sum_{i\in\mathcal{K}_j^+}\pi R_i^2 v_{v,i}|_{\boldsymbol{y}_j} - \sum_{i\in\mathcal{K}_j^-}\pi R_i^2 v_{v,i}|_{\boldsymbol{y}_j}\right] + \sum_{i\in\mathcal{E}}\overline{p}_v\,\pi R_i^2 v_v|_{\boldsymbol{z}_i} + \sum_{i\in\mathcal{B}}\left[\overline{p}_v\,\pi R_i^2 v_v|_{\boldsymbol{x}_i^+} - \overline{p}_v\,\pi R_i^2 v_v|_{\boldsymbol{x}_i^-}\right],$$

where $\boldsymbol{x}_i^-$ and $\boldsymbol{x}_i^+$ indicates the outflow and inflow boundary respectively.
In other words, the expression has been rearranged as:

$$\sum_i \Big(\textit{Contributes of starting and end point of each vessel}\Big) = \sum_i \Big(\textit{Contributes of juction points}\Big) + \sum_i \Big(\textit{Contributes of dead ends}\Big) + \sum_i \Big(\textit{Contributes of boundary ends}\Big). \quad (3.28)$$

Boundary conditions have been enforced using the last term, namely the term with $\sum_{i\in\mathcal{B}}$, substituting $\overline{p}_v|_{\boldsymbol{x}_i^+} = g_v^+$ and $\overline{p}_v|_{\boldsymbol{x}_i^-} = g_v^-$ for any $i \in \mathcal{B}$.

For the 1D continuity equation, the test function $q_v \in Q_v$ has been considered. Generally, $Q_v \subset L^2(\Lambda)$ is sufficient, but, according to the sixth equation in 3.22, the continuity of pressures at the junctions has been required. The flow rate conservation has been weakly imposed by multiplying the fifth equation in 3.22 and adding it to the third of the same system, resulting in:

$$\sum_i \Big(\,\partial_s(\pi R_i^2\overline{u}_{v,i}\,,\,q_v\,\Big)_{\Lambda_i} + \sum_i \Big(\,2\pi R f(\overline{\overline{p}}_t,\overline{p}_v)\,,\,q_v\,\Big)_{\Lambda_i} - \sum_{i\in\mathcal{E}} q_v\pi R_i^2\overline{u}_{v,i}|_{\boldsymbol{z}_i} - \sum_j q_v|_{\boldsymbol{y}_j}\left[\sum_{i\in\mathcal{K}_j^+}\pi R_i^2\overline{u}_{v,i}|_{\boldsymbol{y}_j} - \sum_{i\in\mathcal{K}_j^-}\pi R_i^2\overline{u}_{v,i}|_{\boldsymbol{y}_j}\right] = 0 \quad \forall q_v \in Q_v,$$

Summarizing, the weak formulation of the 3D-1D flow problem 3.15 reads as follow:

$$
\begin{cases}
\Big(\nabla\cdot\mathbf{u}_t\,,\,q_t\Big)_\Omega - \Big(2\pi R f(\overline{\overline{p}}_t,\overline{p}_v)\delta_\Lambda\,,\,q_t\Big)_\Omega + \Big(\phi_{lymphatics}\,,\,q_t\Big)_\Omega = 0 & \forall q_t\in Q_t,\\[2ex]
\frac{\mu_t}{K}\Big(\mathbf{u}_t\,,\,\boldsymbol{v}_t\Big)_\Omega - \Big(p_t\,,\,\nabla\cdot\boldsymbol{v}_t\Big)_\Omega = -\Big(g_t\,,\,\boldsymbol{v}_t\cdot\boldsymbol{n}_t\Big)_{\partial\Omega} & \forall\boldsymbol{v}_t\in\boldsymbol{V}_t,\\[2ex]
\sum_i\Big(\partial_s(\pi R_i^2\overline{u}_{v,i}\,,\,q_v\Big)_{\Lambda_i} + \sum_i\Big(2\pi R f(\overline{\overline{p}}_t,\overline{p}_v)\,,\,q_v\Big)_{\Lambda_i}\\
\qquad -\sum_{i\in\mathcal{E}} q_v\pi R_i^2\overline{u}_{v,i}|_{\boldsymbol{z}_i}\\
\qquad -\sum_j q_v|_{\boldsymbol{y}_j}\Big[\sum_{i\in\mathcal{K}_j^+}\pi R_i^2\overline{u}_{v,i}|_{\boldsymbol{y}_j} - \sum_{i\in\mathcal{K}_j^-}\pi R_i^2\overline{u}_{v,i}|_{\boldsymbol{y}_j}\Big] = 0 & \forall q_v\in Q_v,\\[2ex]
\sum_i\Big(-2\frac{\mu_{v,i}}{R_i^2}\phi'(1)\Big(1+\kappa_i^2R_i^2\Big)\pi R_i^2\overline{u}_{v,i}\,,\,v_{v,i}\Big)_{\Lambda_i}\\
\qquad -\sum_i\Big(\overline{p}_v\,,\,\partial_s(\pi R_i^2 v_{v,i})\Big)_{\Lambda_i}\\
\qquad +\sum_j\overline{p}_v|_{\boldsymbol{y}_j}\Big[\sum_{i\in\mathcal{K}_j^+}\pi R_i^2 v_{v,i}|_{\boldsymbol{y}_j} - \sum_{i\in\mathcal{K}_j^-}\pi R_i^2 v_{v,i}|_{\boldsymbol{y}_j}\Big]\\
\qquad +\sum_{i\in\mathcal{E}}\overline{p}_v\,\pi R_i^2 v_v|_{\boldsymbol{z}_i}\\
\qquad = -\sum_{i\in\mathcal{B}}\Big[g_v^+\,\pi R_i^2 v_v|_{\boldsymbol{x}_i^+} - g_v^-\,\pi R_i^2 v_v|_{\boldsymbol{x}_i^-}\Big] & \forall v_v\in V_v.
\end{cases}
\tag{3.29}
$$

For the RBCs transport, the weak formulation has been obtained with a similar approach, multiplying the equation 3.16 by the test function $w_i\in H^1(\Lambda_i)$ and performing a sum over the branches i. Thus, applying again the Green's formula:

$$
\begin{aligned}
\sum_i\Big(\partial_s(\pi R_i^2\overline{u}_{v,i}H_i)\,,\,w_i\Big)_{\Lambda_i} &= -\sum_i\Big(\pi R_i^2\overline{u}_{v,i}H_i\,,\,\partial_s w_i\Big)_{\Lambda_i}\\
&\quad +\sum_i\left[\pi R_i^2\overline{u}_{v,i}H_i w_i|_{s=L} - \pi R_i^2\overline{u}_{v,i}H_i w_i|_{s=0}\right].
\end{aligned}
$$

As done previously for the 1D blood flow equation, and as explained in the equation 3.28, the last term has been rearranged to isolate terms relative to junctions, dead ends and boundary ends:

$$
\begin{aligned}
&+\sum_i\left[\pi R_i^2\overline{u}_{v,i}H_i w_i|_{s=L} - \pi R_i^2\overline{u}_{v,i}H_i w_i|_{s=0}\right]\\
&\qquad = \sum_j\left[\sum_{i\in\mathcal{K}_j^{out}}\pi R_i^2\overline{u}_{v,i}H_i w_i|_{\boldsymbol{y}_j} - \sum_{i\in\mathcal{K}_j^{in}}\pi R_i^2\overline{u}_{v,i}H_i w_i|_{\boldsymbol{y}_j}\right]\\
&\quad +\sum_{i\in\mathcal{B}}\Big[\pi R_i^2\overline{u}_{v,i}H_i w_i|_{\boldsymbol{x}_i^{out}} - \pi R_i^2\overline{u}_{v,i}H_i w_i|_{\boldsymbol{x}_i^{in}}\Big] + \sum_{i\in\mathcal{E}}\pi R_i^2\overline{u}_{v,i}H_i w_i|_{\boldsymbol{z}_i}\,.
\end{aligned}
\tag{3.30}
$$

To include the Zweifach - Fung effect, a general definition of blood flow split $F_{QB,j,i}$ and hematocrit split $F_{QE,j,i}$ is required. Consequently, $F_{QB,j,i}$, namely the fraction of total flow rate entering the vessel i, has been defined as:

$$F_{QB,j,i} = \frac{\pi R_i^2 \overline{u}_{v,i}|_{\boldsymbol{y}_j}}{\sum_{k \in \mathcal{K}_j^{out}} \pi R_k^2 \overline{u}_{v,k}|_{\boldsymbol{y}_j}}, \quad \forall\, i \in \mathcal{K}_j^{in}\,.$$

Similarly, $F_{QE,j,i}$, that is the fraction of RBCs rate entering the vessel i, is:

$$F_{QE,j,i} = \frac{\pi R_i^2 \overline{u}_{v,i} H_{d,i}|_{\boldsymbol{y}_j}}{\sum_{k \in \mathcal{K}_j^{out}} \pi R_k^2 \overline{u}_{v,k} H_{d,k}|_{\boldsymbol{y}_j}}, \quad \forall\, i \in \mathcal{K}_j^{in}\,. \tag{3.31}$$

Starting from the relations of [98] and including also *trivial junctions* and *anastomosis*, namely including the case $\mathrm{card}(\mathcal{K}_j^{in}) = 1$, $F_{QE,j,i}$ can be computed as:

$$\begin{cases} F_{QE,j,i} = 1 & if\ \mathrm{card}(\mathcal{K}_j^{in}) = 1; \\ F_{QE,j,i} = 0 & if\ \mathrm{card}(\mathcal{K}_j^{in}) = 2 \ \wedge\ F_{QB,j,i} \leq X_0; \\ \mathrm{logit}(F_{QE,j,i}) = A + B\mathrm{logit}(\frac{F_{QB,j,i} - X_0}{1-2X_0}) & if\ \mathrm{card}(\mathcal{K}_j^{in}) = 2 \ \wedge\ X_0 < F_{QB,j,i} < 1 - X_0; \\ F_{QE,j,i} = 1 & if\ \mathrm{card}(\mathcal{K}_j^{in}) = 2 \ \wedge\ F_{QB,j,i} \geq 1 - X_0. \end{cases} \tag{3.32}$$

Therefore, computing $F_{QE,j,i}$ from the previous relations and using the equation 3.31:

$$\pi R_i^2 \overline{u}_{v,i} H_i|_{\boldsymbol{y}_j} = F_{QE,j,i} \sum_{k \in \mathcal{K}_j^{out}} \pi R_k^2 \overline{u}_{v,k} H_k|_{\boldsymbol{y}_j}.$$

Thus, in the weak formulation:

$$\sum_{i \in \mathcal{K}_j^{in}} \pi R_i^2 \overline{u}_{v,i} H_i w_i|_{\boldsymbol{y}_j} = \sum_{i \in \mathcal{K}_j^{in}} F_{QE,j,i} w_i|_{\boldsymbol{y}_j} \left(\sum_{k \in \mathcal{K}_j^{out}} \pi R_k^2 \overline{u}_{v,k} H_k|_{\boldsymbol{y}_j} \right).$$

Considering also that for the boundary condition in the inflow vessels $\pi R_i^2 \overline{u}_{v,i} H_i w_i|_{\boldsymbol{x}_i^{in}} = \pi R_i^2 \overline{u}_{v,i} H_0 w_i|_{\boldsymbol{x}_i^{in}}$, the right hand side of the equation 3.30 has been rewritten as:

$$\begin{aligned} &\sum_j \sum_{i \in \mathcal{K}^{out}} \pi R_i^2 \overline{u}_{v,i} H_i w_i|_{\boldsymbol{y}_j} + \sum_{i \in \mathcal{B}} \pi R_i^2 \overline{u}_{v,i} H_i w_i|_{\boldsymbol{x}_i^{out}} + \sum_{i \in \mathcal{E}} \pi R_i^2 \overline{u}_{v,i} H_i w_i|_{\boldsymbol{z}_i} \\ &- \sum_j \sum_{i \in \mathcal{K}_j^{in}} F_{QE,j,i} w_i|_{\boldsymbol{y}_j} \left(\sum_{k \in \mathcal{K}_j^{out}} \pi R_k^2 \overline{u}_{v,k} H_k|_{\boldsymbol{y}_j} \right) - \sum_j \sum_{i \in \mathcal{B}} \pi R_i^2 \overline{u}_{v,i} H_0 w_i|_{\boldsymbol{x}_i^{in}}\,. \end{aligned}$$

Therefore, the weak formulation for the hematocrit problem 3.16 reads as follows:

$$
\begin{aligned}
-\sum_i \Big(\pi R_i^2 \overline{u}_{v,i} H_i \, , \, \partial_s w_i \Big)_{\Lambda_i} &+ \sum_j \sum_{i \in \mathcal{K}^{out}} \pi R_i^2 \overline{u}_{v,i} H_i w_i|_{\boldsymbol{y}_j} \\
&+ \sum_{i \in \mathcal{B}} \pi R_i^2 \overline{u}_{v,i} H_i w_i|_{\boldsymbol{x}_i^{out}} + \sum_{i \in \mathcal{E}} \pi R_i^2 \overline{u}_{v,i} H_i w_i|_{\boldsymbol{z}_i} \\
&- \sum_j \sum_{i \in \mathcal{K}_j^{in}} F_{QE,j,i} w_i|_{\boldsymbol{y}_j} \left(\sum_{k \in \mathcal{K}_j^{out}} \pi R_k^2 \overline{u}_{v,k} H_k|_{\boldsymbol{y}_j} \right) \\
&= \sum_j \sum_{i \in \mathcal{B}} \pi R_i^2 \overline{u}_{v,i} H_0 w_i|_{\boldsymbol{x}_i^{in}} \quad \forall w_i \in H^1(\Lambda_i) \, . \qquad (3.33)
\end{aligned}
$$

3.4 Discrete 3D-1D problem

The variational problem has been discretized to be solved numerically. The discretization has been achieved by means of the finite element method. Therefore partitions of the two domains Ω and Λ are required. To this end, assuming that Ω is a *polygonal* domain, let $\mathcal{T}_t^h$ be an admissible family of partitions of $\bar{\Omega}$ into tetrahedrons K:

$$\bar{\Omega} = \bigcup_{K \in \mathcal{T}_t^h} K,$$

that satisfies the usual conditions of a conforming triangulation of Ω. For the vessels Λ, a similar approach is used, approximating each curved vessel Λ_i by a piecewise linear 1D line, denoted with Λ_i^h. One of the main advantages of this 3D-1D approach consists of this discretization. Indeed, $\mathcal{T}_t^h$ and Λ^h are entirely independent. Thus, the discretization process can be addressed separately for the two domain. Moreover, this approach significantly reduces the mesh-related computational requirements, if compared to a full 3D approach. Starting from $\bar{\Omega}$, the solutions of (3.29), namely interstitial pressure and velocity, are approximated using discontinuous piecewise-polynomial finite elements for pressure and $\boldsymbol{H}_{div}$-conforming *Raviart-Thomas* finite elements [211] for velocity. Consequently,

$$Y_k^h := \{v_h \in L^2(\Omega),\ v_h|_K \in P_k(K) \quad \forall K \in \mathcal{T}_t^h\},$$
$$\boldsymbol{RT}_k^h := \{\mathbf{w}_h \in \boldsymbol{H}_{div}(\Omega),\ \mathbf{w}_h|_K \in P_k(K; \mathbb{R}^d) \oplus \mathbf{x}\, P_k(K) \quad \forall K \in \mathcal{T}_t^h\},$$

for every integer $k \geq 0$, where $\mathcal{P}_k$ indicates the standard space of polynomials of degree $\leq k$ in the variables $\mathbf{x} = (x_1, \ldots, x_d)$. In all the simulations presented in this work, the lowest order *Raviart-Thomas* approximation has been adopted, corresponding to $k = 0$. Conversely, on Λ^h, the solutions, i.e. vessels pressure and velocity, are approximated with continuous piecewise-polynomial finite element spaces. For pressure, the standard approximation has been used (for every integer $k \geq 0$):

$$X_{k+1}^h(\Lambda) := \{w_h \in C^0(\bar{\Lambda}),\ w_h|_S \in P_{k+1}(S) \quad \forall S \in \Lambda^h\}.$$

On the contrary, since the velocity is discontinuous at the junctions, the finite element space has been defined as the collection of local spaces of single branches, namely for every integer $k \geq 0$:

$$W_{k+2}^h(\Lambda) := \bigcup_{i=1}^{N} X_{k+2}^h\left(\Lambda_i^h\right).$$

As a result, we use generalized Taylor-Hood elements on each network branch, satisfying in this way the local stability of the mixed finite element pair for the network. At the same time, we guarantee that the pressure approximation is continuous over the entire network

Λ^h. Also for this case, $k = 0$ has been adopted in all the simulations presented in this work.

Similarly, the approximation of the hematocrit has been conducted with the same approach used for the velocity.

Therefore, defining the discrete subspaces for $k \geq 0$

$$\boldsymbol{V}_t^h = \boldsymbol{RT}_k^h(\Omega) \quad \text{and} \quad Q_t^h = Y_k^h(\Omega)\,,$$
$$V_v^h = W_{k+2}^h(\Lambda^h) \quad \text{and} \quad Q_v^h = X_{k+1}^h(\Lambda^h) \quad \text{and} \quad W_v^h = W_{k+2}^h(\Lambda^h)$$

the discrete problem is:

find $\boldsymbol{u}_t^h \in \mathbf{V}_t^h$, $p_t^h \in Q_t^h$, $u_v^h \in V_v^h$, $p_v^h \in Q_v^h$, $H^h \in W_v^h$ such that

$$\begin{cases}
\Big(\nabla \cdot \boldsymbol{u}_t^h \,,\, q_t^h \Big)_\Omega - \Big(2\pi R f(\overline{\overline{p}}_t^h, \overline{p}_v^h)\delta_\Lambda \,,\, q_t^h \Big)_\Omega = 0 & \forall q_t^h \in Q_t^h, \\
\frac{\mu_t}{K}\Big(\boldsymbol{u}_t^h \,,\, \boldsymbol{v}_t^h \Big)_\Omega - \Big(p_t \,,\, \nabla \cdot \boldsymbol{v}_t^h \Big)_\Omega = -\Big(g_t \,,\, \boldsymbol{v}_t^h \cdot \boldsymbol{n}_t \Big)_{\partial\Omega} & \forall \boldsymbol{v}_t^h \in \boldsymbol{V}_t^h, \\
\sum_i \Big(\partial_s(\pi R_i^2 \overline{u}_{v,i}^h \,,\, q_v^h \Big)_{\Lambda_i^h} + \sum_i \Big(2\pi R f(\overline{\overline{p}}_t^h, \overline{p}_v^h) \,,\, q_v^h \Big)_{\Lambda_i^h} \\
\qquad - \sum_{i\in\mathcal{E}} q_v^h \pi R_i^2 \overline{u}_{v,i}^h|_{\boldsymbol{z}_i} \\
\qquad - \sum_j q_v^h|_{\boldsymbol{y}_j} \Big[\sum_{i\in\mathcal{K}_j^+} \pi R_i^2 \overline{u}_{v,i}^h|_{\boldsymbol{y}_j} - \sum_{i\in\mathcal{K}_j^-} \pi R_i^2 \overline{u}_{v,i}^h|_{\boldsymbol{y}_j} \Big] = 0 & \forall q_v^h \in Q_v^h, \\
\sum_i \Big(-2\frac{\mu_{v,i}}{R_i^2}\phi'(1)\Big(1 + \kappa_i^2 R_i^2\Big)\pi R_i^2 \overline{u}_{v,i}^h \,,\, v_{v,i}^h \Big)_{\Lambda_i} \\
\qquad - \sum_i \Big(\overline{p}_v^h \,,\, \partial_s(\pi R_i^2 v_{v,i}^h) \Big)_{\Lambda_i^h} \\
\qquad + \sum_j \overline{p}_v^h|_{\boldsymbol{y}_j} \Big[\sum_{i\in\mathcal{K}_j^+} \pi R_i^2 v_{v,i}^h|_{\boldsymbol{y}_j} - \sum_{i\in\mathcal{K}_j^-} \pi R_i^2 v_{v,i}^h|_{\boldsymbol{y}_j} \Big] \\
\qquad + \sum_{i\in\mathcal{E}} \overline{p}_v^h \, \pi R_i^2 v_v^h|_{\boldsymbol{z}_i} \\
\qquad = -\sum_{i\in\mathcal{B}} \Big[g_v^+ \, \pi R_i^2 v_v^h|_{\boldsymbol{x}_i^+} - \, g_v^- \, \pi R_i^2 v_v^h|_{\boldsymbol{x}_i^-} \Big] & \forall v_v^h \in V_v^h\,, \\
-\sum_i \Big(\pi R_i^2 \overline{u}_{v,i}^h H_i^h \,,\, \partial_s w_i^h \Big)_{\Lambda_i^h} + \sum_j \sum_{i\in\mathcal{K}^{out}} \pi R_i^2 \overline{u}_{v,i}^h H_i^h w_i^h|_{\boldsymbol{y}_j} \\
\qquad + \sum_{i\in\mathcal{B}} \pi R_i^2 \overline{u}_{v,i}^h H_i^h w_i^h|_{\boldsymbol{x}_i^{out}} + \sum_{i\in\mathcal{E}} \pi R_i^2 \overline{u}_{v,i}^h H_i^h w_i^h|_{\boldsymbol{z}_i} \\
\qquad - \sum_j \sum_{i\in\mathcal{K}_j^{in}} F_{QE,j,i} w_i^h|_{\boldsymbol{y}_j} \Big(\sum_{k\in\mathcal{K}_j^{out}} \pi R_k^2 \overline{u}_{v,k}^h H_k^h|_{\boldsymbol{y}_j} \Big) \\
\qquad = \sum_j \sum_{i\in\mathcal{B}} \pi R_i^2 \overline{u}_{v,i}^h H_0 w_i^h|_{\boldsymbol{x}_i^{in}} & \forall w_i^h \in W_v^h\,.
\end{cases} \tag{3.34}$$

The global error related to this numerical problem is affected by multiple factors. First, since the numerical scheme has been derived from the variational formulation computing all the integral exactly when applying the discrete functions, it is strongly consistent with the exact equations. Secondly, regarding the interpolation properties of the finite element

spaces, the chosen formulations ensure, with respect to the mesh characteristic size, linear convergence for both velocity and pressure in Ω and quadratic convergence in Λ. Thirdly, the error due to the difference between the network Λ with Λ^h scales quadratically on Λ^h. Fourthly, it should be considered also the error related to the approximation of the exact curved geometry by piecewise linear segments, ensuring a sufficient number of nodes per segment. The discrete scheme (equation 3.34) has been written in algebraic form:

$$\begin{bmatrix} \mathbb{M}_{tt} & -\mathbb{D}_{tt}^T & \mathbb{O} & \mathbb{O} \\ \mathbb{D}_{tt} & \mathbb{B}_{tt} & \mathbb{O} & -\mathbb{B}_{tv} \\ \mathbb{O} & \mathbb{O} & \mathbb{M}_{vv}(\mu_v^{k-1}) & -\mathbb{D}_{vv}^T - \mathbb{J}_{vv}^T \\ \mathbb{O} & -\mathbb{B}_{vt} & \mathbb{D}_{vv} + \mathbb{J}_{vv} & \mathbb{B}_{vv} \end{bmatrix} \begin{bmatrix} \mathbf{U}_t^* \\ \mathbf{P}_t^* \\ \mathbf{U}_v^* \\ \mathbf{P}_v^* \end{bmatrix} = \begin{bmatrix} \mathbf{F}_t \\ -\mathbb{B}_{tt}\delta\pi + \mathbb{M}_L\phi_{\mathbf{L}}(\mathbf{P}_t^{k-1}) \\ \mathbf{F}_v \\ \mathbb{B}_{vv}\delta\pi \end{bmatrix},$$

$$\left[\mathbb{B}_h(u_v^{h,k}) + \mathbb{J}_h(u_v^{h,k}) + \mathbb{O}_h(u_v^{h,k} + \mathbb{D}_h)\right] \left[\mathbf{H}^*\right] = \left[\mathbf{F}_h\right],$$

where the matrices have been defined as:

$$[\mathbb{M}_{tt}]_{ij} := (\frac{\mu_t}{K_t}\boldsymbol{\varphi}_t^j, \boldsymbol{\varphi}_t^i)_\Omega \qquad \mathbb{M}_{tt} \in \mathbb{R}^{N_t^h \times N_t^h},$$

$$[\mathbb{D}_{tt}]_{ij} := (\nabla \cdot \boldsymbol{\varphi}_t^j, \psi_t^i)_\Omega \qquad \mathbb{D}_{tt} \in \mathbb{R}^{N_t^h \times M_t^h},$$

$$[\mathbb{B}_{tt}]_{ij} := (2\pi R L_p \overline{\overline{\psi}}_t^j \delta_{\Lambda_h}, \psi_t^i)_\Omega \qquad \mathbb{B}_{tt} \in \mathbb{R}^{M_t^h \times M_t^h},$$

$$[\mathbb{B}_{tv}]_{ij} := (2\pi R L_p \overline{\psi}_v^j \delta_{\Lambda_h}, \psi_t^i)_\Omega \qquad \mathbb{B}_{tv} \in \mathbb{R}^{M_t^h \times M_v^h},$$

$$[\mathbb{M}_L]_{ij} := (\boldsymbol{\varphi}_t^j, \boldsymbol{\varphi}_t^i)_\Omega \qquad \mathbb{M}_L \in \mathbb{R}^{N_t^h \times N_t^h},$$

$$[\mathbb{B}_{vt}]_{ij} := (2\pi R L_p \overline{\overline{\psi}}_t^j, \psi_v^i)_\Lambda \qquad \mathbb{B}_{vt} \in \mathbb{R}^{M_v^h \times M_t^h},$$

$$[\mathbb{B}_{vv}]_{ij} := (2\pi R L_p \overline{\psi}_v^j, \psi_v^i)_\Lambda \qquad \mathbb{B}_{vv} \in \mathbb{R}^{M_v^h \times M_v^h},$$

$$[\mathbb{M}_{vv}]_{ij} := (-2\pi\mu_{v,i}\phi'(1)\left(1 + \kappa_i^2 R_i^2\right)\pi R_i^2 \overline{\varphi}_v^j, \varphi_v^i) \qquad \mathbb{M}_{vv} \in \mathbb{R}^{N_v^h \times N_v^h},$$

$$[\mathbb{D}_{vv}]_{ij} := (\pi R^2 \partial\overline{\varphi}_v^j, \psi_v^i)_\Lambda \qquad \mathbb{D}_{vv} \in \mathbb{R}^{N_v^h \times M_v^h},$$

$$[\mathbb{J}_{vv}]_{ij} := \langle \varphi_v^j, \overline{\psi}_v^i \rangle_J \qquad \mathbb{J}_{vv} \in \mathbb{R}^{N_v^h \times M_v^h},$$

$$[\mathbf{F}_t]_i := -(g_t^h, \boldsymbol{\varphi}_t^i \cdot \mathbf{n})_{\Gamma_p} \qquad \mathbf{F}_t \in \mathbb{R}^{N_t^h},$$

$$[\mathbf{F}_v]_i := -\sum_{i \in \mathcal{B}} \left[g_v^+ \pi R_i^2 v_v^h|_{\boldsymbol{x}_i^+} - g_v^- \pi R_i^2 v_v^h|_{\boldsymbol{x}_i^-} \right] \qquad \mathbf{F}_v \in \mathbb{R}^{N_v^h},$$

$$[\mathbb{B}_h]_{i,j} := \left(\pi R_i^2 \overline{u}_{v,p} \varphi^p \phi_j \, , \, \partial_s \phi_i \right)_\Lambda \qquad \mathbb{B}_h \in \mathbb{R}^{S_v^h},$$

$$[\mathbb{J}_h]_{i,j} := \langle\langle FQE_j \phi_v^j, \phi_v^i \rangle\rangle_{in} \qquad \mathbb{J}_h \in \mathbb{R}^{S_v^h},$$

$$[\mathbb{O}_h]_{i,j} := \langle\langle \phi_h^j \phi_h^i \rangle\rangle_{out} \qquad \mathbb{O}_h \in \mathbb{R}^{S_v^h},$$

$$[\mathbf{F}_h]_i := \sum_{k \in \mathcal{B}} \pi R_k^2 \overline{u}_{v,k}^h H_0 w_k^h|_{\boldsymbol{x}_k^{in}} \qquad \mathbf{F}_h \in \mathbb{R}^{S_v^h},$$

$$[\mathbb{D}_h]_{i,j} := (D^{art} \, \partial_s \psi_h^j, \partial_s \psi_h^i)_\Lambda \qquad \mathbb{D}_h \in \mathbb{R}^{P^h \times P^h}.$$

However, it is important to note that the problem cannot be solved directly. Indeed, two different sources of non-linearity are present:

- the coupling between RBCs transport and the fluid flow, namely $\mathbb{M}_{vv} = \mathbb{M}_{vv}(\mu_v)$, $\mu_v = \mu_v(\mathbf{H}, D)$, and $\mathbf{H}$ is influenced by the flow distribution in the network;
- the lymphatic drainage description, i.e. $\phi_{\mathbf{L}} = \phi_{\mathbf{L}}(\mathbf{P}_t)$.

To solve this non-linearity, an iterative strategy has been adopted using the *fix-point* method. Thus, the two non-linear terms have been computed based on previous iteration results, considering *under relaxation*, if necessary. For clarity in the iterative process description, concerning the algebraic form, from now on the two sub-problems will be identified by:

$$[\boldsymbol{u}_t^h, u_v^h, p_t^h, p_v^h] = \mathcal{F}^h(\mu_v, p_t^h) \, ,$$
$$H^h = \mathcal{H}^h(u_v^h) \, .$$

Based on this definition, the iterative process has been described as follow:

1. initialize the problem $\mathcal{F}^h$ with the initial guess of viscosity μ_{start} and with $\phi_{\mathbf{L}} = 0$, namely solving $[\boldsymbol{u}_t^{h,0}, u_v^{h,0}, p_t^{h,0}, p_v^{h,0}] = \mathcal{F}^h(\mu_{v,start}, 0)$;
2. initialize the problem $\mathcal{H}^h$ with $u_v^{h,0}$, obtaining $H^{h,0} = \mathcal{H}(u_v^{h,0})$;
3. compute the viscosity $\mu_v^0 = \mu_v(H^{h,0})$;
4. build the matrices $\mathbb{M}_{vv}(\mu_v^{k-1})$ and $\phi_{\mathbf{L}}(\mathbf{P}_t^{k-1})$;
5. solve $[\boldsymbol{u}_t^{h,*}, u_v^{h,*}, p_t^{h,*}, p_v^{h,*}] = \mathcal{F}^h(\mu_{k-1}, \mathbf{P}_t^{k-1})$;
6. apply *under-relaxation* to velocity and pressure fields (if necessary) to enhance convergence, i.e. for a given $\alpha \in (0, 1]$

$$\boldsymbol{u}_t^{h,k} = \alpha \boldsymbol{u}_t^{h,*} + (1-\alpha)\boldsymbol{u}_t^{h,k-1} \, , \qquad u_v^{h,k} = \alpha u_v^{h,*} + (1-\alpha) u_v^{h,k-1};$$
$$p_t^{h,k} = \alpha p_t^{h,*} + (1-\alpha) p_t^{h,k-1} \, , \qquad p_v^{h,k} = \alpha p_v^{h,*} + (1-\alpha) p_v^{h,k-1} \, ;$$

7. solve $H^{h,*} = \mathcal{H}(u_v^{h,k})$;

8. apply *under-relaxation* to hematocrit field (if necessary), namely:

$$H^{h,k} = \beta H^{h,*} + (1-\beta) H^{h,k-1} \text{ with } \beta \in (0,1]\,; \tag{3.35}$$

9. compute the viscosity $\mu_v^{k-1} = \mu_v(H^{h,k-1})$;

10. test the convergence by comparing the given tolerances $\epsilon_{\mathcal{F}}$, $\epsilon_{\mathcal{H}}$ with

$$\frac{\left\|\mathbf{U}_v^{k+1} - \mathbf{U}_v^k\right\|}{\|\mathbf{U}_v^k\|} + \frac{\left\|\mathbf{P}_v^{k+1} - \mathbf{P}_v^k\right\|}{\|\mathbf{P}_v^k\|} + \frac{\left\|\mathbf{U}_t^{k+1} - \mathbf{U}_t^k\right\|}{\left\|\mathbf{U}_t^k\right\|} + \frac{\left\|\mathbf{P}_t^{k+1} - \mathbf{P}_t^k\right\|}{\left\|\mathbf{P}_t^k\right\|} < \epsilon_{\mathcal{F}}\,,$$

$$\frac{\left\|\mathbf{H}^{k+1} - \mathbf{H}^k\right\|}{\|\mathbf{H}^k\|} < \epsilon_{\mathcal{H}}$$

where $\|\ \|$ indicates the L^2 norm on the proper domain. If the condition is not satisfied, go back to the point 4.

Being the equation of RBCs transport a pure advection equation, artificial diffusion is required to stabilize the problem. Thus, the local Péclét number $Pe = \frac{h_m \boldsymbol{u}_v}{2\, D_{art}}$ must be lower than 1, where h_m is the mesh dimension [212]. Consequently, the required D_{art} has been set to:

$$D^{art} = 2max(\boldsymbol{u}_v)\, max(h_m)\,.$$

This term should be added in the left hand side variational formulation of the hematocrit problem by:

$$D^{art}(\partial_s H^h, \partial_s w^h)_{\Lambda^h}$$

with the boundary condition $\partial_s H^h = 0|_{\boldsymbol{x}_i^{out}}$. Finally in the algebraic problem, the artificial diffusion has been described by the matrix $\mathbb{D}_h$.

As a final remark, it should be noted that the problem has been implemented in its dimensionless form, following the process shown in [162], leading to a better computational implementation. The block-structured linear system has been solved by means of the LU factorization (SuperLU library) or by the GMRES iterative solver, accelerated by a block preconditioner based on the Schur complements of pressure problems.

3.5 A generator of artificial geometry

3.5.1 Voronoi tesselation based geometries

Several approaches have been adopted in literature to model vascular morphology. Starting for the well-known Krogh cylinder model, in which a single straight capillary is considered, the complexity of the microvascular network can be increased, considering the schematic unit proposed in [66] or in [157], up to real network geometry [112, 162] or artificial network geometry. [107, 108, 213]. Considering this small spatial scale, a significant variability among different tissues has been observed. However, as described in the first chapter, given some exceptions, the *tree-like* structure is usually lost and replaced by a *network-like* structure approaching the microvasculature. In this context, an artificial network generator has been developed to obtain network-like structures to be used in the simulations. It is based on the Voronoi tessellation. Therefore, the space is partitioned in sub-regions starting for seed points in the domain. The sub-region related to a seed point is defined as the set of all the points in the domain for which that seed point is the closest among all the other seed points. In a Euclidean space, the Voronoi tessellation is the dual of Delaunay triangulation. This tessellation has been used to describe the microvasculature by different authors [107, 214–216]. The 2D version of the tessellation (figure 3.6) results in a network composed only by bifurcations and anastomosis, namely 3 vessels are involved in each junction. Conversely, the 3D version does not. Indeed, when considering

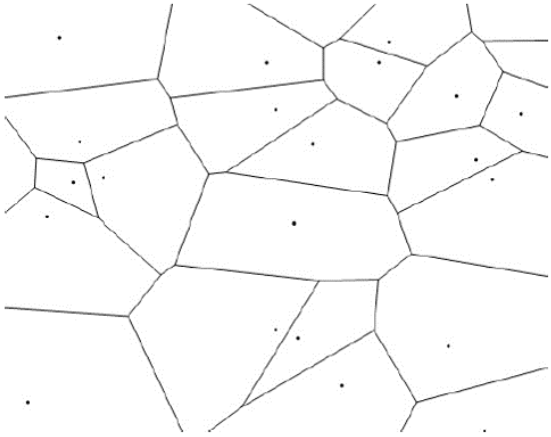

Figure 3.6: *Example of 2D Voronoi tessellation. From [99].*

this version, the junction should be adjusted by removing some vessels [216]. For this reason, the 2D version has been adopted in this work, and the resulting networks have

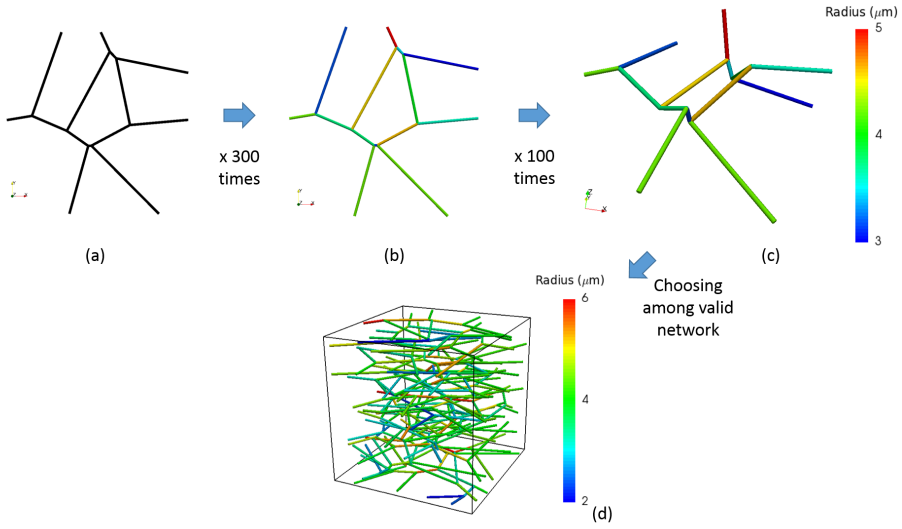

Figure 3.7: *Steps of the artificial network generator. (a) 2D Voronoi tessellation. (b) Radii computation. (c) 3D perturbation. (d) Final assembly, stacking geometries in a* $500\mu m$ *cube.*

been randomly perturbed along the third direction to avoid perfect planar geometries (figure 3.7). Therefore, using Matlab® (The MathWorks Inc., Natick, MA, USA) an artificial network generator has been developed. The number of seed points is the main parameter influencing the morphology of the network. Consequently, several network configurations spanning from 5 to 15 seeds have been screened, leading to the choice of random distributions of 8 points on a 500 μm side square. Doing so, a sufficiently high aspect ratio is guaranteed for an average radius of 4 μm (about $L_i/R_i = 4$). 100 different network configurations have been created by random variation of these 8 points.

3.5.2 Radius assignment

Murray's law has been applied to define vessels radii:

$$\text{bifurcation} \quad R_{in,0}^3 = R_{out,1}^3 + R_{out,2}^3; \quad \text{for a given split ratio } a = \frac{R_{in,0}}{R_{out,1}}$$

$$\text{anastomosis} \quad R_{in,1}^3 + R_{in,2}^3 = R_{out,0}^3;$$

where the split ratio a is randomly selected in the interval $(0.67, 0.89)$ (i.e. $a^3 \in (0.3, 0.7)$ where $a^3 = 0.5$ stands for symmetric bifurcation). Since the direction of flow can vary due to the applied boundary conditions, an iterative process has been implemented to as-

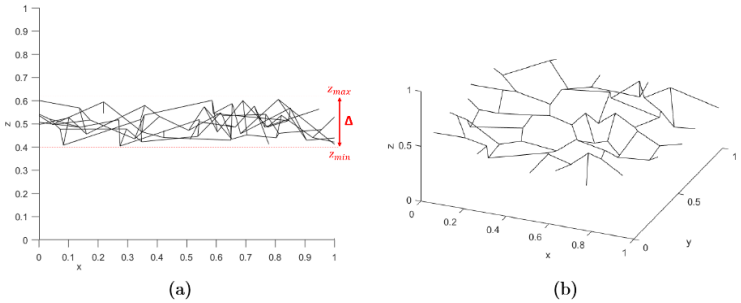

Figure 3.8: *Example of 3D perturbation of a 2D Voronoi tessellation: (a) $z - x$ plane view (b) 3D view. From [99].*

sign radius values. Such an iterative process requires to solve the fluid dynamic problem. Therefore, one iteration is made by solving the problem and applying the Murray's law. In particular, the fluid dynamic problem has been solved applying $32\,mmHg$ and $15\,mmHg$ at networks ends, to achieve flow distribution, and thus classifying junctions as bifurcation or anastomosis. Then, Murray's law has been applied, computing the radius for each vessel starting from an initial value of the radius (specified at the inflow ends). This process has been iterated until the flow direction is conserved in two subsequent iterations. This iterative process has been applied to the 100 previously-generated 2D networks. More precisely, 100 radius variation have been generated starting from 3 different initial radii ($4\mu m$, $4.25\mu m$, $4.5\mu m$ chosen with reference to the literature, e.g. [5, 61, 181, 194, 217]) for a total of 300 radius configuration for each 2D network.

3.5.3 3D perturbation and network selection

The obtained networks have been perturbed to obtain 3D geometry (figure 3.8) that fits in a thin tissue slab with height Δ. The 3D perturbation changes the morphology of the network in terms of both length and spatial distribution within the interstitium (therefore related to the coupling with the environment). In particular, such a perturbation results in longer vessels further spreading within the interstitium. If the height Δ is small, e.g. $50\,\mu m$, as is in the presented cases, these effect are negligible: difference in length $\simeq 2\,\%$. As a consequence, difference in mean interstitial pressure would be low. On the other hand, even if these conditions are not represented in this work, we point out that if Δ is big, significant differences in both intra- and extra-vascular fluid dynamics may occur since the network morphology is definitely different. The 3D perturbation has been performed 100 times on each network radius configuration. Among these 3×10^4 networks, only those satisfying the following criteria have been selected: (i) radii inside the interval

$2 - 6$ μm, and (ii) mean value of radius (i.e. $\sum_i R_i L_i / \sum_i L_i$) equal to 4 μm $\pm 5\%$. Consequently, 10^4 valid configurations have been obtained and used in the final step. Finally, the resulting 3D networks have been stacked to obtain the desired capillary density (e.g. for physiological conditions $\simeq 7000\, m^{-1}$ [199]). One of the resulting geometries is shown in figure 3.9.

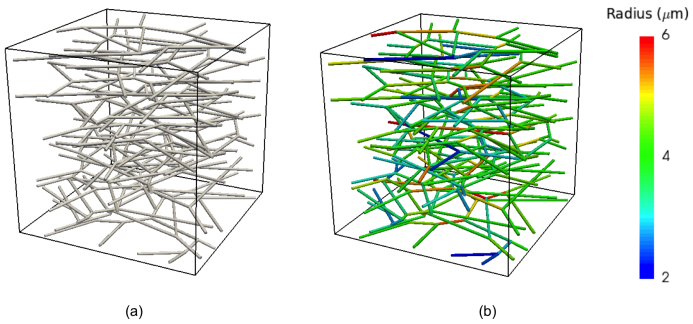

Figure 3.9: *Example of an artificial generated network: (a) network with constant radius, (b) network with radius computed by the Murray's law.*

3.5.4 Geometries used in this work

Generally speaking, several different geometries have been used in this work (figure 3.10). The simplest one is composed only by a straight capillary that crosses the interstitial domain Ω. This geometry has been considered also in its *curved version*, with different values of kR, i.e. considering a fixed radius R, a different curvature radius $1/k$ is obtained. A further step towards a complex network consists in a network with one junction. This can be either bifurcation or anastomosis. Also for the bifurcation, a *curved version* has been modeled. Then, to increase geometrical complexity, a hexagonal structure has been considered, namely a network with two junctions: one bifurcation and one anastomosis. Even more complex networks result from the artificial generator described in this paragraph, including a large number of junctions. All these geometries can be repeated within the domain Ω to achieve a desired capillary density, expressed as S/V ratio, i.e. the vessel lateral surface per unit volume of Ω. As a final remark of the paragraph, also the geometry of an *in vitro* vascular networks have been considered as explained in the chapter 5.

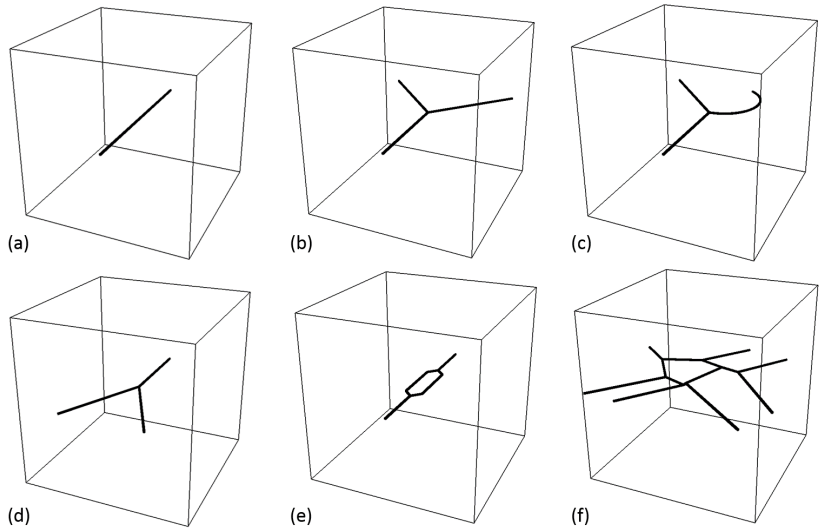

Figure 3.10: *Examples of geometries used in this work. (a) Single straight capillary. (b) Bifurcation composed by straight vessels. (c) Bifurcation with a curved vessel. (d) Anastomosis of straight vessels. (e) Hexagonal structure comprehending a bifurcation and an anastomosis. (f) Single Voronoi network used for the composition of a complex network with* $S/V = 7000\,m^{-1}$.

3.6 Computational test benches

Several and increasingly complex test cases have been analyzed to prove to what extent this model can describe the involved phenomena. Consequently, peculiar effects of the microvasculature have been tested (considering impermeable vessels, namely with $L_p = 0$). Then filtration, curvature of the vessel and lymphatic drainage have been addressed. Model results have been compared to analytical solutions, real data (when available) of with other computational simulations (i.e. 3D full approach by finite volume method).

3.6.1 Poiseuille's flow and Fåhraeus - Lindqvist effect

First, the Poiseuille's flow has been tested on a single straight capillary. To this end, the values of parameters are specified as in the table 3.1. Given these parameters, the

Table 3.1: *Parameter used for Poiseuille's flow simulation.*

SYMBOL	PARAMETER	UNITS	VALUE	REF.
d	Characteristic capillary length	m	5×10^{-4}	[218]
R	Mean radius	m	4×10^{-6}	[181]
μ_v	Viscosity of blood	cP	9.33	[98]
P_a	Arteriolar side pressure	$mmHg$	32	[194]
P_v	Venular side pressure	$mmHg$	15	[194]
P	Characteristic pressure for adimensionalization	Pa	133.32	
U	Characteristic velocity for adimensionalization	$\mathrm{m\,s^{-1}}$	1×10^{-3}	[104]

Poiseuille's equation allows us to compute:

$$Q_b = \frac{\pi R^4}{8\mu_v L}\,\Delta p \simeq 4.9 \times 10^{-14} m^3/s = 4.9 \times 10^{-5} mm^3/s. \tag{3.36}$$

Then, the velocity $\boldsymbol{u}_v$ can be computed as:

$$\boldsymbol{u}_v = \frac{Q_b}{\pi R^2} \simeq 0.97 mm/s,$$

in agreement with the characteristic velocity reported in [104]. Results of the simulation are shown in figure 3.11. The velocity is constant along the vessel due to mass conser-

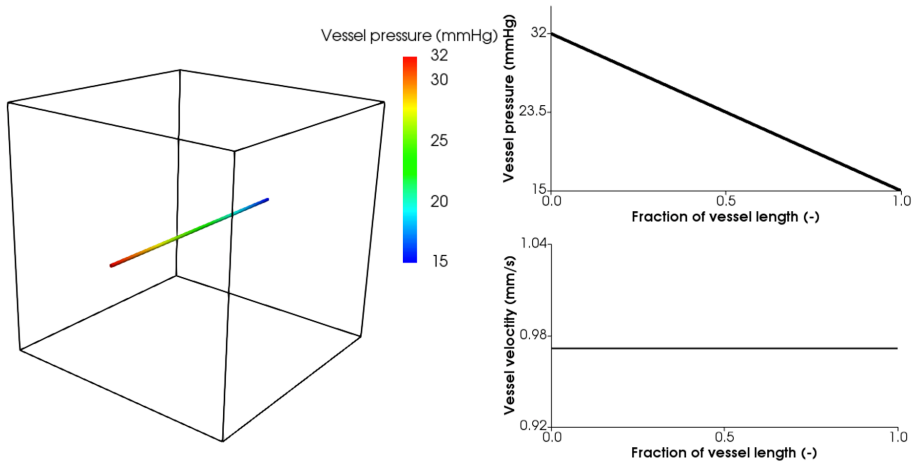

Figure 3.11: *Results of the Poiseuille test case. On the left, contour of pressure within the vessel in the 3D domain. On the right top: pressure distribution along the vessel (results shown with reference to the fraction of vessel length x/L). On right bottom: distribution of velocity in the vessel.*

vation, and it is equal to $0.97\,mm/s$, in agreement with the expected value. Conversely, the pressure is not constant, but it linearly decreases along the vessel, as predicted by the theory. This test has been conducted with a discharge hematocrit $H = 0.45$ which results in $9.33\,cP$ applying the Pries formula. Spanning in a larger interval of H, i.e. $[0.30, 0.60]$, the Fåhraeus - Lindqvist effect can be appreciated, namely the change in apparent viscosity that results in different blood velocity when setting the same difference of pressure. A comparison of theoretical prediction, i.e. derived from equation 3.36, and numerical results is presented in the figure 3.12. Given the agreement shown in that figure, the Fåhraeus - Lindqvist effect is correctly reproduced by the model.

3.6.2 Zweifach - Fung effect

To test and appreciate the Zweifach - Fung effect, at least three vessels are required. Thus, either a bifurcation of an anastomosis (or both) shall be considered. The effect cannot be observed by analyzing the anastomosis as only the conservation of RBSs at the junctions is sufficient to describe the phenomenon (figure 3.13). Therefore, in this case test, the mass conservation has been checked with reference to an anastomosis composed by vessels with different radii(table 3.2), modeling flow driven by the same Δp used for the single branch simulations. Q_H has been reported with a positive sign if $i \in \mathcal{K}_j^{out}$ and negative otherwise.

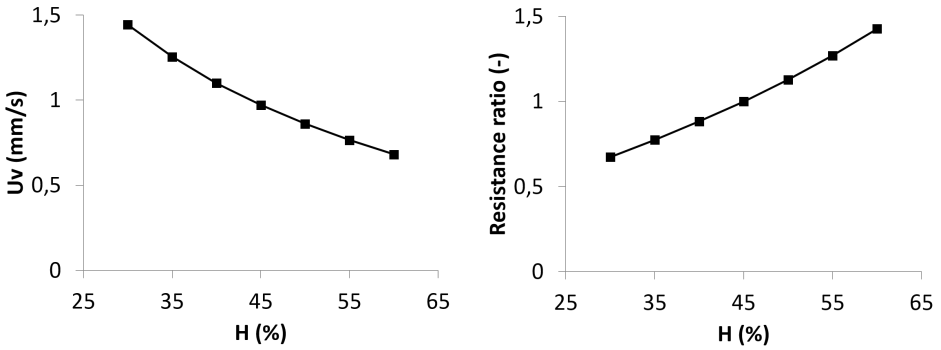

Figure 3.12: *Graphs showing the effect of H variation in a single capillary test. On the left, variation of velocity within the vessel, on the right, variation of the resistance ratio. The latter is defined by the ratio of the hydraulic resistance for a given H over the one obtained with $H = 0.45$. The hydraulic resistance is computed as $(8\mu_v L)/(\pi R^4)$. Continuous lines show theoretical prediction, whereas squares report numerical results.*

Consequently, the sum of all the Q_H is expected to be null for mass conservation, as obtained from results in table 3.2. Conversely, with reference to a more interesting case,

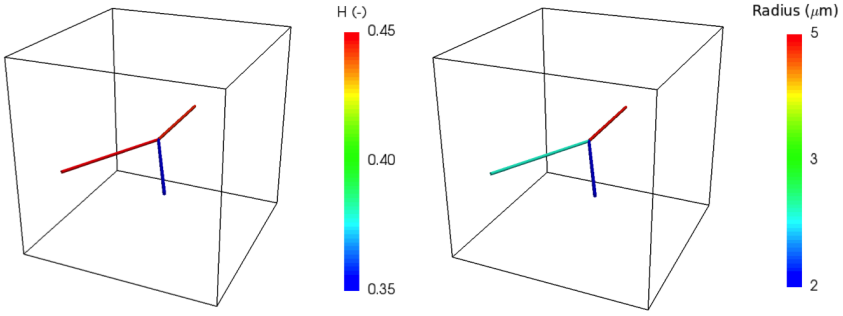

Figure 3.13: *Variations of H for given R in an anastomosis.*

such as the bifurcation, the heterogeneity of hematocrit distribution can be observed if the radii of the daughter vessels are different. To model the problem a smaller domain has been considered, that is a cube Ω with a $100\mu m$ side. For this reason, the pressure boundary conditions to be applied have been recomputed, so that the characteristic velocity $U = 1mm/s$ would be obtained in a straight single branch leading to $\Delta p \simeq 3.5mmHg$. Three different geometries have been used, with different daughter branches radii $R_1 = R_2$

Table 3.2: *Adimensional results in terms of H, $\boldsymbol{u}_v$ and Q_h for an anastomosis.*

	$Branch1$	$Branch2$	$Outletbranch$
H [-]	0.35	0.45	0.44
$\boldsymbol{u}_v$ [-]	0.69	3.83	1.02
R [-]	0.003	0.005	0.01
Q_H [-]	$+6.84 \cdot 10^{-6}$	$+1.35 \cdot 10^{-4}$	$-1.42 \cdot 10^{-4}$

(whereas $*0$ indicates variable referred to the father vessel). In the first one, the daughter branches have the same radius, i.e. $R_1 = R_2 = 3.17\mu m$, which have been computed by applying Murray's law starting from $R0 = 4\mu m$. Starting from it, the other two geometries have been generated by applying a variation of 5% and 10% to one daughter vessel, and an equal negative variation to the other branch. Referring to figure 3.14, the upper branches have undergone a positive variation, resulting in a bigger radius. The influence of these radius variations has been studied in terms of velocity, hematocrit, and viscosity (figure 3.14).

A quantitative analysis has been also reported in Table 3.3. In terms of velocity, results are highly sensitive to radii variation, as expected by the theoretical description (equation 3.36). Indeed, since the radius is considered in the relationship with a 4^{th} power, a small variation of R produces large variations of flow rate and, thus, of velocity. Concerning hematocrit, variations are also amplified according the magnitude of the perturbation. In other words, RBCs hardly enter into the daughter branch with a smaller radius. Consequently, in the branch where the radius has been decreased the hematocrit is lower than in the one where it was increased. The viscosity is determined by both radius and hematocrit. Therefore, lower hematocrit results in lower viscosity, but this effect has been hidden by the radius dependence. This highlights the complex interaction of blood velocity, hematocrit, and viscosity at bifurcations. Their complex and non-linear interaction, which was obtained by breaking the symmetry of the junction, is hardly predictable with simple models that do not take into account their combined effects.

Considering a *hexagonal structure*, both a bifurcation and an anastomosis can be observed at the same time (table 3.4), leading to the previously described conclusion. The applied geometry is shown in figure 3.15. The side of the interstitial cube is $500\,\mu m$, and the vessels downstream the bifurcation are separated by $50\,\mu m$. Therefore, $32\,mmHg$ and $15\,mmHg$ have been set as boundary conditions. As found in the previous test, heterogeneity of the velocity and the hematocrit is generated downstream the bifurcation. For mass conservation, the flow rate ($\pi R^2 \boldsymbol{u}_v$) and the hematocrit flow rate ($\pi R^2 \boldsymbol{u}_v H$) have

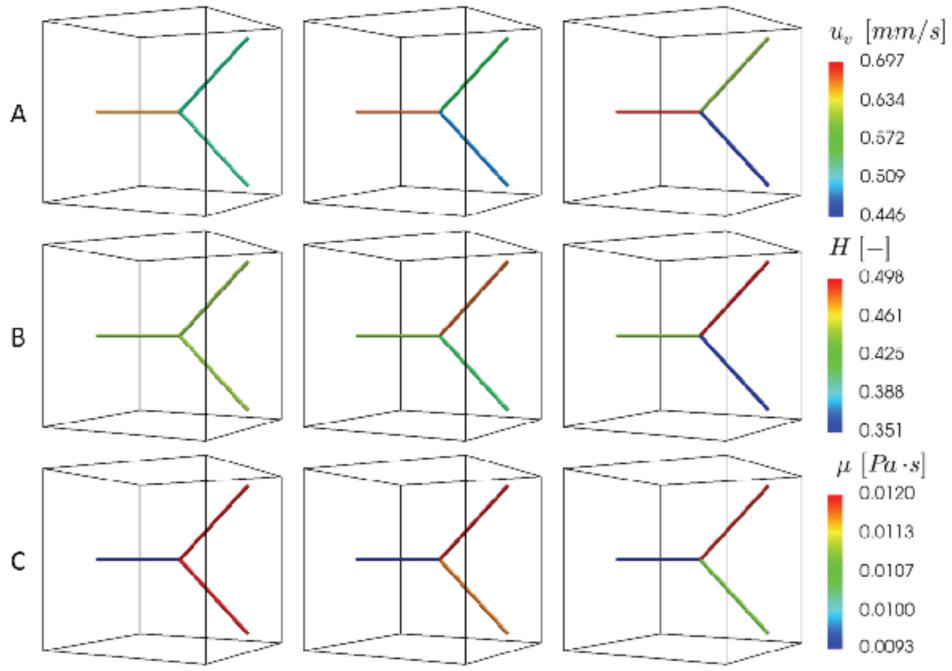

Figure 3.14: *Influence of radius variation in a bifurcation, as reported in Possenti et al. [206]. In the first column, the daughter branches have equal radii $R_1 = R_2 = 3.17\mu m$, whereas in the second column $\pm 5\%$ variation has been applied to the daughter vessel and in the third $\pm 10\%$. The upper branch has undergone positive variation. Results have been reported in terms of velocities (panel A), hematocrit (penel B) and effective viscosity (panel C) ranking from top to bottom.*

been restored downstream the anastomosis. The mass imbalance for the hematocrit has been computed in the order of magnitude of 10^{-10}, namely 5 orders of magnitude lower than Q_h.

A further analysis has been conducted employing the artificial generated vascular network. This network is planar and it has been obtained by the aforementioned Voronoi tessellation. The side of the surrounding cube is again $500\,\mu m$. The same boundary conditions have been applied, namely $32\,mmHg$ and $15\,mmHg$, at the arteriolar and the venular ends respectively. Including in the problem a larger number of bifurcations, a larger range of variability characterizes the solution of H and μ_v as shown in figure 3.16. This is in agreement with the reported heterogeneity of RBCs distribution within the microvasculature. In real vessels, under physiological conditions, this heterogeneity can also lead to the extreme condition in which $H = 0$, namely vessels without RBCs. Although

Table 3.3: *Quantitative analysis of the simulations illustrated in Figure 3.14, as reported in Possenti et al. [206].*

	reference			5%			10%		
Branch	0	1	2	0	1	2	0	1	2
R	4.000	3.170	3.170	4.000	3.330	3.020	4.000	3.490	2.860
$\overline{u}_v$	0.656	0.522	0.522	0.669	0.568	0.483	0.697	0.617	0.446
$\%\overline{u}_v$				2%	9%	-8%	6%	18%	-15%
H	0.450	0.450	0.450	0.450	0.480	0.407	0.450	0.498	0.351
$\%H$				0%	7%	-10%	0%	11%	-22%
μ	0.009	0.012	0.012	0.009	0.012	0.012	0.009	0.012	0.011
$\%\mu$				0%	0%	-3%	0%	-2%	-8%

Table 3.4: *Results in terms of H, $\boldsymbol{u}_v$ and Q_h for an hexagonal structure.*

	$Intletbranch$	$Branch1$	$Branch2$	$Outletbranch$
R (μm)	4.5	3.85	3.25	4.5
$\boldsymbol{u}_v\ (mm/s)$	1.07	0.96	0.72	1.07
H (-)	0.45	0.49	0.38	0.45
$Q_h(mm^3/s)$	3.07×10^{-05}	2.18×10^{-05}	8.97×10^{-06}	3.07×10^{-05}

this extreme condition has not been found in the figure 3.16, the reported variability has shown that such condition can be met. However, this is strictly related to the network morphology.

An experimental comparison has been performed considering data from microfluidic devices. As discussed in the first chapter, the main limitation of such devices is related to the cross-section of the device. Therefore, when considering those models for a comparison with the 3D-1D model (i.e. a computational model considering circular cross-sections), the proper diameter of the vessel should be considered as well. To this aim, the hydraulic diameter has been used for the vessels. It has been computed as $D_h = 4A/2P$, where A is the experimental square cross-section and $2P$ is the perimeter. As a consequence, considering a rectangular cross section channel and its approximation to a circular vessel with the diameter D_h, the same flow rate is obtained with the same Δp. The considered experimental data have been taken by the work of Clavica and colleagues [114]. They proposed an analysis of the Zweifach - Fung effect in a simple network which consists of

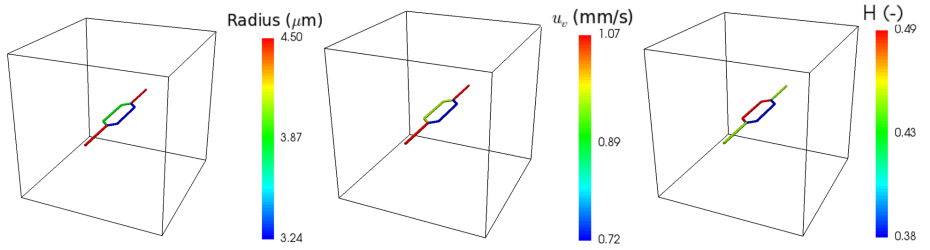

Figure 3.15: *Zweifach - Fung effect in an hexagonal structure.*

a bifurcation and a downstream anastomosis (figure 3.17). Three different versions of this simple geometry have been used in the experimental test by the authors: (i) symmetric model, in which the daughter vessels are equal; (ii) dilated model, in which one daughter vessel is larger than the other one; (iii) stretched model, in which one daughter vessel is longer than the other one. In their work, RBCs velocity and hematocrit density and flux have been analyzed in the parent vessel and in the daughter vessels. Starting from the tube hematocrit reported, the H has been computed along with the ratio between RBCs velocity and the bulk velocity using the relation proposed by Pries and colleagues [97]. Since the glycocalyx was not present in their in vitro model, the viscosity has been computed by means of the in vitro law of viscosity described in the first chapter. Boundary conditions have been adjusted to match the flow rate in the parent vessel for each configuration. Results of the comparison are shown in the table 3.5. They conducted several experiments with different Δp driving the flow, resulting in different flow rate within the network. In the table, all the experimental results have been included, reporting the median values. Experimental ranges shown by the authors are wider (e.g. between 0.5 and 3.5 for the experimental flux ratio in the symmetric model), producing oscillations interpreted by the author as a consequence of the non-linear rheology. Given all the differences among experimental and computational setup (e.g. the cross-section of the vessel, which may influence the RBCs distribution at the bifurcation), and the very sharp angle considered in the *in vitro* experiment, the model has reproduced the phenomenon quite well and always within the experimental ranges (in table 3.5 only median values are shown). In addition, also the possible inversion of the Zweifach - Fung effect has been addressed in their work, namely a different distribution of RBCs in the same bifurcation while considering the same flow rates. This phenomenon has not been reproduced by the model so far since for a given geometry and a determined flow rate distribution (i.e. F_{QB}), the fraction of RBCs entering the daughter vessels (i.e. F_{QE}) is uniquely determined. However, once this phenomenon is completely understood, it shall be included in the model, by modifying the function which determines F_{QE}.

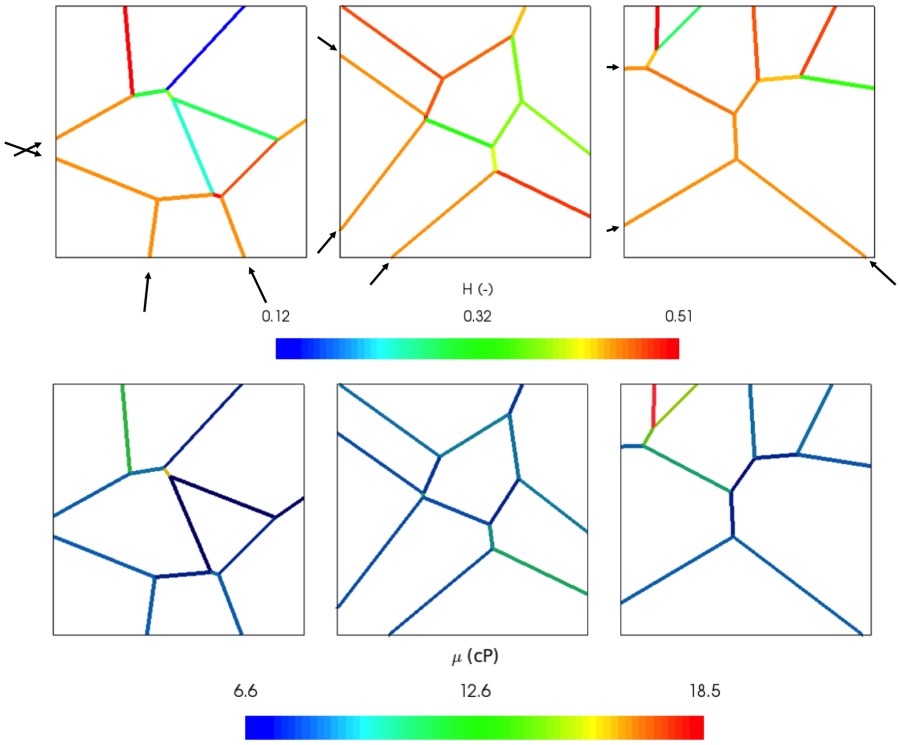

Figure 3.16: *Zweifach - Fung effect in an artificially generated planar Voronoi network. Black arrows indicate direction of flow.*

Table 3.5: *Result of the comparison with experimental data of [114]. Both experimental and computational ratios are referred to B'/B as shown in figure 3.17. Median values resulting from different experiments (in terms of Δp applied) have been reported, but experimental ranges are wider (in the brackets the maximum of the 3^{rd} quartile and the minimum of the 1^{st} quartile considering all the conditions). In particular, computational results always fall in the experimental ranges.*

Geometry	Experimental flux ratio	Computational H ratio
Symmetric	$\simeq 1$ (0.82-1.41)	1
Dilated	1.03-1.14 (0.77-1.63)	1.2
Stretched	0.41-0.58 (0.33-0.71)	0.66

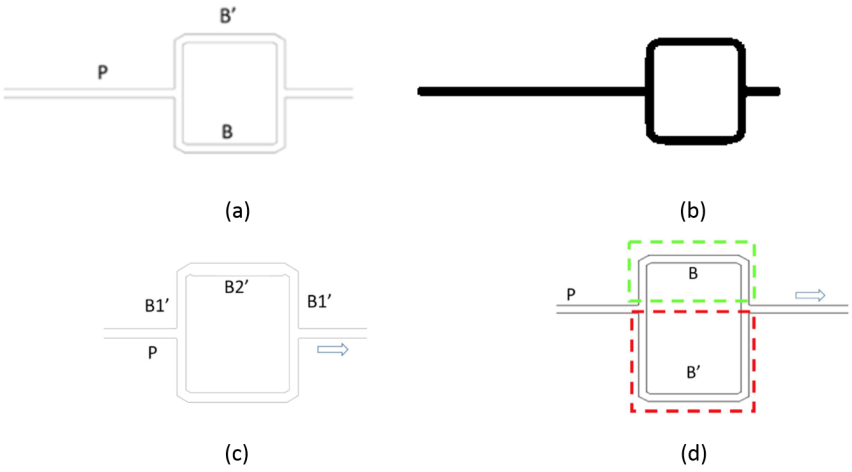

Figure 3.17: *Experimental geometries considered in [114]. (a) Symmetric model. (b) Computational geometry reconstructed for the symmetric model. (c) Dilated model: the upper vessel is dilated with respect to the same vessel in the symmetric geometry. (d) Stretched geometry: the bottom vessel has been stretched resulting longer than the upper.*

3.6.3 Vessel permeability

In this section, the coupling between the vascular networks is presented. To this end, a single straight capillary has been first analyzed. The parameters for this test have been chosen from literature to model the exchange of fluid between the two domains (table 3.6). Due to the filtration from the vessel, a slight flow rate has been generated within the interstitium (figure 3.18a). The interstitial velocity is definitely lower than reported *in vivo*, but this is consistent with the fact that only one capillary vessel has been considered in a large portion of the Ω domain. This movement of fluid within the interstitium has been associated with an increase in interstitial pressure (figure 3.18b). The value of velocity within the vessel is in agreement with the case $L_p = 0$, since the filtration rate is definitely lower than the flow rate flowing within the vessel. The main difference regards the velocity profile along the vessel (figure 3.18c). Due to net filtration, a portion of the flow rate flowing in the vessel goes out from the lateral surface of the vessel. Therefore, the term $\partial_s \pi R^2 \boldsymbol{u}_v$ is no longer equal to 0, namely $\boldsymbol{u}_v$ is not constant along the vessel. In particular, when filtration happens (i.e. arteriolar side), $\boldsymbol{u}_v$ decreases, whereas when fluid is absorbed by the vessel (i.e. venular side) $\boldsymbol{u}_v$ increase. Again, given a physiological L_p value, the abovementioned phenomeno has a low effect, since filtration has a lower order of magnitude with respect to the vessel flow rate. Although less evidently, also the pressure within the vessel is affected by filtration in a similar way (figure 3.18d). At this low level of complexity, the solution can be compared with the analytical one with a couple of assumptions: (i) p_t constant on the domain Ω, and (ii) μ_v constant over the vessel, namely neglecting the influence of hematocrit. Computationally, the first assumption is well satisfied if the value of the tissue hydraulic conductivity K is sufficiently high. Therefore, four computational tests have been run using with $K = 10^{-8} m^2$ and testing $L_p = 10^{-12}, 10^{-10}, 10^{-8}, 10^{-6} m^2\, s\, kg^{-1}$. These last values are far from the physiological and pathological values, but they allow us to test the model by producing larger variations in both the velocity and the pressure profile. The analytic solution can be derived from:

$$\frac{\partial^2 \overline{p}_v}{\partial s^2} - \frac{2\pi R L_p}{\pi R^4} 8\mu_v \Big(1 + \kappa^2(s) R^2\Big) \overline{p}_v(s) = -\frac{2\pi R L_p}{\pi R^4} 8\mu_v \Big(1 + \kappa^2(s) R^2\Big) [\bar{\bar{p}}_t + \sigma \Delta\pi] \,,$$
$$\overline{p}_v(s = 0) = 32 \,, \quad \overline{p}_v(s = L) = 15 \,,$$

where a straight vessel is considered, namely $\kappa = 0$, and due to the first assumption $\bar{\bar{p}}_t \simeq p0$. Thus, the solution has been obtained as:

$$\overline{p}_v(s) = A e^{-\sqrt{\frac{2\pi R L_p}{8\pi R^4}\mu_v}\, s} + B e^{\sqrt{\frac{2\pi R L_p}{8\pi R^4}\mu_v}\, s} + C \,,$$

where A, B, C have been computed by setting the boundary conditions for each case. As shown in the figure 3.19, the numeric solution is in agreement with the numerical

Table 3.6: *Parameter used for simulate 3D-1D interactions.*

SYMBOL	PARAMETER	UNITS	VALUE	REF.
d	Characteristic capillary length	m	5×10^{-4}	[218]
R	Mean radius	m	4×10^{-6}	[181]
μ_v	Viscosity of blood	cP	9.33	[98]
P_a	Arteriolar side pressure	$mmHg$	32	[194]
P_v	Venular side pressure	$mmHg$	15	[194]
P	Characteristic pressure for adimensionalization	Pa	133.32	
U	Characteristic velocity for adimensionalization	$\mathrm{m\,s^{-1}}$	1×10^{-3}	[104]
K	Tissue hydraulic conductivity	$\mathrm{m^2}$	1×10^{-18}	[162]
L_p	Wall hydraulic conductivity	$\mathrm{m^2\,s\,kg^{-1}}$	10^{-12}	[162]
$\delta\pi$	Oncotic pressure gradient	$mmHg$	25	[194]
σ	Reflection coefficient	$[-]$	0.95	[219]
β_t	Boundary conductivity of $\partial\Omega$	m^2s/kg	8×10^{-12}	computed as [162]
p_0	Far field pressure	$mmHg$	-1	[30]
H_0	Hematocrit at inlet of capillary	$-$	0.45	[5]

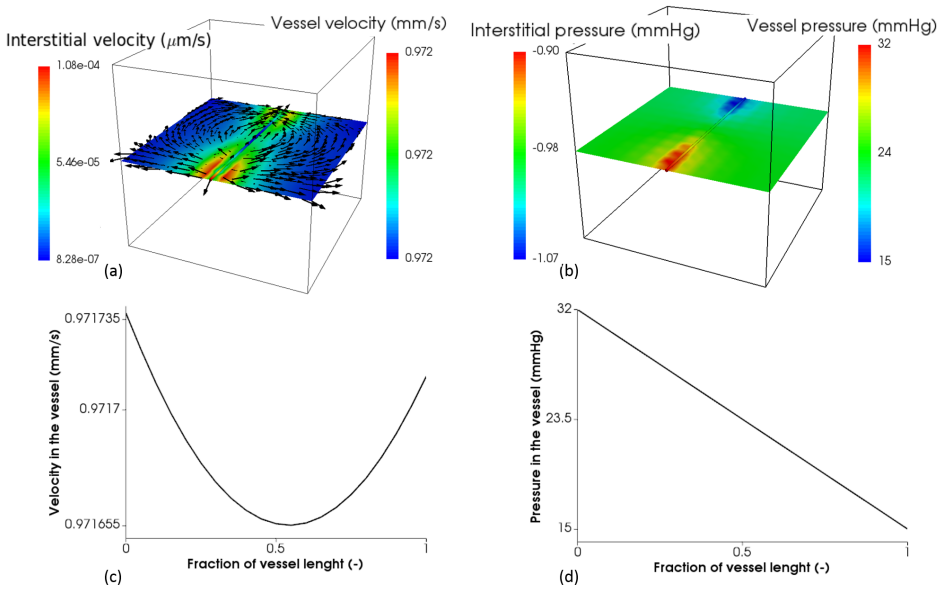

Figure 3.18: *Modeling of filtration from a single straight vessel in a cubic domain Ω. The side of the cube is $500\mu m$. Distribution of velocity (a) and pressure (b) in both the vessel and the interstitium. Plot of the velocity (c) and pressure (d) profile along the vessel.*

one. Moreover, the larger L_p is, the larger the variation of the pressure profile is. In particular, also the extreme behavior produced by a very high L_p is correctly reproduced by the model. Indeed, the plateau reached in the middle of the vessel corresponds to the condition $p_v = p_t + \sigma\Delta\pi$, where no filtration/absorption occurs. Such variation in the pressure profile is caused by the hydraulic conductivity of the capillary membrane, which certainly produces also a variation of the flow rate within the vessel and thus a variation of velocity. In particular, in the middle of the vessel, where the pressure profile is almost flat, the velocity is close to 0.

A further interesting test has been conducted by repeating the single vessel 3 and 10 times, namely increasing the available surface area for the filtration/absorption. Vessels are arranged as shown figure 3.20. As expected, a linear relation is obtained between total length (i.e. the lateral surface area since the radius is constant for this test) and the filtration rate. Interestingly, when analyzing planar Voronoi networks this clear trend has not been reported. This because the morphology of the network influences the pressure distribution, resulting in different pressure conditions eventually leading to different filtration rate. This result highlights that accounting for the geometry is important to capture local phenomena.

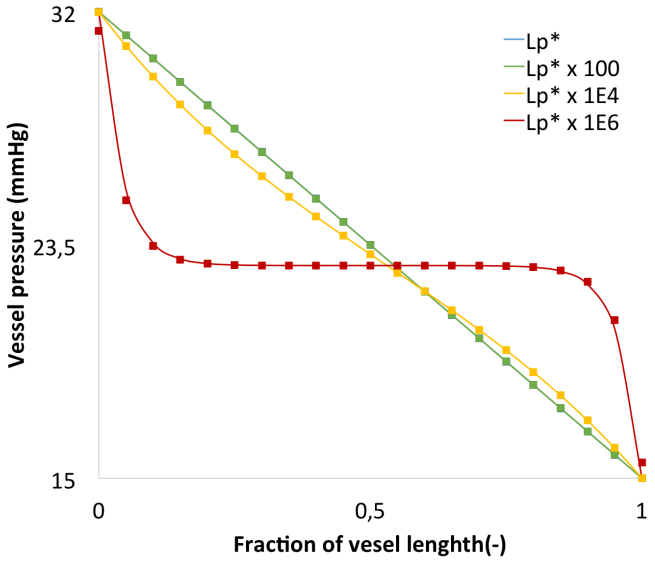

Figure 3.19: *Test case for vessel filtration using a straight vessel. Lines report theoretical prediction from the analytical solution, squares show modeling results.*

In addition, the filtration has also effect on RBCs because they cannot pass through the membrane. As confirmed by the core analytic equation 3.17, this has a small impact if compared to the heterogeneity due to the Zweifach - Fung effect. Anyway, it is still naturally present in the model (figure 3.21). This test has been conducted on a single straight capillary with $L_p = 10^{-12}$ and $H_{in} = 0.45$. Results of the model have been compared to the analytic solution, which is, known the velocity profile along the vessel:

$$H(s) = \frac{\boldsymbol{u}_v(s=0)}{\boldsymbol{u}_v(s)} H(s=0)\,.$$

As seen in the previous test, the velocity is no longer constant along the vessel due to vessel permeability (figure 3.21a). In particular, the velocity within the vessel decreases because of filtration (i.e. variations happening at the arteriolar side). Indeed the flow rate decreases, consistently to mass conservation, due to the filtration from the vasculature. As clearly shown by the analytical solution, the hematocrit profile is affected by this velocity variation. More precisely, a decrease in the velocity induces an increase in H (figure 3.21c). This variation is reflected also in the viscosity (figure 3.21b). However, as discussed above, the filtration rate is low if compared to the vessel flow rate. Therefore, the variations of velocity are low. Indeed, they reflect the variation of flow rate due to filtration/absorption across the capillary membrane. Such low variations of velocity con-

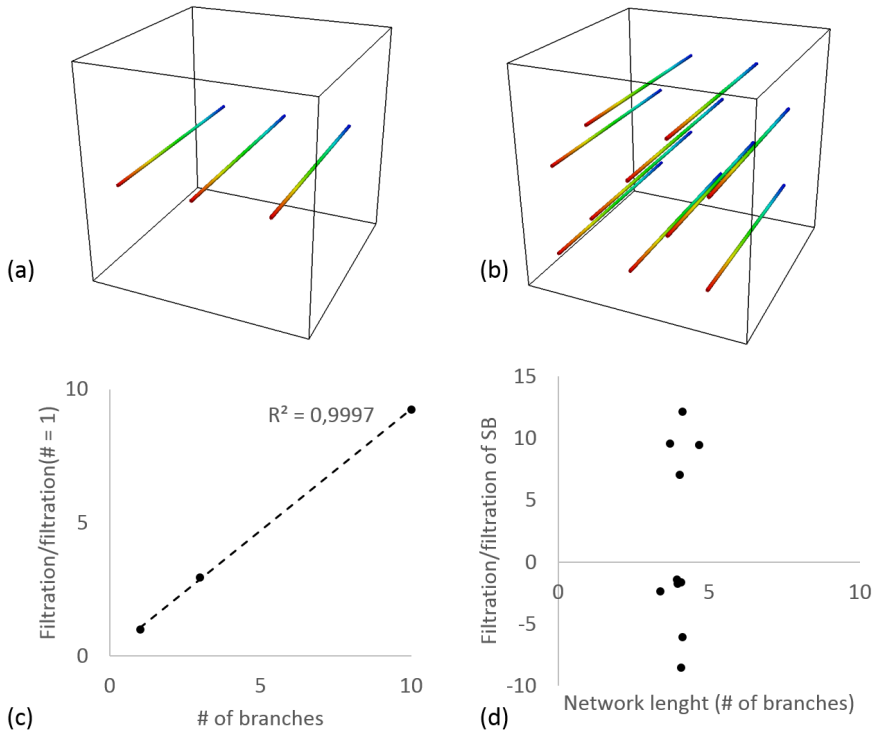

Figure 3.20: *Test case for network surface area, i.e. vessel length when considering a fixed radius. On the top: space arrangement of the 3-vessel (a) and the 10-vessel (b) geometry. On the bottom: graph showing the filtration-network length relation for repeated single straight vessel (c) and for several different planar Voronoi network (d). Negative filtration depicts absorption of fluid by the network.*

sequently produce low variations of H and μ_v. Since also μ_v affects the velocity profile, the inverse interaction should also be considered. Nevertheless, the velocity profile is not significantly affected by these little changes of viscosity (i.e. a comparison between figure 3.21a and figure 3.18 in which RBCs transport has not been modeled). If a greater Lp is considered, these coupled phenomena may become relevant to the point of producing significant variations when modeling a single vessel. However, by using parameter values depicting physiological conditions, these effects have a lower magnitude than the Zweifach - Fung effect.

The last considered test on vessel permeability is more complex than the abovementioned cases. Indeeed, it comprehends the Fåhraeus - Lindqvist effect, Zweifach - Fung

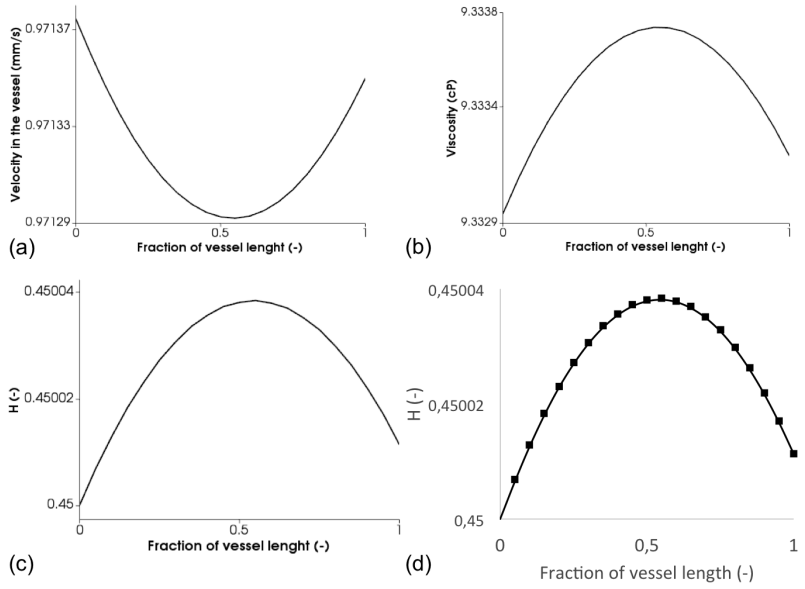

Figure 3.21: *Results of the test to consider the effect of the filtration on the hematocrit. Velocity (a), viscosity (b), and hematocrit (c) profile along the vessel are shown. The agreement between the analytic and the numerical solution is reported in (d).*

effect and the capillary wall permeability. A network with a physiological capillary density has been created ($\simeq 7000\, m^{-1}$) by stacking different Voronoi networks as described in the section 3.5. Results are shown in figure 3.22. The hydraulic pressure within the network decreases from the arteriolar (i.e. $\simeq 32\, mmHg$) to the venular end ($\simeq 15\, mmHg$), as expected. This variation of pressure through the capillary bed influences the pressure in the interstitial space, as shown in the middle left panel by the slice of the interstitial pressure field. Close to the arteriolar end of the network, an increased interstitial pressure level is visible, while it decreases below average next to the venules. The subsequent number of junctions intensifies the overall influence of the Zweifach - Fung effect, leading to a large heterogeneity of hematocrit. The blood velocity (shown in the top right panel) is not uniformly distributed and several branches are characterized by a flow rate that is significantly lower than the average. Apparent viscosity is less heterogeneous, in agreement with the observations of Figure 3.14.

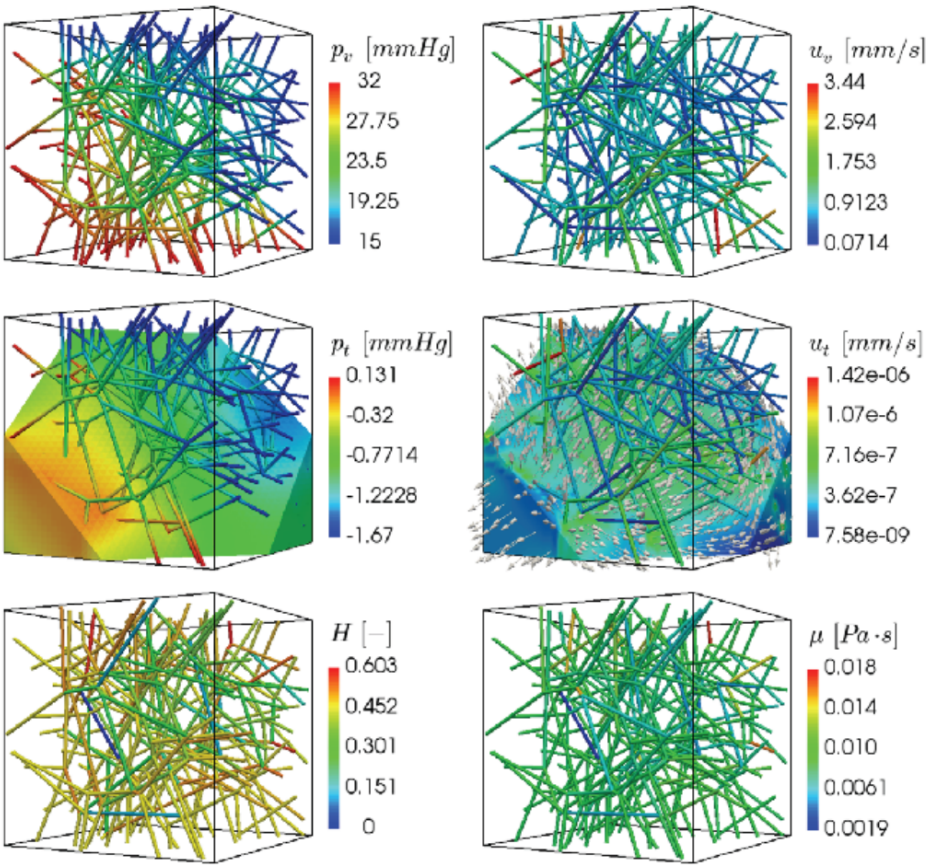

Figure 3.22: *Visualization of the flow in a complex network interacting with the interstitial volume, as reported in Possenti et al. [206]. In particular, the panels show: the pressure drop along the network (top left); the velocity magnitude (top right); the pressure variation along a slice of the interstitial volume combined with the pressure in the network (middle left); the velocity field along a slice of the interstitial volume (the vectors show the direction and the colors the magnitude, middle right); the hematocrit distribution in the network (bottom left); and the effective viscosity (bottom right).*

3.6.4 Vessel curvature

Up to this section, only straight vessels have been considered. However, the model has been derived accounting also for the curvature of the vessel. To analyze the effect of the curvature, a simple test case has been considered. A small portion of a capillary has been used (i.e. $100\mu m$) with one straight and two curved configurations (figure 3.23). These

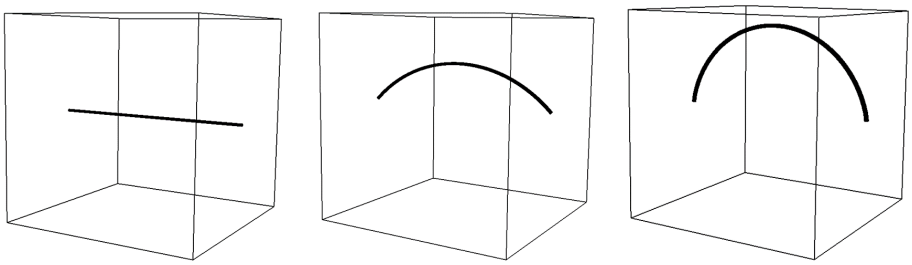

Figure 3.23: *Geometry used for the curved vessel test. From the left: straight vessel, vessel with* $\kappa R = 0.06$ *and* $\kappa R = 0.11$.

have been computed to obtain a constant curvature along the vessel, namely a circular arch, such that $\kappa R = 0.06$ and $\kappa R = 0.11$. The length of the vessels is the same in all the three cases. Since a small portion has been considered, boundary conditions are the same adopted before for a similar case. Therefore, a difference of pressure of $3.5\, mmHg$ has been applied. Considering impermeable vessel that is $L_p = 0$, the velocity is constant along the vessel and the solution of the straight vessel coincides with the Poiseuille case already computed. For the other cases, by the theoretical prediction, lower velocities are expected with an increase of the curvature:

$$\boldsymbol{u}_v(s) = \frac{\boldsymbol{u}_v(s)|_{\kappa=0}}{1+\kappa^2 R^2}\,.$$

A comparison between the theoretical prediction and the results of the model is shown in figure 3.24. The numerical solution well reproduces the theoretical prediction. In particular, the velocity results constant, and it decreases with higher curvature, as expected. A comparison for the two curved cases has also been conducted with a standard computational approach by finite volume method [220] using as solver ANSYS Fluent® (ANSYS Inc., Canonsburg, PA). Therefore, 3D domains have replicated for the two curved configurations. At the ends of the domain, the vessels have been extended in order to apply boundary condition far from the region of interest. Vessels have been discretized by hexahedral elements ($\simeq 3 \times 10^5$). After a mesh sensitivity analysis, a velocity inlet condition has been set using the value obtained from the 3D-1D model, allowing the comparison

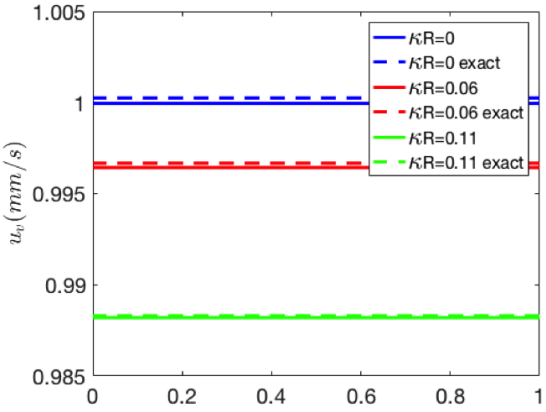

Figure 3.24: *Comparison of the velocity profile in a straight vessel, a vessel with* $\kappa R = 0.06$ *and* $\kappa R = 0.11$*, as shown in Possenti et al. [206]. Continuous lines show model result, whereas dotted line theoretical prediction.*

of the pressure difference driving the flow in the curved part of the network. Given this problem setup, the expected pressure difference at the ends of the curved portion of the vessel is $3.5 mmHg$. Data from the 3D model (figure 3.25) resulted in agreement with those of the 3D-1D model as reported in the table 3.7. In particular differences in the Δp are low, about 1-2 %.

Table 3.7: *Comparison between the classical 3D CFD approach and the proposed 3D-1D approach.*

κR	0.06	0.11
$\boldsymbol{u}_v\|_{3D-1D}$ (mm/s)	0.9964	0. 9880
$\Delta p_v\|_{3D-1D}$ (mmHg)	3.50	3.50
$\boldsymbol{u}_v\|_{CFD}$ (mm/s)	0.9964	0. 9880
$\Delta p_v\|_{CFD}$ (mmHg)	3.47	3.44
$Error \Delta p_v$ (%)	0.4	1.8

In addition, those simulations support the assumptions made when deriving the model. Indeed the axial velocity is clearly the dominant velocity, as shown in the figure 3.26 by comparing the velocity magnitude and the axial velocity. Consequently, as shown in the

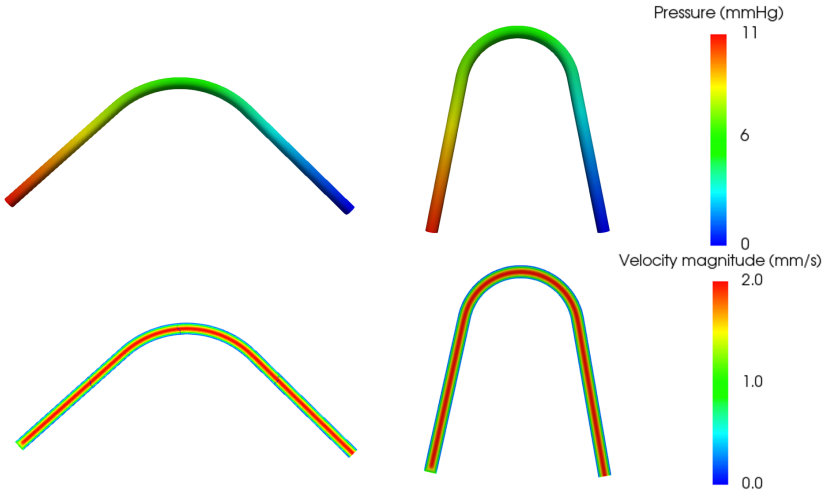

Figure 3.25: *Results of the 3D model solved by finite volume method. On the left the geometry characterized by $\kappa R = 0.06$, and $\kappa R = 0.11$ on the right. The top line shows the distribution of pressure, whereas the bottom line shows the velocity distribution.*

same figure, the pressure is almost constant over the cross-section. These two observations validate the assumption of dominant axial velocity on which the model for curved vessels has been built.

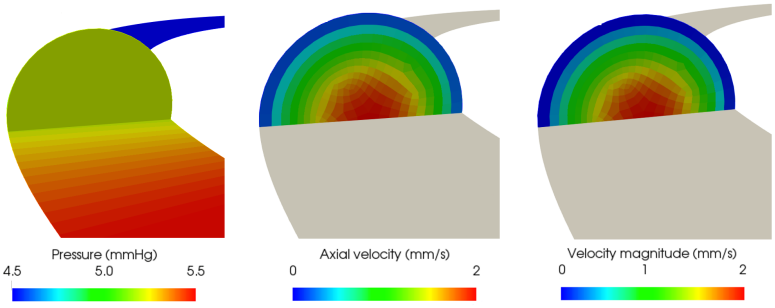

Figure 3.26: *Section of the 3D model. From the left: pressure, axial velocity, and velocity magnitude. Contours show constant pressure over the cross section and negligible differences between axial and magnitude velocity.*

3.6.5 Lymphatic modeling

Last tests have been performed to analyze the lymphatic drainage modeling. To this aim, 2 different formulations have been compared: (i) a linear formulation, i.e. based on classical Straling's equation neglecting osmotic differences across the lymphatic membrane; (ii) the proposed non-linear formulation. For the linear formulation, two different values of L_p have been considered. To guarantee meaningful results, a correct S/V ratio must be used to define the vasculature. For clarity, a simple hexagonal network has been chosen, and repeated within a $500\,\mu m$-side cube, in order to obtain the proper S/V ratio. This unit has been arranged on parallel horizontal planes along two orthogonal directions to avoid perfect alignment of the network. Higher-pressure ends have been kept in two adjacent faces of the tissue sample, creating high and low p_v zones. Considering the coupling with interstitium, such pressure conditions shape areas where filtration from the network is mainly expected, and others (close to venular ends) in which absorption of fluids happens. For the boundary $\partial\Omega$, namely the boundary of the interstitial domain, a *no-flow* condition has been set by using homogeneous Neumann conditions. Doing so, equilibrium conditions have been addressed, in which no volume is accumulated within the tissue. Thus, if we consider $\mathbf{n}$ the normal vector to $\partial\Omega$, the condition is:

$$\mathbf{u_t} \cdot \mathbf{n} \;=\; 0 \qquad on\ \partial\Omega\,.$$

Different working points have been modeled to observe the behavior of the lymphatic drainage modeling. Consequently, physiological and uremic conditions are reproduced by the parameters (table 3.8). The choice of these parameters will be further discussed in the chapter 4. In this test, the viscosity of blood has been considered constant, i.e. the heterogeneity of the RBCs distribution has not been included. A total of six cases have been simulated, combining the 3 models with the 2 conditions addressed, as summarized in the table 3.9. Consequently, the following cases have been defined:

- CASE A: physiological conditions with a linear lymphatic drainage formulation using the maximum slope of the non-linear function (green line in figure 3.27);
- CASE B: physiological conditions with a linear lymphatic drainage formulation considering the slope defined by Chamney et al. [56] (red line in figure 3.27);
- CASE C: physiological conditions with the proposed non-linear lymphatic drainage formulation - (blue line in figure 3.27);
- CASE D: pathological conditions (uremia) with a linear lymphatic drainage formulation considering the maximum slope of the non-linear function;

Table 3.8: *Values of the parameters used in the analysis.*

Symbol	Parameter	Physiological conditions	Ref.	Pathological conditions	Ref.
L	Average capillary length (m)	5×10^{-4}	[218]	5×10^{-4}	[218]
R	Average capillary radius (m)	4×10^{-6}	[5]	4×10^{-6}	[5]
k	Hydraulic conductivity of the tissue (m^2)	10^{-18}	[71, 162]	10^{-18}	[71, 162]
μ_t	Interstitial fluid viscosity $(Pa\,s)$	1.2×10^{-3}	[71]	1.2×10^{-3}	[71]
H_d	Discharge hematocrit $(\%)$	45	[5]	35	[200, 201]
μ_v	Blood viscosity $(Pa\,s)$	9.3×10^{-3}	[98]	7.2×10^{-3}	[98]
σ	Capillary wall reflection coefficient (-)	0.95	[219]	0.75	[127, 219]
$\Delta\pi$	Oncotic pressure gradient $(mmHg)$	25	[194]	19	[54, 200, 201]
S/V	Density (m^{-1})	7000	[199]	4900	[183, 199]
L_p	Capillary wall hydraulic conductivity $(m^2\,s\,kg^{-1})$	10^{-12}	[162]	8.8×10^{-12}	[127]

- CASE E: pathological conditions (uremia) with a linear lymphatic drainage formulation considering the slope defined by Chamney et al. [56];
- CASE F: pathological conditions (uremia) with the proposed non-linear lymphatic drainage formulation.

Necessary parameters to define the non-linear model have been adopted as described in the section 3.2.3. Conversely, the parameters $S/V|_L L_{p,L}$ and p_l have been computed as follow. First, $S/V|_L L_{p,L}$ has been defined as the slope of: (i) the linear portion of the function reported by [56], for CASE A and CASE D; (ii) the maximum slope of the sigmoid function, for CASE B and CASE E. Then, p_L has been determined in both the cases, so that the physiological working point (i.e. $p_l = -1\,mmHg$ and $\phi_{lymphatics} = 2\,ml/min$ in the figure 3.27) belongs to the linear function.

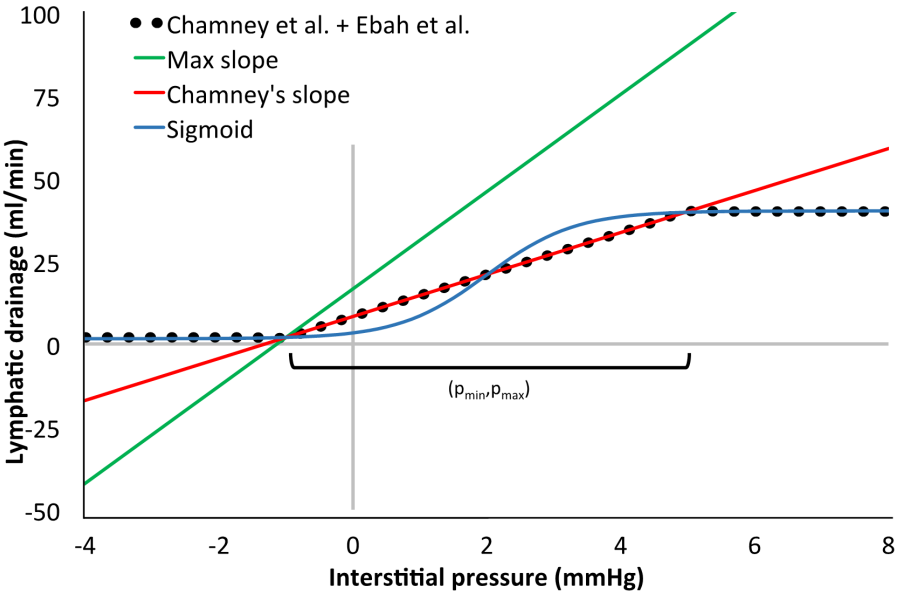

Figure 3.27: *Lymphatic drainage formulations as a function of interstitial hydraulic pressure, as shown in Possenti et al. [221]. Formulation of Camney et al. [56] adapted to match interstitial pressure at the working point reported by Ebah et al. [30] - dotted black line. Linear formulation (by means of Starling's principle) with lymphatic wall hydraulic conductivity equal to the maximum slope of non-linear function - green line. Linear formulation with lymphatic wall hydraulic conductivity as Chamney et al. [56] - red line. Proposed sigmoid formulation - blue line. Flow rate values are scaled up to the overall extra vascular reference volume equal to 39 l [5]*

Table 3.9: *Summary of the analyzed cases.*

Lymphatic drainage description	Physiological conditions	Pathological conditions *(Uremia)*
Maximum slope (linear)	CASE A	CASE D
Mean slope (linear)	CASE B	CASE E
Non-linear	CASE C	CASE F

Results of the simulations have been evaluated in terms of three variables:

- interstitial fluid pressure (p_t), expressed in $mmHg$;
- lymphatic drainage ($\varphi_{lymphatics}$), expressed in percentage of the maximum admissible value reported in literature [5, 56];
- vessel to tissue net flow rate (NFR) of fluids, expressed in ml/min; NFR results are scaled up so that they represent the whole extra-vascular volume in the body [5].

These three variables are presented in terms of both spatial distribution and average values, which have been computed as an integral mean over the considered domain. When using the linear modeling approach, the lymphatic system acts by keeping the interstitial pressure as close as possible to p_l, even if a back-flow is required (figure 3.28). Interestingly, the higher $L_{p,LF}$ is, namely the hydraulic conductivity of the lymphatic capillary wall, the larger back-flow zones are (i.e. comparing CASE A and B). Specifically, a higher $L_{p,LF}$ allows for an emphasized action of the lymphatic system (local maximum drainage CASE A: $19\,\%$, CASE B: $13\,\%$), resulting in a lower variation of interstitial pressure. By considering a *non-linear* function, back-flow is prevented in CASE C. Consequently, this case yields different results compared to the two above mentioned cases, in terms of both interstitial pressure and NFR with averaged differences bigger than $10\,\%$.
The second analyzed working point, depicting uremic conditions (i.e. CASE D, E and F), results in higher interstitial pressures $3.5\,mmHg$ and $5.9\,mmHg$ (table 3.10). Consequently, the working point is located in the right part of the figure 3.27. In these cases, no back-flow is reported. On the other hand, in some areas, a net lymphatic flow rate obtained was too intense. It is greater than the expected 20-fold increase compared to physiological conditions [5, 56] and it is highlighted by *grey color*. This phenomenon is present only when using *linear model*. Again, a greater $L_{p,LF}$ produces a lower variation

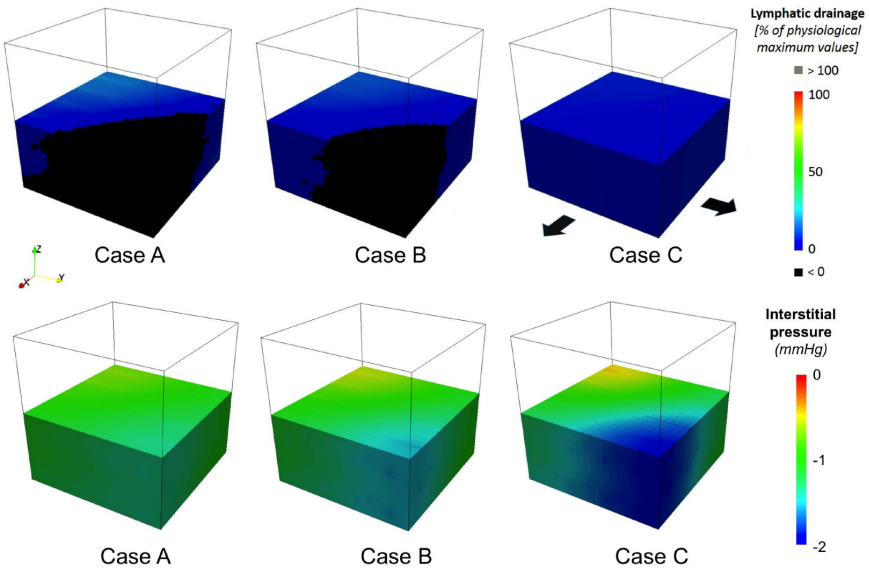

Figure 3.28: *Lymphatic drainage (top) and interstitial fluid pressure (bottom) for physiological conditions considering the three different formulations, as shown in Possenti et al. [221]. Contours are shown on half the domain* Ω *(identified by the black wire box). Negative lymphatic drainage, that is lymphatic non-physiological behavior, is marked in black. Direction of flow within the vascular network is the same for all the presented cases, and it is indicated by the arrows in the top right case.*

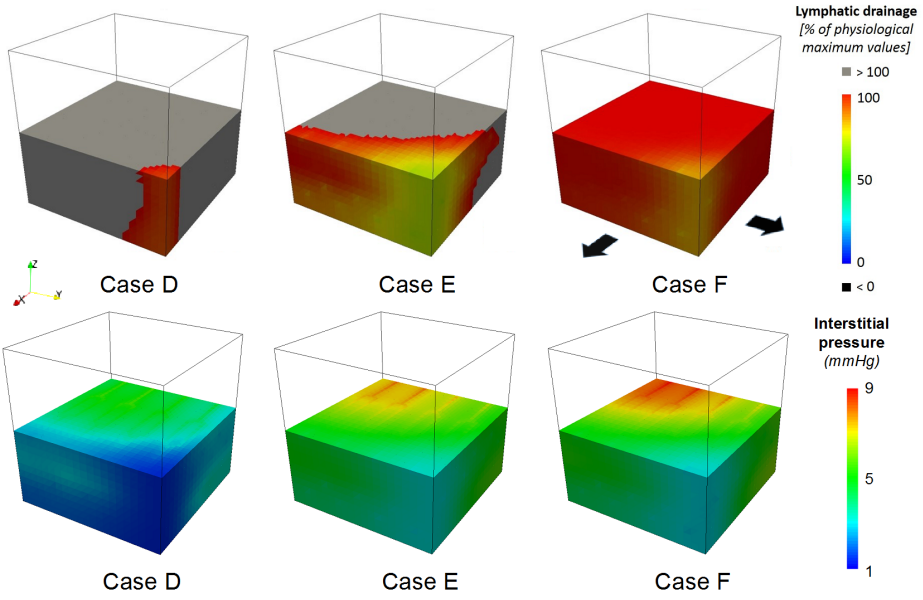

Figure 3.29: *Lymphatic drainage (top) and interstitial fluid pressure (bottom) under pathological conditions is considered for the three different formulation, as shown in Possenti et al. [221]. Contours are shown on half the domain* Ω *(identified by the black wire box). Excessive drainage, that is lymphatic non-physiological behavior, was marked in grey. Direction of flow within the vascular network is the same for all the presented cases, and it is indicated by the arrows in the top right case.*

Table 3.10: *Averaged results for both physiological and pathological conditions, as reported in Possenti et al. [221]. Physiological conditions in the upper part of the table (*CASE A*,* CASE B *and* CASE C*), and pathological conditions at the bottom (*CASE D*,* CASE E *and* CASE F*). Net filtration rate (NFR) is scaled to indicate the value for the whole extra-vascular volume in the body [5]. Percentage variations are taken with respect to simulation with the proposed non-linear formulation (*CASE C *and* CASE F*).*

Physiological	CASE A	CASE B	CASE C
$p_t\ (mmHg)$	-1.02	-1.04	-1.17
	+13 %	+11 %	-
$NFR\ (ml/min)$	1.64	1.69	1.96
	-16 %	-14 %	-
Pathological	CASE D	CASE E	CASE F
$p_t\ (mmHg)$	3.53	5.58	5.91
	-40 %	-6 %	-
$NFR\ (ml/min)$	68.3	43.7	39.6
	+72 %	+10 %	-

of interstitial pressure from the value of p_l (figure 3.29, CASE D vs E). On the other hand, similarities in the interstitial pressure are found when analyzing CASE E and F (table 3.10) if considering averaged values. This is due to the proximity of the two curves for pressure around $5.5\,mmHg$ (figure 3.27). As a general observation, *linear* models can be used as an approximation of a *non-linear* phenomenon in precise working conditions. However, in the proposed model the right conditions for the linearization cannot be identified, due to the spatial variation of p_t. Because of the filtration/absorption, an interstitial pressure gradient has been induced by the pressure gradient inside the network. For these reasons, a *non-linear* modeling approach is necessary to model fluid homeostasis at the microscale. Indeed, even if mean values may look similar for interstitial pressure in table 3.10, the spatial distribution is different as shown in figure 3.28 and 3.29. These local differences and effects are not negligible when trying to accurately describe homeostasis within the microenvironment.

As a remark, the contribution of lymphatic nodes in fluid reabsorption can be included in the model. In particular, since the estimate of $2\,ml/min$ for the whole body is based

on thoracic duct flow, their inclusion would result in a greater lymphatic drainage. Taking reference values from the literature (e.g. $5.5\,ml/min$ from [34]) and assuming that the 20-fold increase still holds true, the lymphatic drainage function can be redrawn. Doing so, all the three functions considered in the analysis change by a factor k equals to the ratio of the reference values ($5.5/2 = 2.75$). The physiological reference condition under these conditions ($p_t \simeq -1\,mmHg$, and $\phi_{lymphatics} \simeq 5.5\,ml/min$)is reached by prescribing $36\,mmHg$ and $15\,mmHg$ and the inlet and outlet ends of the vascular network, namely within the ranges defined in [34]. Additional numerical simulations (not shown in these work) obtained by modifying these parameters support the conclusion that the different value for the lymphatic drainage does not affect qualitatively the results. On the other hand, some quantitative difference are present, but the resulting value of the interstitial pressure are still within the experimental range defined by [30]. As a consequence, the conclusion of the present research are not affected by such a modification. A deeper investigation on parameters value, along with the inclusion of the glycocalyx on filtration, will represent one of the next points toward the development of a more detailed model. Future work should deal with the set up of a suitable methodology for parameter estimation, also considering different types of tissue.

CHAPTER 4

Use of the 3D-1D model under uremic conditions

In this chapter two applications of the 3D-1D model are presented. First, the application to uremic microcirculation is discussed and then a sensitivity analysis is described. Finally, the chapter ends with a general discussion of the results and the two applications of the model. A portion of the content of this chapter has been also included in the work:

- *'Computational modeling of the interaction of lymphatic and vascular microcirculation in uremia', by Possenti et al., presented at the GNB2018 conference.*

4.1 Uremic microvasculature

The 3D-1D model described in the previous chapter has been used to simulate physiological and uremic microcirculation. The aim of this simulation is to analyze the fluid balance in the micro-environment with reference to the uremic pathology. As further described in the first chapter, microvascular changes due to uremic pathology are still not fully understood, and neither their role in the development of the pathology. In this framework, a computational tool able to describe phenomena at the microscale is useful to understand them. In particular, coupled with *in vitro* models, such computational approach enables a step-by-step process which may eventually lead to a deeper understanding of the involved phenomena.

4.1.1 Methods

The method used in this section is presented describing: geometries, parameters and considered output variables.

Geometries To model the effects produced by pathological microvascular alterations, the 3D-1D model has been used to describe a representative healthy and uremic microvasculature. Therefore, two artificial networks have been generated as described in the previous chapter, in order to depict two different S/V ratios. Different values of capillary density, namely the S/V ratio, can be found in literature showing the variability among tissues, subjects, and species. In an interesting study, Ebah and colleagues [30] have reported data of interstitial pressures for both healthy and uremic patients, showing an increase of pressure related to fluid accumulation, with reference to the subcutaneous tissue. Therefore, in our model, we consider the subcutaneous tissue as a reference. The capillary density is often addressed by different measure techniques such as the number of vessels in a region of interest (2D or 3D). The value reported by Baxter and Jain in their study [199] has been adopted as reference for the healthy tissue: $S/V = 70\,cm^{-1}$. Then, since microvascular impairment has been observed both in animal studies and in uremic patients reporting a lower capillary density, S/V under uremic conditions should be lower. The work of Amann and colleagues has been considered to compute this value [183], since they directly report the capillary density alteration by the S/V ratio. By comparing the values they reported, a reduction of about the 30% has been computed. Consequently, the S/V ratio under uremic conditions has been set to $49\,cm^{-1}$. The two considered geometries are shown in the figure 4.1. To complete the vascular description, the pressure boundary conditions have been set as $32\,mmHg$ and $15\,mmHg$ for both cases, and the arteriolar and venular ends have been arranged as in figure 4.1. The computational setup

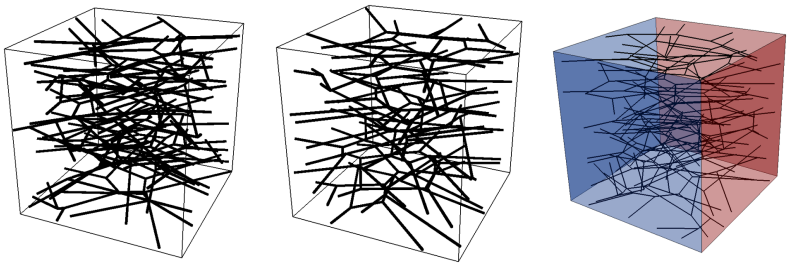

Figure 4.1: *Geometries for the healthy and the uremic conditions. On the left: healthy condition.* $S/V \simeq 70\,cm^{-1}$. *Center: uremic condition.* $S/V \simeq 49\,cm^{-1}$. *On the right: boundary conditions arrangement; faces highlighted by red color correspond to arterial ends of the network, blue to venular ends.*

has been similar to the one used for lymphatic drainage test cases. The two vascular networks have been modeled within a cubic domain Ω, with a side of $500\mu m$. The boundary of the interstitial domain are considered closed, namely, no fluid can exit from the domain through the face of the cube. Such a setup allows the description of the equilibrium condition, in which fluid is not accumulated within the tissue.

Parameters All the parameters used for this simulation are shown in the table 4.1. Five parameters have been changed between healthy and uremic microvasculature: (i) H, and consequently μ_v; (ii) σ; (iii) $\Delta\pi$; (iv) S/V; and (v) L_p. The alteration of S/V has already been discussed. The change in H has been set replicating the change in blood hematocrit available from clinical data [5, 200, 201]. The apparent reduction in the RBCs content is mainly caused by an increase of the plasma volume, which induces a dilution of all the blood content. For the same reason, the protein concentration in the blood is lower, leading to a lower difference of oncotic pressure π. Since direct measurement of the interstitial fluid pressure in healthy subject and uremic patients is challenging, the estimated value given by the computational model of [53] has been used. Their model is based on clinical data, and by means of a compartmental approach, it provides an estimate of compartmental volume and fluid concentration. The data they reported have been used to set $\Delta\pi$, which in the model is not a function of the spatial coordinate. The other two changed parameters regard capillary membrane properties. Uremic toxins may affect those properties, as shown by Harper and colleagues [127]. They studied the alteration of L_p and σ by means of an animal model perfused with plasma from both a normal subject and a uremic patient. Doing so, they addressed the change of these parameters due to the overall effect of the uremic toxins accumulated in the blood (hundreds of solute, chapter 1). The relative

Table 4.1: *Values of the parameters used in the uremic alteration analysis.*

Symbol	Parameter	Physiological conditions	Ref.	Pathological conditions	Ref.
L	Average capillary length (m)	5×10^{-4}	[218]	5×10^{-4}	[218]
R	Average capillary radius (m)	4×10^{-6}	[5]	4×10^{-6}	[5]
k	Hydraulic conductivity of the tissue (m^2)	10^{-18}	[71, 162]	10^{-18}	[71, 162]
μ_t	Interstitial fluid viscosity ($Pa\,s$)	1.2×10^{-3}	[71]	1.2×10^{-3}	[71]
H	Inlet condition for hematocrit ($\%$)	45	[5]	35	[200, 201]
μ_v	Blood viscosity ($Pa\,s$)	9.3×10^{-3}	[98]	7.2×10^{-3}	[98]
σ	Capillary wall reflection coefficient (-)	0.95	[219]	0.75	[127, 219]
$\Delta\pi$	Oncotic pressure gradient ($mmHg$)	25	[194]	19	[54, 200, 201]
S/V	Density (m^{-1})	7000	[199]	4900	[183, 199]
L_p	Capillary wall hydraulic conductivity ($m^2\,s\,kg^{-1}$)	10^{-12}	[162]	8.8×10^{-12}	[127]

change reported by the author has been considered to model L_p alteration. As a consequence, the healthy reference value for L_p, 10^{-12} [162], has been corrected by a factor 8.8, resulting in 8.8×10^{-12}. They reported also a decrease of the reflection coefficient of the capillary membrane, i.e. the ability of the membrane to keep plasma protein inside the vasculature. Thus, the parameter σ has been decreased in the uremic model. However the value reported in their study was very low (0.53), and in particular lower than the human ranges defined by Levick [219] for this parameter: $0.75 - 1$. Therefore, the lower value of this interval has been chosen for the analysis. Since no data have been found concerning changes of the other parameters, those have been kept unchanged under the two conditions. In addition, also the same lymphatic system description has been used under both the simulated conditions.

Output variables considered Results of the two simulations have been shown in terms of averaged values and spatial distribution of the variable considered. As previously done for the lymphatic test case, the averaged interstitial fluid pressure (p_t) and the vessel to tissue net flow rate (NFR) of fluids have been considered. Moreover, spatial heterogeneity of velocity, hematocrit, and viscosity have been discussed. One of the advantages of a computational approach is that it allows an easy outline of the effects of different parameter variations. Therefore, five additional simulations have been run, changing one parameter at a time, to show their respective effect on the interstitial pressure and the NFR. Concerning pressure, variations of the output have been computed as:

$$p_t|_{var,i} = p_{t,i} - p_{f,physiological} \, .$$

Conversely, the variation of NFR have been normalized as follows:

$$NFR|_{var,i} = \frac{NFR_i - NFR_{physiological}}{NFR_{physiological}} \, .$$

4.1.2 Results

Spatial distribution of interstitial pressure, lymphatic drainage, hematocrit H, and blood velocity are shown in figure 4.2. Under both the two conditions analyzed, a gradient in the interstitial pressure has been reported. Such gradient reflects the gradient of existing pressure within the vasculature, i.e. from the arteriolar to the venular ends. Indeed, the two domains Ω and Λ are coupled because of the semi-permeability of the capillary membrane. In particular, the vascular pressure is determined by the boundary conditions applied, the network morphology and the consequent flow rate. On the other hand, the interstitial pressure is determined by the interactions with both the vascular network (i.e. filtration and absorption) and the lymphatic system. Despite the pressure within the network has been

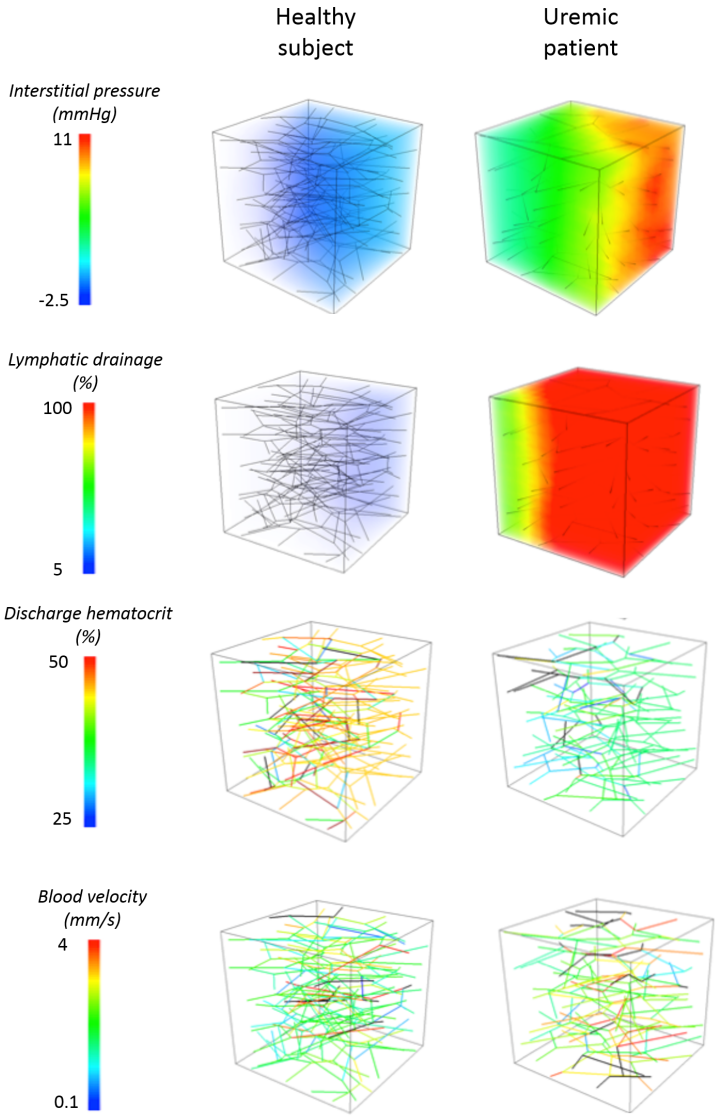

Figure 4.2: *Results under both healthy and uremic conditions. First row: interstitial pressure* ($mmHg$)*. Second row: lymphatic drainage expressed as percentage of* ϕ_{max}*. Third row: hematocrit within the vasculature. Fourth row: blood velocity* (mm/s)*. For velocity, black color highlights vessel with velocity greater than* $4\,mm/s$*. For hematocrit, out of range vessel are identified by black if* $H < 25\%$*, or by deep red if* $H > 50\%$*.*

set at the same values under the two conditions and the lymphatic drainage formulation is the same, different values of the interstitial pressure have been reported in the uremic case. Thus, the variation of the parameters affects the interstitial pressure, leading to an increase with respect to physiological conditions. Also, the spatial gradient of pressure is greater under pathological conditions. This is also confirmed by the larger velocity magnitude within the interstitium. Under uremic conditions, the model predicts a 3.7-fold increase of the u_t median value. In addition, the increase in interstitial pressure is in agreement with the *in vivo* data reported in [30] (figure 4.3). They have reported a mean interstitial

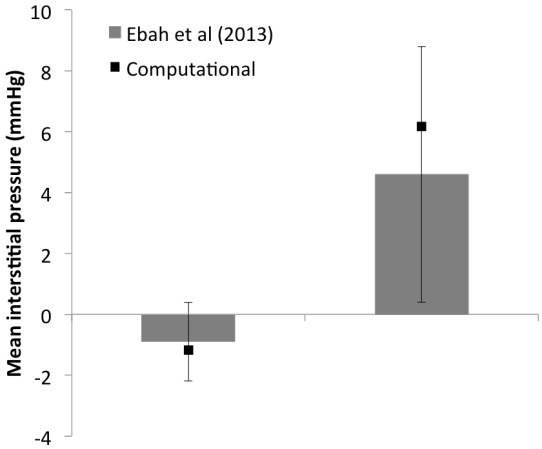

Figure 4.3: *Comparison of the average interstitial pressure between the 3D-1D model and in vivo data reported by [30]. Grey bars show the mean value reported by the authors, along with the standard deviation by means of error bar. Computational results are shown by black squares.*

pressure for healthy subject equal to $-0.9 \pm 1.3\, mmHg$. The averaged value, namely the integral mean over the domain Ω, for p_t in our model is $-1.2\, mmHg$. Such value is close to the mean *in vivo* value, and it falls in the experimental range. Interestingly, the increase of pressure reported by the model is in agreement with the increase of pressure described in the same work. The model has resulted in $6.2\, mmHg$, namely falling within the range $4.6 \pm 4.2\, mmHg$. Consequently, considering all the variability between subjects and intra-subjects, the increase of interstitial pressure described experimentally has been well reproduced by the model.

Regarding the NFR, results agree with the physiological data after a scale up to match the total interstitial volume (the inverse operation performed when computing lymphatic parameters). The reference data is $2\, ml/min$ and the model results in a very close NFR:

$2.09\,ml/min$. Moreover, when modeling pathological conditions, a greater NFR has been reported. Such a greater filtration is balanced by the lymphatic system, since no flow is allowed to leave the domain Ω by the boundary of the cube. Therefore, the increase of both the NFR and the lymphatic flow rate in the cube is expected to be lower than a 20-fold increase, as described in the first chapter. Indeed, comparing healthy and uremic conditions an 18-fold increase has been found, namely within the prescribed boundaries.

Results on the domain Λ, i.e. the vascular network, are characterized by a great spatial variability, which can be addressed in term of velocity, hematocrit and viscosity (data not shown). In particular, the magnitude of the velocity (mm/s) is in agreement with the expected values. However, it is quite variable with values that span over an order of magnitude. Black vessels in the plot report vessel with velocity greater than $4\,mm/s$. A similar heterogeneity characterizes the hematocrit distribution. In the figure 4.2, the limits of the contours have been limited to the interval $25\% - 50\%$ to make the reader appreciate this variability. However, some of the vessels are out of such interval and they have been highlighted with black if $H < 25\%$, or with deep red if $H > 50\%$. Therefore, a variability of velocity, hematocrit, and viscosity has been obtained. This variability, related also to the heterogeneity of the radii within the vascular network, is a consequence of the interdependence of those parameters, and it would be hardly predicted without considering the non-linear phenomena in between them.

Effect of parameters alterations in terms of average interstitial pressure and NFR are shown in figure 4.4 and 4.5. The increase of interstitial pressure and NFR previously discussed can be observed by looking the last column on the right, . In addition, starting from the physiological conditions the contribution of each parameter has been highlighted by setting one parameter at a time as under uremic conditions. One first consideration compares between the single effects and the overall effect, i.e. uremic conditions. Indeed the sum of the variations produced by single parameter alterations is not equal to the overall variation. Secondly, the most influencing parameters are the $\Delta\pi$, σ, and L_p. These parameters are related to the capillary membrane and the oncotic pressure difference across it. The other two variables (H and S/V) appear to have a minor effect on the two output variable considered under these conditions.

4.1.3 Discussion

Results have highlighted an increase of both the lymphatic drainage and the interstitial pressure. This is consistent with the fact that the interstitial pressure determines the lymphatic drainage. Indeed, considering the "lymphatic drainage - interstitial pressure" plot, two different working ranges can be identified (figure 4.6). Under pathological conditions, the working range of interstitial pressure is shifted towards greater pressure with respect

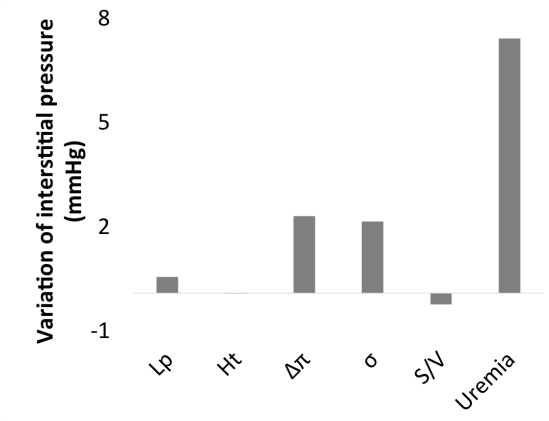

Figure 4.4: *Variation of the average interstitial pressure due to alterations of the input. One parameter at a time has been set equal to pathological condition while the others are kept equal to the physiological values. Last column on the right shows uremic condition, namely all the parameters have been varied.*

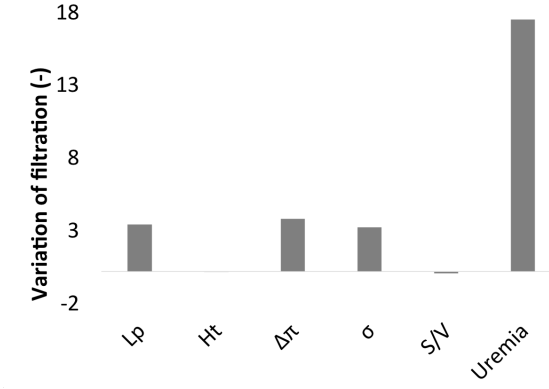

Figure 4.5: *Variation of the net filtration rate due to alterations of the input. One parameter at a time has been set equal to pathological condition while the others are kept equal to the physiological values. Last column on the right shows uremic condition, namely all the parameters have been varied.*

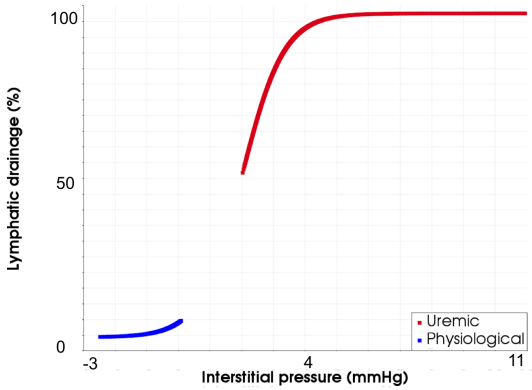

Figure 4.6: *Working conditions under physiological and uremic conditions shown on the lymphatic drainge - interstitial pressure graph.*

to physiological conditions. As discussed, greater interstitial pressure is in agreement with data reported by [30]. A variation of the lymphatic flow rate has also been reported by [55] in their model. Based on a compartmental approach, they have estimated several parameters to describe fluid balance in uremic patients. Half of the patients they studied have a greater lymphatic drainage with respect to the basal value they use. However, it should be considered that they have identified also the value of the capillary pressure p_c, namely the averaged capillary pressure. Instead, the pressure in the vasculature has not been changed in the presented model. In the same work, an increase of L_p has also been identified by using the same model on all the patients. Certainly, the variability among patients is very high, but the increase is consistent in all of them. Authors have concluded that such an increase of L_p may be related to an inflammatory process, consistently with data reported in literature regarding uremic toxins.

In addition, comparing this computational test with a simpler one, which has been conducted with a hexagonal structure network for the vasculature, some differences have been found. Therefore, even if the described phenomena are qualitatively the same, the morphology of the network has affected not only the local distribution but also the averaged interstitial pressure and NFR. For example, the increase in the NFR was greater with a simpler network, $\simeq 20-$fold increase. This can be related to spatial heterogeneity of the Voronoi-based network which affects the filtration (as discussed in the test case, chapter 3). Therefore, these results seems to justify the greater effort toward the understanding of the morphological changes under pathological conditions. Indeed, spatial heterogeneity seems to affect both the local fluid dynamics and the overall exchange of fluid.

Concerning the alterations of the parameters, interactions between them have been highlighted by the fact that the overall variation is not equal to the sum of output alterations produced by a single parameter variation. Indeed, considering one vessel, the NFR can be written as:

$$\int_{\Lambda_i} 2\pi R_i(s) L_p \Big((\overline{p}_v - \overline{\overline{p}}_t) - \sigma(\pi_v - \pi_t) \Big) ds \,. \tag{4.1}$$

As a consequence, simultaneous alterations of L_p, σ and $\Delta\pi$ will produce a greater effect on filtration, amplifying the effect of each single variation. Also the parameter S/V is related to them by the same formula. Indeed the integral has been computed over the domain Λ, consequently including also the number of vessels and their radius, i.e. including the lateral surface area. One advantage of the presented model with respect to a compartmental one is that it accounts for spatial variability. Consequently, $\overline{p}_v = \overline{p}_v(s)$ and $p_t = p_t(\boldsymbol{x})$. Therefore, even two morphologically different networks, characterized by the same S/V (i.e. comparison of this case with the simper hexagonal structure), may result in different NFR. However, *in vivo* one of the main differences due to morphology and density of the network is the distance between cells and the vasculature. A longer distance to travel for nutrients, e.g. oxygen, results in a less efficient exchange. Such low efficient delivery of nutrients can be associated with the development of skin defect, or more important with organs damage in CKD patients. Therefore, the oxygen transport in both the domain Λ and Ω will be an interesting future improvement of this model. At this point, the low impact of hematocrit variation on filtration should be discussed. A variation of H directly affects the apparent viscosity and therefore the viscosity μ_v. However, since boundary conditions of the problem have been defined in terms of pressure, a change of viscosity does not change the pressure profile along the network. For example, with reference to a single straight capillary modeled with this boundary conditions, a change of viscosity produces a change in the flow rate and negligible effect on the pressure profile. The interaction with the lumped parameter model (chapter 2) enabled by this work may overcome this limitation, by considering the variations of pressure boundary conditions due to H variations, with a more global approach. In particular, without considering filtration, the latter effect would be null. As a consequence of this setup, the variation of hematocrit eventually produces a higher flow rate within a single network that in some cases can reach also $\simeq 40\%$ of difference. However, this comparison is affected also by differences between single networks, resulting in a great heterogeneity when comparing networks one-to-one. This tendency to have an increased flow rate in a unit of the network (i.e. a single Voronoi network of the stacked group) is not sufficient to guarantee a greater overall flow rate. Indeed, with a more consistent comparison, the overall flow rate can be compared, namely considering all the modeled vasculature and therefore the different S/V ratio. Doing so, the flow rate under uremic conditions is lower than in physiological conditions, reporting a $\simeq 16\%$ reduction.

This is consistent with the available literature data depicting possible vascular impairment in terms of both reduced capillary density and reduced blood flow. Regarding the effects of parameter alterations, the most important parameters are the oncotic pressure difference and the properties of the capillary membrane, i.e. L_p and σ. Therefore, the alterations of the capillary membrane induced by uremic toxins have been confirmed as a key variable when modeling fluid balance in uremic patients. Such properties directly affect plasma refilling and solutes compartmentalization, eventually affecting the cardiovascular stability and the efficiency of solutes removal during dialysis. In this framework, the experimental setup can be an important tool (chapter 5).

Despite the complexity of the model in terms of mathematical formulation and of the amount of described phenomena, the model still carries some limitations. First, the inlet pressure has not been changed when modeling uremic conditions. Whether this pressure may change or not under such conditions is not fully understood, even if the role in vascular regulations is known to keep the vascular environment as stable as possible in terms of vascular pressure and perfusion. This type of information can be obtained by future interactions between this model and the lumped parameter model presented in the next chapter. Accounting for vascular alterations, the variability of the capillary pressure can be addressed.

Concerning the lymphatic system, the proposed non-linear model is not tissue-specific. Variability in the lymphatic system (e.g. morphology, vessel density) is expected considering different tissues. However, in order to model them, some tissue-specific data are required. Such data are not easily retrievable, due to difficulties in measurements. In addition, considering the filtration, the classical Starling's principle formulation has been adopted in this study. Doing so, the possible effects of the glycocalyx have not been considered. They may have an impact, in particular they may reduce the absorption of fluids reported close to the venular ends. The inclusion of these phenomena represents an important future improvement to the description of the fluid balance within the microvasculature. However, as a remark, these are not usually included in computational models, as the one proposed in this work. To model the Zweifach - Fung effect, the gold standard empirical formulation, defined by the group of Pries and Secomb [61], has been adopted. Such formulation is not sensible to the angle of the bifurcation, despite the fact that it can affect the RBCs distribution [113]. In addition, the possible inversion of this phenomenon has not been accounted for [114, 115]. Once these phenomena are described by an equation similar to the used one, they can be easily included in the model. Moreover, the rheology of blood has been described with the widely used formulation proposed by [98]. Nevertheless, this formulation is not influenced by the shear rate. This limitation will be further discussed along with the H value in the section 4.3.

4.2 Sensitivity analysis [222]

4.2.1 Introduction to sensitivity analysis

The model presented in the previous section has been analyzed by a sensitivity analysis of the input parameters. The methods of such analysis are presented in this paragraph. Sensitivity analysis may have different aims:

- research prioritization, namely the understanding of which factor is mostly worth further analysis or measurement;
- model simplification, i.e. knowing if some factors have negligible influence on the outputs;
- outline parameters influence on the output, i.e. to build an efficient parameter identification tool;
- test of the robustness of the model and its assumptions in a wide region of the input factors space.

In the presented case, the first and the last aims are the most important. Several methods can be applied to address a sensitivity analysis. One first measure of the sensitivity of a general output Y to variations of an input X_i has been defined as the partial derivative $\partial Y/\partial X$. Dealing with non-analytical models, namely models in which Y cannot be described as a simple and derivable function of X, such derivative is usually approximated by the discrete incremental ratio $\Big(Y(X+\Delta) - Y(X)\Big)/\Delta$. When considering non-linear models, the results of this measure is affected by the point X^* in which the derivative has been computed. As a consequence, this measure is often named as *local*. A different approach has been considered to achieve a more *global* description. It is based on the variance of the output Y, indicated by $V(Y)$ from now on. By fixing a factor $X_i = X_i^*$, namely computing the conditional variance of the output variable Y as $V_{X_{\backsim i}}(Y|X_i = X_i^*)$, a measure of the importance of the factor X_i has be obtained. In particular, the lower the conditional variance is, the more important the factor results. Nevertheless, if expressed in this way, the method is still a *local* measure, i.e. it is still affected by the choice of X_i^*. By taking the average over all the possible points X_i^*, and based on the relation $E_{X_i}\Big(V_{X_{\backsim i}}(Y|X_i = X_i*)\Big) + V_{X_i}\Big(E_{X\backsim}(Y|X_i = X_i*)\Big) = V(Y)$ a *global* measure can be obtained as:

$$S_i = \frac{V_{X_i}\Big(E_{X_{\backsim i}}(Y|X_i)\Big)}{V(Y)}\,.$$

S_i is called the first order sensitivity index, and because of the previous relation it is always included in the interval $[0; 1]$. In particular, the more important a parameter is, the higher S_i will be. For an additive model $\Sigma_i S_i = 1$, namely the variation of the output can be decomposed by separating the single effects of input parameters. Conversely, if interactions between parameters are present, the sum of the first order indexes is not equal to 1. To address interactions between parameters, higher order indexes can be computed. For example, the joined effect of the parameters X_i and X_j can be measured by

$$S_{i,j} = \frac{V_{X_i,X_j}\left(E_{X_{\sim i,j}}(Y|X_i, X_j)\right)}{V(Y)} - S_i - S_j \,.$$

The number of these higher order terms increases with the number of the parameters. The total effect indexes account for the overall contribution related to one parameter, i.e. accounting the interactions with other parameters:

$$S_{Ti} = S_i + \Sigma_j S_{i,j} + \Sigma_{j,k} S_{i,j,k} + \ldots \,.$$

For example, for a model with 3 parameters the total effect is $S_{T1} = S_1 + S_{1,2} + S_{1,2,3}$. Therefore, a $S_{Ti} = 0$ is a necessary and sufficient condition to claim that X_i is not affecting the output variable. Similarly, $S_{Ti} \simeq 0$ means that the parameter has a low influence on the output.

4.2.2 The elementary effect method

Several methods can be used to perform a sensitivity analysis, as described by Cariboni and colleagues. With reference to the graph shown in [223] the proper methodology to use in this case is the Morris' method, known also as *elementary effect* method (figure 4.7). It provides an estimate of the total sensitivity index S_{Ti} for each of the analyzed parameters using a numerically efficient method. As a consequence, it is particularly indicated when analyzing a set of factors in a model which requires several minutes to be solved. Therefore, the analysis of some factors affecting results of the 3D-1D fits well these conditions.

To apply such method, the space of the input parameters should be defined. Considering k parameters among the input of the model, this space is a subspace of $\mathtt{R}^k$. In particular, the theoretical framework has been developed with reference to the $k-$dimensional unit cube Γ. This space has to be divided in a grid, obtained by discretizing each input in p levels. To compute the elementary effect of a parameter X_i given a value of $\boldsymbol{X}$ within Γ, two points are required. Defining as U_i the unitary vector in the i-th direction of the space Γ (i.e. a vector of 0 in all the element but i where it assumes a unitary value) and Δ the distance in between the two points, they are defined as $\boldsymbol{X}$ and $\boldsymbol{X} + \Delta \boldsymbol{U}_i$. Δ has to be

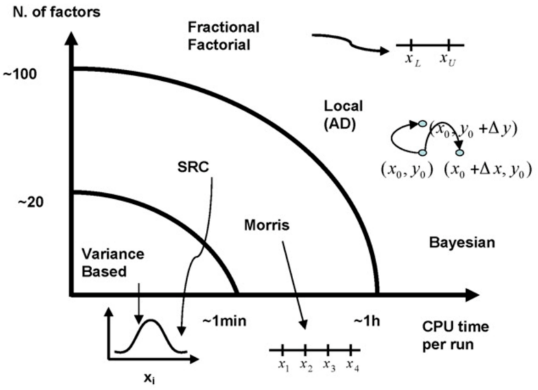

Figure 4.7: *Scheme reported by Carboni and colleagues [223] to show the proper methodology to use in the sensitivity analysis. reprinted with permission from [223].*

chosen such that is a multiple of the width of a level, namely $n/(p-1)$ and $\boldsymbol{X} + \Delta \boldsymbol{U}_i$ is still within Γ. Doing so, the second point is still one of the points of the drawn computational grid and the two points are different only by the input X_i, separating by a distance Δ. The elementary effect is then defined as:

$$EE_i = \frac{Y(\boldsymbol{X} + \Delta \boldsymbol{U}_i) - Y(\boldsymbol{X})}{\Delta} .$$

The distribution of this EE_i within the domain Γ can be obtained by sampling different points $\boldsymbol{X}$. The total number of these elementary effects is determined by the number of levels p and by Δ. Using a typical value of Δ, such as $p/(2(p-1))$, the total number of EE are $p^{k-1}(p - \Delta(p-1))$. As an example, with $p = 4$, $k = 6$, and $\Delta = 2/3$, the total number is 2048. Different sampling strategies of the EE distribution have been proposed in literature to obtain an efficient design. In particular Morris [224] suggested to sample the space Γ with r different trajectories. Each of these trajectories should be composed by $k+1$ points, in order to allow the computation of k elementary effects, precisely one for each input parameter. These trajectories have to be generated so that two subsequent points are different only by one of the input factor, and the distance in between them is Δ. In other words, given a trajectory j the point $\boldsymbol{X}_2 = \boldsymbol{X}_1 + \Delta \boldsymbol{U}_i$.

Starting from a randomly selected $\boldsymbol{X}$ within Γ, the points composing the trajectory are then defined by randomly selecting the index i among the set of the parameters, i.e. 1,...k. One additional condition is that an index i can be selected only once within a trajectory. As a consequence, each trajectory is composed by points separated by Δ for each direction i in the space Γ. An example of a trajectory generated following this procedure is shown

in the figure 4.8.

In some studies [225–227], the choice $r = 10$ and $p = 4$ have produced valuable results.

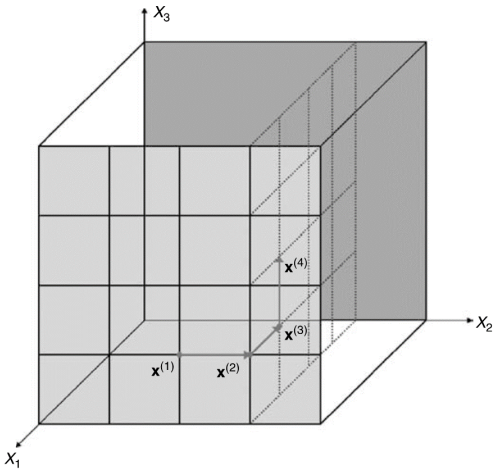

Figure 4.8: *Example of a trajectory generated by the Morris method in a 3-dimensional input space. Reprinted with permission from [222]*

In addition, the proper value of Δ should be chosen to ensure that all the points defined by the level p have the same probability to be sampled. Since all these points must be inside the domain Γ both a positive and a negative variation by a factor Δ are allowed. When considering a negative variation, the definition of the elementary effects must be modified to account for it. Therefore, considering a trajectory j and naming x^k and x^{k+1} the two subsequent points differing for the i-th input, a more precise definition of the elementary effect is:

$$EE_i^j(\boldsymbol{X}_k) = \frac{Y(\boldsymbol{X}_{k+1}) - Y(\boldsymbol{X}_k)}{\Delta} \qquad if\ \boldsymbol{X}_{k+1} = \boldsymbol{X}_k + \Delta \boldsymbol{U}_i$$
$$EE_i^j(\boldsymbol{X}_k) = \frac{Y(\boldsymbol{X}_k) - Y(\boldsymbol{X}_{k+1})}{\Delta} \qquad if\ \boldsymbol{X}_{k+1} = \boldsymbol{X}_k - \Delta \boldsymbol{U}_i\,.$$

The mean and the standard deviation of their distribution can be estimated accordingly. In particular, recalling that the total number of trajectory j is indicated by r, and referring to the input i, the mean of the distribution μ_i is computed as:

$$\mu_i \;=\; \frac{1}{r}\,\Sigma_{j=1}^{r} EE_i^j\,.$$

Moreover, the variance σ^2 of the distribution is estimated by:

$$\sigma_i^2 \;=\; \frac{1}{r-1}\Sigma_{j=1}^{r}\Big(EE_i^j \;-\; \mu_i\Big)^2 .$$

Doing so, μ_i depicts the overall influence of the i-th input, whereas the value of σ_i reveals non-linearity and interactions between the other inputs. More precisely, a large value of σ_i means that the value of EE_i strongly depends on the point $\boldsymbol{X}$ in which is computed, i.e. the values of the other parameters, or the value of the same parameter, highlighting non-linear effects. Another index has been proposed by Campolongo and colleagues [228], replacing μ_i with μ_i*. Such an index helps in the identification of the influence of factors when considering models in which the EE_i may assume both positive and negative values. In such cases, ΣEE_i may result low even if EE_i are definitely non-zero, due to cancel-out effect. The μ_i* is thus defined as:

$$\mu_i* \;=\; \frac{1}{r}\,\Sigma_{j=1}^{r}|EE_i^r|\,.$$

The same authors have also shown that this index gives a good idea of the total sensitivity indexes S_{Ti}. As a final methodological remark, the levels for each input parameter should be derived from the unitary hypercube by considering the parameter distribution. Since the aim of the analysis is to figure out which parameter is the most influential on the output, a uniform distribution has been considered for all of them.

4.2.3 Selection of the simulation setup

The first step to design the sensitivity analysis has consisted in the definition of the subset of the parameters to be tested and the output to be considered. The two chosen output variables, NFR and average interstitial pressure, have already been described in the previous section. For clarity, we recall that the NFR is the integral of the term $2\pi\, R_i\, L_p \left(\bar{p}_v(s) \;-\; \bar{\bar{p}}_t(s) \;-\; (\pi_v \;-\; \pi_t)\right)$ over the network Λ. Conversely, the average interstitial pressure has been computed as an integral mean over the domain Ω. This analysis is in the framework of the application to uremic microvasculature. Therefore, the parameters altered by the pathology have been selected for the analysis (table 4.2). The ranges of variation of these parameters have been defined with reference to the literature values for both healthy and uremic microvasculature. By assuming a uniform distribution, these parameters are then associated with a unitary 6-dimensional hypercube. Therefore, in this specific case the vector $\boldsymbol{X}$ has dimension 6, namely $k = 6$. As a consequence, the values of the input corresponding to a coordinate X_i has been computed as $\tilde{X}_i = min_i + X_i\,(max_i - min_i)$, where $\tilde{X}_i$ is the dimensional i-th input, min_i and max_i are the minimum and the maximum dimensional value respectively, as reported in

Table 4.2: *Input parameters considered in the sensitivity analysis along with their range of variation.*

	Variable	Reference healthy value	Reference CKD value	Minimum	Maximum	Ref.
$\tilde{X}1$	$\frac{S}{V}$ (m^{-1})	7000	4900	4900	7000	[183, 199]
$\tilde{X}2$	$\Delta\pi$ $(mmHg)$	25	19	19	25	[194, 200, 201]
$\tilde{X}3$	H $(-)$	45	35	30	50	[5, 200, 201]
$\tilde{X}4$	L_p $(m^2\,s\,kg^{-1})$	10^{-12}	8.8×10^{-12}	10^{-12}	10^{-11}	[127, 162]
$\tilde{X}5$	σ $(-)$	.95	.75	.7	1.0	[127, 219]
$\tilde{X}6$	$p_{v,IN}$ $(mmHg)$	32	/	31	34	[194]

the table 4.2, and X_i is the i-th coordinate in the unitary hypercube. The number of levels to discretize each parameter, the distance Δ, and the number of trajectories r have been defined as suggested by the literature. In particularly, $p = 4$, $r = 10$, and $\Delta = 2/3$. Therefore, the parameters values are shown in table 4.3. The Morris' sequence has been generated by means of a *ad hoc* random code developed by Matlab® (The MathWorks Inc., Natick, MA, USA). First, a random point $\boldsymbol{X}$ has been selected in the hypercube, then by randomly selecting a direction i in the set 1,...,6 and applying a variation $\pm\Delta$ the second point has been selected. The variation applied has been positive if $X_i = 0$ or $X_i = 1/3$ and negative otherwise. In this way, the second point is certainly inside the unitary hypercube. The process is then repeated by selecting i in the set of parameters without the one previously selected. For example, if $i = 3$ has been considered to retrieve the second

Table 4.3: *Input parameters considered in the sensitivity analysis associated to their level.*

	Variable	Minimum	$p = 2$	$p = 3$	Maximum
$X1$	$\frac{S}{V}\,(m^{-1})$	4900	5600	6300	7000
$X2$	$\Delta\pi\,(mmHg)$	19	21	23	25
$X3$	$H\,(-)$	35	40	45	50
$X4$	$L_p\,(m^2\,s\,kg^{-1})$	10^{-12}	4×10^{-12}	7×10^{-12}	10^{-11}
$X5$	$\sigma\,(-)$	0.7	0.8	0.9	1.0
$X6$	$p_{v,IN}\,(mmHg)$	31	32	33	34

point, i for computing the third point has to be chosen from $\{1, 2, 4, 5, 6\}$. Doing so, all the indexes i are varied in the $k + 1$ point of the trajectory, and every variation in the i-th direction is present in the trajectory only once. This operation has been repeated 10 times to built 10 different trajectories. The other input has been specified as defined in the uremic microvascular test (table 4.1). The only difference regards the boundary conditions for the domain Ω. In particular, the analysis has been repeated twice, using two different boundary conditions. The first is the *equilibrium condition* already used in the uremic test, namely the condition in which the fluid is not allowed to exit the interstitial domain through the faces $\partial\Omega$. Conversely, in the second one, the interstitial fluid can pass through these faces, exiting the domain. This flow rate is determined by a far-field pressure $p0$ and a boundary conductivity β. Following the procedure of [162, 206] the boundary condition has been specified as:

$$\boldsymbol{u}_t \cdot \boldsymbol{n} \;=\; \beta(p_t - p0) \;=\; \frac{K}{\mu_t\, D}(p_t - p0)\,.$$

For one analysis the total number of simulations is $r(k + 1) = 70$. Considering the two different boundary conditions on $\partial\Omega$, twice this number have been run. To this end, a Python script has been considered to run the simulation and to post-process the results extracting the value of the two output analyzed. Results of this simulation are presented by means of scatterplot (obtained by Matlab® *ad hoc* code) and by the parameters μ, μ^*, and σ, which have been computed using Excel© (Microsoft).

4.2.4 Results of the sensitivity analysis

First results related to the *equilibrium condition* are presented. The scatterplot are shown in figure 4.9 and 4.10. From them, some idea about the most influencing factors can

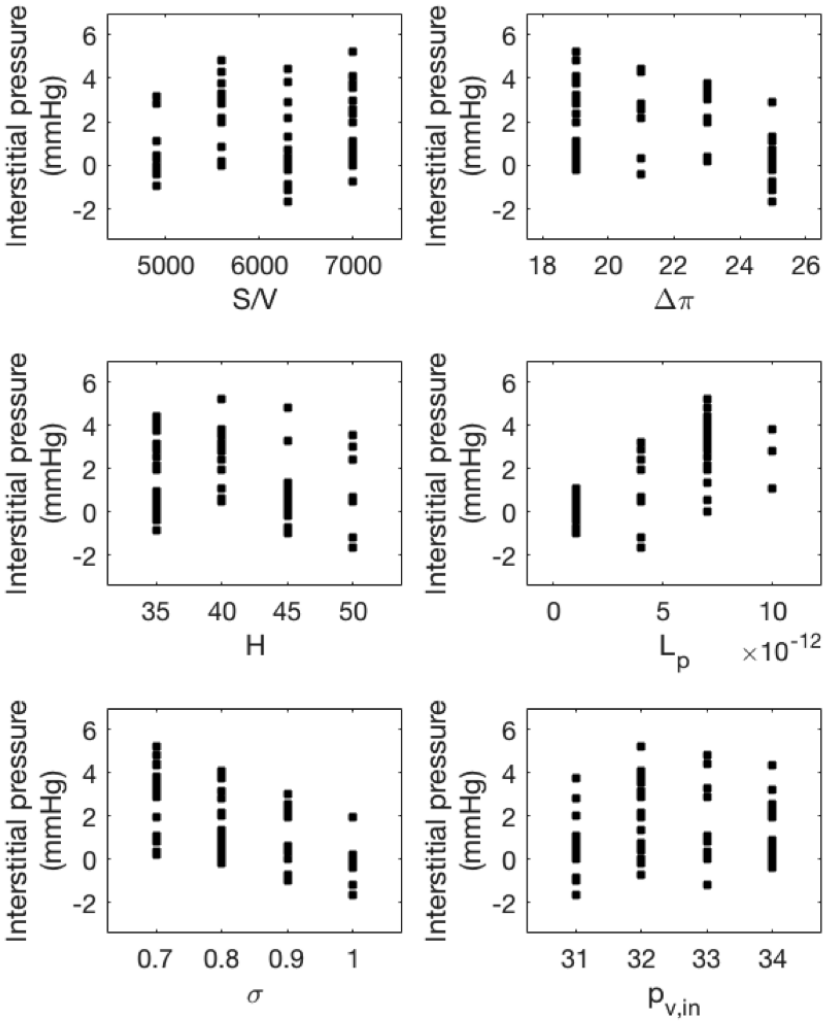

Figure 4.9: *Scatterplots for the average interstitial pressure in the closed configuration.*

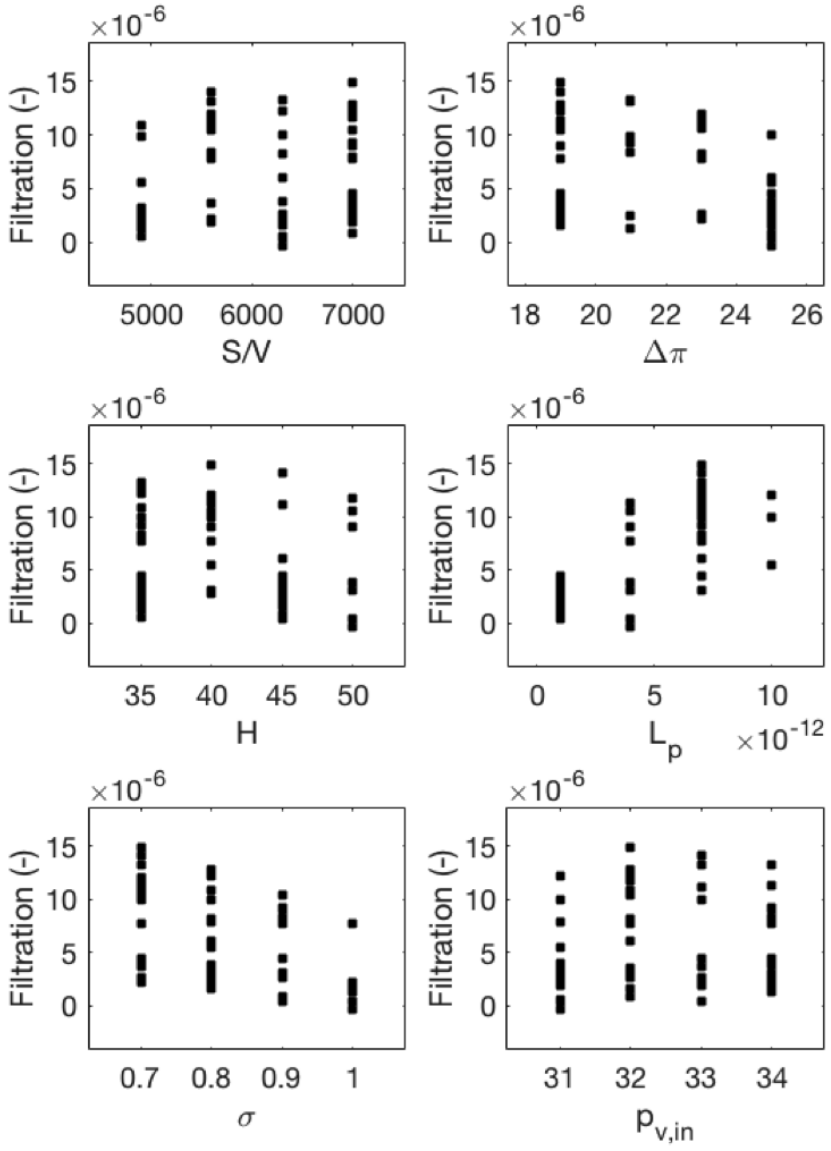

Figure 4.10: *Scatterplots for the NFR in the closed configuration.*

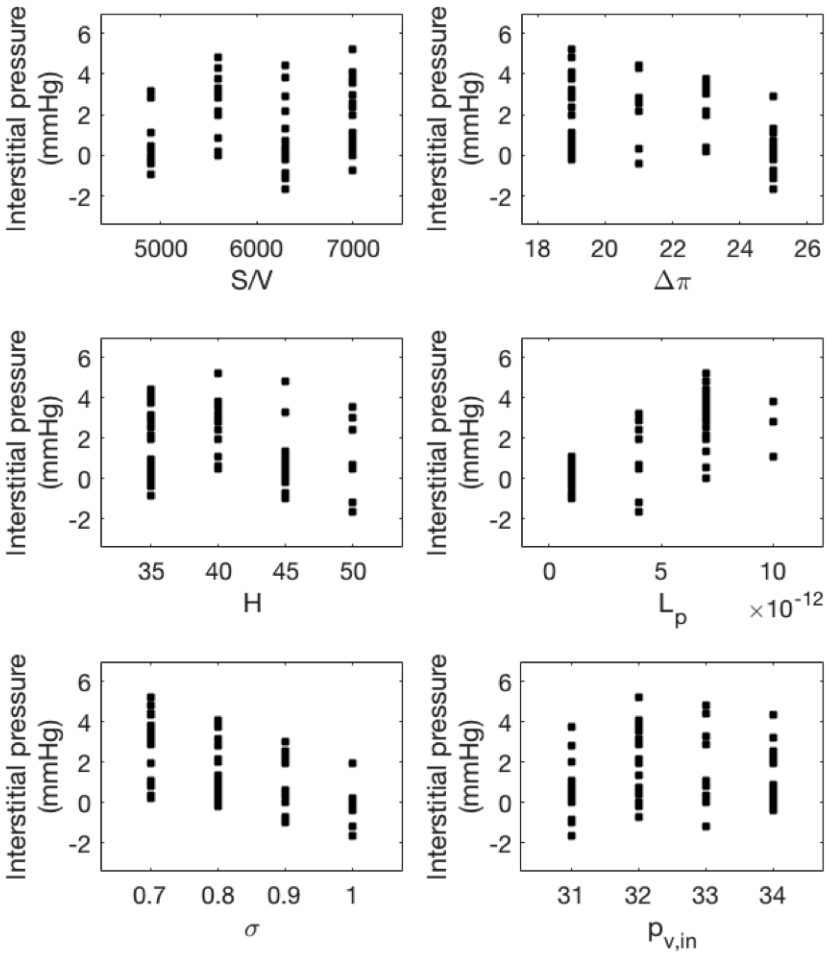

Figure 4.11: *Scatterplots for the average interstitial pressure in the opened configuration.*

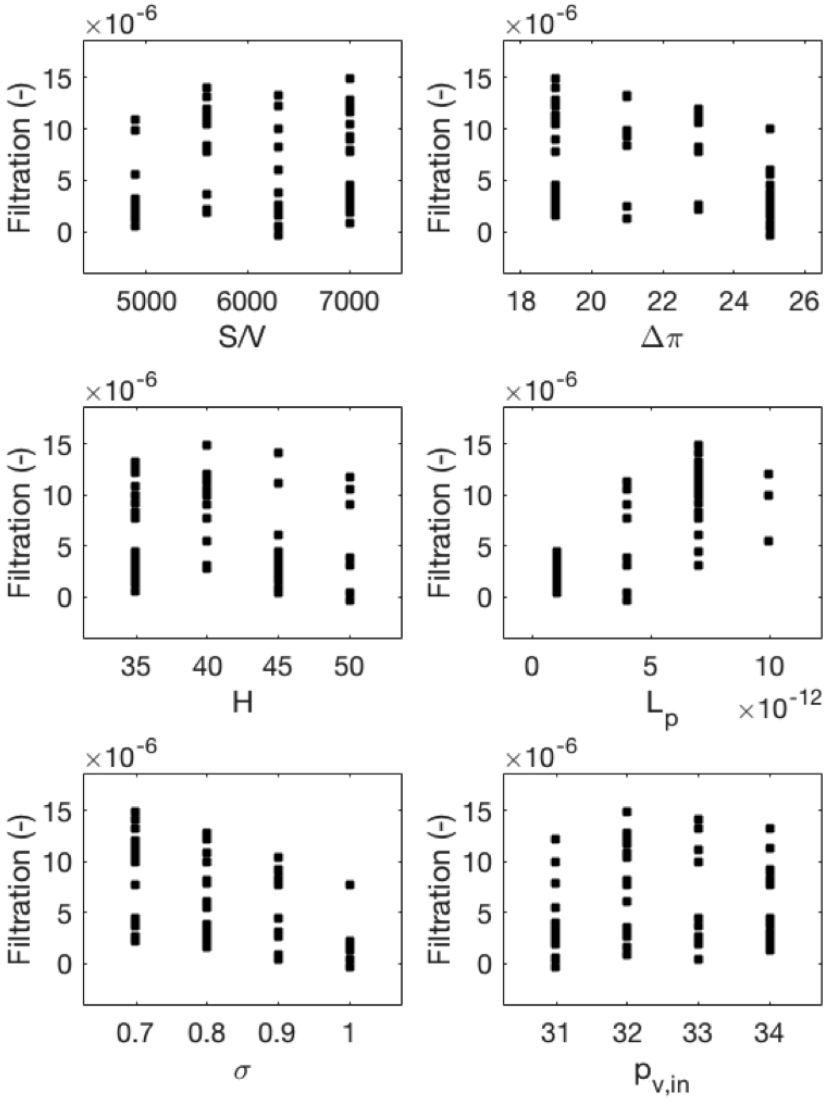

Figure 4.12: *Scatterplots for the NFR in the opened configuration.*

be inferred. For example, L_p and σ appear to cause more pronounced variations on the interstitial pressure than the others (e.g. figure 4.9). However, extracting quantitative information from them is difficult. Such an information can be obtained by means of the aforementioned indexes. Indexes for the closed configuration are shown in the table 4.4 and 4.5. By looking at the index μ^* in the table 4.4, L_p, $\Delta\pi$ and σ have been identified as the most influencing parameters. This is in agreement with what resulted of the analysis conducted in the modeling of the uremic microvasculature. The same three input parameters have also a quite larger σ with respect to other parameters, highlighting interactions between parameters. The less influencing factor appears to be H. Although in the table 4.5 the trend is less evident because of the magnitude of the NFR, by looking at the order of magnitude, a greater μ^* and σ can be identified for the very same three variables. Indeed, the values of the output variable have been reported in the dimensionless form, as results from the code, since here only the relative value is important. When comparing closed and open configurations, all the indexes related to the interstitial pressure are found to be lower in the latter. Actually, a rising of p_t causes a flow rate through the faces $\partial\Omega$, helping the system to keep the p_t closer to the value $p0$, namely reducing p_t variations (table 4.6). However, the same consideration done for the previous cases are confirmed also in this configuration. Also for the filtration similar results have been obtained (table 4.7), but here the values of μ^* are larger than in the closed configuration.

The same results are reported in the figure 4.13, in a σ-μ^* plot. The horizontal position on these graphs highlights the importance of the factors, namely μ^*, whereas the vertical position reveals the non-linearity or the interactions with other parameters. Consequently, the right top corner includes influential parameters that presents non-linearity or interaction with other parameters. Conversely, the left-bottom region shows parameters with a low influence on the output and with low non-linear/interaction effects. Such a graphical representation helps to visualize the results of the analysis already shown in the tables.

4.2.5 Discussion

These results have confirmed the trend highlighted in the analysis performed in the framework of the uremic microvasculature. Indeed, this analysis has produced more global results about the influence of the input parameter on the output NFR and average interstitial pressure. In particular, the most influencing parameters have been identified in L_p, σ, and $\Delta\pi$. These are linked to the properties of the capillary membrane and the difference in oncotic pressure across it. Also this difference in oncotic pressure is related to the semi-permeability of the capillary membrane, namely its capacity to maintain them inside the vasculature. Indeed, the study of the alterations of the capillary membrane due to the uremic pathology assumes a key role. The capillary membrane is not related only to

Table 4.4: *Values of the indexes μ, μ^*, and σ for the variable p_t in the closed configuration.*

Parameter	μ	μ^*	σ
S/V	-0.19	0.55	0.36
$\Delta\pi$	-1.39	2.89	1.39
H	0.03	0.21	0.45
L_p	2.86	4.12	2.58
σ	1.86	2.82	1.95
$p_{v,in}$	0.05	0.54	0.44

Table 4.5: *Values of the indexes μ, μ^*, and σ for the variable NFR in the closed configuration.*

Parameter	μ	μ^*	σ
S/V	3.2×10^{-7}	4.9×10^{-7}	5.3×10^{-7}
$\Delta\pi$	-2.4×10^{-6}	2.4×10^{-6}	1.3×10^{-6}
H	-6.3×10^{-8}	4.0×10^{-7}	9.5×10^{-7}
L_p	5.3×10^{-6}	5.3×10^{-6}	2.8×10^{-6}
σ	-2.4×10^{-6}	2.4×10^{-6}	1.1×10^{-6}
$p_{v,in}$	6.0×10^{-7}	6.0×10^{-7}	3.0×10^{-7}

Table 4.6: *Values of the indexes μ, μ^*, and σ for the variable p_t in the open configuration.*

Parameter	μ	μ^*	σ
S/V	-0.07	0.49	0.27
$\Delta\pi$	-1.01	2.07	0.81
H	0.00	0.00	0.00
L_p	2.25	3.43	1.64
σ	2.07	2.07	1.14
$p_{v,in}$	0.06	0.39	0.24

Table 4.7: *Values of the indexes μ, μ^*, and σ for the variable NFR in the open configuration.*

Parameter	μ	μ^*	σ
S/V	1.12×10^{-6}	1.12×10^{-6}	5.98×10^{-7}
$\Delta\pi$	-4.78×10^{-6}	4.78×10^{-6}	1.95×10^{-6}
H	7.37×10^{-10}	2.38×10^{-9}	3.37×10^{-9}
L_p	9.28×10^{-6}	9.28×10^{-6}	4.47×10^{-6}
σ	-4.33×10^{-6}	4.33×10^{-6}	2.49×10^{-6}
$p_{v,in}$	8.40×10^{-7}	8.40×10^{-7}	5.40×10^{-7}

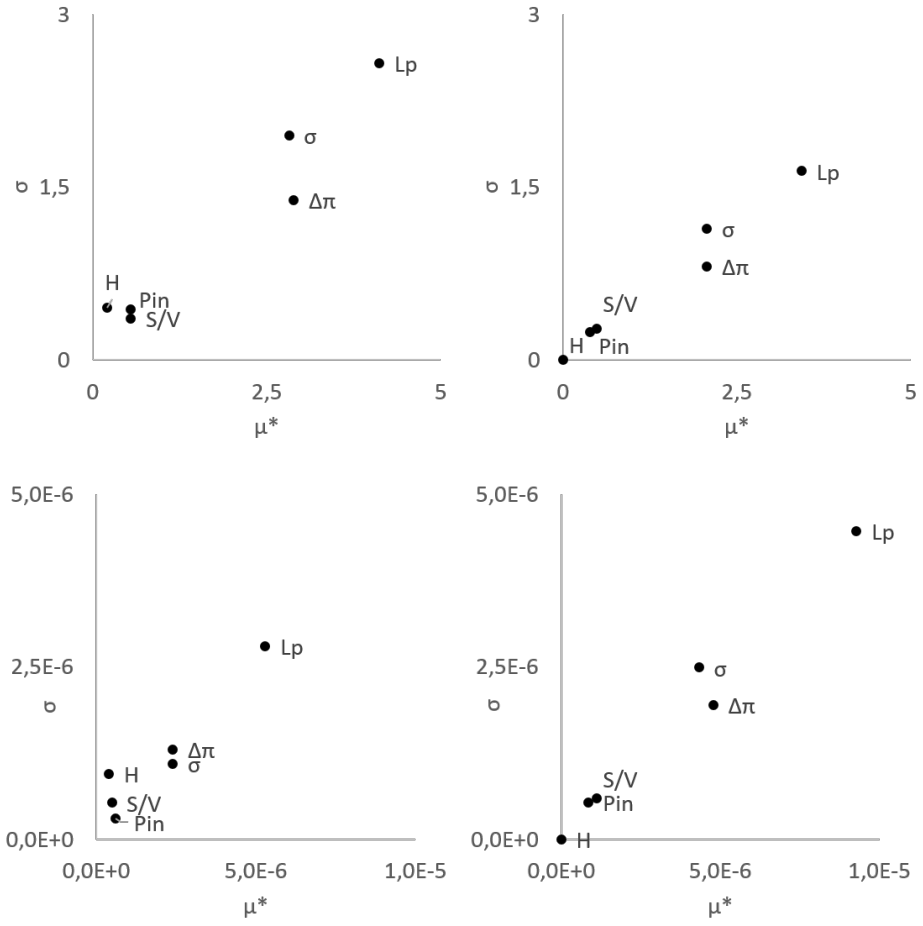

Figure 4.13: *σ-μ^* plot for the cases considered. Top line: results for interstitial pressure. Bottom line: results for NFR. Left column: results for closed configuration. Right column: results for open configuration. Each of the σ-μ^* plot shows on the right top corner influential parameters that presents non-linearity or interaction with other parameters and on the left-bottom region parameters with a low influence on the output and with low non-linear/interaction effect.*

fluid balance in the microvasculature but also to solute compartmentalization. As a consequence, it is ultimately related to the efficiency of the dialysis, in terms of fluid balance (i.e. avoiding too severe reduction of the blood volume) and solute removal. The three most influencing alterations have also some interactions, as shown by the σ index values. These alterations can be explained by the description of the NFR, as described in the previous section (equation 4.1). In addition, these results have confirmed that H variations have a small influence on filtration and the interstitial pressure. As previously discussed, this phenomenon is a direct consequence of the applied boundary conditions. Instead, alterations of the vascular pressure are worth to be discussed with more attention. The amount of variation of this pressure is not known, indeed no reference has been included in the table 4.2. In this sensitivity analysis, little variations around the value $p_v = 32mmHg$ have been screened, based on the hypothesis that big variations are prevented by the vascular controls. Results of the sensitivity analysis have highlighted that this parameter has a low influence on the output. However, it should be considered that if larger variations of p_v are possible, they will certainly result in larger variations of the output. This is the kind of information, which eventually will be made available by future interactions of this 3D-1D model with the lumped parameter model. Such interactions, however, have not been addressed in this work, and they represent an interesting future development of it.

4.3 Discussion of the application

Considering the results of both the sensitivity analysis and the application to uremic microvasculature some key points have been revealed. The model has reproduced the rising of interstitial pressure, typical of the uremic pathology, by comparing results for healthy and uremic conditions. This increase of pressure has been related to the retention of fluid in CKD. Even if this interstitial pressure plays a role in determining the fluid exchange, it has been measured in uremic patients only by [30]. Such a measure has been conducted in the subcutaneous tissue, because it is easily accessible and because it is inclined to fluid accumulation. By comparing our results with the *in vivo* values they reported, it can be concluded that the model has correctly reproduced the phenomenon. However, the model is still affected by some limitations. First, the interstitial space can be modeled as a poroelastic media, considering also the mechanical properties of the matrix. This represents an interesting development of the present model, since poroelastic phenomena may have an effect when accumulating fluid within the interstitium, however more data are required to draw any conclusion. Secondly, the solute transport can be considered in the model. Such an improvement enables the study of the spatial distribution of proteins and consequently of oncotic pressures, allowing the study of their possible effect. Moreover, the viscosity of blood has been modeled with the *in vivo* formulation proposed by Pries and colleagues [98]. Although this formulation is widely used in this kind of models, it is not sensitive to shear rate variation. By contrast, rheology of blood is known to depend on shear rate, classifying it as a non-Newtonian fluid. Several models have been proposed in literature, and they have been comprehensively reviewed by [229]. However, such models are referred to blood flowing in big arteries, and they can not be directly applied to microvasculature. In particular, RBCs interaction with the glycocalyx may influence the viscosity of the blood at such small-scale vessels. In addition, the relation required in this model is similar to the one already used to model the dependency from H and the radius, due to the mesoscale approach. Both computational and experimental models can be considered to study this phenomenon and to obtain such relation. One main possibility to achieve this description is represented by *in vitro* microfluidics setup composed by channels covered by either endothelial cells (therefore forming the glycocalyx) or polymers (i.e. mimic the glycocalyx), which can be used to flow blood and study the flow rate - Δp relation. Once such a relation is available, it can be included in the model improving the vascular description. This may influence the RBCs distribution along the network,and it may consequently affect all related phenomena, from flow rate distribution within the network to oxygen delivery to tissues. In figure 4.14, only velocity lower than $1\,mm/s$ are shown because the apparent viscosity may be affected by the shear rate at this low

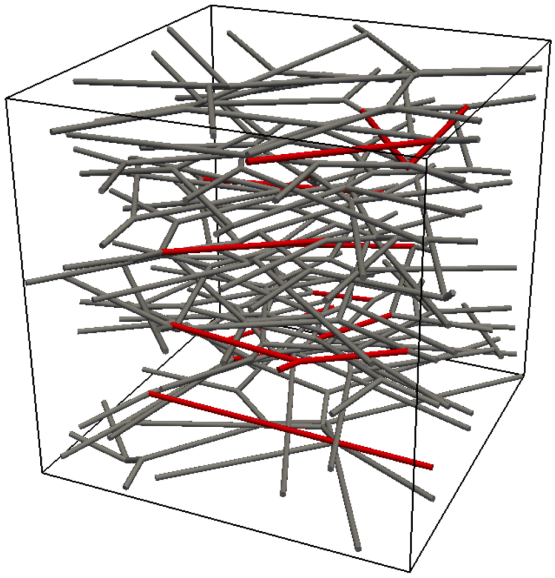

Figure 4.14: *Branches of the network characterized by a velocity lower than* $1\,mm/s$ *under physiological conditions (red).*

paces [196–198]. The number of branches below this threshold is small, supporting the validity of the presented results, but it is still not completely negligible.

In addition, the value of H in the simulations has been set by using the systemic H_t data. However, the hematocrit in the microcirculation may be lower, i.e. several bifurcations may be present at the arteriolar level, in which the Zweifach - Fung effect can play a role. In our model, the H_t is lower than the H applied, as it can be computed by the formula proposed by Pries and colleagues [61]. Interestingly, the sensitivity analysis has revealed the low influence of H variations on p_t and NFR. As already discussed, this may be related to the computational setup. However, the small influence on those values suggests that results are meaningful even considering the previously mentioned limitations of H modeling.

CHAPTER 5

The *in vitro* model

In this chapter, the in vitro model is described highlighting its critical components. Consequently, an improvement of the experimental technique is presented. The computational 3D-1D model has also been used to analyze the experimental setup. The study of the urea effect is then presented, and finally, applications, limitation, and possible future improvements are discussed.

5.1 Introduction of in vitro vascular networks [129]

Over the last decades, microvasculature generation on microfluidic chip has been used to understand microvasculature formation and how it responds to different kind of signals (e.g. mechanical or biochemical). The first section of this chapter presents the methodology used to generate self-assembled microvascular networks in a chip. Such methods are widely used in literature, with some variation among different groups, regarding the type of cells, the type of gel, the material and the structure of the microfluidics chip, and the culture media. Therefore, the adopted experimental setup is now presented, by highlighting the possible alternatives reported in literature for each component. The overall setup can be divided into: microfluidic chip, gel, cells, and media.

Microfluidic chip Concerning the microfluidic chip, several different geometries have been reported. Chips are usually organized with parallel channels, separated by structures which contain the hydrogel (figure 5.1). These structure can be either *post* or *postless*.

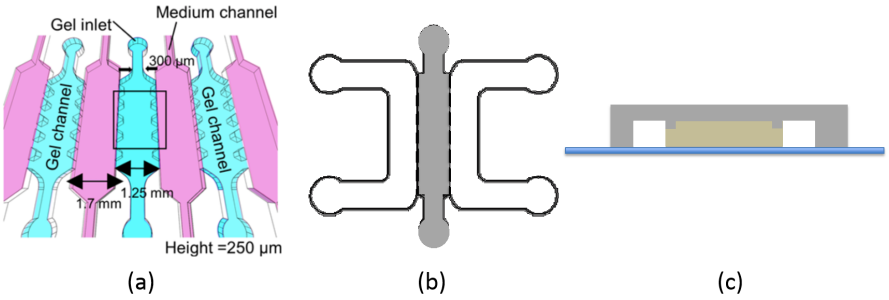

Figure 5.1: *Example of microfluidics platform. (a) Multiple channel with posts. From [230]. (b) Scheme of the postless device used in this work. (c) Lateral view of (b), showing lips on the top of the device.*

Posts are triangular structures, aligned along the side of the gel-filled channel. They allow the containment of the gel, forming a discontinuous interface between the gel and the side channel (usually the media channel). Conversely, *postless* systems are able to contain the hydrogel thanks to lips on the top of the channel and their hydrophobicity. This structure allows the generation of networks without concentrating the opening of the vessels in the specific intra-post region. Moreover, when a monolayer of endothelial cells (ECs) is built on the side of the gel, the *postless* system allows a more continuous monolayer. In this work, a single gel channel *postless* chip has been used (figure 5.1). The width of the gel

channel, namely the distance between the two media channel, is $3\,mm$. Such configuration is getting out from the strict definition of a microfluidic device, embracing millimeter scale. Even if the definition of microfluidic chip is no strictly applied here, in this chapter the device will be identified with this name. Another important feature of the chip is the material used to build it. The most common material is the Poly(dimethylsiloxane) (PDMS), because of its properties [231]. Indeed, it is transparent (i.e. allowing the imaging of the sample), permeable to gases, in particular to oxygen, and moreover inert and cheap. Even if other materials could have been considered, the PDMS has been adopted for this analysis.

Gel There are several possibilities also regarding the hydrogel. Its main function is to provide a support in order to obtain a 3D structure necessary to have a self-assembled network. This gel is usually generated by a gelation process of two components: fibrin and alternatively collagen or thrombin (e.g. [130]). An important remark concerns mechanical properties of the gel and the velocity of the gelation process. They are both influenced by the protein concentration, the temperature, and the pH. The velocity of gelation directly affects the 3D shape of the network. For example, a very slow gelation allows the sedimentation of the cells seeded within it, eventually producing a gradient of cell concentration along the vertical direction. Such a gradient can affect experimental results, for example leading to too vascularized regions. Moreover, the mechanical properties of the gel also influence the network morphology and behavior. For example, a stiffer gel results in a smaller lumen and lower migration ability [232]. For this work, a thrombin-fibrin gel has been considered.

Cells Concerning cells, at least two types of cells are required to build a self-assembled network. ECs are certainly the first, since they compose the capillary vessel structures. As discussed in the first chapter, several types of EC have been used in literature. However, human umbilical vein endothelial cells (HUVECs) are the most commonly used for self-assembled network formation. ECs are usually seeded within the gel with other types of cells such as mesenchymal stem cells (MSCs) of fibroblasts (FBs). FBs, in particular, have been found to promote vascular network stability, avoiding network regression. The resulting vascular network depends on cells concentration, in terms of number of vessels, branching, and perfusion. In particular, the optimal seeding concentration may be different for different batches of cells. It should be optimized for the considered batch of cells, due to the intrinsic variability of the cells population, in particular with reference to their proliferation ability. However, the *in vitro* networks are commonly characterized by larger

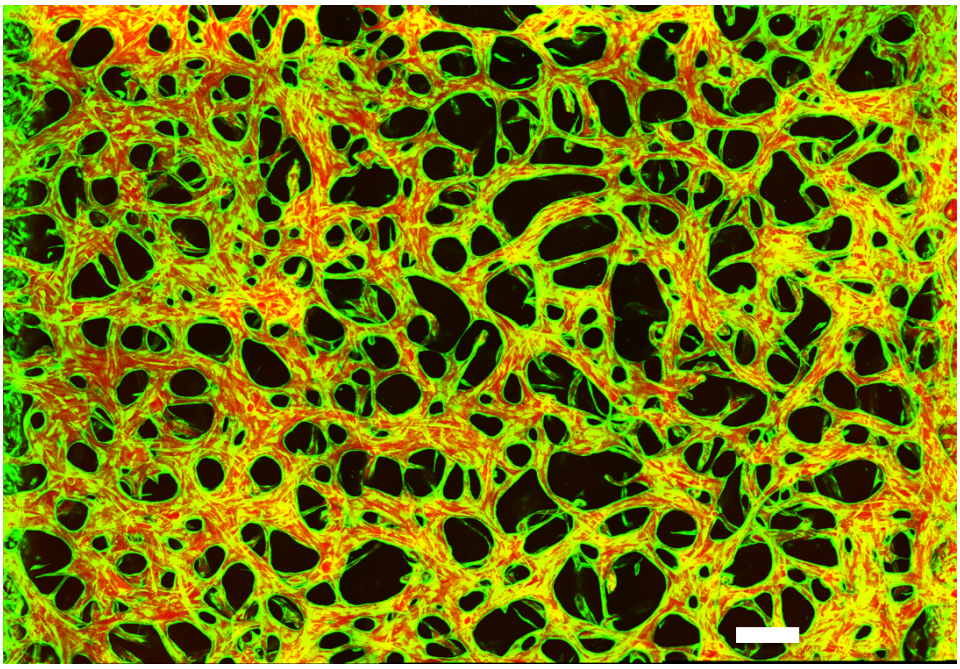

Figure 5.2: *Example of perfusable network obtained in this work. Green: GFP postive ECs. Red: Texan red dextran 40 kDa. White bar* $= 200\,\mu m$.

diameters ($50\,\mu m$) if compared to the *in vivo* capillaries ($\simeq 8 - 10\,\mu m$). The vascular structure and the possible perfusion of the networks have been typically addressed in this kind of models. The latter is usually addressed by perfusing the network with a fluorescent dye or micro-beads. By inserting them in one side of the network, and applying a sight difference of pressure (e.g. only by the gravitational effects of half a millimeter water column within the reservoir of the device), the perfusion of the network is observed. An example is shown in figure 5.2, in which a vascular network formed using GFP-positive HUVECs has been perfused with a green fluorescent dye. Conversely, the vascular structure is usually addressed by immunostaining. For example, the conservation of the endothelial phenotype can be confirmed by the expression of vascular endothelial (VE)-cadherin or CD31. In addition, ECs within a mature network form tight junction proteins. The presence of such junctions can be detected for example by the presence of zonula occludens-1 (ZO-1). In this work, HUVECs and human lung fibroblasts (HLFs) have been used for network generation.

Culture media Cells and gel within the device are immersed in the culture media. The composition of this culture media varies on the basis of the cell type and of the manufacturer. Two important points have been considered when choosing the media. The quantity of grown factors (e.g. vascular endothelial growth factor - VEGF) influences the network formation and morphology. The second is related to the presence of solutes that can affect the gelation process. For example, the presence of heparin, usually contained in the media, may prevent gel formation.

Summarizing, the PDMS chip has been filled with the fibrin-thrombin gel containing HUVECs and HLFs. This setup have produced a perfusable network as shown in figure 5.2. Details of the methods are presented in the next section.

5.1.1 Perfusable microvasculature

The methodology used for the generation of microvascular perfusable networks is presented in details. The operations required to build the microfluidic PDMS chip (figure 5.3) are described first, and then the seeding and culturing process are illustrated. The PDMS devices have been obtained starting from an acrylic mold (courtesy of Dr. Kristina Haase) which was made by laser cutting. The process consists of the following steps.

1. The mold, containing several repetitions of the chip *negative*, has been filled by PDMS (Sylgard 184, Dow-Chemical).

2. The PDMS has been cured for 4 hours at $60°C$.

3. Devices were then cut out form the overall PDMS sheet and reservoirs of the channel were punched. In particular, the media channel reservoirs have been characterized by a diameter of $4\,mm$, whereas the media channel reservoirs are $1\,mm$ and $3\,mm$.

4. Devices were then sterilized by autoclave along with glasses and then dried at $70°C$ overnight.

5. Glasses were bounded to the device after an oxygen plasma treatment of 2 minutes (Harrick Plasma).

6. Bounded devices were then stored at $70°C$ for 2 days. This is a key passage since it allows the PDMS to restore its hydrophobic status after the modification induced by the plasma treatment. Indeed, hydrophobic surfaces are required to keep the hydrogel in the center channels.

Once the devices have been prepared, the cells and the gel are inserted in the central channel following these steps.

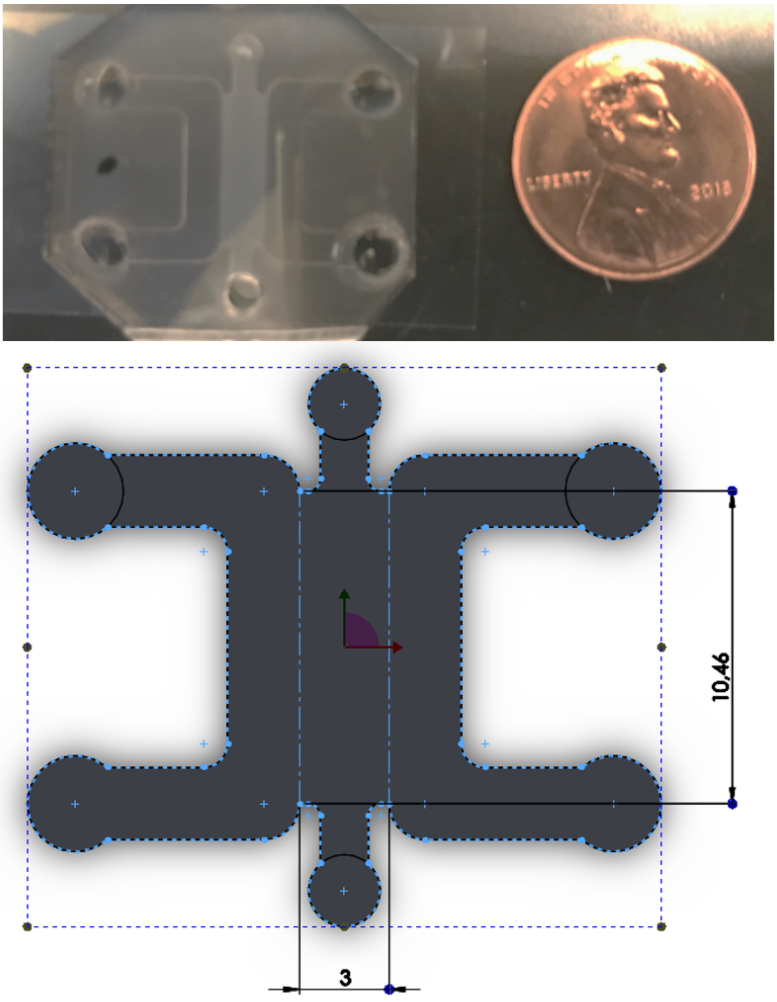

Figure 5.3: *Top view of the PDMS device with the scheme at the bottom of the image. Measures are reported in* mm.

1. A solution was obtained dissolving $40\,\mu l$ of thrombin ($100\,U/ml$) in $1\,ml$ of ECs media. In these experiments VascuLife® ECs culture media (Lifeline cell technology) has been used.
2. ECs and HLFs are resuspended to match the desired concentration. Two different type of ECs has been used, both from Lonza. The GFP positive cells (passage 6) has been resuspended at $20\,M/ml$ along with $10\,M/ml$ HLFs. Conversely, the non-transfected version (passage 4) has been used at $28\,M/ml$, with $4\,M/ml$ HLFs. The ECs and HLFs suspension were then mixed 1:1 to obtain the cell suspension.
3. The fibrinogen was dissolved in PBS at $37°C$ to have a $6\,mg/ml$ solution.
4. Fibrinogen and thrombin solutions have been divided in $20\,\mu l$ aliquots. Then they were mixed 1:1 and inserted in the device via the $1\,mm$ diameter reservoir. Given the mixing procedures, the final concentration of cells suspension can be obtained dividing by 4 the initial concentration.
5. After the filling with the cell-enriched gel, devices were incubated for 20 minutes in a humid chamber at $37°C$.
6. Then, following the gelation process, ECs medium was added in the side channels ($100\,\mu l$ per channel) and devices were stored in the incubator.
7. Culture medium has been replaced daily (inserting $80\,\mu l$ of new media) up to day 4.
8. At day 4 ECs were seeded in the media channel to build a monolayer on the side of the channel. The procedure used in this passage will be further discussed later on.
9. From day 4 to day 7, media has been replaced *asymmetrically* to promote convection of the new media through the gel. Therefore $120\,\mu l$ and $40\,\mu l$ were inserted.
10. At day 7 a mature network has been obtained.

This protocol has led to perfusable microvascular network with both the ECs considered. An example of the 3D microvasculature is shown in the figure 5.4.

5.1.2 Permeability analysis

Such *in vitro* generated microvascular networks have been used in literature with multiple aims. Two examples of application are: (i) to study the migration of cancer cells, in order to understand mechanisms involved in cancer cells intra- or extra-vasation (e.g. [140]); (ii) to analyze capillary membrane permeability to solutes (e.g. [130]). The latter application is interesting with reference to this work. This type of analysis is usually performed using

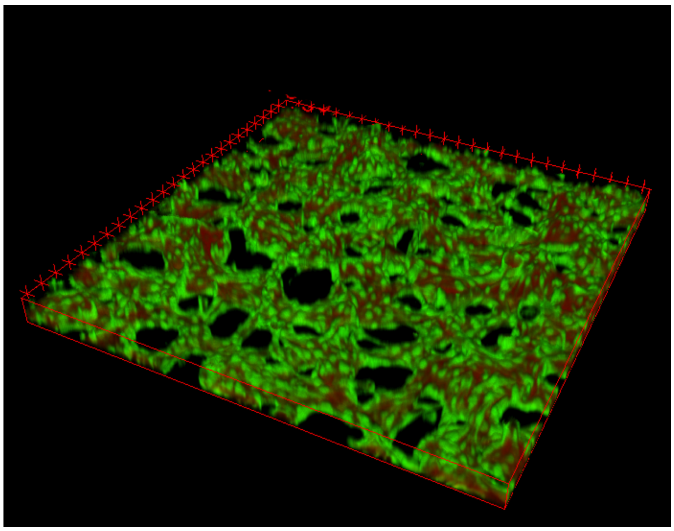

Figure 5.4: *3D view of a perfusable network. Green: GFP positive ECs. Red: Texan red dextran, 40 kDa.*

a fluorescent-labeled solute. One example of this is fluorescent dextran (also available in different molecular weight), but also other solutes are available such as albumin. After the insertion of the labeled solutions, permeability is computed by measuring the increase of fluorescence within the gel over time. The volume has been imaged by means of a confocal microscope (Olympus IX81) obtaining 3D information in both the vasculature and the gel. Under the assumption that the intensity is linearly dependent on the concentration, the fluorescence intensity can be used to estimate the permeability. This assumption is not valid if the intensity approaches the saturation of the signal. Therefore, permeability has been computed with reference to a region of interest (ROI) as:

$$P_{ROI} = \frac{(I_{g,t_2} - I_{g,t_1})\, V_g}{A_v\, \Delta t\, (I_{v,t_1} - I_{g,t_1})}, \tag{5.1}$$

where I is the fluorescence intensity, V and A stands for volume and area within the ROI respectively, Δt is the time between the two measures, and subscripts v and g indicate vasculature and gel. To derive this formula, some other assumptions have been made. A first assumption regards diffusion within the gel. Diffusion has been assumed to be fast and, in particular, faster than the passage of the solute through the membrane. As a consequence, $I_g(x, y, z) \simeq I_g$. This assumption has been verified a posteriori, analyzing the profile of the intensity along lines within the gel. A second assumption concerns the intensity within the vasculature. Also in this case, it is assumingly homogeneous, and

therefore independent from the spatial coordinate, namely $I_v(x, y, z) \simeq I_v$. A further assumption regards the difference between the intensity I_v and I_g. It is assumed to be constant, which experimentally means that the difference can undergo only to few variations. Thus, $I_{v,t_1} - I_{g,t_1} \simeq I_{v,t_2} - I_{g,t_2}$. Given the usual value of permeability, this condition is usually satisfied during a test. However, it should be considered when analyzing very small solutes, which can easily travel through the membrane.

The analysis has been conducted by means of open source software Fiji (`https://fiji.sc`) with the *3D ImageJ Suite* [233]. An ImageJ macro has been written to automatize the intensity computation starting from the fluorescent dye channel. It has been based on the following steps.

1. User interaction to define the ROI and to avoid mismatch of the sample due to temperature related drift.
2. Thresholding by the method 'Otsu stack', and an 'Erode' operation to account for the thickness of vessel wall membrane.
3. 3D segmentation based on a classifier previously trained (courtesy of Dr. Giovanni Offeddu).
4. 3D geometrical measure to obtain volume and area data, based on the segmentation previously done.
5. Average intensity measure within the vasculature and in the gel for both the time steps.

Such an automatized process allows the computation of required variables to estimate the permeability, namely the averaged intensity values I_{g,t_1}, I_{g,t_2}, I_{v,t_1}, and I_{v,t_2}, and the geometrical measures V_g and A_v.

5.2 Methods: applying a trans-mural difference of pressure

5.2.1 Experimental setup

The aim of the work is analyzing the alterations of membrane properties, and top of them all alterations of L_p, due to the presence of uremic toxins. Therefore a trans-mural pressure is required. In particular, with the method described in the previous section, only the filtration can be measured. As a consequence, the vascular pressure should be increased. To this end, the pressure has been increased in the side channels, and this increase of pressure has been carried to the vasculature. These two domains are connected since the vasculature reaches the side of the gel, generating opening within the ECs monolayer. A scheme of the experimental setup is shown in figure 5.5. 3 of the 6 reservoirs are blocked

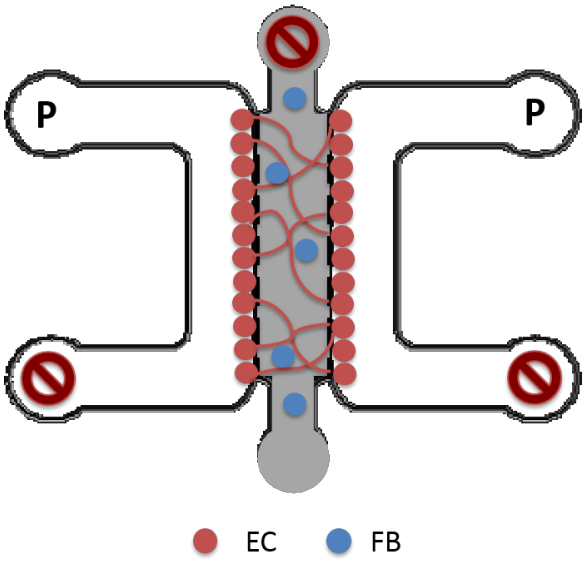

Figure 5.5: *Scheme of the experimental setup. 'P' indicates reservoirs used to set pressure. Blocked signals mark the blocked outlets. Grey color indicates the gel region, whose outlet is kept unblocked.*

by polymeric pins, whereas one reservoir per media channel has been connected to the pressure controller (Fluigent FlowEZ). The remaining $3\,mm$ outlet of the gel channel has been left open. Assuming the generation of this trans-mural pressure, the measure of permeability can be performed. Due to the presence of convective phenomena, the measured value does not depict a real permeability of the membrane, i.e. it does not account only for

diffusion processes. From now on, this computed value is named *effective permeability*, to highlight that it contains information also about convective phenomena. Considering both diffusive and convective phenomena, the flux of a solute can be computed as:

$$j = P\,\Delta C_{v,g} + L_p\,(1-\sigma)\,\Delta\,p\,C_v\,. \tag{5.2}$$

If the gel concentration, and thus the intensity, is low compared to the difference $\Delta C = C_v - C_g$ (as it usually is in this kind of experiments), C_v can reasonable approximate ΔC. That said, the previous equation can be written as:

$$j = P\,C_v + L_p\,(1-\sigma)\,\Delta\,p\,C_v = P_{eff}C_v\,. \tag{5.3}$$

As a consequence, P_{eff} has been defined as $P + L_p\,(1-\sigma)\,\Delta\,p$, namely identifying a portion which does not dependent of trans-mural pressure and a portion that does. Therefore, the coefficient $L_p\,(1-\sigma)$ can be estimated by the slope of the curve in the P_{eff} - trans-mural pressure graph.

As a remark, this measurement technique can be applied, provided that a trans-mural pressure is generated. In the next section, the role of the ECs monolayer on the side of the gel has been analyzed, here anticipating its fundamental role in the generation of the desired gradient of pressure.

5.2.2 The role of the endothelial cells monolayer

The endothelial monolayer plays a key role when generating a trans-mural pressure between vessels and gel. Indeed, it allows the separation of two 'compartments': the media channels (along with the vasculature) and the gel. The gel is a highly porous gel, with porosity higher than 90 %. This is certainly subjected to experimental variability, however, its contribution to the pressure loss due to flow is really small. Indeed, the value of the gel hydraulic permeability has been estimated at $4.1 \times 10^{-13} m^2$ (courtesy of Dr. Giovanni Offeddu). To prove the role of the ECs monolayer, simulations using both the finite volume method (FVM, by ANSYS Fluent®) and the 3D-1D model have been run. First, all the compartments in the geometry of microfluidic chip have been considered by FVM. More precisely, thanks to the symmetry, half of the chip has been modeled. The viscosity of the fluid has been set to $8 \times 10^{-4}\,Pa\,s$ [234]. Mimicking experimental technique, the pressure has been imposed at the inlet. An *ad hoc* function has been written to set the value of the static pressure at the inlet, which is a non-standard option for the software. The geometrical description of the lips have been neglected. However, their presence has been accounted for when computing the monolayer L_p for the computational model. Therefore, the real L_p value has been scaled by $(h_{chip} - h_{lip})/h_{chip}$, where h_{chip} is $500\mu m$ and the deepness of the lip has been assumed as $200\mu m$. The presence of the

monolayer has been included by considering the *porous jump* condition [235], and tuning it to reproduce the desired L_p. A summary of the numerical set up is shown in figure 5.6. Two numerical tests have been conducted: (i) the chip without considering an ECs monolayer; (ii) the chip considering a monolayer 4 order of magnitude leakier than the network. As a remark, the presence of the network has not been considered in this test. Contours of pressure are shown in figure 5.7. The L_p of the ECs monolayer clearly affects the pressure within the gel. In particular, when the ECs monolayer is not considered, a difference of pressure between the gel and the media channel does not occur. In addition, the fluid travels through the gel mainly close to the outlet reservoir, namely traveling along the least resistance path. Conversely, even a monolayer being 4 order of magnitude leakier than the reference value for the vasculature is sufficient to create a difference of pressure within the gel. Moreover, the pressure within the media channel is fairly constant when the monolayer is present. This result allows the analysis of the problem by means of the 3D-1D model, by validating the assumption of constant pressure along the media channel. Doing so, the contribution of the vascular network can be included in the analysis. Starting from a confocal 3D image, a computational vascular network has been reconstructed (details of the method can be found in the next section). The 3D-1D computational model of the chip has been built considering only the gel channel and applying the media channel pressure as a boundary condition. Parameters of the analysis are summarized in table 5.1. A difference with the *in vivo* conditions is characterized by the presence of plasma proteins. As a consequence, there is no difference of oncotic pressures across the membrane.

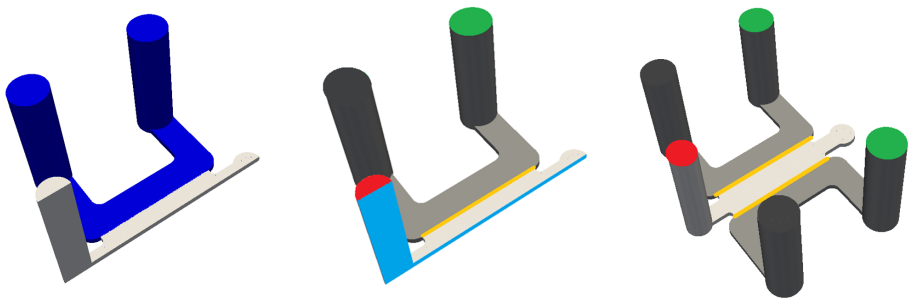

Figure 5.6: *Scheme of the computational setup solved by means of the FVM. On the left, the two considered domains are shown: media channel (blue), gel channel (grey). In the center, the simulated geometry is reported along with boundary conditions: inlets (green), outlet (red), symmetry (cyan), and the possible presence of the monolayer (yellow). On the right, the mirrored sample.*

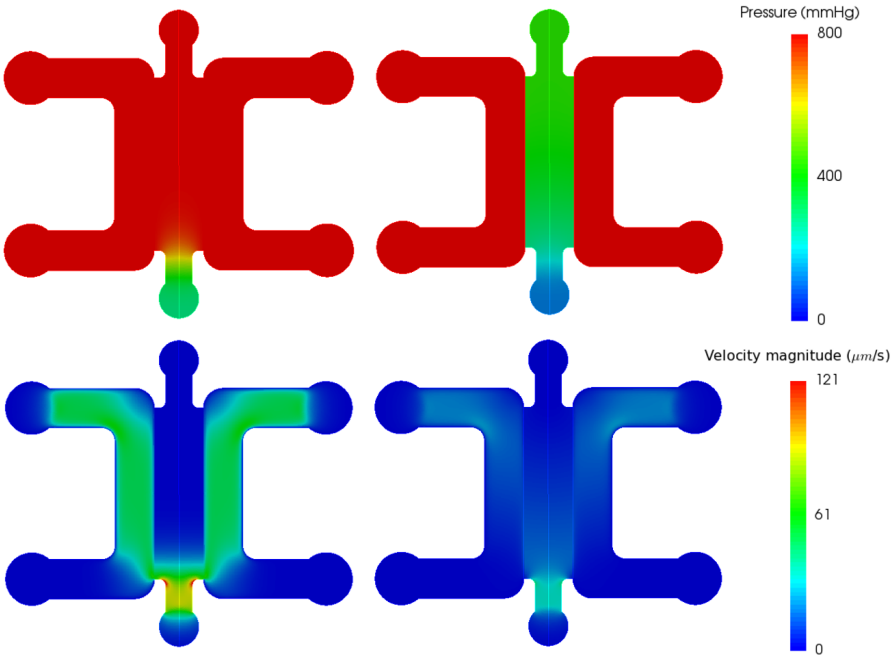

Figure 5.7: *Results of the computational setup for the case without (left) and (with) monolayer. The monolayer considered in this simulation is 4 orders of magnitude leakier than the reference value of the vasculature. Top row: pressure within the device. Bottom row: velocity magnitude in the device.*

Six different hydraulic conductivities have been tested for the monolayer. As a remark, the equivalent L_p has been computed as previously done in the FVM analysis, since the geometrical description of the lips has not been included. The outlet condition has been set by considering the piece of devices not considered (i.e. the connection with the reservoir). The first condition corresponds to such a tight ECs monolayer that the boundary can be considered closed. This represents a not real condition, but it allows the understanding of the network contribute to the total flow rate since fluid can enter the gel only through the capillary membrane. Then, other 5 L_p values have been tested: (i) a monolayer as leaky as the vasculature; (ii) a monolayer 10-times leakier than the vasculature; (iii) then 100-times leakier; and (iv) 500-times leakier; (v) 1000-times leakier; Results in terms of pressure distribution and velocity within the gel are shown in figure 5.8 and 5.9. These results suggest that when building a good monolayer on the side of the gel, a trans-mural pressure can be generated between the vasculature and the gel. Moreover, the leakier the

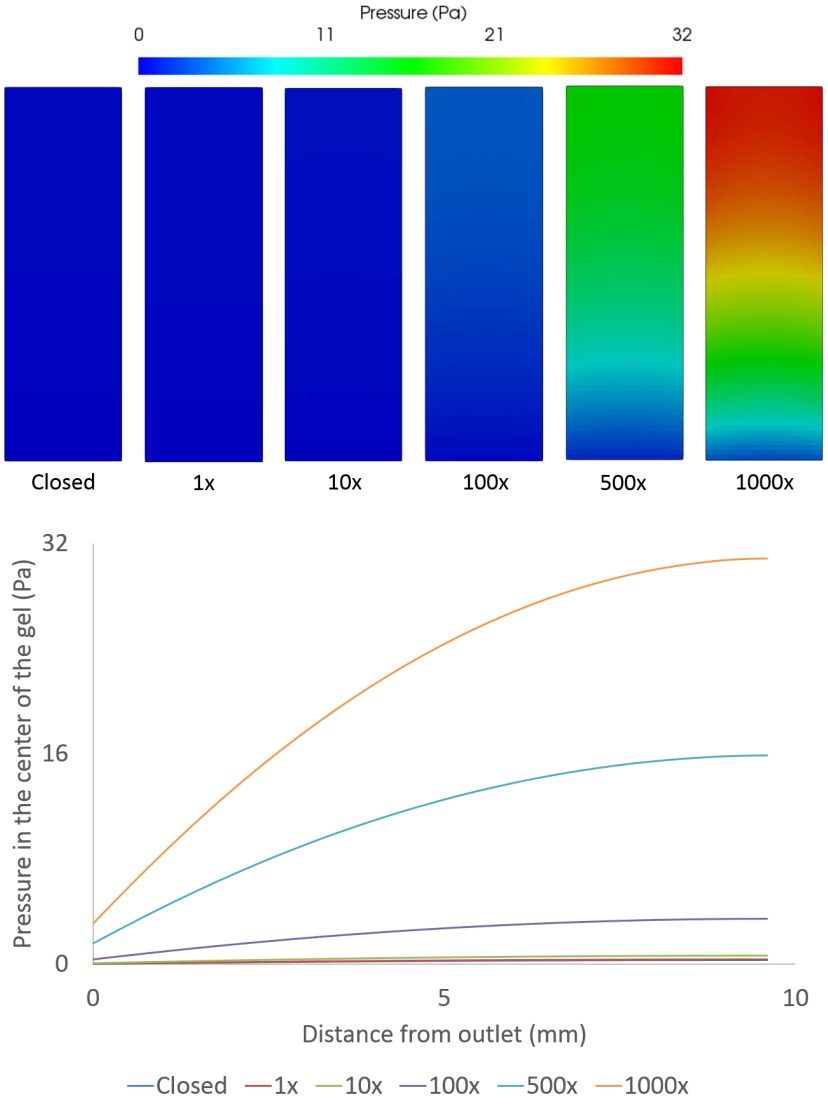

Figure 5.8: *Results of the simulations run with the 3D-1D model. Top view: spatial distribution of the pressure into the gel. Bottom view: profile of the pressure along a line in the center of the gel, varying the applied inlet pressure.*

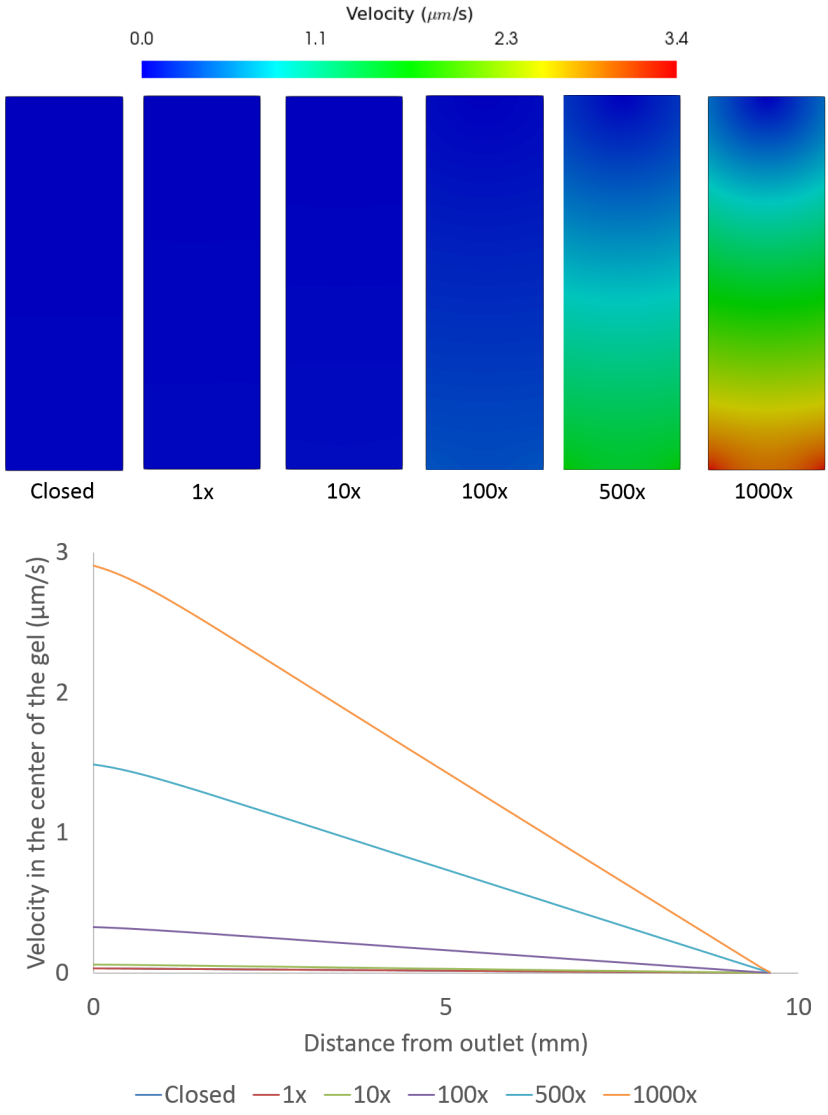

Figure 5.9: *Results of the simulations run with the 3D-1D model. Top view: spatial distribution of the velocity into the gel. Bottom view: profile of the velocity along a line in the center of the gel, varying the applied inlet pressure.*

Table 5.1: *Values of parameter used in chip simulation with the 3D-1D model. Pro = from experimental protocol. Data = from experimental data. Design = chip design data. * = courtesy of Dr. Giovanni Offeddu.*

Parameter	Value	Ref./computing procedure
Channel pressure (Pa)	800	Pro
Outlet pressure (Pa)	0	Pro
Height of the gel channel (μm)	500	Design
Lip depth (μm)	200	Estimated
Hydraulic conductivity of the gel (m^2)	4.1 $\times 10^{-13}$	*
Hydraulic conductivity of the capillary walls $m^2 s/kg$	1 $\times 10^{-12}$	[162]
Hydraulic conductivity of the monolayer $m^2 s/kg$	variable	
Average radius of the capillary vessels (μm)	23.7	Data
Media Viscosity $(Pa\,s)$	8×10^{-4}	[234]

monolayer is, the higher the gel pressure is, as shown in the graph. The results also highlight how the hydraulic conductivity of the monolayer mainly determines the fluid velocity within the gel. In addition, the fluid velocity appears to vary linearly along the length of the chip, as shown in the graph. The magnitude of the L_p tested for the monolayer (e.g. 500x - 1000x) is in agreement with literature data from monolayer (e.g. [236]). Under the leakier condition, the maximum pressure within the gel is $32\,Pa$, namely reducing the transmural pressure by the $4\,\%$. The basic value used as a reference is the L_p considered for the 3D-1D model, namely for *in vivo* conditions. In the *in vitro* experiments, its value is usually greater.

5.2.3 Building the ECs monolayer

Since these results proved the key role of the monolayer in generating a transmural pressure between the vasculature and the gel, the experimental technique to seed the monolayer

has been analyzed and developed. One of the main experimental problems is represented by an incomplete monolayer. This might happen for two reasons. The first is related to the number of seeded ECs. Indeed, if not enough cells are seeded, the monolayer will not cover the entire surface with possible pinholes on the surface. Such holes affect the hydraulic conductivity of the monolayer offering a preferential path for fluid. Moreover, when using fluorescent dye, such pinholes constitute concentrated leaks that eventually affect the measurements. The second reason is related to the fact the ECs may not reach precise locations of the monolayer. For example, if ECs are seeded at the bottom of the chip, they will grow on the side of the gel, due to the affinity with the proteins, which compose the gel. However, they hardly reach the top of the device, especially if considering a quite high device, i.e. some hundreds of μm. Moreover, ECs grow on the side of the gel better than on PDMS, possibly not covering the lip or the corner of the device. To avoid these problems and to improve the quality of the ECs monolayer, a different experimental technique has been developed. It is based on two different concepts: (i) minimizing the seeding suspension volume, to put cells as close as possible to the gel; and (ii) tilting the device to lay down cells on the gel by gravity. Several ECs seeding concentrations have been tested, to optimize the technique. Interestingly, a too high concentration leads to cell death, eventually invalidating the sample due to both vascular regression and accumulation of dead cells within the media. A tilting procedure has been identified, to avoid ECs accumulation close to the opening of the network, consequently avoiding the obstruction of the vasculature. The seeding protocol reads as follow:

1. dilute ECs to have $1.5\, M/ml^*$ in ECs media;
2. remove media from one channel of the device;
3. insert $50\, \mu l^*$ of the cell suspension in the channel;
4. keep devices tilted in the tip box inside the incubator for 10 minutes;
5. fill the channel up to $100\, \mu l$ slowly;
6. repeat the process for the other channel.

The number of cells and the volume of the suspension to use have been marked by a *, because they may slightly change if a different batch of cells or a different chip geometry are considered. Doing so, ECs are seeded both at the top and at the bottom of the device, letting them grow on the lateral area of the gel.

5.2.4 Building a computational vascular network

The 3D-1D model has been used to simulate a vascular network inside a gel region. To obtain the vascular geometry, an *ad hoc* process has been set, starting from a 3D confocal image. Summarizing the process, the steps have been organized as follow (figure 5.10):

- import the 3D image on Fiji, and select the dextran channel;
- obtain a binary image by thresholding;
- apply the algorithm 'Skeletonize 3D' to obtain the centerlines of the network;
- export from Fiji the coordinate of the skeleton by an *ad hoc* script and importing them on Matlab;
- perform an interpolation of the vessel coordinate and a subsequent parametrization;
- divide each branch in N equally spaced nodes;
- write the geometry input file for the 3D-1D model.

Particular attention has been carried when handling the coordinate on Matlab. Indeed, the 3D-1D computational model identifies junction points by comparing the end coordinates of each branch. Therefore, constraints should be considered when performing the interpolation, namely, the endpoints should be kept unchanged. Considering $\boldsymbol{X} = (x_1, x_2, x_3)$ the spatial coordinate, and naming $\boldsymbol{X}^0$ and $\boldsymbol{X}^E$ the start and the end point of the vessel respectively, the parametrization has been performed defining each component of $\boldsymbol{X}$ as function of a parameter t such that:

$$
\begin{aligned}
&x_i = a_i + b_i\, t + c_i\, t^2 + d_i\, t^3 + e_i\, t^4 \\
&x_i = x_i^0 \quad for\, t = 0 \\
&x_i = x_i^E \quad for\, t = 1\,.
\end{aligned}
$$

Then the interpolation has been conducted by minimizing the difference between skeletonized data and the functions x_i determining the parameters a_i, b_i, c_i, and d_i, with $i = 1, 2, 3$. An exception to this process has been represented by short vessels. Even if they cannot be removed directly without badly affecting the connectivity of the network, they can be treated in a different way. Such a method prevents bad interpolation, which would results if a small number of points is considered. However, since they are small vessels, the overall area is not greatly affected by this assumption. Thus, after selecting them by a threshold based on the number of points resulting from the skeletonize process, short vessels have been interpolated by a line, namely by $x_i = x_i^0 + t\, x_i^E$. Once the analytical

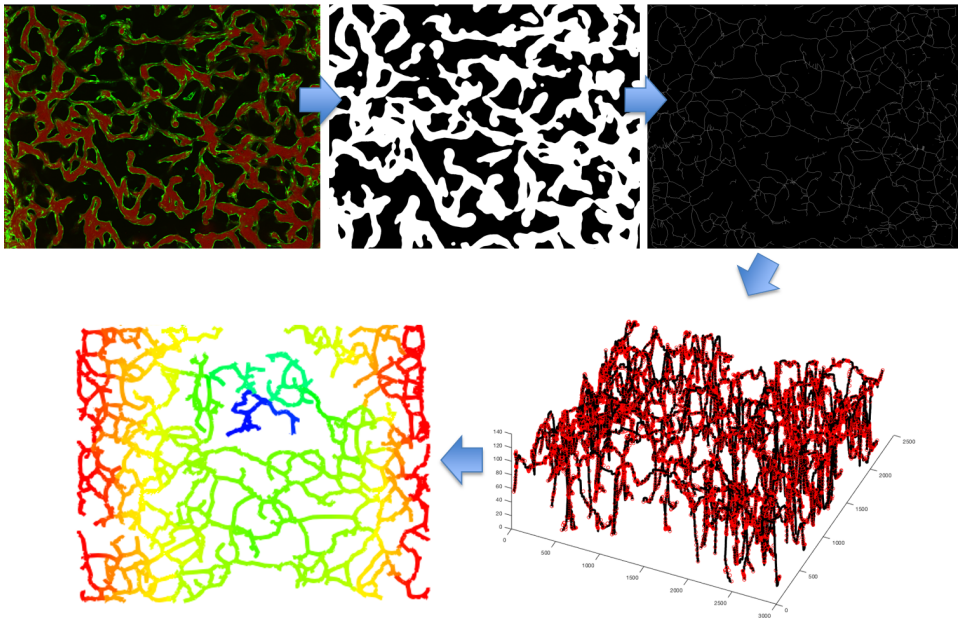

Figure 5.10: *Summary of the geometry reconstruction process. Following the path indicated by the arrows: confocal images of the network perfused with fluorescent dye, binary version of the image, skeleton of the image, interpolation and discretization of the network, and sample simulation with the 3D-1D model.*

description of the vessels was obtained, it has been divided into N equally spaced nodes, by using the parameter t. An example of the resulting description is shown in the figure 5.10.

At this point two further operations are required: (i) identification of the boundary conditions; (ii) radius computation. For the first one, two different steps have been implemented. All the junction points have been identified, namely the points which can be found as endpoint of more than one vessel. Consequently, all the remaining points are referred to one vessel solely. These points can either be inlet points, i.e. points of the network which are connected to the media channel, or dead ends. To discriminate among them, a threshold has been used based on the distance from the lateral boundary, namely the boundary of the gel on which the ECs monolayer has been built. In particular, such threshold has been defined as a percentage of the gel channel width. The network reconstruction may fail to recognize some interconnections with the monolayer, i.e. the opening to the media channel, because of the loss of a good tube-like shape of the vessel in that re-

gion. Therefore, the percentage has been selected as 5%, namely comprehending a region close to the boundary. The inlet pressure has been set equal in the two media channels. Due to this boundary conditions arrangement, no net flow rate is expected from one side to the other. Instead, to balance the filtration from the network, an inlet flow rate is foreseen from both the sides. Concerning the radius, a mean value has been computed, on the basis of the volume and the surface area of the network. Such operation allows a good estimate of the overall surface area of the network, but it is not accounting for radius heterogeneity. As a remark, to compute radius for each vessel, a new interaction between the skeleton and the 3D data is required. This may become an interesting future improvement of this algorithm.

5.2.5 Comparison between computational and experimental results

To compare experimental results with the computational, the velocity within the gel has been measured by means of Fluorescence Recovery After Photo-bleaching (FRAP) technique. To apply this technique, the gel should be previously filled with a fluorescent dye. Due to the presence of the ECs restricting the flux of the dye through both the monolayer and the vascular network, this process may take several hours to obtain a good signal to noise ratio. Once, the gel is filled with the dye, a spot is bleached by using the laser. Then two different phenomena happen. First, due to diffusion of the dye, the fluorescence is recovered, eventually making the spot disappear. Second, if any convective flux is present, the center of the spot moves accordingly to the flow. As a consequence, by tracking the spot, the velocity of the fluid can be estimated. To perform such a tracking procedure, a Matlab plugin has been used [1]. The velocity in the gel is consistent with the magnitude reported by the 3D-1D model, given that the monolayer is leakier than the network (see section 5.3.4). This is usually true because the vessel structure results to be tighter. Moreover, the L_p of the network in vitro may be greater than the one used in the simulations. Given these two clarifications, the experimental results fall in the same order of magnitude identified by the computational analysis.
Another qualitative proof of the trans-mural pressure has been obtained by looking at vessel deformations. In figure 5.11, two different frames of a video recorded at the inverted fluorescent microscope (Nikon Eclipse Ti-E) are reported, applying $18.7\,mmHg$ at the side channels. By comparing the two images, a slight radial displacement of the vessel can be seen, consequently suggesting that the pressure has increased more in the vasculature than in the gel, thus producing a trans-mural pressure difference.

[1] `https://it.mathworks.com/matlabcentral/fileexchange/29388-frap_analysis`

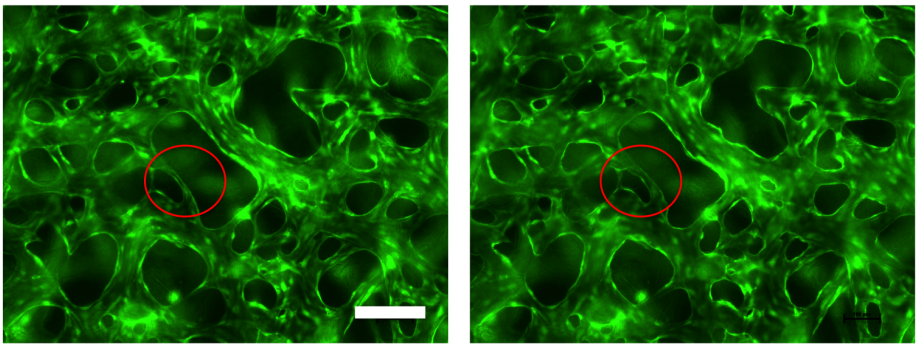

Figure 5.11: *Effect of inlet pressure on the vessel geometry (green signal depict GFP positive cells). On the left, geometry at zero inlet pressure. On the right: geometry for inlet pressure equal to* $18.7\,mmHg$*. White bar is* $100\,\mu m$*.*

5.3 Effects of urea on cells culture

Under uremic conditions, toxins are accumulated within the body both in the vasculature and in the interstitium, as presented in the first chapter. As recently reviewed by Vanholder and colleagues [168], urea has been largely used as a marker of solute retention, since it has been considered biologically inert. Recently, such a role has been discussed [168, 237] for two reasons. First, the kinetics of urea, classified as a small solute [44], is not representative of the removal kinetics of all the solutes. For this reason, models aimed at an overall description have been proposed (e.g. [54]). Second, the urea retention has been associated with several alterations, also linked to insulin resistance [238]. According to Vanholder and colleagues' work, the most common urea concentration among the studies related to uremic conditions is $20\,mM$. Such concentration has been used to study urea effect with reference to uremia. The urea effect has been tested by means of different types of cells: (i) vascular smooth muscle cells [239]; (ii) intestinal epithelial cells [240]; (iii) aortic endothelial cells [241]; and (iv) pancreatic β-cells [242]. D'Apolito and colleagues [241], in particular, study the urea effects on endothelial cells. They found an activation of pro-inflammatory markers, (e.g. reactive oxygen species, leukocyte vascular cell adhesion molecule-1, and monocyte chemotactic protein-1). In addition, it is well known that an increased inflammatory state may lead to a leakier vascular network. Another interesting study on vascular smooth muscle cells shows that increased concentration of urea may lead to apoptosis [239]. Conversely, Vaziri and colleagues analyzed the resistance of an epithelial cells monolayer (by testing its electrical resistance), to study the urea effect on the intestinal barrier [240]. Interestingly, the monolayer was found to be leakier when exposed to urea. In addition, they reported also a decrease in the expression of the tight junction proteins, such as ZO-1, claudin-1, and occludin.

Given these literature data, the *in vitro* platform has been used to study the effect of urea on the capillary membrane properties. Therefore, proper experiments have been run to analyze:

- the effect of urea on cells cultured in a plate;
- the expression of tight junction proteins (in particular VE-cadherin and ZO-1);
- the effects on the capillary membrane;
- the effects on the velocity distribution within the gel;
- the effects on the flow rate flowing in the chip due to the applied pressure.

5.3.1 Effect of urea on cells cultured in a plate

For all these tests HUVECs from Lonza® have been used. For the first experiment, ECs were plated with Vasculife® in a 24-multiwell, using $0.5\,ml$ at $50\,k/ml$. Culture media was replaced every 2 days. Three different media were used: (i) normal media; (ii) media + $1.3\,mg/ml$ of urea (EMD®); (iii) media + $2.6\,mg/ml$ of urea. Such concentrations have been computed on the basis of the median of a database of clinical data referred to uremic patients [200], and they are in agreement with the values reported in Vanholder and colleagues' review. The number of cells has been used as a marker of toxicity. ECs were stained by Hoechst, a fluorescent dye staining the DNA, and they were then imaged at the inverted fluorescent microscope (Nikon - Eclipse Ti-E). Doing so, the number of cells has been estimated by counting the number of nuclei. To count them, the Fiji plugin has been used after the application of the *watershed separation* to separate touching nuclei (due to microscope resolution), as it is usually done for this type of data. Among the 24-well, 8 have been used for each media condition. These 8 were divided by 4, analyzing 2 of them for each time point: 2, 4, 5, and 6 days of culture. The experiment was repeated twice. The normality of the data has been confirmed by a Kolmogorov-Smirnov test. Subsequently, the ANOVA test has been considered to test the presence of any difference among the sample. If found, the difference is further investigated comparing 2 groups per time. Results are shown in the figure 5.12 and 5.13. Results show no difference after 2 days of culture, whereas after 4 days the presence of urea within the media seems to have an effect. More precisely, the number of cells in a ROI is lower under the treated conditions. This effect is more evident considering a higher concentration. Comparing day 2 and 4, the number of cells in the control case increase, whereas both the treated condition do not. With the highest concentration, a decrease trend in the number of cells is clear after day 4. In particular, statistical differences have been found after day 4, as shown in the graph by the * and **. The schedule of the subsequent tests have been built because of these results.

5.3.2 Expression of tight junction proteins

As already discussed, the possible reduction of the tight junction protein expression has been addressed in the literature [240]. Even if that study has been conducted with reference to epithelial cells, a staining has been done to understand whether HUVECs are affected in a similar by way analyzing VE-cadherin and ZO-1 expression (by immunostaining with antibodies from R&D Scientific). The experimental protocol to obtain the urea-treated vascular network is now presented. Such a protocol has been used in the presented experiment and in all the experiments described from now on. The vascular network was

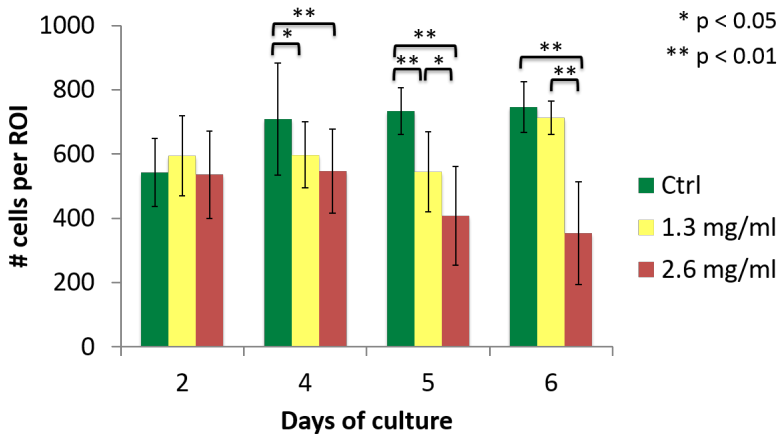

Figure 5.12: *Results for the test performed on multiwells. Statistical difference is highlighted as described in the graph, when present.*

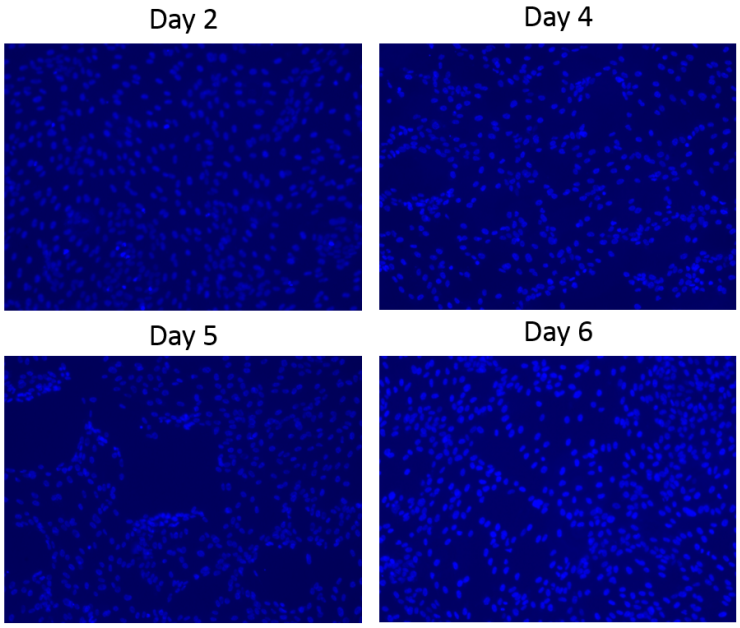

Figure 5.13: *Sample images on which the graph of the multiwell test is based. Different days are shown for a treated condition, in particular with* $1.3\,mg/ml$ *of urea. Hoescht stain was used to count cells nuclei.*

generated as described in the first section of this chapter, obtaining perfusable network by day 7. Once mature networks have been obtained, they have been cultured for 5 more days, using either normal media (control sample) or urea-enriched media (treated sample, with the same concentration used in the previous test $1.3\,mg/ml$ and $2.6\,mg/ml$). This protocol, summarized in figure 5.14, has been used for all the experiments described from now on. For this experiment only two conditions have been considered, namely the control and

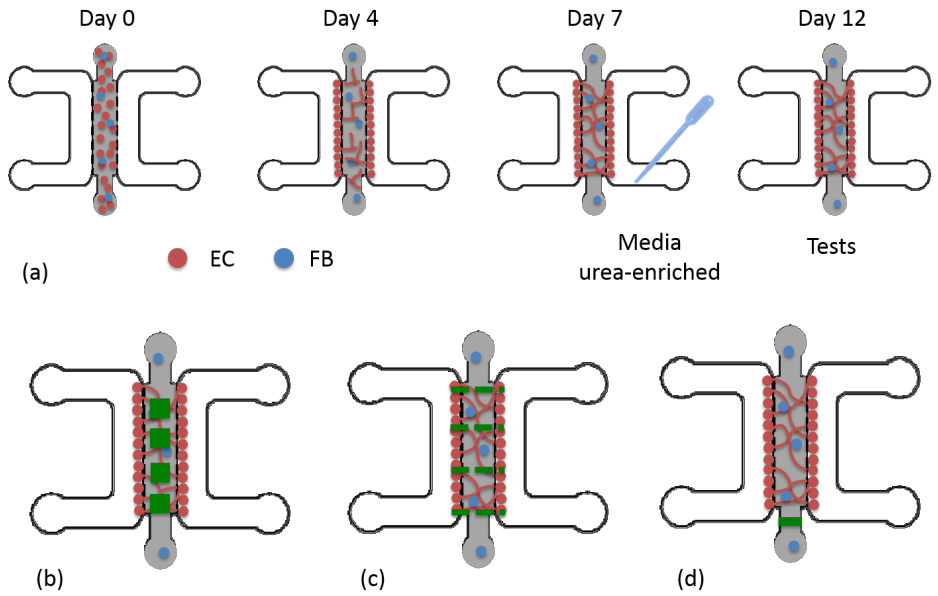

Figure 5.14: *Summary of the process to obtain vascular networks and test them. (a) From left to right: seeding (day 0), seeding of the ECs monolayer (day 4), starting the treatment after vessel maturation (day 7), and test (day 12). (b) ROI for the effective permeability test. (c) Lines considered for the FRAP analysis. (d) Location of the neck for the second FRAP experiment.*

the $1.3\,mg/ml$. To evaluate the expression of the tight junction proteins, an immunostaining has been performed with primary and secondary antibodies. Images depicting results of the staining are shown in figure 5.15. DAPI has been reported as blue, VE-cadherin in green and ZO-1 in red. The vascular structure is clearly recognizable in both the cases, with cell nuclei and VE-cadherin showing the vessel structure. In addition, the red color is present on the wall of the vessel although less visible. By looking at the particular image, ZO-1 seems to be less expressed than under the control conditions (figure 5.16). Yet, this should be verified by a more quantitative method, e.g. western blot. However, in both the

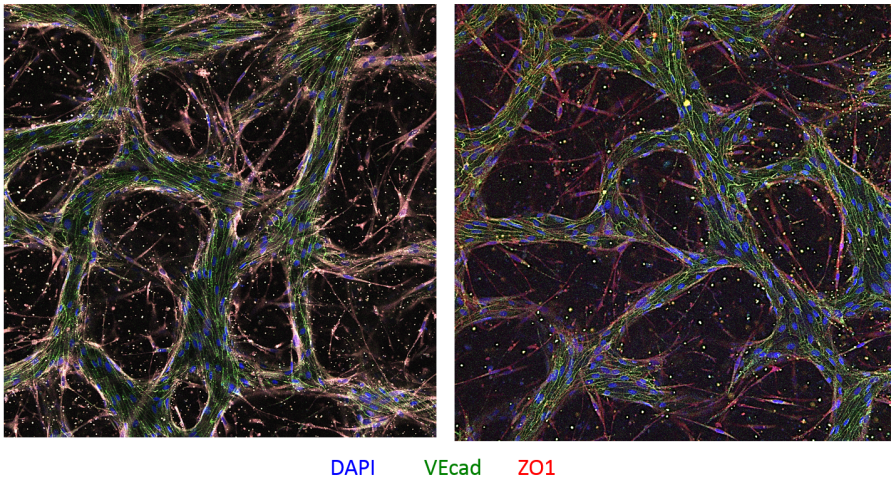

Figure 5.15: *Stained samples under control condition and treated with* $1.3\,mg/ml$ *of urea. DAPI shows cell nuclei (blue). Red and green color report junction proteins: VE-cadherin (green) and ZO-1 (red).*

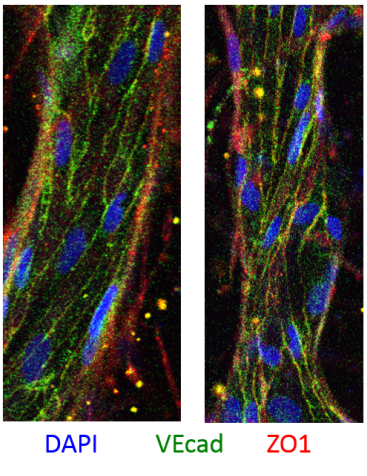

Figure 5.16: *Particular of the stained samples under control condition and treated with* $1.3\,mg/ml$ *of urea. DAPI shows cell nuclei (blue). Red and green color report junction proteins: VE-cadherin (green) and ZO-1 (red).*

cases, the two proteins seem to be co-localized, identifying cells membrane. Moreover, it should be noted that also the fibroblasts have resulted positive to the ZO-1 staining, highlighting possible unspecific binding. Fibroblasts are clearly recognizable by the elongated and branched structure. In order to extract quantitative information, this unspecific binding should be prevented.

5.3.3 The effects on capillary membrane

As described in the previous section, vascular networks have been cultured for 7 days and then treated (or not when considering controls) for other 5 days, reaching day 12. At that point, all the media were slowly removed from the side channel, and a solution of 40 kDa dextran (Sigma-Aldrich) at $0.1 mg/ml$ has been inserted in the lateral channels. Then the device has been prepared for the pressure test and located on the confocal microscope. Four different ROI are identified at $3\,mm$, $6\,mm$, $9\,mm$, and $12\,mm$ taking as a reference the outlet reservoir. The number of slices (i.e. the dimension of the sample in the vertical direction) has been defined as such that all signals can be captured and the duration of the test allows the use of a $\Delta t = 6\,min$ between two subsequent measure on the same ROI. Δz, namely the distance between two slices, has been set to $5\,\mu m$. Indeed, two different time points are required to perform a permeability measure. Five different pressure have been applied for each test: $0\,Pa$, $200\,Pa$, $400\,Pa$, $600\,Pa$, $800\,Pa$. The condition relative to $0\,Pa$ corresponds to the real permeability measure, in which convective phenomena are not considered. Conversely, when an inlet pressure is applied, the effective permeability can be computed as previously discussed and from those data the factor $L_p\,(1-\sigma)$ can be outlined. Results of the permeability test are shown in figure 5.17. According to previous results regarding the effect of urea, the control seems to provide a better barrier effect. In particular both the permeability and the estimated $L_p\,(1-\sigma)$ (table 5.2) are lower than under treated conditions. Such coefficient seems to highlight a difference also due to

Table 5.2: *Results of the effective permeability analysis.*

Condition	$L_p\,(1-\sigma)\,(cm\,s^{-1}\,Pa^{-1})$
Control	6×10^{-11}
$1.3\,mg/ml$	1×10^{-10}
$2.6\,mg/ml$	5×10^{-10}

urea concentrations. However, by noting the large error bar in the graph, it is clear that a higher number of samples should be considered to draw statistically significant conclu-

sions. Moreover, an interesting local phenomenon has been observed, as shown in figure 5.18 in agreement with what reported by [139]. Authors have reported similar phenomena during permeability tests (i.e. without applying pressure), in HUVECs vasculature treated by TNFα. They explained these local leaks with possible cell death due to the high concentration of the substance. Here similar effects may be produced by the urea treatment. However, it might be caused by the increase of pressure. This phenomenon may contribute to the high standard deviation of the results. In addition, in some cases they have appeared to be transient. Indeed, imaging the same ROI 6 minutes later, the local leak has not been found. The dextran inserted into the gel has been transported through the gel, eventually reaching a *pseudo-flat* intensity profile. However, specific experiments should be run to investigate this phenomena.

5.3.4 Velocity distribution within the gel

The velocity distribution within the gel has been estimated by the aforementioned FRAP technique. To have an estimate of the velocity distribution within the gel a total of 24 points have been analyzed for each experiment. These points have been aligned on parallel lines across the width of the chip, in correspondence of the 4 ROI previously used in the effective permeability quantification (figure 5.14). As a consequence, 6 points have been defined for each of these lines. Starting from this data the median, the 1^{st}, and the 3^{rd} quartile have been computed. First, a test on a control chip has been performed, varying the inlet pressure. Results are reported in the figure 5.19. The median velocity increases with the pressure as expected. Indeed, a higher inlet pressure causes a greater filtration rate, leading to a larger flow rate, and consequently increasing the velocity within the gel. A similar test has been conducted by applying the inlet pressure of $400\ Pa$ considering a control chip and two treated chip, one for each concentration considered. Results are reported in figure 5.20. The median of the velocity within the gel increases with the concentration of urea in the media. However, such an increase may reflect a greater filtration rate as already discussed. In this case, this higher filtration rate has been caused by the presence of the urea. To further analyze these data, a velocity map has been built on these 24 points. Even if the resolution of the data is not high considering the dimension of the chip, some important information have been revealed (figure 5.21). Indeed, the greater velocity within the gel has resulted to depend more on local phenomena than on distributed effects of urea. This is in agreement with the local phenomena described in the previous section. Moreover, these results suggest that such local leaks are more frequent with a higher urea concentration. By looking at the figure referred to urea, two different kind leaks can be identified. The first one, occurred in both the sample with urea, happens close to the angle. It is more plausible that this condition has been caused by a leak at the corner of the monolayer rather than a

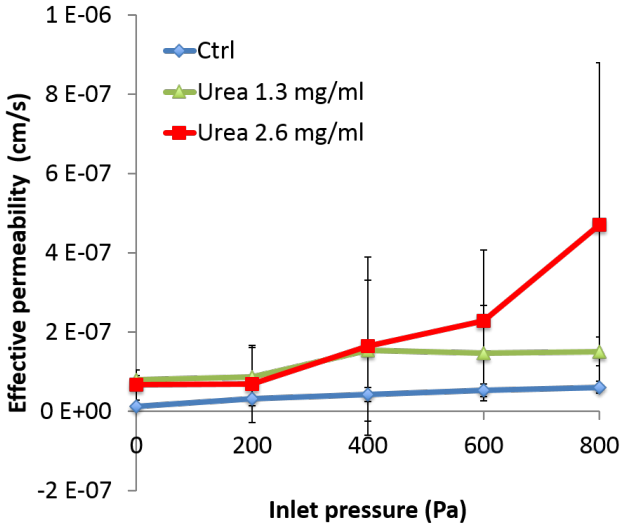

Figure 5.17: *Graph of the effective permeability under control and treated conditions.*

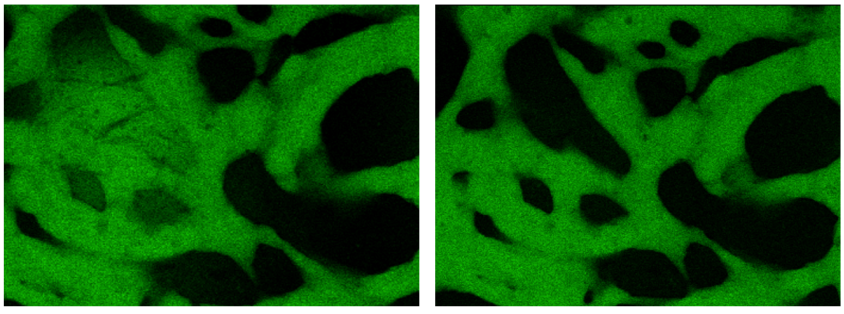

Figure 5.18: *Local leak in the network. On the right the same ROI, 6 minutes later.*

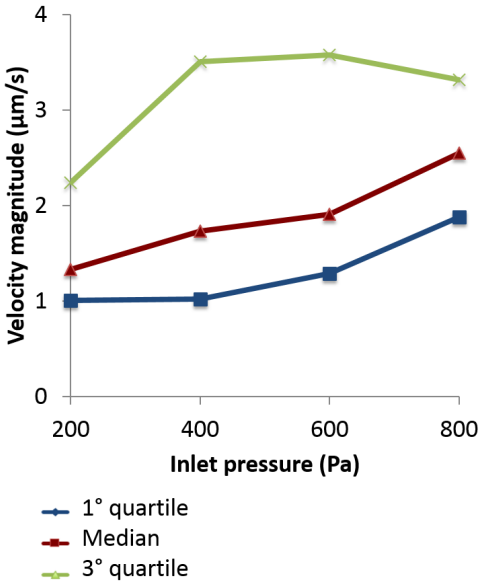

Figure 5.19: *Results of the FRAP analysis varying the inlet pressure under control conditions.*

leak from the network. The second one, occurred only in the case with the highest urea concentration happens in the center of the chip. This is more likely due to a local leak from the network.

5.3.5 Flow rate estimation

A similar experiment has been conducted by applying an inlet pressure and measuring velocity by FRAP. Conversely to what was described in the previous section, the velocity has been estimated with a more dense sampling, accounting for 20 points, located within the neck of the chip (figure 5.14). Considering these values, an estimate of the average velocity can be obtained. From this value, an estimate of the flow rate flowing within the chip can be performed. By comparing the averaged values of the velocity, the relative increase of the hydraulic conductivity can be estimated as:

$$\frac{L_p}{L_{p,ctrl}} \simeq \frac{v_{avg}}{v_{avg,ctrl}} .$$

Such an equation has been obtained on the following assumptions: (i) negligible variations of the dimensions of the chip; (ii) negligible variations of the network density and morphology, i.e. $\simeq$ exchange area; (iii) comparable area of the monolayer; (iv) the treatment

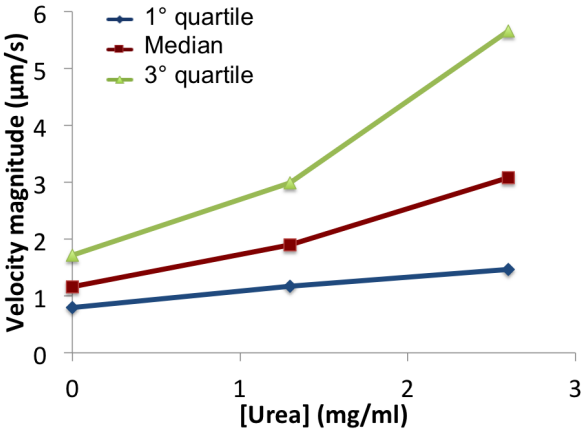

Figure 5.20: *Results of the FRAP analysis varying the urea concentration in the media.*

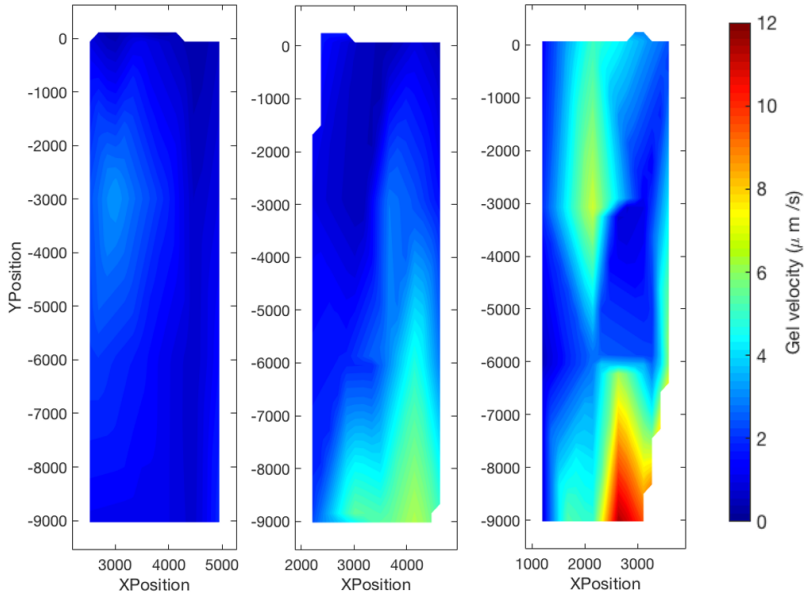

Figure 5.21: *Velocity magnitude distribution interpolated with a Matlab script, with reference to the FRAP analysis varying the urea concentration in the media. For left to right: control,* $1.3\,mg/ml$*, and* $2.6\,mg/ml$*.*

does not affect the gel. Based on that equation, results are shown in the figure 5.22. Even in

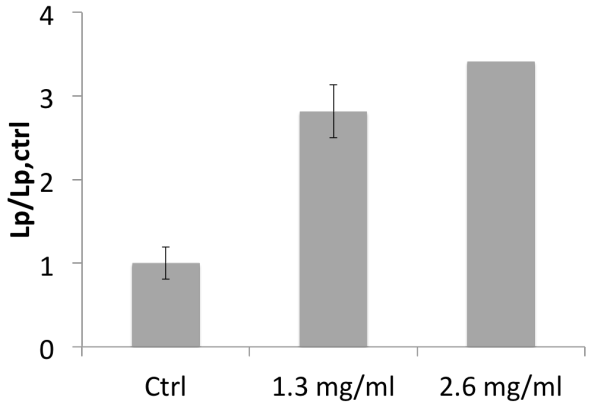

Figure 5.22: *Results of the FRAP analysis for the estimation of the flow rate flowing within the network.*

this case, the treatment with urea seems to produce a greater hydraulic conductivity of the membrane. This effect also seems to increase along with urea concentration. However, as denoted by the absence of the error bars, as for the greatest considered concentration only one sample has been successfully tested. The described effect can either derive from local phenomena as described in the previous sections, or it can be due to a more distributed effect. However, the two effects cannot be distinguished by this kind of test. Anyway, the validity of the assumptions should be further discussed. All the geometrical assumption, i.e. $i - iii$, can be investigated by comparing several samples measuring all these quantities. From them, an uncertainty propagation analysis can be performed, to understand how the variation of these quantities can affect the results. Moreover, a test which uses only with gel can validate the iv-th assumption, by showing differences, if any, due to the presence of the urea. As a remark, the contribution to this increase cannot be ascribed to the vascular network only. Actually, the presence of the monolayer should be considered, resulting in a more general information about the effect on both the vasculature and the monolayer. In particular, the contribution of the latter is probably the most significant, as described by means of the 3D-1D simulations varying its L_p.

5.4 Discussion

The proposed method to generate microvasculature on a chip has been widely used in literature [129]. By applying pressure at the media channel, the generation of a trans-mural pressure has been computationally analyzed using two different methodologies. This trans-mural pressure difference is generated when an ECs monolayer is built on the side of the gel, namely separating the gel and the media channel. Computational results highlight that a tighter monolayer provides a better trans-mural pressure generation and it allows the analysis of the permeability considering filtration from the network. Despite the fact that the described experimental setup enables the *in vitro* analysis of uremic toxins on the capillary membrane, it is still affected by several limitations. First, the intrinsic biological variability affects the analysis. Therefore, a higher number of samples is required to provide significant results validated also by statistical analysis. Second, the effect of shear stress [243] has not been considered since no flow rate is allowed through the two sides of the vascular network. Finally, the overall system is quite delicate. Therefore, failures may result from gel detaching, incomplete monolayer, rupture of the monolayer, or low perfusion of the network resulting in vascular fluorescence variations over time. An example of the failure of the monolayer is shown in figure 5.23. In that image, a defect in the monolayer generates a local important leak, which allows dextran to enter the gel directly from the side. However, these problems can be prevented by refining the experimental technique and minimizing its possible variations.

Some specific features of the presented test should be discussed. First, the velocity obtained by the FRAP is the fluid velocity, whereas the velocity resulting from the computational model is the Darcy velocity. It is linked to the real velocity of the fluid flowing through the pores by the porosity of the media, namely $v_D = v_{real} * \psi$, where ψ is the porosity which can assume values between 0 and 1. As a consequence, a certain value of v_D corresponds to a slightly greater value of v_{real}, precisely by a factor $1/\psi$, which is strictly greater than 1. Given that the porosity of the gel is close to 1, the difference between these two velocities is small. Such difference affects the result comparison, but it has a small effect if compared to the inter-sample experimental variability. Therefore, keeping in mind this little discrepancy, the computational and the experimental results have been directly compared. Second, in the junction protein analysis, a quantitative information can be extracted by the western blot procedure. However, such an operation has found to be affected by the presence of urea in the sample. Therefore, the quantitative information have not been extracted in this case. Moreover, HUVECs has been considered in this analysis, since they are the most used ECs in microvascular network formation. However, more specific ECs can be used, such as microvascular endothelial cells, or specific ECs to

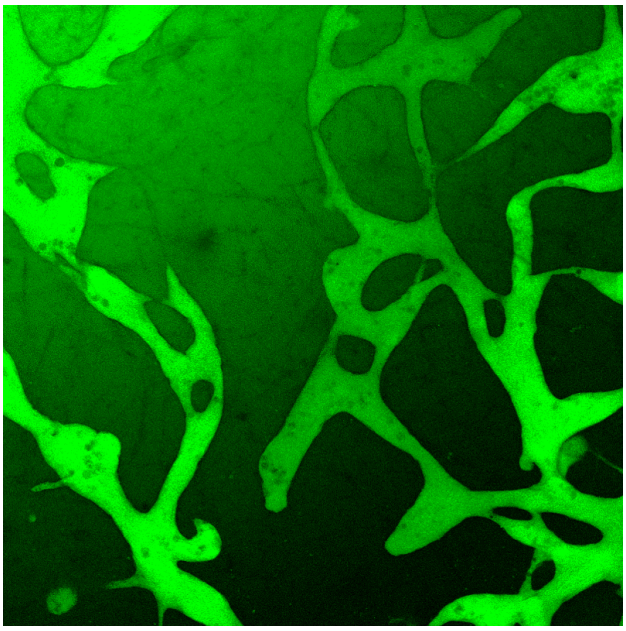

Figure 5.23: *Example of a local leak from the monolayer which cause the failure of the sample.*

model a determined tissue. Doing so, a protocol to obtain microvascular network should be set up first, if it is not available in literature. Finally, addressing the $L_p\,(1-\sigma)$ factor, an analysis with a very small solute can be performed, namely using a solute for which $\sigma \simeq 0$. However, this condition rapidly evolves into a condition in which one of the assumptions does not hold true, specifically the approximation of the difference of intensity with the intensity within the vasculature. This reduces the amount of time available for a test, leading to a more experimentally complex handling of the technique.

Even considering these limitations, the presented setup allows the analysis of urea effects on the capillary wall membrane. Since the number of successful tests was low, the statistical definition of alterations produced by the solute was not possible. However, all the different performed test suggest an effect of urea concentration. This approach, with a higher numerosity of the sample, can be applied to study the effect of uremic toxins on cells and on the capillary membrane, to better understand microvasculature under uremic conditions. Uremic solutes toxicity has also been recently addressed by different works, and some key points such as the toxicity of urea are being re-discussed. This *in vitro* approach represents a good platform to analyze such toxicity. Moreover, it can also be applied to study different phenomena related to the pathology or to its treatments. For

example, the decrease of the reflection coefficient of plasma proteins [127] can be investigated. As shown by the sensitivity analysis performed by the 3D-1D model, this variable directly affects the fluid balance within the microvasculature. Another possible application is the study of solutes kinetics in the micro-environment. Indeed, some solutes are not easily removed by dialysis, and they may suffer from compartmentalization. For example, a solute store within the interstitial space has to go through the capillary membrane first, before reaching the blood and being transported to the dialyzer (if hemodialysis is considered). The further understanding of such phenomena represents a first step toward a possible improvement of the dialysis therapy. A further interaction with the 3D-1D model would be possible thanks to the implementation of the mass transport on the computational model. This improvement will allow the deeper analysis of the dextran transport, strictly coupling experimental data with the computational model.

CHAPTER 6

General discussion and conclusions

In this conclusive chapter, a discussion of the overall approach is given. Finally, research activities enabled by the present work are discussed.

6.1 The overall modeling approach

In this work, a comprehensive modeling approach to study microvasculature has been proposed in order to analyze the uremic microvasculature. Such a modeling approach consists of three different models, and their possible interactions (figure 6.1). First, the peripheral description of the lumped parameter model has been analyzed. A modification of such description has been proposed to better describe fluid balance. This modification enables the interaction with the 3D-1D model, given the coherence of the descriptions. Simulations have been run to show the key role of the lymphatic drainage and the requirements for a comprehensive approach, therefore confirming the role of this model in the overall modeling approach. Secondly, the 3D-1D model has been built accounting also for non-linearities in the description of the lymphatic flow rate and the typical phenomena related to blood flow within the microvasculature. Starting from the available literature data, this model has been used to simulate the effect of uremic microvascular alterations on the filtration and on the interstitial pressure. The effects of these alterations have been deeper looked into through a sensitivity analysis. Furthermore, an *in vitro* model has been proposed to analyze the effect of uremic toxins on the vessel membrane by applying a trans-mural pressure difference. The experimental setup has been analyzed through computational models in order to highlight the key role of the ECs monolayer to obtain the trans-mural pressure. Finally, the model has been applied to study the effect of urea on the capillary membrane.

Together, these models enable the study of uremic alterations accounting for macro- and micro- vasculature, towards a full multiscale model. Each of these models has its own limitations and advantages, which have been discussed in the work. Besides these limitations, the models represent an advanced tool to study the uremic microvascular alterations. Moreover, one of the advantages of such a comprehensive approach is the possible interactions between the three models. For example, alterations of the capillary membrane studied with the *in vitro* model can be used to tune the 3D-1D model. In the figure 6.1 the interactions are described highlighting the ones already addressed in this work and those enabled by these modeling approaches. For instance, the lumped parameter model has been used to analyze the flow assumptions for microcirculation, computing typical dimensionless numbers, and confirming viscous forces dominance. In addition, the improvement of the peripheral description has paved the way for an interaction between the two computational models, which may serve several purposes. Among others, it helps describe and understand possible variations of capillary pressure in pathological subjects. Direct measurement of such alterations is challenging for multiple reasons. Accounting for vascular regulation, the lumped parameter model can be used to figure out vascular pres-

sure variations to be further studied with the 3D-1D model. However, it should be noted that vascular regulation may be impaired under uremic conditions, due to the presence of uremic toxins and fluid overload. For example, the presence of urea may induce accumulation of advanced glycation end products [241], which are known to affect vascular response to shear stress [244,245]. As a consequence, a validation and adjustment process is required to go further with the vascular regulation modeling. Concerning interactions of the 3D-1D model and the *in vitro*, the first has been used to describe the experimental setup, addressing the trans-mural pressure generation. By means of this analysis, a weakness of the experimental technique has been identified. This has allowed the improvement of the technique, enabling a better analysis of the capillary membrane properties. Moreover, a qualitative similarity has been observed between the *in vitro* vascular network and the generated artificial networks. The latter have been generated by a random algorithm based on a 2D version of the Voronoi tessellation (which ensure only bifurcations within the network) and a subsequent 3D perturbation. This result supports the proposed artificial network-generation process. In addition, this work enabled a key interaction between these two models. More precisely, by coupling the 3D-1D and the *in vitro* model, the alterations of the capillary wall induced by uremic toxins can be studied and modeled. Their identification, together with their concentrations, is currently being addressed by different groups, and the total number of uremic toxins has exceeded one hundred. Possible changes in the morphology of the network can be also addressed by the *in vitro* model and then included in the 3D-1D model. If necessary, mass transport and diffusion modeling can be included in the model thanks to the model structure. Indeed, the transport of RBCs is already present in the model. This feature allows a further analysis of the experimental setup. For example, by including albumin in the media and analyzing its distribution, researchers can study the distribution of oncotic pressures. Another possible interaction enabled by this model is the study of the red blood cells flow in complex network, by coupling the 3D-1D model and the experimental model. RBCs interaction with the glycocalyx and the possible variations of such an interaction due to the uremic pathology can be studied and further analyzed.

The presented models and their interactions can be applied in future studies aimed at enhancing our understanding of uremia. The *in vitro* model can be used to identify the effect of uremic toxins on microvascular wall properties leading to a better understanding of pathological variations of vascular-interstitial fluid and mass transport. In addition, the possible effects of uremic toxins on the glycocalyx can be assessed by specifically analyzing that structure using the already developed experimental protocol similar to those presented in this work. The inclusion of glycocalyx-related phenomena in the 3D-1D computational model will allow an interaction with the *in vitro* model to describe pro-

tein transport in both the vasculature and the interstitium. Such experiments can support the research efforts towards the understanding of glycocalyx-related effects on filtration. They will allow the study of proteins transport, their interaction with uremic toxins and how such interaction affects their transport under pathological conditions. Further experiments should also deal with the possible modification of vascular regulations due to the pathology, also involving patients' real data if necessary (e.g. variations of the shear-stress-related regulation). This kind of variations can also be investigated by using the lumped parameter model.

As a final remark, these models and their iterations may also be applied to other contexts. One example is the tumor micro-environment. The 3D-1D and the *in vitro* model can be used to analyze possible treatments, or phenomena involving the micro-environment.

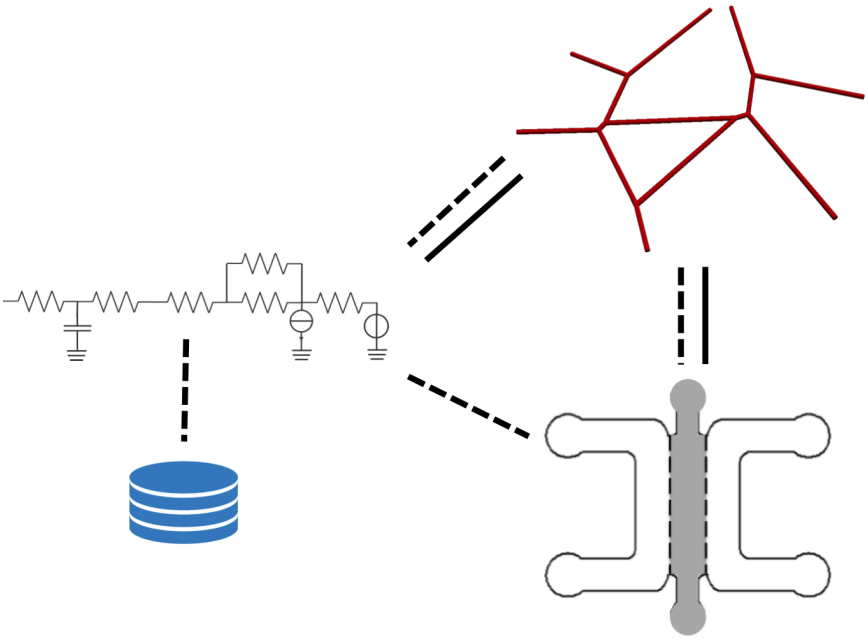

Figure 6.1: *Schematic of the models considered in the work. Solid lines indicate current interactions between the models. Dotted lines stand for possible useful interactions enabled by the adopted modeling approach. The blue database depicts clinical data that can be used for model validation as discussed in the text.*

6.2 Conclusion

Over the last few years, the interest in microvascular alterations under uremic conditions has significantly grown. Many phenomena are involved in these alterations resulting in a very complex scenario. In this work, a wide and multifaceted modeling approach has been developed to analyze them, exploiting both computational and experimental tools. Such an approach allows the study of complex phenomena from manifold different points of view, including aspects that have not been deeply studied yet, such as the effects of uremic toxins on the capillary wall membrane, capillary rarefaction, and the role of microvascular morphology. Based on these results, the role of different quantities or parameters can be outlined and assessed. Moreover, the results have verified the effectiveness of the applied models in investigating microvascular wall membrane alterations. It can be concluded that this work has paved the way for subsequent studies dealing with alterations in microvasculature under uremic conditions. Applying extensively these methods to analyze such alterations in uremic patients will result in a better understanding of their effects. These researches can eventually lead to a better design of the dialysis treatment.

Publications

Papers

Possenti, Di Gregorio, Gerosa, Raimondi, Casagrande, Costantino and Zunino. A computational model for microcirculation including Fahraeus-Lindqvist effect, plasma skimming and fluid exchange with the tissue interstitium. *International Journal for Numerical Methods in Biomedical Engineering*, (*in press*).

Possenti, Casagrande, Di Gregorio, Zunino and Costantino. Numerical simulations of the microvascular fluid balance with a non-linear model of the lymphatic system. *Microvascular Research*, (*in press*).

Proceedings

Offeddu, **Possenti**, Loessberg-Zahl, Costantino, Hickman, Knutson, Kamm. Perfusable microvascular networks on-chip enable direct measurement of physiologically-relevant transendothelial molecular transport *Proceedings of the 2018 MRS Fall Meeting, November 25th-30th, Boston.*

Possenti, Casagrande, Costantino. A lumped parameter model of vascular peripheries for CKD patients: a step towards multiscale modelling. *Proceedings of the XLV ESAO Congress, September 12th - 15th 2018, Madrid.*

Possenti, Casagrande, Di Gregorio, Zunino, and Costantino. Computational modeling of the interaction of lymphatic and vascular microcirculation in uremia. *Proceedings of the GNB conference, June 25th - 27th, 2018, Milano.*

Possenti, Casagrande, Di Gregorio, Laurino, Costantino, and Zunino. A computational model for vascular fluid balance at the microscale. *Proceedings of the ECCM 6 and ECFD 7, June 11th -15th 2018, Glasgow.*

Possenti, Casagrande, Di Gregorio, Costantino and Zunino. A computational model of the interaction between continua and networks: application to microcirculation and uremy. *Proceedings of the 33rd international CAE conference and exhibition, November 6th - 7th 2017, Vicenza.*

Possenti, Casagrande, Costantino, Zunino. Numerical modelling of microcirculation fluid exchanges in uremic patients accounting for the non-linear effect of lymphatic system. *Proceedings of the 44th ESAO and 7th IFAO Congress, September 6th - 9th 2017, Vienna.*

Casagrande, **Possenti**, Costantino. Modelling of cardiovascular alterations during CKD progression. *Proceedings of the 44th ESAO and 7th IFAO Congress, September 6th - 9th 2017, Vienna.*

Possenti, Casagrande, Costantino, Zunino. A computational model of the interaction between microcirculation and tissue interstitium. *Proceedings of the Prediction and Modeling of response to Molecular and External Beam Radiotherapies, September 20th - 23th 2017, Le Bono.*

List of Figures

List of Tables

Bibliography

[1] W. J. KOLFF, H. TH J. BERK, NURSE M. WELLE, A. J.W. van der LEY, E. C. van DIJK, and J. van NOORDWIJK. The Artificial Kidney: a dialyser with a great area. *Acta Medica Scandinavica*, 117(2):121–134, 1944.

[2] Garabed Eknoyan. Meeting the challenges of the new K/DOQI guidelines. *American Journal of Kidney Diseases*, 41(6):3–10, 2003.

[3] Eli A Friedman. Introduction and Options in Therapy. pages 1–7. mar 2010.

[4] Clare B. Jones and Joanne M. Bargman. Should we look beyond Kt / V urea in assessing dialysis adequacy? *Seminars in Dialysis*, 31(4):420–429, 2018.

[5] John Hall. *Guyton and Hall Textbook of Medical Physiology 13th Edition*. 2015.

[6] Ahmad Taher Azar. *Modeling and Control of Dialysis Systems*, volume 53. 2013.

[7] Ravindra L. Mehta and et al. Kellum. Acute kidney injury network: Report of an initiative to improve outcomes in acute kidney injury. *Critical Care*, 11(2):1–8, 2007.

[8] R Bellomo, J A Kellum, and C Ronco. Acute renal failure: time for consensus. *Intensive Care Med*, 27:1685–1688, 2001.

[9] Kai Singbartl and John A. Kellum. AKI in the ICU: Definition, epidemiology, risk stratification, and outcomes. *Kidney International*, 81(9):819–825, 2012.

[10] Linda Y. Belayev and Paul M. Palevsky. The link between acute kidney injury and chronic kidney disease. *Current Opinion in Nephrology and Hypertension*, 23(2):149–154, 2014.

[11] National Kidney Foundation. *K/DOQI Clinical Practice Guidelines for Chronic Kidney Disease: Evaluation, Clasification and Stratification*, volume 39. 2002.

[12] Noreen Chikotas, Annette Gunderman, and Terina Oman. Uremic syndrome and end-stage renal disease: Physical manifestations and beyond. *Journal of the American Academy of Nurse Practitioners*, 18(5):195–202, 2006.

[13] Timothy W. Meyer and Thomas H. Hostetter. Uremia. *New England Journal of Medicine*, 357(13):1316–1325, sep 2007.

[14] ERA-EDTA. ERA-EDTA Annual Report 2016. Technical report, 2016.

[15] SP Chakraborty. PHYSIOLOGICAL COMPLICATIONS IN CHRONIC KIDNEY DISEASE. *International Journal of Recent Scientific Research*, 9(4):25588–25593, 2018.

[16] Shadi Ahmadmehrabi and W. H.Wilson Tang. Hemodialysis-induced cardiovascular disease. *Seminars in Dialysis*, 31(3):258–267, 2018.

[17] Bahman Jabbari and Nosratola D. Vaziri. The nature, consequences, and management of neurological disorders in chronic kidney disease. *Hemodialysis International*, 22(2):150–160, 2018.

[18] Hamid Moradi, Domenic A. Sica, and Kamyar Kalantar-Zadeh. Cardiovascular burden associated with uremic toxins in patients with chronic kidney disease. *American Journal of Nephrology*, 38(2):136–148, 2013.

[19] Srisakul Chirakarnjanakorn, Sankar D. Navaneethan, Gary S. Francis, and W.H. Wilson Tang. Cardiovascular impact in patients undergoing maintenance hemodialysis: Clinical management considerations. *International Journal of Cardiology*, 232:12–23, 2017.

[20] Christoph Wanner, Kerstin Amann, and Tetsuo Shoji. The heart and vascular system in dialysis. *The Lancet*, 388(10041):276–284, 2016.

[21] USRDS. 2017 USRDS Annual Data Report: Executive Summary. Technical Report 3, 2017.

[22] Jan Malik. Heart disease in chronic kidney disease - review of the mechanisms and the role of dialysis access. *The Journal of Vascular Access*, pages 0–0, 2017.

[23] T. Graham. The Bakerian Lecture: On Osmotic Force. *Philosophical Transactions of the Royal Society of London*, 144:177–228, jan 1854.

[24] J J Abel, L G Rowntree, and B B Turner. On the removal of diffusable substances from the circulating blood by means of dialysis. Transactions of the Association of American Physicians, 1913. *Transfusion science*, 11(2):164–5, 1990.

[25] J Benedum. [Georg Haas (1886-1971), pioneer in hemodialysis]. *Schweizerische Rundschau fur Medizin Praxis = Revue suisse de medecine Praxis*, 75(14):390–4, apr 1986.

[26] Jan Kurkus, Marie Nykvist, Birger Lindergård, and Mårten Segelmark. Thirty-Five Years of Hemodialysis: Two Case Reports as a Tribute to Nils Alwall. *American Journal of Kidney Diseases*, 49(3):471–476, 2007.

[27] Ben J Lipps, Richard D Stewart, Herbert A Perkins, George W Holmes, Earl A McLain, Mary R Rolfs, and Phyllis D Oja. The hollow fibr artificial kidney. *ASAIO Journal*, 13(1):200–207, 1967.

[28] B. Canaud, J. L. Bragg-Gresham, M. R. Marshall, S. Desmeules, B. W. Gillespie, T. Depner, P. Klassen, and F. K. Port. Mortality risk for patients receiving hemodiafiltration versus hemodialysis: European results from the DOPPS. *Kidney International*, 69(11):2087–2093, 2006.

[29] Ernest H. Starling. On the Absorption of Fluids from the Connective Tissue Spaces. *The Journal of Physiology*, 19(4):312–326, may 1896.

[30] Leonard M. Ebah, Helge Wiig, Idalia Dawidowska, Charlotte O'Toole, Angela Summers, Milind Nikam, Anuradha Jayanti, Beatrice Coupes, Paul Brenchley, and Sandip Mitra. Subcutaneous interstitial pressure and volume characteristics in renal impairment associated with edema. *Kidney International*, 84(5):980–988, 2013.

[31] Mauro Pietribiasi, Jacek Waniewski, Alicja Załuska, Wojciech Załuska, and Bengt Lindholm. Modelling transcapillary transport of fluid and proteins in hemodialysis patients. *PLoS ONE*, 11(8):1–22, 2016.

[32] Domenico Vito, Giustina Casagrande, Giulia Cappoli, Camilla Bianchi, Giuseppe Pontoriero, Carlo Schoenholzer, Claudio Minoretti, Giuseppe Rombolà, Maria Laura Costantino, Domenico Vito, Giustina Casagrande, Giulia Cappoli, and Camilla Bianchi. A predictive index of intra-dialysis IDH A statistical clinical data mining approach. *INTERNATIONAL JOURNAL OF ADVANCES IN SOFTWARE ENGINEERING & RESEARCH METHODOLOGY*, 2(2):109–113, 2015.

[33] Daniel Schneditz, Johannes Roob, Martina Oswald, Helmuth Pogglitsch, Maximilian Moser, Thomas Kenner, and Ulrich Binswanger. Nature and rate of vascular refilling during hemodialysis and ultrafiltration. *Kidney International*, 42(6):1425–1433, 1992.

[34] J. Rodney Levick and C. Charles Michel. Microvascular fluid exchange and the revised Starling principle. *Cardiovascular Research*, 87(2):198–210, 2010.

[35] F Ikomi, J Hunt, G Hanna, and G W Schmid-Schönbein. Interstitial fluid, plasma protein, colloid, and leukocyte uptake into initial lymphatics. *Journal of applied physiology (Bethesda, Md. : 1985)*, 81(5):2060–2067, 1996.

[36] James E. Moore and Christopher D Bertram. Lymphatic System Flows. *Annual Review of Fluid Mechanics*, 50(1):459–482, jan 2018.

[37] L. Rügheimer, P. Hansell, and M. Wolgast. Determination of the charge of the plasma proteins and consequent Donnan equilibrium across the capillary barriers in the rat microvasculature. *Acta Physiologica*, 194(4):335–339, 2008.

[38] Manoj K. Sharma, Fokko P. Wieringa, Arjan J.H. Frijns, and Jeroen P. Kooman. On-line monitoring of electrolytes in hemodialysis: on the road towards individualizing treatment. *Expert Review of Medical Devices*, 13(10):933–943, 2016.

[39] Camilla Bianchi. *Patient-specific Modelling for Hemodialysis Therapy Setting Optimization*. Phd thesis, Politecnico di Milano, 2017.

[40] Flavio M. De Paula, Aldo J. Peixoto, Luciano V. Pinto, David Dorigo, Pedro J.M. Patricio, and Sergio F.F. Santos. Clinical consequences of an individualized dialysate sodium prescription in hemodialysis patients. *Kidney International*, 66(3):1232–1238, 2004.

[41] Csaba P. Kovesdy, Deborah L. Regidor, Rajnish Mehrotra, Jennie Jing, Charles J. McAllister, Sander Greenland, Joel D. Kopple, and Kamyar Kalantar-Zadeh. Serum and dialysate potassium concentrations and survival in hemodialysis patients. *Clinical Journal of the American Society of Nephrology*, 2(5):999–1007, 2007.

[42] A. Santoro, E. Mancini, R. Gaggi, S. Cavalcanti, S. Severi, L. Cagnoli, F. Badiali, B. Perrone, G. London, H. Fessy, L. Mercadal, and F. Grandi. Electrophysiological Response to Dialysis: The Role of Dialysate Potassium Content and Profiling. In *Cardiovascular Disorders in Hemodialysis*, pages 295–305. KARGER, Basel, 2005.

[43] John Kyriazis, John Glotsos, Leonidas Bilirakis, Nikos Smirnioudis, Maria Tripolitou, Fotios Georgiakodis, and Irene Grimani. Dialysate calcium profiling during hemodialysis: Use and clinical implications. *Kidney International*, 61(1):276–287, 2002.

[44] Raymond Vanholder, Rita De Smet, Griet Glorieux, Angel Argilés, Ulrich Baurmeister, Philippe Brunet, William Clark, Gerald Cohen, Peter Paul De Deyn, Reinhold Deppisch, Beatrice Descamps-Latscha, Thomas Henle, Achim Jörres, Horst Dieter Lemke, Ziad A. Massy, Jutta Passlick-Deetjen, Mariano Rodriguez, Bernd Stegmayr, Peter Stenvinkel, Ciro Tetta, Christoph Wanner, and Walter Zidek. Review on uremic toxins: Classification, concentration, and interindividual variability. *Kidney International*, 63(5):1934–1943, 2003.

[45] Barbara Lisowska-Myjak. Uremic toxins and their effects on multiple organ systems. *Nephron - Clinical Practice*, 128:303–311, 2014.

[46] F. Duranton, G. Cohen, R. De Smet, M. Rodriguez, J. Jankowski, R. Vanholder, and A. Argiles. Normal and Pathologic Concentrations of Uremic Toxins. *Journal of the American Society of Nephrology*, 23(7):1258–1270, 2012.

[47] Richard L. Amdur, Harold I. Feldman, Jayanta Gupta, Wei Yang, Peter Kanetsky, Michael Shlipak, Mahboob Rahman, James P. Lash, Raymond R. Townsend, Akinlolu Ojo, Akshay Roy-Chaudhury, Alan S. Go, Marshall Joffe, Jiang He, Vaidyanathapuram S. Balakrishnan, Paul L. Kimmel, John W. Kusek, and Dominic S. Raj. Inflammation and progression of CKD: The CRIC study. *Clinical Journal of the American Society of Nephrology*, 11(9):1546–1556, 2016.

[48] Jayanta Gupta, Nandita Mitra, Peter A. Kanetsky, Joe Devaney, Maria R. Wing, Muredach Reilly, Vallabh O. Shah, Vaidyanathapura S. Balakrishnan, Nicolas J. Guzman, Matthias Girndt, Brian G. Periera, Harold I. Feldman, John W. Kusek, Marshall M. Joffe, Dominic S. Raj, and CRIC Study Investigators. Association between albuminuria, kidney function, and inflammatory biomarker profile in CKD in CRIC. *Clinical journal of the American Society of Nephrology : CJASN*, 7(12):1938–1946, 2012.

[49] Hana Zelová and Jan Hošek. TNF-α signalling and inflammation: Interactions between old acquaintances. *Inflammation Research*, 62(7):641–651, 2013.

[50] JR Bradley. Tnf-mediated inflammatory disease. *The Journal of Pathology*, 214(2):149–160, 2008.

[51] Salvatore di Filippo, Fabio Carfagna, Vincenzo la Milia, Antonio Bellasi, Giustina Casagrande, Camilla Bianchi, Domenico Vito, Maria Laura Costantino, Giuseppe Rombolà, Claudio Minoretti, Carlo Schönholzer, Giuseppe Pontoriero, and Francesco Locatelli. Assessment of intradialysis calcium mass balance by a single pool variable-volume calcium kinetic model. *Hemodialysis International*, 22(1):126–135, 2018.

[52] John K. Leypoldt, Baris U. Agar, Alfred K. Cheung, and Angelito A. Bernardo. A Pseudo-One Compartment Model of Phosphorus Kinetics During Hemodialysis: Further Supporting Evidence. *Artificial Organs*, 41(11):1043–1048, 2017.

[53] Camilla Bianchi, Ettore Lanzarone, Giustina Casagrande, and Maria Laura Costantino. Identification of Patient-Specific Parameters in a Kinetic Model of Fluid and Mass Transfer During Dialysis. pages 139–149. 2017.

[54] Giustina Casagrande, Camilla Bianchi, Domenico Vito, Fabio Carfagna, Claudio Minoretti, Giuseppe Pontoriero, Giuseppe Rombolà, Carlo Schoenholzer, and Maria Laura Costantino. Patient-specific modeling of multicompartmental fluid and mass exchange during dialysis. *International Journal of Artificial Organs*, 39(5):220–227, 2016.

[55] Aurelio A. De Los Reyes V, Doris H. Fuertinger, Franz Kappel, Anna Meyring-Wösten, Stephan Thijssen, and Peter Kotanko. A physiologically based model of vascular refilling during ultrafiltration in hemodialysis. *Journal of Theoretical Biology*, 390:146–155, 2016.

[56] P. W. Chamney, C. Johner, C. Aldridge, M. Krämer, N. Valasco, J. E. Tattersall, T. Aukaidey, R. Gordon, and R. N. Greenwood. Fluid balance modelling in patients with kidney failure. *Journal of Medical Engineering and Technology*, 23(2):45–52, 1999.

[57] Kaoru Tabei, Hirofumi Nagashima, Osamu Imura, Toshihiro Sakurai, and Yasushi Asano. An index of plasma refilling in hemodialysis patients? *Nephron*, 74(2):266–274, 1996.

[58] RN Pittman. *Regulation of Tissue Oxygenation*. Morgan & Claypool Life Sciences, San Rafael (CA), 2011.

[59] AB Ritter, S Reisman, and BB Michniak. *Biomedical Engineering Principles*. CRC Press, Boca Raton, FL, 2005.

[60] Alfio Quarteroni. Cardiovascular Mathematics. In *Proceedings of the International Congress of Mathematicians, Madrid, Spain*, 2009.

[61] T. W. Secomb. Blood flow in the microcircaulation. *Annual Review of Fluid Mechanics*, 49:443–461, 2017.

[62] Michael Potente and Taija Mäkinen. Vascular heterogeneity and specialization in development and disease. *Nature Reviews Molecular Cell Biology*, 18(8):477–494, 2017.

[63] Amy F. Smith, Timothy W. Secomb, Axel R. Pries, Nicolas P. Smith, and Rebecca J. Shipley. Structure-based algorithms for microvessel classification. *Microcirculation*, 22(2):99–108, 2015.

[64] Matthias Jacob, Daniel Chappell, and Bernhard F. Becker. Regulation of blood flow and volume exchange across the microcirculation. *Critical Care*, 20(1):1–13, 2016.

[65] David D. Gutterman, Dawid S. Chabowski, Andrew O. Kadlec, Matthew J. Durand, Julie K. Freed, Karima Ait-Aissa, and Andreas M. Beyer. The Human Microcirculation: Regulation of Flow and beyond. *Circulation Research*, 118(1):157–172, 2016.

[66] David A. Rubenstein, Wei Yin, and Mary D. Frame. *Biofluid mechanics : an introduction to fluid mechanics, macrocirculation, and microcirculation*.

[67] Richard Daneman and Alexandre Prat. The Blood Brain Barrier. *Cold Spring Harbor Perspectives in Biology*, 7(1):a020412, jan 2015.

[68] W M Deen. What determines glomerualr capillary permeability? *J Clin Invest*, 114(10):1412–1414, 2004.

[69] Benjamin William Zweifach. The structure and reactions of the small blood vessels in Amphibia. *The american journal of anatomy*, 60(3):473–514, 1937.

[70] Tatsuo Sakai and Yasue Hosoyamada. Are the precapillary sphincters and metarterioles universal components of the microcirculation? An historical review. *Journal of Physiological Sciences*, 63(5):319–331, 2013.

[71] Melody A. Swartz and Mark E. Fleury. Interstitial Flow and Its Effects in Soft Tissues. *Annual Review of Biomedical Engineering*, 9(1):229–256, 2007.

[72] Petros C. Benias, Rebecca G. Wells, Bridget Sackey-Aboagye, Heather Klavan, Jason Reidy, Darren Buonocore, Markus Miranda, Susan Kornacki, Michael Wayne, David L. Carr-Locke, and Neil D. Theise. Structure and distribution of an unrecognized interstitium in human tissues. *Scientific Reports*, 8(1):1–8, 2018.

[73] S. R. Chary and R. K. Jain. Direct measurement of interstitial convection and diffusion of albumin in normal and neoplastic tissues by fluorescence photobleaching. *Proceedings of the National Academy of Sciences*, 86(14):5385–5389, 1989.

[74] Hagit Dafni, Tomer Israely, Zaver M. Bhujwalla, Laura E. Benjamin, and Michal Neeman. Overexpression of vascular endothelial growth factor 165 drives peritumor interstitial convection and induces lymphatic drain: Magnetic resonance imaging, confocal microscopy, and histological tracking of triple-labeled albumin. *Cancer Research*, 62(22):6731–6739, 2002.

[75] Rakesh K Jain. Transport of Molecules, Particles, and Cells in Solid Tumors. *Annu. Rev. Biomed. Eng*, 01(96):241–263, 1999.

[76] K. Sven and F. Josipa. Interstitial Hydrostatic Pressure: a Manual for Students. *AJP: Advances in Physiology Education*, 31(1):116–117, 2007.

[77] Samira Jamalian, Mohammad Jafarnejad, Scott D Zawieja, Christopher D Bertram, Anatoliy A Gashev, David C Zawieja, Michael J Davis, and James E Moore. Demonstration and Analysis of the Suction Effect for Pumping Lymph from Tissue Beds at Subatmospheric Pressure. *Scientific Reports*, 7(1):12080, 2017.

[78] Melody A Swartz. The physiology of the lymphatic system. *Advanced Drug Delivery Reviews*, 50:3–20, 2001.

[79] H. Wiig and M. A. Swartz. Interstitial Fluid and Lymph Formation and Transport: Physiological Regulation and Roles in Inflammation and Cancer. *Physiological Reviews*, 92(3):1005–1060, 2012.

[80] Antoine Louveau, Igor Smirnov, Timothy J. Keyes, Jacob D. Eccles, Sherin J. Rouhani, J. David Peske, Noel C. Derecki, David Castle, James W. Mandell, Kevin S. Lee, Tajie H. Harris, and Jonathan Kipnis. Structural and functional features of central nervous system lymphatic vessels. *Nature*, 523(7560):337–341, 2015.

[81] Eleni Bazigou, John T. Wilson, and James E. Moore. Primary and secondary lymphatic valve development: Molecular, functional and mechanical insights. *Microvascular Research*, 96(3):38–45, nov 2014.

[82] J. TRZEWIK. Evidence for a second valve system in lymphatics: endothelial microvalves. *The FASEB Journal*, 15(10):1711–1717, 2001.

[83] Peter Baluk, Jonas Fuxe, Hiroya Hashizume, Talia Romano, Erin Lashnits, Stefan Butz, Dietmar Vestweber, Monica Corada, Cinzia Molendini, Elisabetta Dejana, and Donald M. McDonald. Functionally specialized junctions between endothelial cells of lymphatic vessels. *The Journal of Experimental Medicine*, 204(10):2349–2362, 2007.

[84] Jerome W Breslin. Mechanical Forces and Lymphatic Transport. *Microvasc Res*, 0(813):46–54, 2014.

[85] Mahmoud Al-Kofahi, J. Winny Yun, Alireza Minagar, and J. Steven Alexander. Anatomy and roles of lymphatics in inflammatory diseases. *Clinical and Experimental Neuroimmunology*, 8(3):199–214, 2017.

[86] Daniel Vittet. Lymphatic collecting vessel maturation and valve morphogenesis. *Microvascular Research*, 96:31–37, 2014.

[87] Peter Galie and Robert L. Spilker. A Two-Dimensional Computational Model of Lymph Transport Across Primary Lymphatic Valves. *Journal of Biomechanical Engineering*, 131(11):111004, 2009.

[88] Ernesto Mendoza, Geert W., and Schmid-Schonbein. A Model for Mechanics of Primary Lymphatic Valves. *Journal of Biomechanical Engineering*, 125(3):407, 2003.

[89] Patrick M. Lynch, Frank A. DeLano, and Geert W. Schmid-Schönbein. The Primary Valves in the Initial Lymphatics during Inflammation. *Lymphatic Research and Biology*, 5(1):3–10, 2007.

[90] K. N. Margaris and R. A. Black. Modelling the lymphatic system: challenges and opportunities. *Journal of The Royal Society Interface*, 9(69):601–612, 2012.

[91] Robin Fåhraeus. THE SUSPENSION STABILITY OF THE BLOOD. *Physiological Reviews*, 9(2):241–274, apr 1929.

[92] Robin Fåhræus and Torsten Lindqvist. THE VISCOSITY OF THE BLOOD IN NARROW CAPILLARY TUBES. *American Journal of Physiology-Legacy Content*, 96(3):562–568, mar 1931.

[93] K. Svanes and B. W. Zweifach. Variations in small blood vessel hematocrits produced in hypothermic rats by micro-occlusion. *Microvascular Research*, 1(2):210–220, 1968.

[94] Y C Fung. Stochastic flow in capillary blood vessels. *Microvascular Research*, 5(1):34–48, 1973.

[95] S. P. Sutera, V. Seshadri, P. A. Croce, and R. M. Hochmuth. Capillary blood flow. II. Deformable model cells in tube flow. *Microvascular Research*, 2(4):420–433, 1970.

[96] Peter Gaehtgens. Flow of blood through narrow capillaries: Rheological mechanisms determining capillary hematocrit and apparent viscosity1. *Biorheology*, 17(1-2):183–189, dec 1980.

[97] A. R. Pries, D. Neuhaus, and P. Gaehtgens. Blood viscosity in tube flow: dependence on diameter and hematocrit. *American Journal of Physiology-Heart and Circulatory Physiology*, 263(6):H1770–H1778, dec 1992.

[98] A. R. Pries, T. W. Secomb, T. Gessner, M. B. Sperandio, J. F. Gross, and P. Gaehtgens. Resistance to blood flow in microvessels in vivo. *Circulation Research*, 75(5):904–915, 1994.

[99] Simone DI GREGORIO. *Mathematical and numerical model of red blood cells transport in the microvasculature*. Master thesis, Politecnico di Milano, 2017.

[100] A. R. Pries, T. W. Secomb, and P. Gaehtgens. The endothelial surface layer. *Pflugers Archiv European Journal of Physiology*, 440(5):653–666, 2000.

[101] Dominik Obrist, Bruno Weber, Alfred Buck, and Patrick Jenny. Red blood cell distribution in simplified capillary networks. *Philosophical Transactions of the Royal Society A: Mathematical, Physical and Engineering Sciences*, 368(1921):2897–2918, 2010.

[102] Franca Schmid, Johannes Reichold, Bruno Weber, and Patrick Jenny. The impact of capillary dilation on the distribution of red blood cells in artificial networks. *American Journal of Physiology - Heart and Circulatory Physiology*, 308(7):H733–H742, 2015.

[103] Sung Yang, Akif Ündar, and Jeffrey D. Zahn. A microfluidic device for continuous, real time blood plasma separation. *Lab on a Chip*, 6(7):871–880, 2006.

[104] A. R. Pries. Microvascular blood viscosity in vivo and the endothelial surface layer. *AJP: Heart and Circulatory Physiology*, 289(6):H2657–H2664, 2005.

[105] G. W. Schmid-Schönbein, R. Skalak, S. Usami, and S. Chien. Cell distribution in capillary networks. *Microvascular Research*, 19(1):18–44, 1980.

[106] A. R. Pries, K. Ley, M. Claassen, and P. Gaehtgens. Red cell distribution at microvascular bifurcations. *Microvascular Research*, 38(1):81–101, 1989.

[107] Navid Safaeian and Tim David. A computational model of oxygen transport in the cerebrocapillary levels for normal and pathologic brain function. *Journal of Cerebral Blood Flow & Metabolism*, 33(10):1633–1641, 2013.

[108] Daniel Goldman and Aleksander S. Popel. A computational study of the effect of capillary network anastomoses and tortuosity on oxygen transport. *Journal of Theoretical Biology*, 206(2):181–194, 2000.

[109] BRENDAN C. FRY, JACK LEE, NICOLAS P. SMITH, and TIMOTHY W. SECOMB. Estimation of Blood Flow Rates in Large Microvascular Networks. *Microcirculation*, 19(6):530–538, aug 2012.

[110] Graham M Fraser. *Modeling Oxygen Transport in Three-Dimensional Capillary Networks*. Phd thesis, Western University, 2012.

[111] Peter M. Rasmussen, Timothy W. Secomb, and Axel R. Pries. Modeling the hematocrit distribution in microcirculatory networks: A quantitative evaluation of a phase separation model. *Microcirculation*, 25(3):1–17, 2018.

[112] Ian G. Gould and Andreas A. Linninger. Hematocrit distribution and tissue oxygenation in large microcirculatory networks. *Microcirculation*, 22(1):1–18, 2015.

[113] Toru Hyakutake and Shinya Nagai. Numerical simulation of red blood cell distributions in three-dimensional microvascular bifurcations. *Microvascular Research*, 97:115–123, 2015.

[114] Francesco Clavica, Alexandra Homsy, Laure Jeandupeux, and Dominik Obrist. Red blood cell phase separation in symmetric and asymmetric microchannel networks: Effect of capillary dilation and inflow velocity. *Scientific Reports*, 6(October):1–12, 2016.

[115] Zaiyi Shen, Gwennou Coupier, Badr Kaoui, Benoît Polack, Jens Harting, Chaouqi Misbah, and Thomas Podgorski. Inversion of hematocrit partition at microfluidic bifurcations. *Microvascular Research*, 105:40–46, 2016.

[116] A. J. Staverman. The theory of measurement of osmotic pressure. *Recueil des Travaux Chimiques des Pays-Bas*, 70(4):344–352, 1951.

[117] O. Kedem and A. Katchalsky. Thermodynamic analysis of the permeability of biological membranes to non-electrolytes. *BBA - Biochimica et Biophysica Acta*, 27(C):229–246, 1958.

[118] Eugene M. Landis. MICRO-INJECTION STUDIES OF CAPILLARY PERMEABILITY - II. *American Journal of Physiology-Legacy Content*, 82(2):217–238, oct 1927.

[119] John R Pappenheimer and Armando Soto-Rivera. EFFECTIVE OSMOTIC PRESSURE OF THE PLASMA PROTEINS AND OTHER QUANTITIES ASSOCIATED WITH THE CAPILLARY CIRCULATION IN THE HINDLIMBS OF CATS AND DOGS. *American Journal of Physiology-Legacy Content*, 152(3):471–491, feb 1948.

[120] Eugene M. Landis. MICRO-INJECTION STUDIES OF CAPILLARY PERMEABILITY - I. *American Journal of Physiology-Legacy Content*, 81(1):124–142, jun 1927.

[121] C C Michel and Mary E Phillips. Steady-state fluid filtration at different capillary pressures in perfused frog mesenteric capillaries. *The Journal of physiology*, 388:421–35, jul 1987.

[122] C. C. Michel. Starling: The formulation of his hypothesis of microvascular fluid exchange and its significance after 100 years. *Experimental Physiology*, 82(1):1–30, 1997.

[123] Sheldon Weinbaum. 1997 Whitaker distinguished lecture: Models to solve mysteries in biomechanics at the cellular level; a new view of fiber matrix layers. *Annals of Biomedical Engineering*, 26(4):627–643, 1998.

[124] E.M. Gabriel, D.T. Fisher, S. Evans, K. Takabe, and J.J. Skitzki. Intravital microscopy in the study of the tumor microenvironment: From bench to human application. *Oncotarget*, 9(28):20165–20178, 2018.

[125] Isik Ocak, Atila Kara, and Can Ince. Monitoring microcirculation. *Best Practice and Research: Clinical Anaesthesiology*, 30(4):407–418, 2016.

[126] Yu Chang Yeh, Anne Chao, Chih-Yuan Lee, Chen-Tse Lee, Chi-Chuan Yeh, Chih-Min Liu, and Meng-Kun Tsai. An observational study of microcirculation in dialysis patients and kidney transplant recipients. *European Journal of Clinical Investigation*, pages 1–8, 2017.

[127] Steven J. Harper, Charles R.V. Tomson, and David O. Bates. Human uremic plasma increases microvascular permeability to water and proteins in vivo. *Kidney International*, 61(4):1416–1422, 2002.

[128] Yongzhi Qiu, Byungwook Ahn, Yumiko Sakurai, Caroline E. Hansen, Reginald Tran, Patrice N. Mimche, Robert G. Mannino, Jordan C. Ciciliano, Tracey J. Lamb, Clinton H. Joiner, Solomon F. Ofori-Acquah, and Wilbur A. Lam. Microvasculature-on-a-chip for the long-term study of endothelial barrier dysfunction and microvascular obstruction in disease. *Nature Biomedical Engineering*, pages 1–11, 2018.

[129] Kristina Haase and Roger D Kamm. Advances in on-chip vascularization. *Regenerative Medicine*, 12(3):285–302, 2017.

[130] Jessie S. Jeon, Simone Bersini, Jordan A. Whisler, Michelle B. Chen, Gabriele Dubini, Joseph L. Charest, Matteo Moretti, and Roger D. Kamm. Generation of 3D functional microvascular networks with mural cell-differentiated human mesenchymal stem cells in microfluidic vasculogenesis systems. *Integrative Biology*, 100(2):130–134, 2015.

[131] Jennie M. Burns, Xiaoxi Yang, Omid Forouzan, Jose M. Sosa, and Sergey S. Shevkoplyas. Artificial microvascular network: A new tool for measuring rheologic properties of stored red blood cells. *Transfusion*, 52(5):1010–1023, 2012.

[132] Sergey S. Shevkoplyas, Sean C. Gifford, Tatsuro Yoshida, and Mark W. Bitensky. Prototype of an in vitro model of the microcirculation. *Microvascular Research*, 65(2):132–136, 2003.

[133] Hagit Stauber, Dan Waisman, Netanel Korin, and JosuïÂ¿Â$\frac{1}{2}$ Sznitman. Red blood cell dynamics in biomimetic microfluidic networks of pulmonary alveolar capillaries. *Biomicrofluidics*, 11(1), 2017.

[134] Judith C.A. Cluitmans, Venkatachalam Chokkalingam, Arno M. Janssen, Roland Brock, Wilhelm T.S. Huck, and Giel J.C.G.M. Bosman. Alterations in Red Blood Cell Deformability during Storage: A Microfluidic Approach. *BioMed Research International*, 2014, 2014.

[135] Walter H. Reinhart, Nathaniel Z. Piety, and Sergey S. Shevkoplyas. Influence of feeding hematocrit and perfusion pressure on hematocrit reduction (Fåhræus effect) in an artificial microvascular network. *Microcirculation*, 24(8):1–10, 2017.

[136] Kristen T. Morin and Robert T. Tranquillo. In vitro models of angiogenesis and vasculogenesis in fibrin gel. *Experimental Cell Research*, 319(16):2409–2417, oct 2013.

[137] Jordan A. Whisler, Michelle B. Chen, and Roger D. Kamm. Control of Perfusable Microvascular Network Morphology Using a Multiculture Microfluidic System. *Tissue Engineering Part C: Methods*, 20(7):543–552, 2014.

[138] Sudong Kim, Hyunjae Lee, Minhwan Chung, and Noo Li Jeon. Engineering of functional, perfusable 3D microvascular networks on a chip. *Lab on a Chip*, 13(8):1489–1500, 2013.

[139] Michelle B. Chen, Jordan A. Whisler, Jessie S. Jeon, and Roger D. Kamm. Mechanisms of tumor cell extravasation in an in vitro microvascular network platform. *Integrative Biology*, 5(10):1262, 2013.

[140] Michelle B. Chen, Jordan A. Whisler, Julia Fröse, Cathy Yu, Yoojin Shin, and Roger D. Kamm. On-chip human microvasculature assay for visualization and quantification of tumor cell extravasation dynamics. *Nature Protocols*, 12(5):865–880, 2017.

[141] Seema M Ehsan, Katrina M Welch-Reardon, Marian L Waterman, C W Christopher, Steven C George, Molecular Genetics, Christopher C W Hughes, Steven C George, C W Christopher, Steven C George, and Molecular Genetics. A three-dimensional in vitro model of tumor cell intravasation. *Integrative Biology*, 6(6):603–610, 2014.

[142] Julia C. Arciero, Paola Causin, and Francesca Malgaroli. Mathematical methods for modeling the microcirculation. *AIMS Biophysics*, 4(3):362–399, 2017.

[143] Dmitry A. Fedosov, Bruce Caswell, Aleksander S. Popel, and George E M Karniadakis. Blood Flow and Cell-Free Layer in Microvessels. *Microcirculation*, 17(8):615–628, 2010.

[144] Peter Balogh and Prosenjit Bagchi. A computational approach to modeling cellular-scale blood flow in complex geometry. *Journal of Computational Physics*, 334:280–307, 2017.

[145] Prosenjit Bagchi. Mesoscale simulation of blood flow in small vessels. *Biophysical Journal*, 92(6):1858–1877, 2007.

[146] Chenghai Sun, Rakesh K. Jain, and Lance L. Munn. Non-Uniform Plasma Leakage Affects Local Hematocrit and Blood Flow: Implications for Inflammation and Tumor Perfusion. *Annals of Biomedical Engineering*, 35(12):2121–2129, nov 2007.

[147] Richard Hsu and Timothy W. Secomb. A Green's function method for analysis of oxygen delivery to tissue by microvascular networks. *Mathematical Biosciences*, 96(1):61–78, 1989.

[148] Timothy w. Secomb. A Green's function method for simulation of time-dependent solute transport and reaction in realistic microvascular geometries. *Mathematical Medicine and Biology*, 33(4):475–494, 2016.

[149] A. N. Cookson, J. Lee, C. Michler, R. Chabiniok, E. Hyde, D. Nordsletten, and N. P. Smith. A spatially-distributed computational model to quantify behaviour of contrast agents in MR perfusion imaging. *Medical Image Analysis*, 18(7):1200–1216, 2014.

[150] Eoin R. Hyde, Andrew N. Cookson, Jack Lee, Christian Michler, Ayush Goyal, Taha Sochi, Radomir Chabiniok, Matthew Sinclair, David A. Nordsletten, Jos Spaan, Jeroen P.H.M. Van Den Wijngaard, Maria Siebes, and Nicolas P. Smith. Multi-scale parameterisation of a myocardial perfusion model using whole-organ arterial networks. *Annals of Biomedical Engineering*, 42(4):797–811, 2014.

[151] N. Zhao and K. Iramina. Numerical simulation of effect of convection-diffusion on oxygen transport in microcirculation. *Applied Mathematics and Mechanics (English Edition)*, 36(2):179–200, 2015.

[152] B. Tully and Y. Ventikos. Cerebral water transport using multiple-network poroelastic theory: Application to normal pressure hydrocephalus. *Journal of Fluid Mechanics*, 667:188–215, 2011.

[153] Jeonghun J. Lee, Eleonora Piersanti, Kent-Andre Mardal, and Marie E. Rognes. A mixed finite element method for nearly incompressible multiple-network poroelasticity. pages 1–27, apr 2018.

[154] James W. Baish, Paolo A. Netti, and Rakesh K. Jain. Transmural coupling of fluid flow in microcirculatory network and interstitium in tumors. *Microvascular Research*, 53(2):128–141, 1997.

[155] Paola Causin, Giovanna Guidoboni, Francesca Malgaroli, Riccardo Sacco, and Alon Harris. Blood flow mechanics and oxygen transport and delivery in the retinal microcirculation: multiscale mathematical modeling and numerical simulation. *Biomechanics and Modeling in Mechanobiology*, 15(3):525–542, 2016.

[156] M. Sefidgar, M. Soltani, K. Raahemifar, M. Sadeghi, H. Bazmara, M. Bazargan, and M. Mousavi Naeenian. Numerical modeling of drug delivery in a dynamic solid tumor microvasculature. *Microvascular Research*, 99:43–56, 2015.

[157] Jennifer H. Siggers, Kritsada Leungchavaphongse, Chong Hang Ho, and Rodolfo Repetto. Mathematical model of blood and interstitial flow and lymph production in the liver. *Biomechanics and Modeling in Mechanobiology*, 13(2):363–378, 2014.

[158] Paola Causin and Francesca Malgaroli. Mathematical modeling of local perfusion in large distensible microvascular networks. *Computer Methods in Applied Mechanics and Engineering*, 323:303–329, 2017.

[159] A. R. Pries and T. W. Secomb. Making Microvascular Networks Work: Angiogenesis, Remodeling, and Pruning. *Physiology*, 29(6):446–455, 2014.

[160] C. Pozrikidis and D. A. Farrow. A model of fluid flow in solid tumors. *Annals of Biomedical Engineering*, 31(2):181–194, 2003.

[161] Carlo D'Angelo. *Multicale Modelling of Metabolism and Transport Phenomena in Living Tissues*. Phd thesis, ÉCOLE POLYTECHNIQUE FÉDÉRALE DE LAUSANNE, 2007.

[162] L Cattaneo and P Zunino. Computational models for fluid exchange between microcirculation and tissue interstitium. *Networks and Heterogeneous Media*, 9(1):135–159, 2014.

[163] L. Cattaneo and P. Zunino. A computational model of drug delivery through microcirculation to compare different tumor treatments. *International Journal for Numerical Methods in Biomedical Engineering*, 30(11):1347–1371, nov 2014.

[164] Louis Gagnon, Amy F. Smith, David A. Boas, Anna Devor, Timothy W. Secomb, and Sava Sakadžić. Modeling of Cerebral Oxygen Transport Based on In vivo Microscopic Imaging of Microvascular Network Structure, Blood Flow, and Oxygenation. *Frontiers in Computational Neuroscience*, 10(August):1–20, 2016.

[165] Ian Gopal Gould, Philbert Tsai, David Kleinfeld, and Andreas Linninger. The capillary bed offers the largest hemodynamic resistance to the cortical blood supply. *Journal of Cerebral Blood Flow and Metabolism*, 37(1):52–68, 2017.

[166] C D'ANGELO and Alfio Quarteroni. On the coupling of 1d and 3d diffusion-reaction equations: Application to tissue perfusion problems. *Mathematical Models and Methods in ...*, (28):23, 2008.

[167] Tobias Köppl, Ettore Vidotto, Barbara Wohlmuth, and Paolo Zunino. Mathematical modeling, analysis and numerical approximation of second-order elliptic problems with inclusions. *Mathematical Models and Methods in Applied Sciences*, 28(05):953–978, 2018.

[168] Raymond Vanholder, Tessa Gryp, and Griet Glorieux. Urea and chronic kidney disease: the comeback of the century? (in uraemia research). *Nephrology Dialysis Transplantation*, 33(1):4–12, jan 2017.

[169] R. Vanholder, U. Baurmeister, P. Brunet, G. Cohen, G. Glorieux, and J. Jankowski. A Bench to Bedside View of Uremic Toxins. *Journal of the American Society of Nephrology*, 19(5):863–870, 2008.

[170] Antonietta Gigante, Biagio Barbano, Giuseppe Barilaro, Silvia Quarta, Maria Ludovica Gasperini, Francesca Di Mario, Antonella Romaniello, Antonio Amoroso, Rosario Cianci, and Edoardo Rosato. Serum uric acid as a marker of microvascular damage in systemic sclerosis patients. *Microvascular Research*, 106:39–43, 2016.

[171] Lacy A Holowatz, Caitlin S Thompson-torgerson, and W Larry Kenney. The human cutaneous circulation as a model of generalized microvascular function. *J Appl Physiol*, 105(1):370–372, 2008.

[172] F. Jung, G. Pindur, P. Ohlmann, G. Spitzer, R. Sternitzky, R. P. Franke, B. Leithäuser, S. Wolf, and J. W. Park. Microcirculation in hypertensive patients. *Biorheology*, 50(5-6):241–255, 2013.

[173] Chris W. McIntyre, Stephen G. John, and Helen J. Jefferies. Advances in the cardiovascular assessment of patients with chronic kidney disease. *NDT Plus*, 1(6):383–391, 2008.

[174] William E. Moody, Nicola C. Edwards, Melanie Madhani, Colin D. Chue, Richard P. Steeds, Charles J. Ferro, and Jonathan N. Townend. Endothelial dysfunction and cardiovascular disease in early-stage chronic kidney disease: Cause or association? *Atherosclerosis*, 223(1):86–94, 2012.

[175] Chrysoula Pipili, Eirini Grapsa, Elli Sophia Tripodaki, Sophia Ioannidou, Christos Manetos, Maria Parisi, and Serafim Nanas. Changes in skeletal muscle microcirculation after a hemodialysis session correlates with adequacy of dialysis. *International Journal of Nephrology and Renovascular Disease*, 8:59–64, 2015.

[176] Toshihide Naganuma, Yoshiaki Takemoto, Tetsuo Shoji, Eiji Ishimura, Mikio Okamura, and Tatsuya Nakatani. Cerebral Microbleeds Predict Intracerebral Hemorrhage in Hemodialysis Patients. *Stroke; a journal of cerebral circulation*, 46(8):2107–2112, 2015.

[177] Nicos Mitsides, Tom Cornelis, Natascha J.H. Broers, Nanda M.P. Diederen, Paul Brenchley, Frank M. Van Der Sande, Casper G. Schalkwijk, Jeroen P. Kooman, and Sandip Mitra. Extracellular overhydration linked with endothelial dysfunction in the context of inflammation in haemodialysis dependent chronic kidney disease. *PLoS ONE*, 12(8):1–15, 2017.

[178] Erik Mistrík, Sylvie Dusilová Sulková, Vladimír Bláha, Marta Kalousová, Jirí Knzek, Petr Moucka, Vladimr Herout, Mirko Kadlec, Roman Stilec, and Lubos Sobotka. Evaluation of skin microcirculation during hemodialysis. *Renal Failure*, 32(1):21–26, 2010.

[179] Erik Mistrík, Sylvie Dusilová-Sulková, Vladimír Bláha, and Luboš Sobotka. Plasma albumin levels correlate with decreased microcirculation and the development of skin defects in hemodialyzed patients. *Nutrition*, 26(9):880–885, 2010.

[180] Stephen L. Seliger, Shabnam Salimi, Valerie Pierre, Jamie Giffuni, Leslie Katzel, and Afshin Parsa. Microvascular endothelial dysfunction is associated with albuminuria and CKD in older adults. *BMC Nephrology*, 17(1):1–8, 2016.

[181] Michael Welter and Heiko Rieger. Interstitial Fluid Flow and Drug Delivery in Vascularized Tumors: A Computational Model. *PLoS ONE*, 8(8), 2013.

[182] MaggieS El-Nahid and AliM El-Ashmaoui. Functional and structural abnormalities of the skin microcirculation in hemodialysis patients. *The Egyptian Journal of Internal Medicine*, 26(3):116, 2014.

[183] K Amann, G Wiest, G Zimmer, N Gretz, E Ritz, and G Mall. Reduced capillary density in the myocardium of uremic rats–a stereological study. *Kidney international*, 42(5):1079–1085, 1992.

[184] Kerstin Amann and Eberhard Ritz. Microvascular disease - the Cinderella of uraemic heart disease. *Nephrology, dialysis, transplantation : official publication of the European Dialysis and Transplant Association - European Renal Association*, 15(September 1999):1493–1503, 2000.

[185] Arend-Jan Meinders, Laurens Nieuwenhuis, Can Ince, Willem-Jan Bos, and Paul W.G. Elbers. Haemodialysis Impairs the Human Microcirculation Independent from Macrohemodynamic Parameters. *Blood Purification*, 40(1):38–44, 2015.

[186] Hans Ulrich Prommer, Johannes Maurer, Karoline Von Websky, Christian Freise, Kerstin Sommer, Hamoud Nasser, Rudi Samapati, Bettina Reglin, Pedro Guimarães, Axel Radlach Pries, and Uwe Querfeld. Chronic kidney disease induces a systemic microangiopathy, tissue hypoxia and dysfunctional angiogenesis. *Scientific Reports*, 8(1):1–14, 2018.

[187] Dorothea Burkhardt, Maria Bartosova, Betti Schaefer, Niels Grabe, Bernd Lahrmann, Hamoud Nasser, Christian Freise, Axel Schneider, Anja Lingnau, Petra Degenhardt, Bruno Ranchin, Peter Sallay, Rimante Cerkauskiene, Michal Malina, Gema Ariceta, Claus Peter Schmitt, and Uwe Querfeld. Reduced microvascular density in omental biopsies of children with chronic kidney disease. *PLoS ONE*, 11(11):1–14, 2016.

[188] S. Beckert, K. Sundermann, S. Wolf, A. Königsrainer, and S. Coerper. Haemodialysis is associated with changes in cutaneous microcirculation in diabetes mellitus. *Diabetic Medicine*, 26(1):89–92, 2009.

[189] E. Lanzarone, P. Liani, G. Baselli, and M. L. Costantino. Model of arterial tree and peripheral control for the study of physiological and assisted circulation. *Medical Engineering and Physics*, 29(5):542–555, 2007.

[190] Nico Westerhof, F Bosman, C J De Vries, and Abraham Noordergraaf. Analog studies of the human systemic arterial tree. *J. Biomech.*, 2(2):121–43, 1969.

[191] W M Swanson and R E Clark. Cardiovascular system simulation re- quirements, design and performance. *J. Bioeng.*, 1977.

[192] Yuan-Cheng Fung. *Biomechanics*. Springer New York, New York, NY, 1993.

[193] Rodney J Levick. *An Introduction to Cardiovascular Physiology*, volume i. 5 edition, 2009.

[194] Silverthorn. *Human Physiology*. 2010.

[195] Ettore Lanzarone. *Il ruolo attivo dell'endotelio nella risposta sistemica ad una perfusione continua o pulsatile*. Phd thesis, Politecnico di Milano, 2008.

[196] T W Secomb, R Hsu, and A R Pries. A model for red blood cell motion in glycocalyx-lined capillaries. *The American journal of physiology*, 274(3 Pt 2):H1016–22, mar 1998.

[197] T. Secomb, R. Hsu, and A. Pries. Motion of red blood cells in a capillary with an endothelial surface layer: effect of flow velocity. *American Journal of Physiology. Heart and Circulatory Physiology*, 281(2):H629–36, 2001.

[198] Young Il Cho and Daniel J. Cho. Hemorheology and microvascular disorders. *Korean Circulation Journal*, 41(6):287–295, 2011.

[199] Laurence T. Baxter and Rakesh K. Jain. Transport of fluid and macromolecules in tumors. II. Role of heterogeneous perfusion and lymphatics. *Microvascular Research*, 40(2):246–263, sep 1990.

[200] Database from INTERREG IT-CH 2007-2013: DialysIS (Dialysis therapy between Italy and Switzerland) Project - Grant ID 33570710. `www.dialysis-project.eu`.

[201] Domenico Vito, Giustina Casagrande, Camilla Bianchi, and Maria L. Costantino. How to extract clinically useful information from large amount of dialysis related stored data. *Proceedings of the Annual International Conference of the IEEE Engineering in Medicine and Biology Society, EMBS*, 2015-Novem:6812–6815, 2015.

[202] G. W. Schmid-Schonbein. Microlymphatics and lymph flow. *Physiological Reviews*, 70(4):987–1028, oct 1990.

[203] Andrea Moriondo, Federica Boschetti, Francesca Bianchin, Simone Lattanzio, Cristiana Marcozzi, and Daniela Negrini. Tissue contribution to the mechanical features of diaphragmatic initial lymphatics. *Journal of Physiology*, 588(20):3957–3969, 2010.

[204] Domenico Notaro, Laura Cattaneo, Luca Formaggia, Anna Scotti, and Paolo Zunino. A mixed finite element method for modeling the fluid exchange between microcirculation and tissue interstitium. In Giulio Ventura and Elena Benvenuti, editors, *Advances in Discretization Methods: Discontinuities, Virtual Elements, Fictitious Domain Methods*, pages 3–25. Springer International Publishing, Cham, 2016.

[205] Domenico Notaro. Mixed finite element methods for coupled 3d/1d fluid problems. Master's thesis, Politecnico di Milano, 2015.

[206] Luca Possenti, Simone Di Gregorio, Fannie Maria Gerosa, Giorgio Raimondi, Giustina Casagrande, Maria Laura Costantino, and Paolo Zunino. A computational model for microcirculation including Fahraeus-Lindqvist effect, plasma skimming and fluid exchange with the tissue interstitium. *International Journal of Numerical Methods in Bioengineering*, in press.

[207] Russell T Carr and Jewen Xiao. Plasma Skimming in Vascular Trees: Numerical Estimates of Symmetry Recovery Lengths. *Microcirculation*, 2(4):345–353, jan 1995.

[208] John M. Higgins, David T. Eddington, Sangeeta N. Bhatia, and L. Mahadevan. Statistical dynamics of flowing red blood cells by morphological image processing. *PLoS Computational Biology*, 5(2), 2009.

[209] Mostafa Sefidgar, M Soltani, Kaamran Raahemifar, and Hossein Bazmara. Effect of Fluid Friction on Interstitial Fluid Flow Coupled with Blood Flow through Solid Tumor Microvascular Network Effect of Fluid Friction on Interstitial Fluid Flow Coupled with Blood Flow through Solid Tumor Microvascular Network. *Computational and Mathematical Methods in Medicine*, 2015(MAY 2015), 2016.

[210] T. Köppl and B. Wohlmuth. Optimal A Priori Error Estimates for an Elliptic Problem with Dirac Right-Hand Side. *SIAM Journal on Numerical Analysis*, 52(4):1753–1769, jan 2014.

[211] Franco Brezzi and Michel Fortin. *Mixed and hybrid finite element methods*, volume 15 of *Springer Series in Computational Mathematics*. Springer-Verlag, New York, 1991.

[212] Alfio Quarteroni. *Modellistica numerica per problemi differenziali*. Springer-Verlag, Milan, Italy, 3rd edition, 2006.

[213] Vladimir Kozlov, Sergei Nazarov, and German Zavorokhin. A fractal graph model of capillary type systems. *Complex Variables and Elliptic Equations*, pages 1–25, 2017.

[214] Francis Cassot, Frederic Lauwers, Céline Fouard, Steffen Prohaska, and Valerie Lauwers-Cances. A novel three-dimensional computer-assisted method for a quantitative study of microvascular networks of the human cerebral cortex. *Microcirculation*, 13(1):1–18, 2006.

[215] Navid Safaeian, Mathieu Sellier, and Tim David. A computational model of hemodynamic parameters in cortical capillary networks. *Journal of Theoretical Biology*, 271(1):145–156, 2011.

[216] Sylvie Smith, Amy and Larue, Anne and Peyrounette, Myriam and Lorthois. Structural and hemodynamic comparison of synthetic and anatomical cerebral capillary networks. In *22nd Congress of the European Society of Biomechanics*, volume 2016, 2016.

[217] Kim. E. Barret et al. *Ganong's Review of Medical Physiology*. 2012.

[218] B. J. McGuire and T W Secomb. Estimation of capillary density in human skeletal muscle based on maximal oxygen consumption rates. *American Journal of Physiology-Heart and Circulatory Physiology*, 285(6):H2382–H2391, dec 2003.

[219] J R Levick. Capillary filtration-absorption balance reconsidered in light of dynamic extravascular factors. *Experimental physiology*, 76:825–857, 1991.

[220] Suhas V. Patankar. Numerical heat transfer and fluid flow. 67, 01 1980.

[221] L. Possenti, G. Casagrande, S. Di Gregorio, M.L. Costantino, and P. Zunino. A finite element model of the vascular fluid balance at the microscale: influence of a non-linear model of the lymphatic system. *Microvascular Research*, in press.

[222] S Saltelli, A and Ratto, M and Andres, T and Campolongo, F and Cariboni, J and Gatelli, D and Saisana, M and Tarantola. *Global sensitivity analysis. The primer*. Number c. John Wiley & Sons Ltd, Chichester, England, 2008.

[223] J. Cariboni, D. Gatelli, R. Liska, and A. Saltelli. The role of sensitivity analysis in ecological modelling. *Ecological Modelling*, 203(1-2):167–182, 2007.

[224] M D Morris. Factorial plans for preliminary computational experiments. *Technometrics*, 33(2):161–174, 1991.

[225] F Campolongo. Sensitivity analysis of an environmental model: an application of different analysis methods. *Reliability Engineering & System Safety*, 57(1):49–69, 1997.

[226] F. Campolongo, A. Saltelli, N. R. Jensen, J. Wilson, and J. Hjorth. The role of multiphase chemistry in the oxidation of dimethylsulphide (DMS). A latitude dependent analysis. *Journal of Atmospheric Chemistry*, 32(3):327–356, 1999.

[227] E. M. Saltelli, A and Chan, K. and Scott. *Sensitivity Analysis*. John Wiley & Sons Ltd, 2000.

[228] Francesca Campolongo, Jessica Cariboni, and Andrea Saltelli. An effective screening design for sensitivity analysis of large models. *Environmental Modelling and Software*, 22(10):1509–1518, 2007.

[229] Fuat Yilmaz and Mehmet Yasar Gundogdu. A critical review on blood flow in large arteries; relevance to blood rheology, viscoisty models and physiologic conditions. *Kore-Australia Rheology Journal*, 20(4):197–211, 2008.

[230] Tatsuya Osaki, Vivek Sivathanu, and Roger D. Kamm. Engineered 3D vascular and neuronal networks in a microfluidic platform. *Scientific Reports*, 8(1):1–13, 2018.

[231] J. Cooper McDonald, David C. Duffy, Janelle R. Anderson, Daniel T. Chiu, Hongkai Wu, Olivier J.A. Schueller, and George M. Whitesides. Fabrication of microfluidic systems in poly(dimethylsiloxane), 200.

[232] Seok Chung, Ryo Sudo, Peter J. MacK, Chen Rei Wan, Vernella Vickerman, and Roger D. Kamm. Cell migration into scaffolds under co-culture conditions in a microfluidic platform. *Lab on a Chip*, 9(2):269–275, 2009.

[233] Jean Ollion, Julien Cochennec, François Loll, Christophe Escudé, and Thomas Boudier. TANGO: A generic tool for high-throughput 3D image analysis for studying nuclear organization. *Bioinformatics*, 29(14):1840–1841, 2013.

[234] Amogh Sivarapatna, Mahboobe Ghaedi, Andrew V. Le, Julio J. Mendez, Yibing Qyang, and Laura E. Niklason. Arterial specification of endothelial cells derived from human induced pluripotent stem cells in a biomimetic flow bioreactor. *Biomaterials*, 53:621–633, 2016.

[235] *ANSYS Fluent User's Guide*.

[236] P. M. Luckett, J. Fischbarg, J. Bhattacharya, and S. C. Silverstein. Hydraulic conductivity of endothelial cell monolayers cultured on human amnion. *American Journal of Physiology-Heart and Circulatory Physiology*, 256(6):H1675–H1683, 1989. PMID: 2735436.

[237] Ida Giardino, Maria D'Apolito, Michael Brownlee, Angela Bruna Maffione, Anna Laura Colia, Michele Sacco, Pietro Ferrara, and Massimo Pettoello-Mantovani. Vascular toxicity of urea, a new old player in the pathogenesis of chronic renal failure induced cardiovascular diseases. *Turk Pediatri Arsivi*, 52(4):187–193, 2017.

[238] Maria D'Apolito, Xueliang Du, Haihong Zong, Alessandra Catucci, Luigi Maiuri, Tiziana Trivisano, Massimo Pettoello-mantovani, Angelo Campanozzi, Valeria Raia, Jeffrey E Pessin, Michael Brownlee, and Ida Giardino. Urea-induced ROS generation causes insulin resistance in mice with chronic renal failure. *Insulin*, 120(1):203–213, 2010.

[239] Eric Trécherel, Corinne Godin, Christophe Louandre, Joyce Benchitrit, Sabrina Poirot, Jean Claude Mazière, Ziad A. Massy, and Antoine Galmiche. Upregulation of BAD, a pro-apoptotic protein of the BCL2 family, in vascular smooth muscle cells exposed to uremic conditions. *Biochemical and Biophysical Research Communications*, 417(1):479–483, 2012.

[240] N. D. Vaziri, J. Yuan, and K. Norris. Role of urea in intestinal barrier dysfunction and disruption of epithelial tight junction in CKD. *American Journal of Nephrology*, 37(1):1–6, 2014.

[241] Maria D'Apolito, Xueliang Du, Daniela Pisanelli, Massimo Pettoello-Mantovani, Angelo Campanozzi, Ferdinando Giacco, Angela Bruna Maffione, Anna Laura Colia, Michael Brownlee, and Ida Giardino. Urea-induced ROS cause endothelial dysfunction in chronic renal failure. *Atherosclerosis*, 239(2):393–400, apr 2015.

[242] Laetitia Koppe, Elsa Nyam, Kevin Vivot, Jocelyn E.Manning Fox, Xiao Qing Dai, Bich N. Nguyen, Dominique Trudel, Camille Attané, Valentine S. Moullé, Patrick E. MacDonald, Julien Ghislain, and Vincent Poitout. Urea impairs β cell glycolysis and insulin secretion in chronic kidney disease. *Journal of Clinical Investigation*, 126(9):3598–3612, 2016.

[243] John M. Tarbell. Shear stress and the endothelial transport barrier. *Cardiovascular Research*, 87(2):320–330, 2010.

[244] Cerami a. Bucala R, Tracey KJ. Advanced glycosylation produces quench nitric oxide and mediate defective endothelium-dependent vasodilation in experimental diabetes. *J Clin Invest*, 87(2):432–438, 1991.

[245] Xiaomei Ren, Liqun Ren, Qin Wei, Hua Shao, Long Chen, and Naifeng Liu. Advanced glycation end-products decreases expression of endothelial nitric oxide synthase through oxidative stress in human coronary artery endothelial cells. *Cardiovascular Diabetology*, 16(1):1–12, 2017.